Gaseous Oxo-Clusters as Model Systems for C–H Bond Activation and Oxidation Processes

–

Towards a Better Understanding of Catalytic Mechanisms

vorgelegt von
Diplom-Chemiker
Nicolas Paul Richard Dietl
aus Berlin

Von der Fakultät II - Mathematik und Naturwissenschaften
der Technischen Universität Berlin
zur Erlangung des akademischen Grades
Doktor der Naturwissenschaften

–Dr. rer. nat.–

genehmigte Dissertation

Promotionsausschuss:

Vorsitzender	Prof. Dr. rer. nat. Martin Lerch
1. Berichterstatter	Prof. Dr. rer. nat. Drs. h.c. Helmut Schwarz
2. Berichterstatter	Prof. Dr. scient. Einar Uggerud

Tag der wissenschaftlichen Aussprache: 01.03.2013

Berlin 2013
D83

Für Sabrina

„I have been and still am a seeker, but I have ceased to question stars and books; I have begun to listen to the teaching my blood whispers to me."

– Hermann Hesse, *Demian*

Acknowledgment

First of all, I would like to thank my supervisor Prof. Dr. Drs. h.c. **Helmut Schwarz** for giving me the chance to carry out my Ph.D. in his group, as well as for his kind generosity concerning traveling fees and the ongoing supply on scientific resources and inspiration. Due to this support, the past three and a half years were truly a unique experience.

Furthermore, I am truly grateful to Prof. Dr. **Einar Uggerud** for accepting my request to become the second supervisor of this thesis, even though this meant to travel all the way from Oslo to Berlin. Moreover, my thanks go to Prof. Dr. **Martin Lerch** for being president of the examination committee.

I also would like to thank all the friendly people over the world I had the chance to talk and work with during the conduction of the work presented here. Besides many more, this particularly includes: Prof. **Martin Beyer**, Dr. **Robert Höckendorf**, Dr. **Christian van der Linde**, Dr. **Marianne Engeser**, Dr. **Knut Asmis**, Dr. **Torsten Wende**, Dr. **Anna Troiani**, Prof. **Giulia de Petris**, Prof. **Yitzhak Apeloig** and Dr. **Xinhao Zhang**.

Concerning my time at the TU Berlin, I am very grateful to the people I worked with who made it an enriching period in my life: First and foremost, I would like to thank Dr. **Maria Schlangen** for her countless support and many hours of proofreading - I hope that one day I will become just half as patient and supportive as you are. Moreover, I am very grateful to Dr. **Burkhard Butschke** who turned in the past years from a distinguished colleague to a real friend. Further, my thanks go also to Dr. **Robert Kretschmer** whose creative and open manner was a veritable source of joy and inspiration. Certainly, I am indebted to Dr. **Thomas Weiske** for his essential assistance concerning the technical maintenance of the machines. Last but not least, I am grateful to all my colleagues in the group, past and present, for their kind support and their ongoing contribution to the pleasant working atmosphere, including **Andrea Beck**, **Tom Burks**, **Jia-Bi Ma**, Dr. **Francesca Novara**, Dr. **Nicole Rijs**, Dr. **Zhe-Chen Wang**, Dr. **Xiao-Nan Wu** and Dr. **Hai-Tao Zhao**.

More personally, I warmly express my gratitude to all of my friends in- and outside of the university. Notably, I would specially like to thank **Adrian Carl**, **Björn Eckhardt** and **Verena Strempel** for our „weekly therapy session“ at lunch time as well as some of the best nights of my life. Furthermore, I am truly indebted to my family, especially my parents **Barbara** and **Volkmar**, as well as my sister **Stella**, for their infinite support along my personal way.

Finally, my last and biggest „Thank You“ goes to **Sabrina** - trying to put into words how you supported and helped me throughout these difficult three and a half years would be simply reductive. I could not have been through all of this without you. You complete me!

Zusammenfassung

Die vorliegende Arbeit strebt durch Kombination massenspektrometrischer Untersuchungen mit quantenchemischen Rechnungen ein verbessertes Verständnis über die elementaren Schritte katalytischer Prozesse an. Hierzu werden systematisch ausgewählte Oxid-Cluster mittels unterschiedlicher Ionisierungsmethoden erzeugt und anschließend auf ihre elektronische Struktur sowie auf ihre Reaktivität gegenüber verschiedenen Kohlenwasserstoffen untersucht. Die zugehörigen Reaktionsmechanismen werden mit Isotopenmarkierungs-Experimenten und DFT- und *ab initio*-Rechnungen aufgeklärt.

Durch vergleichende Reaktivitätsstudien mit massenselektierten, heteronuklearen Vanadium-Phosphor-Sauerstoff-Clusterionen unterschiedlicher Stöchiometrie werden die spezifischen Eigenschaften beider Elemente in ihrer Reaktivität gegenüber kleinen Kohlenwasserstoffen verdeutlicht. Bezüglich der homolytischen C−H-Bindungsaktivierung zeigt sich - im Widerspruch zu früheren Annahmen aus oberflächenbasierten Studien - eine bemerkenswerte Reaktivität der phosphorhaltigen Cluster, die in bestimmten Fällen die Reaktivität der analogen Vanadiumcluster sogar übersteigt. Nicht zuletzt ermöglicht die Kombination beider Elemente die Erzeugung völlig neuer Reaktionsprodukte: Während Phosphor die homolytische C−H-Bindungsaktivierung erleichtert, kommt der Gegenwart von Vanadium im Cluster durch dessen höheres Redoxpotential eine Schlüsselrolle zu. Das enorme Interesse an solchen Systemen hängt auch mit ihrer engen Beziehung zu den *VPO*-Katalysatoren zusammen, die in der heterogenen Katalyse eine große Anwendung finden, obwohl die zu Grunde liegenden Mechanismen noch größtenteils im Dunkeln liegen.

Desweiteren wird die aktuelle Diskussion über die strukturellen und elektronischen Voraussetzungen für die Übertragung eines Wasserstoffatoms aufgegriffen und analysiert. In vorangegangenen und hier aufgegriffenen Studien zu massenselektierten Aluminiumoxid-Clustern zeigt sich, dass die Spindichte am abstrahierenden Atom ein entscheidendes Kriterium für die homolytische Aktivierung starker und chemisch inerter C−H-Bindungen darstellt. Dies gilt auch für die Reaktivität der kleinen, zweiatomigen Systeme $[CuO]^+$, $[CO]^{\bullet+}$ und $[SiO]^{\bullet+}$ gegenüber Methan. $[CuO]^+$ wurde vor ca. zehn Jahren ein hohes Potenzial für die Umwandlung von Methan zu Methanol vorausgesagt; der experimentelle Beweis liegt nun in dieser Arbeit vor. Weiterhin bildet $[CO]^{\bullet+}$ mit Methan drei verschiedene Reaktionsprodukte, während $[SiO]^{\bullet+}$ einzig via Wasserstoffatomabstraktion reagiert. Eine theoretische Analyse der zugrunde liegenden Wasserstoffatomtransfer-Prozesse ergibt zwei unterschiedliche Reaktionsmechanismen, und ein Vergleich mit den schwereren Metalloxiden der 14. Gruppe unterstreicht die besondere Rolle des Kohlenstoff als p-Element der 2 Periode.

Abschließend werden regioselektive C−H und C−C Bindungsaktivierungen in Ion/Molekül-Reaktionen unterschiedlicher Metalloxid-Kationen $[MO]^+$ (M = Mg, Ca, Mn) mit Valeronitril (n-C_4H_9CN) beschrieben, die weitere Beweise für das Konzept der *Remote Functionalization* in der Gasphase liefern.

Abstract

In the present thesis, various fundamental chemical processes with relevance to catalytic reaction mechanisms are addressed by means of mass spectrometric experiments in conjunction with quantum-chemical calculations. Selected oxygen-containing gas-phase clusters are generated by various ionization methods, *e.g.* electrospray ionization or laser desorption/ionization, and further probed in terms of their electronic structure as well as their reactivity towards several hydrocarbons; the associated reaction mechanisms are revealed using isotope-labeling studies and state-of-the-art DFT and *ab initio* calculations.

In reactivity studies with mass-selected, mixed vanadium-phosphorous oxygen-cluster ions of various stoichiometries, the intrinsic features of both elements, *i.e.* vanadium and phosphorous, become obvious when comparing their reactivity towards small hydrocarbons, respectively. Hence, contrary to earlier assumptions based on surface studies, phosphorous-containing oxo-clusters exhibit a remarkable reactivity in terms of C−H bond activation, exceeding in certain cases the reactivity of the analogous vanadium-containing cluster ions. Furthermore, the combination of both elements enables completely new product distribution by taking advantage of their intrinsic features; while phosphorous is much more reactive in terms of homolytic C−H bond activation, the presence of vanadium in the cluster represents a key factor in terms of its redox-chemistry potential. These results are of particular interest with respect to the so-called *VPO*-catalysts that are widely used in industry, even though their underlying reaction mechanisms are only poorly understood.

Moreover, the ongoing discussion on the nature and structural and electronic prerequisites of hydrogen-atom transfer processes are summarized and discussed. As convincingly demonstrated in previous and present studies on mass-selected aluminum-oxide clusters, a high spin density at the abstracting atom is a requirement to bring about the homolytic activation of strong and chemically inert C−H bonds in the gas phase at ambient conditions. This holds true also for small diatomic systems, as shown for the ion/molecule reaction of $[CuO]^+$, $[CO]^{\bullet+}$, and $[SiO]^{\bullet+}$ with methane, respectively. $[CuO]^+$ was predicted a decade ago to be an effective methane-to-methanol converter, which is finally proven in this work. Regarding the main-group oxides, $[CO]^{\bullet+}$ gives rise to three different reaction channels, while $[SiO]^{\bullet+}$ reacts only via hydrogen-atom transfer. A theoretical analysis of the respective HAT processes reveals two distinctly different mechanistic pathways, and a comparison with the heavier metal oxides of group 14 emphasizes the particular role of carbon as a second row p element.

Finally, deuterium-labeling experiments and computational studies reveal the regioselective gas-phase C−H and C−C bond activation for the reaction of valeronitrile (n-C_4H_9CN) with different metal-oxide cations $[MO]^+$ (M = Mg, Ca, Mn), thus providing further evidences for the concept of *remote functionalization* in the gas phase.

Parts of this work have been published:

- *Room-Temperature C−H Bond Activation of Methane by Bare* $[P_4O_{10}]^{\bullet+}$, N. Dietl, M. Engeser, H. Schwarz, *Angew. Chem. Int. Ed.* **2009**, *48*, 4863.
- *Competitive Hydrogen-Atom Abstraction versus Oxygen-Atom and Electron Transfers in Gas-Phase Reactions of* $[X_4O_{10}]^{\bullet+}$ *(X = P, V) with* C_2H_4, N. Dietl, M. Engeser, H. Schwarz, *Chem. Eur. J.* **2010**, *16*, 4452.
- *Generation, Reactivity Towards Hydrocarbons, and Electronic Structure of Heteronuclear Vanadium Phosphorous Oxygen Cluster Ions*, N. Dietl, R. F. Höckendorf, M. Schlangen, M. Lerch, M. K. Beyer, H. Schwarz, *Angew. Chem. Int. Ed.* **2011**, *50*, 1466.
- *Directed, Remote Gas-Phase C−H and C−C Bond Activations by Metal Oxide Cations Anchored to a Nitrile Group*, N. Dietl, M. Schlangen, H. Schwarz, *Chem. Eur. J.* **2011**, *17*, 1783.
- *Diatomic* $[CuO]^+$ *and Its Role in the Spin-Selective Hydrogen- and Oxygen-Atom Transfers in the Thermal Activation of Methane*, N. Dietl, C. van der Linde, M. Schlangen, M. K. Beyer, H. Schwarz, *Angew. Chem. Int. Ed.* **2011**, *50*, 5068.
- *Thermal Hydrogen-Atom Transfer from Methane: The Role of Radicals and Spin States in Oxo-Cluster Chemistry* , N. Dietl, M. Schlangen, H. Schwarz, *Angew. Chem. Int. Ed.* **2012**, *51*, 5544.
- *Gas-Phase Reactions of Cationic Vanadium-Phosphorous Oxide Clusters with* C_2H_x *(x = 4,6): A DFT-based Analysis of Reactivity Patterns*, N. Dietl, X. Zhang, C. van der Linde, M. K. Beyer, M. Schlangen, H. Schwarz, *Chem. Eur. J.* **2013**, *19*, 3017.
- *Structure and Chemistry of the Heteronuclear Oxo-Cluster* $[VPO_4]^{\bullet+}$*: A Model System for the Gas-phase Oxidation of Small Hydrocarbons*, N. Dietl, T. Wende, K. Chen, M. Schlangen, X. Zhang, K. R. Asmis, H. Schwarz, *J. Am. Chem. Soc.* **2013**, *135*, 3711.
- *Mechanistic Aspects of Gas-phase Hydrogen-Atom Transfer from Methane to* $[CO]^{\bullet+}$ *and* $[SiO]^{\bullet+}$*: Why do They Differ?*, N. Dietl, A. Troiani, M. Schlangen, O. Ursini, G. Angelini, Y. Apeloig, G. de Petris, H. Schwarz, *Chem. Eur. J.* **2013**, *DOI: 10.1002/chem.201204157*.

Contents

1 Introduction

„Dem Anwenden muss das Erkennen vorausgehen“ [1]

– Max Planck

In the Middle Ages, small amounts of sulfuric acid were obtained by burning sulfur in the presence of humid air and nitric acid. After the discovery that the need of nitric acid can be reduced by admitting additional air to the system, it was assumed that the oxidizing agent is actually the air and not the acid; [2] no one was aware of the fact that one of the very early, artificial catalytic processes was accomplished. With respect to the mechanism, sulfur reacts with molecular oxygen to sulfur dioxide only, while another oxidizing agent, *i.e.* NO_2 gases emanating from nitric acid, acts as catalyst for the oxidation to sulfur trioxide which reacts spontaneously with water to sulfuric acid (Equation 1.1). The catalytic cycle closes with the re-oxidation of NO to NO_2 (Equation 1.2). In contrast to the dictum of Max Planck (see above), it took about 500 years from the first application to the full understanding of this process.

$$S + O_2 \xrightarrow{>250\ ^\circ C} SO_2 \xrightarrow[\text{-NO}]{NO_2} SO_3 \xrightarrow{H_2O} H_2SO_4 \tag{1.1}$$

$$NO + \frac{1}{2}O_2 \longrightarrow NO_2 \tag{1.2}$$

Despite the relative recent understanding of catalysis, its first applications by human beings date back to the dawn of civilization. Already in early times, people benefited for example from various enzymes, thus facilitating the fermentation of alcohol or the preparation of acetic acid. [2] Much later, in 1823 Johann Wolfgang Döbereiner took for the first time advantage of a metallic surface to catalyze a chemical reaction; in his famous „Döbereiners Lampe“ the hydrogen-oxygen or „Knallgas“-reaction is catalyzed on a platinum surface. However, the proper term „catalysis“ was first proposed by Jöns Jakob Berzelius in 1836 after he discovered that some compounds are beneficial for a chemical process, albeit being not consumed in the course of the reaction. [3] Thus he concluded, that these chemicals must provide some „catalytical forces“ upon contact with the reactants permitting the reactions to occur; the word catalysis was chosen from the Greek word $\kappa\alpha\tau\alpha\lambda\nu\sigma\iota\zeta$, meaning „triggering“ or „dissociation“. Finally, at the end of the 19^{th} century it was Wilhelm Ostwald who developed a general definition for a catalyst which still holds valid till present. He stated that a catalyst is a substance that increases the rate of a

chemical reaction without itself being consumed in the process and that does not affect the thermodynamic equilibrium of the reactants and products. [4] Moreover, Ostwald assumed that *„...there is probably no chemical reaction which can not be influenced catalytically and there is no substance, element or compound, which cannot act as a Catalyser*". [5]

With respect to contemporary chemistry, catalysis has turned out as a powerful concept to allow for environmentally benign and economically feasible conversion of natural resources into value-added products. In fact, numerous catalysts are widely employed in large scale, industrial processes and about 90 % of all end-products encouter at least one catalytical step in their manufacturing process. [6,7] However, while the number of heterogeneous, homogeneous and enzymatic catalysts continuously increases, many chemical reactions remain to be mastered. For example, the transformation of non-activated hydrocarbons into value-added products under ambient conditions still constitutes a major challenge in many contemporary fields of chemistry; [8–13] especially, the activation and functionalization of methane as the most inert of all hydrocarbons is of particular interest and has been referred to as a *holy grail* in chemistry. [14,15] These processes are associated with two significant problems that have to be overcome and which prevail for all hydrocarbons: *i*) the C−H bond of alkanes is known to belong to the strongest and most inert single bonds in chemistry; [16] *ii*) the functionalized products are often more reactive than the hydrocarbon, thus often leading to over-oxidation. [10,17]

Concerning homogeneous catalysis, many studies have been performed in the solution phase employing a large number of metallorganic as well as organic catalysts that are capable to bring about the efficient C−H bond activation of various substrates. [18–26] The transformation of methane, however, still requires rather harsh conditions, as *e.g.* for the seminal Shilov system, using $[PtCl_6]^-$ and T = 120 °C. [27] Nevertheless, the understanding about these homogeneous systems is quite advanced with respect to reactive intermediates which are easier accessible due to many established chemical and spectroscopic methods. [20,23]

With respect to heterogeneous catalysis, numerous catalysts are presently used in industry, exhibiting extraordinary chemo-, regio-, stereo-, and enantioselectivities towards hydrocarbons; [28–32] however, compared to their extraordinary role in industrial and academic research, a detailed mechanistic knowledge of the elementary processes and a complete understanding of the functional and structural properties of the reactive sites of *e.g.* solid-state catalysts is still rather limited. [33–41] This lack of knowledge mostly origins from the high complexicity of real surfaces and the more intricate bond activation processes occurring on them.

One of many approaches to address chemistry on surfaces takes advantage of mass spectrometric techniques to investigate model systems in the gas phase. [42–57] The catalytic surface is assumed to consist of a flat and inert supporting material, and only selected

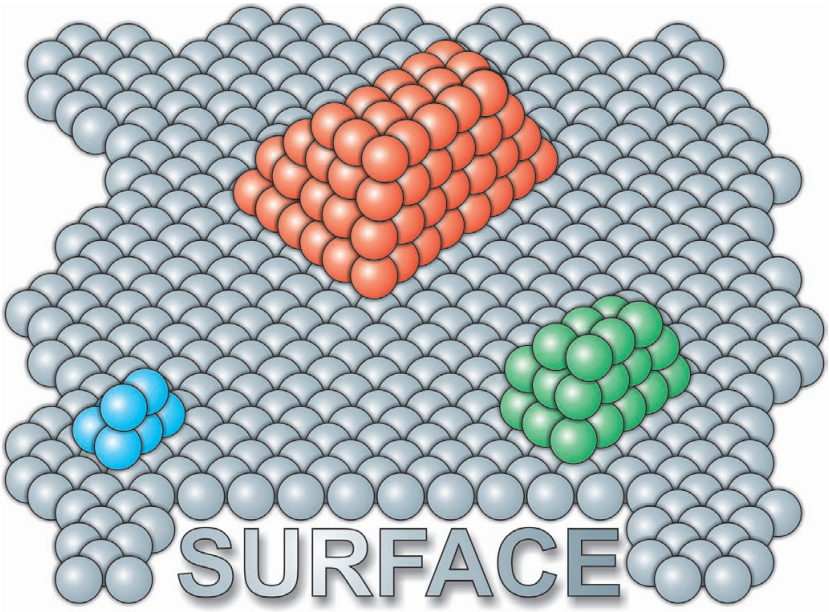

Figure 1.1: Schematic description of stoichiometric clusters (indicated in blue, green, and red) with different sizes on a surface, defining its chemical reactivity.

clusters on this surface are catalytically active (Figure 1.1). Accordingly, such clusters when generated in the gas phase have been previously proposed to serve as suitable model systems for heterogeneous catalysis to unravel possible active centers in surface-mediated bond activation processes. [47,51,58,59] Here, reactivity studies of such well-defined reagents are probed in the gas-phase environment, thus allowing further insights into the intrinsic properties of these systems. In addition to the easy purification via mass selection of the clusters, the investigation in the gas phase provides further advantages. Disturbing side-effects can be neglected, *e.g.* ion/ion interactions or solvent effects, and thus only the intrinsic features of the system affects its chemical behavior and reactivity in this solvent- and support-free environment. Furthermore, more recently developed infrared (IR) techniques enable the structural characterization of selected systems in the gas phase, [47,60–67] and quantum-chemical calculations provide a further, powerful tool to support and verify the experimental conclusions derived from gas-phase experiments. [68–70] Although the conclusions gathered by gas-phase experiments cannot directly be transferred to surface and condensed phase matters, the connection of both realms can be regarded as a fruitful liaison as shown in several studies. [51,53,71–74]

Next to heterogeneous catalysis, gas-phase studies also have proven useful to provide suitable models to explain catalytic reactivity in enzymes. A famous example represents the concept of *two-state reactivity* (TSR), [76–85] derived from the rather simple reactions of $[FeO]^{\bullet+}$ with H_2 and CH_4, [76,86–88] which is also relevant for the oxidation processes catalyzed by *e.g.* enzyme P450 or Nonheme Fe^{IV}=O complexes.[i] The $[FeO]^{\bullet+}/CH_4$ educt couple exhibits

[i] For selected examples, see [79,89–94]

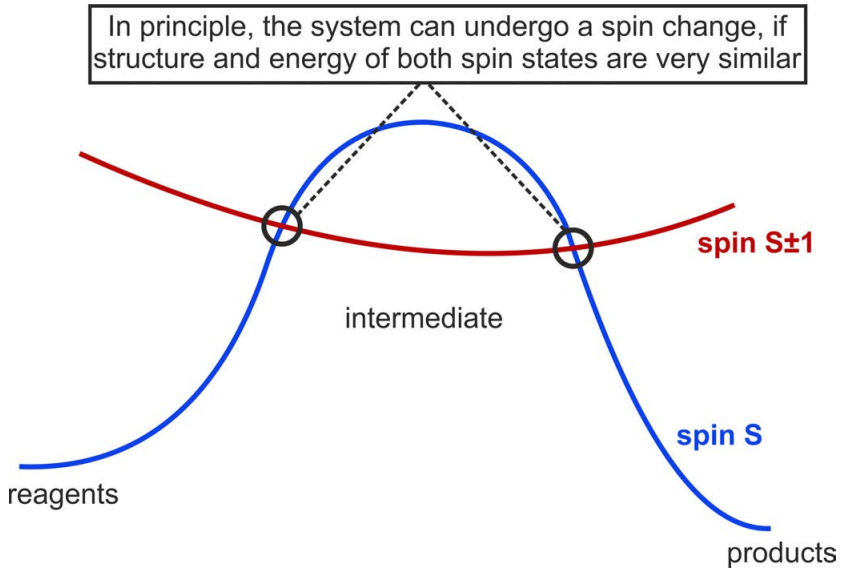

Figure 1.2: Qualitative energy profile for a two-state reactivity scenario (adapted from Ref. [75]).

a sextet ground state; however, the formation of methanol can be accelerated by a spin change to the quartet surface because thus opens up lower-energy pathways. [95] Next to TSR, also the concept of *remote functionalization* [96–99] derived from biochemistry was validated by gas-phase studies, exploring the reaction of naked metal ions with functionalized alkyl chains. [100,101]

The present thesis covers the chemical reactivity of different oxide species in the gas phase in general and is organized as follows:

i) The first part (Chapter 3) concerns the studies on model systems for the exceptional reactivity of the *VPO*-catalysts. New strategies for the generation of mixed vanadium-phosphorous oxygen cluster ions are presented, thus enabling to probe their reactivities towards a series of small hydrocarbons. Larger clusters with the general formula $[V_xP_{4-x}O_{10}]^{\bullet+}$ (x = 0 - 4) are compared by means of mass spectrometry and quantum-chemical theory, as well as the small mixed cluster $[VPO_4]^{\bullet+}$; analysis of the latter includes structural characterization with IRPD measurements and a detailed comparison to the extensively studied $[V_2O_4]^{\bullet+}$ system.

ii) The second part (Chapter 4) outlines the highly disputed discussion on various aspects of hydrogen-atom transfer, a process that is of fundamental importance for many fields of chemistry, including heterogeneous and biological catalysis. In gas phase experiments, the crucial role of the spin state in a variety of systems is revealed, ranging from larger aluminum-oxide clusters to the small diatomic $[CuO]^+$ cation. The latter ion serves as an example for another two-state reactivity scenario, and the result might help to understand

the reactivity of the copper-dependent, particulate methane monoxygenase metalloenzyme. Finally, the comparison of $[CO]^{\bullet+}$ and $[SiO]^{\bullet+}$ completes the studies on the reactivity of the metal oxides of group 14 with methane, known to be excellent mediators of hydrogen-atom transfer reactivity.

iii) In the third and last section (Chapter 5), the concept of *remote functionalization* is expanded from bare metal ions to metal-oxide cations. As a proof-of-principle system, valeronitrile (*n*-C_4H_9CN) was chosen as model substrate; further, deuterated isotopologues of *n*-C_4H_9CN are used to determine the regioselectivities in the reactions with selected metal-oxide cations $[MO]^+$ (M = Mn, Mg, Ca), respectively.

2 Experimental and Theoretical Methods

„Theories should be treated like mistresses. One should never fall in love with them and they should be discarded when the pleasure they provide is over." [102]

– Sydney Brenner

In the present work, several mass spectrometic (MS) techniques have been employed for the investigation of the chemical and physical properties of various metal-oxide clusters, including Fourier-transform ion cyclotron resonance (FT-ICR) mass spectrometry, tandem mass spectrometry, as well as infrared photodissociation spectroscopy. Further, different ionization methods have been applied to generate the ions of interest, *e.g.* electrospray ionization (ESI) and laser desorption/ionization (LDI). After a brief overview of these mass-spectrometry based tools, a general introduction into gas-phase chemistry and ion/molecule reactions is presented, and finally the theoretical and computational methods employed in this work are summarized and described briefly.

2.1 Generation of ions in the gas phase

With respect to the generation of ions, various types of ion sources have been developed in the past century, including chemical/electron ionization (EI/CI), fast-atom bombardment (FAB), or matrix-assisted laser desorption/ionization (MALDI); for the formation of various metal-oxides, investigated in this thesis, electrospray ionization (ESI) and laser desorption/ionization (LDI) have proven to be the methods of choice. In the following section, both methods and the underlying principles are described.

2.1.1 Electrospray ionization

Electrospray ionization (ESI) most probably represents the most popular ionization technique in contemporary mass spectrometry. Initially studied by Dole in the late 1960s, [103] it experienced a true revival after the landmark studies of Fenn in the 1980's, [104–106] who was finally awarded with the Nobel Prize in Chemistry in 2002 for his achievements in this field of research. [107] The „soft" generation of ions at atmospheric pressures and the subsequent transfer into the gas phase by ESI [71,72,108–111] proved to be especially useful for the generation and investigation of high-molecular weight ions, which were not accessible

under harsher ionization conditions due to unwanted fragmentations, thus resulting in a large number of applications in biomedicine [106] as well as in the field of organometallic chemistry. [71,108,109] Based on this tremendous success of ESI, other methods like *e.g.* Desorption-electrospray ionization (DESI) [112] or Sonic-spray ionization (SSI) [113] have been developed.

For the usual ESI-setup (Figure 2.1), the analyte is dissolved in millimolar quantities in a polar and volatile solvent, such as methanol, acetonitrile, isopropanol, ethanol, dichloromethane or water. [110] Then, this solution is is introduced through a fused-silica capillary at very low flow rates of 2 to 8 μl min^{-1} into the ionization source in which nitrogen gas is used as nebulizing and drying gas. A voltage of 3 - 5 kV is applied between the steel capillary and the skimmer thus inducing an electric field which causes the formation of a so-called Taylor cone [114,115] at the tip of the capillary from which small droplets emerge. Depending on the operation mode, the droplets carry an overall positive or negative

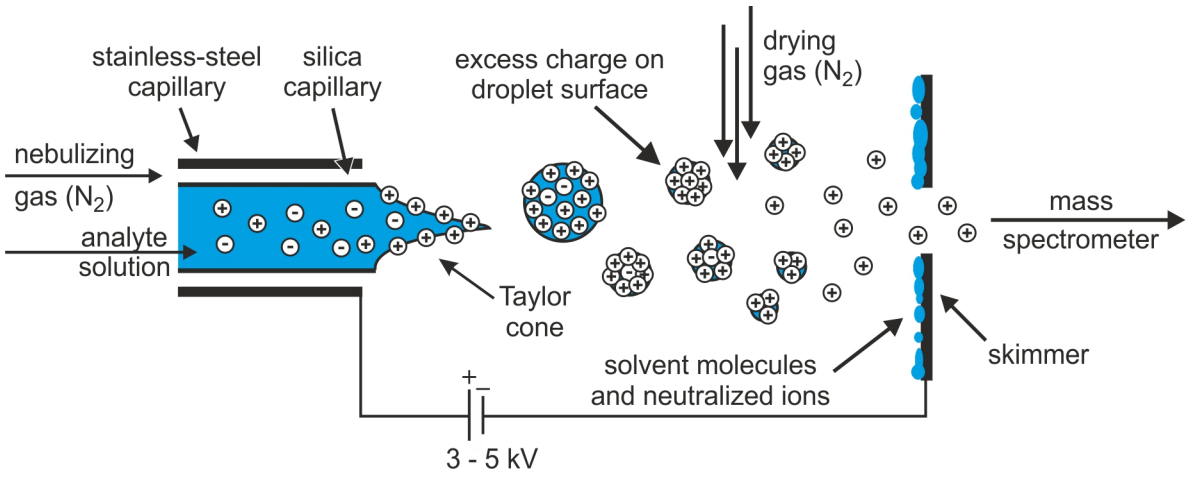

Figure 2.1: Schematic description of the electrospray-ionization process for the generation of positively charged ions.

charge, respectively, which is concentrated at their surfaces, thus leading to a strong electric repulsion among the droplets. [110,115] This effect is further increased by the drying gas (a counter-current nitrogen-gas stream) that serves as a heat supply for the evaporation of solvent molecules from the droplets; the resulting decrease in drop size increases the charge density on the droplets surface.

With respect to the mechanistic details, two models for the description of the ion formation from the droplets exist: The *charge-residue model* (CRM) of Dole, [103] and later extended by Röllgen, [116] is based on the idea that the droplets collapse in a Coulomb explosion, [117] thus producing smaller droplets. The explosion is initiated by a large amount of equally charged ions on the surface, the so-called Rayleigh limit [118,119] at which the electrostatic repulsion on the droplet surface exceeds the surface tension. [120] Also the resulting, smaller droplets undergo Coulomb explosions leading finally to the formation of one single analyte

ion. In contrast, the *ion-evaporation model* (IEM) of Thomson assumes that the increasing surface-charge density rather triggers the spontaneous ejection of a single ion from the droplet. [121,122] The prevailing mechanism depends very much on the analyte: while CRM is suggested to be valid rather for large molecules, the formation of smaller ions is better described by IEM. [110] While these two models describe the ejection/liberation of the ion into the gas phase, many different scenarios have been discussed to explain the formation of individual ions, including charge separation, gas-phase reactions, as well as electrochemical oxidation or reduction of the substrate, respectively, depending on the nature of the precursors and substrates involved in the formation process. [123] Details on the actual precursors employed in this study will follow in the respective sections.

2.1.2 Laser desorption/ionization

Laser desorption/ionization (LDI) represents another very suitable ionization techniques for the generation of metal-oxide clusters. LDI is of great importance for the generation of metal-containing cluster ions, [124,125] and is famous for the application in matrix-assisted laser desorption/ionization (MALDI) allowing the analysis of large organic molecules which tend to be fragile and fragment when ionized by more conventional ionization methods. [126–128] The development of MALDI was honored with the Nobel Prize in Chemistry in 2002 for Koichi Tanaka; [129] the MALDI technique usually employed today has been developed by Karas and Hillenkamp using an organic matrix instead of metal powders. [130,131]

The oxide clusters investigated in this thesis have been generated using a homebuilt, modified Smalley-type [132,133] cluster-ion source developed by Niedner-Schatteburg, Bondybey, and co-workers, [134,135] schematically shown in Figure 2.2. Here, a pulsed Nd:YAG laser (Continuum Surelite II, 10 Hz, 5 mJ pulse energy) is focused onto a rotating target; this is typically performed with bare metal probes, but also sintered oxide targets can be used. The impact of the laser generates a hot metal/metal-oxide plasma consisting of neutral and charged atoms which recombine to form larger clusters. The aggregation to form neutral and ionic clusters is accomplished by a synchronized, triggered carrier-gas pulse (typically around 20 bar) that consumes the excess energy released upon particle condensation. Though the carrier gas generally consists of pure helium, it proved useful for the generation of oxide cluster to add small amounts of oxidizing reagents, *e.g.* N_2O or O_2; [136–144] moreover, the addition of water to the carrier gas enables the generation of hydrated cluster and ions to study the reactivity of „solvated“ ions. [145–147] Further cooling of the cluster is achieved by supersonic expansion which efficiently converts a large fraction of the clusters internal energy into the directed translational motion by collisional coupling. The remaining small portions of internal energy correspond to low effective rotational and vibrational temperatures and thus permit the preparation of weakly-bound systems such as

van-der-Waals complexes. A critical factor for the cluster size is apparently the pulse valve. Using two different pulse valves in this study at an otherwise identical experimental set-up, the generation of bare metal clusters with $[M_x]^+$ (x = 1 - 5) or the straightforward generation of much larger metal or metal-oxide clusters can be achieved, respectively.

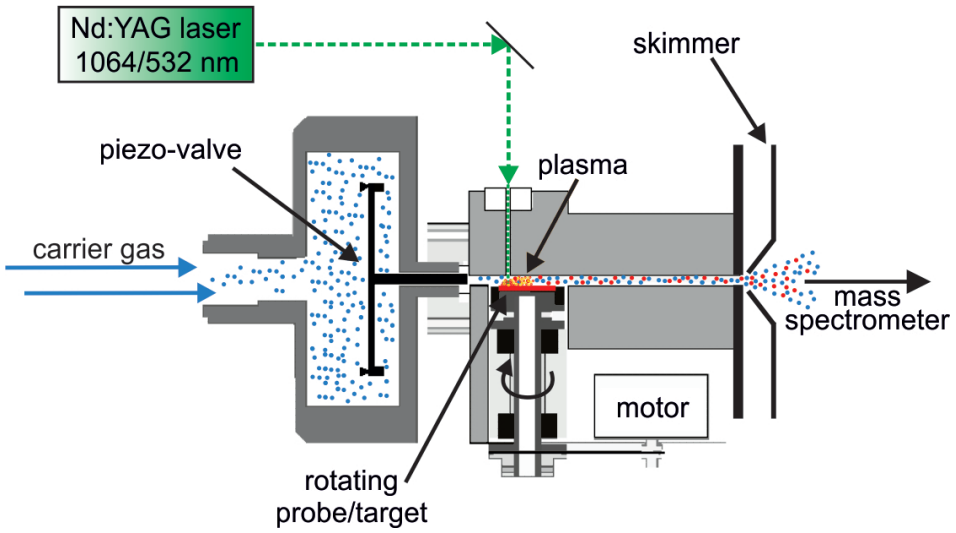

Figure 2.2: Schematic description of the Smalley-type laser desorption/ionization source for the generation of charged cluster ions.

After supersonic expansion, the molecular beam passes a skimmer and a system of electrostatic potentials and lenses which guide the ions into the analyzer cell while the neutral particles are removed by differential pumping. In this context, the time-of-flight delay, together with the pulse-valve delay, is of central importance, since it allows the separation of larger and smaller clusters (according to the molecular weight). Details on the actual targets employed in this study as well as their preparation are given in the respective sections.

2.2 Experiments with ions in the gas phase - Technical setup

The following chapter addresses the experimental setup for the reactivity as well as the collisional studies in the tandem and in the FT-ICR mass spectrometer, respectively. Next to the description of the machines, a short introduction into the fundamental physical aspects of the respective method is given. Finally, a brief summary of infrared photodissociation spectroscopy as tool for structural characterization is presented.

2.2.1 The VG BioQ triple quadrupole mass spectrometer

The ESI-MS reactivity studies were carried out on a commercial VG BioQ mass spectrometer with QHQ configuration (Q: Quadrupole; H: Hexapole); a technical draft is

depicted in Figure 2.3. [148] After the generation in the ESI process, the ions are transferred via the HV lens and the skimmer to the mass analyzer. Between these two building blocks (HV lens and skimmer), a voltage can be applied, *i.e.* the cone voltage U_C (0 - 200 V), which is crucial in terms of metal-oxide ion-formation in this instrument. More precisely, U_C determines the amount of collisional activation of the originally formed ions in the source region, [110] also referred to as *in-source collision-induced dissociation* [149] (For more details on the collisional activation process, see Section 2.3.1).

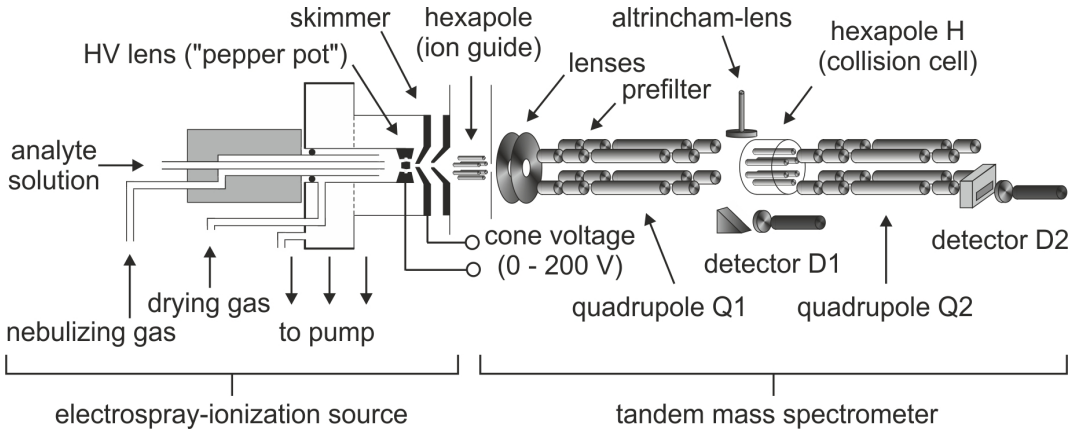

Figure 2.3: Technical draft of the commercial VG Bio-Q tandem mass spectrometer with QHQ configuration (Q: Quadrupole; H: Hexapole).

At low U_C values, solvated ions enter the vacuum system of the mass spectrometer, while weakly bound solvent molecules are evaporated at increased cone voltages. Further increase triggers the expulsion of more strongly bound ligands and even the cleavage of covalent bonds, thus resulting finally in the formation of bare metal or metal-oxide cations at highest cone voltages. [148] For example, the usage of nitrate salts $M(NO_3)_{2,3}$ (M = Ca, Co, Fe, Mg, Mn, and many more) enables the formation of the respective bare metal-oxide cations $[MO]^+$ by the elimination of $NO_2^\bullet$ from the mono-ligated $[M(NO_3)]^+$ cations (Equation 2.1). [150–153] With the choice of the right precursor, also larger metal-oxide clusters can be generated in the gas phase, as shown for various vanadium systems, [154,155] which are otherwise only accessible by use of LDI sources.

$$M(NO_3)_{2,3} \xrightarrow[-\,1{,}2\ [NO_3]^-]{\text{ESI}} [M(NO_3)]^+ \xrightarrow{\text{collision}} [MO]^+ + NO_2^\bullet \qquad (2.1)$$

After the transfer of the ions to the mass analyzer by the ion optics consisting of various lenses and two prefilters, they enter the first quadrupole mass filter Q1 followed by a hexapole H and another quadrupole Q2; the latter serves as reaction/collision cell. The quadrupoles of the instrument consist of four circular metal-rods, respectively, mounted parallel in a square arrangement to each other. [156–158] An electric potential U and a radio-frequency potential with the amplitude V and the frequency ω are applied to all four

rods, whereby the algebraic sign of the overall potential Φ_0 for the adjacent rods always differs (Equation 2.2).

$$\text{Rod}_{1,3}: \quad \Phi_0 = +(U + V \cdot cos(\omega t)) \quad \text{and} \quad \text{Rod}_{2,4}: \quad \Phi_0 = -(U + V \cdot cos(\omega t)) \tag{2.2}$$

The applied potentials on the opposing pairs of rods varies sinusoidally as $cos(\omega t)$ cycles with time t, thus confining oscillating ions which traverse the field free region along the central axis of the four poles. The oscillations result in rather complex ion trajectories, depending on the mass-to-charge ratio m/z of the ions. Specific combinations of the potentials U and V and the frequency ω result in specific ions with fixed m/z having a stable trajectory through the quadrupole. All other ions with different m/z values follow unstable trajectories and are removed by discharging collisions with the rods. However, multipoles can also be operated with radio frequency only ($U = 0$), allowing all ions to pass, thus acting as an ion guide for the transfer of ions with low kinetic energy from one region to another without substantial loss of intensity. [158] In general, the available mass range, as well as the resolution of the instrument is determined by the length and the diameter of the rod electrodes.

Though quadropoles permit a rather low mass resolution compared to other MS techniques, *e.g.* sector-field-, time-of-flight-, or FT-ICR mass spectrometer, they exhibit some advantages in terms of low price, high ion transmission, and high scan speed. [158] Hence, quadrupole mass analyzer became a valuable tool in life- and material science and Wolfgang Paul received in 1989, together with Hans Dehmelt, the Nobel Prize in Physics for his fundamental research on quadrupole mass filters and „the development of the ion trap technique“ in general. [159]

The VG BioQ mass spectrometer can be operated in various modes for structure and reactivity studies: *i*) The *MS* mode corresponds to a scan of Q1 of all ions transferred from the source region, thus recording a complete source spectrum on the first detector D1 (Figure 2.3). *ii*) The second and most important mode is the *Daughter ion* mode, applied for ion/molecule reactions and CID, in which Q1 is used for mass selection of the ion of interest which is subsequently reacted/collided with a neutral gas in the hexapole H; the corresponding product/fragment-ion spectrum is analyzed and recorded in Q2/D2. *iii*) In the *Parent ion* mode it is possible to determine those ionic species that give rise to the generation of a specific product/fragment ion upon reaction/collision with a neutral substrate in H. Here, Q2 is set to the fixed m/z value of the fragment ion, while a specified m/z range is scanned by Q1. Finally, the *iv*) *Neutral-Gain* and *v*) *Neutral-Loss* modes enable to identify those ionic species that give rise to a given mass gain and loss, respectively, upon reaction/collision with a neutral substrate in H by a linked scan of Q1 and Q2; both modes were however not employed in the investigations. In the reactivity and collisional studies,

neutral substrates are introduced into the hexapole at stationary pressures in the range of 10^{-4} – 10^{-3} mbar via an piezoelectric gas doser from Oxford Applied Research; the pressure is recorded by means of an Adwards-PRL 10 Pirani gauge head.

2.2.2 Fourier-transform ion cyclotron resonance (FT-ICR) mass spectrometry

2.2.2.1 Pysical basics of FT-ICR mass spectrometry

The general principle of FT-ICR mass spectrometry is based on the interaction of a charged particle with a magnetic field: If ions with the charge q are moving with a certain velocity $\vec{v}$ in a magnetic field $\vec{B}$, the so-called Lorentz force $\vec{F}_L$ acts upon them (Equation 2.3).

$$\vec{F}_L = q \cdot \vec{v} \cdot \vec{B} \tag{2.3}$$

As the Lorentz force operates perpendicular to the direction of the ions movement, they are confined to a circular path (in the xy-plane) which is perpendicular to both the movement and the magnetic field $\vec{B}$ (Figure 2.4a). Due to the circular motion, the ions are further exposed to the centrifugal force $\vec{F}_C$ as a function of the mass of the ions m, the angular or cyclotron frequency ω and the radius r of the circular path.

$$\vec{F}_C = m \cdot \omega^2 \cdot r \tag{2.4}$$

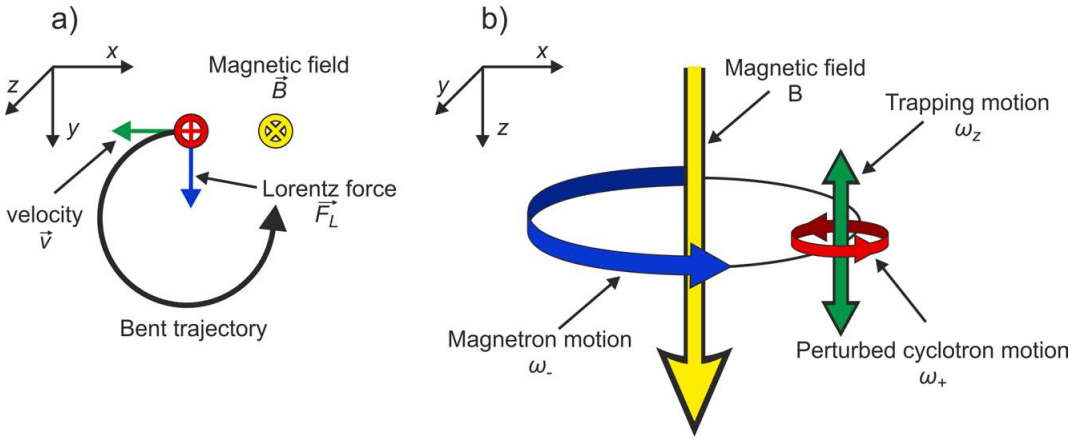

Figure 2.4: Schematic description of the motion pathways of charged particles in a magnetic field: a) Illustration of the Lorentz force as it acts on a positively charged ion; b) indication of the ion motions and the according frequencies in the ICR cell.

In order that the ions move on a stable circular path, the centrifugal force must be equal to the Lorentz force $\vec{F}_C = \vec{F}_L$; thus, taking into account that $\omega = \frac{|v|}{|r|}$ and that the magnetic field remains constant $\vec{B} = \vec{B}_0$, Equation 2.5 results. Solving the equation for the cyclotron frequency ω_c results in a direct relation to m/z, if $q = ez$ (e elementary charge) is considered (Equation 2.6). In other words, for every ion $[A]^+$ with a specific m/z ratio, a specific

cyclotron frequency $\omega_{c,[A]^+}$ can be measured experimentally. [158,160]

$$m \cdot \omega^2 \cdot r = q \cdot r \cdot \omega \cdot \vec{B_0} \tag{2.5}$$

$$\omega_c = \frac{q \cdot \vec{B_0}}{m} = \frac{e \cdot \vec{B_0}}{m/z} \tag{2.6}$$

However, Equation 2.6 only prevails for the unperturbed „cyclotron equation“, [160,161] disregarding the additional electric field that is applied to the trapping plates (See Experimental Setup, Figure 2.6) preventing the escape of the ions from the ICR cell along the z-axis. The respective force F on the ions is a function of the electrostatic potential U_{Trap}, the position along the z-axis z_{Pos}, the radius of the circular motion in the xy-plane r,[ii] and the cell parameters α, γ, and a (Equation 2.7). These latter parameters are independent from the ions since they are defined only by the geometry of the ICR cell; for cylinder-shaped cells such as in *e.g.* the Bruker Spectrospin CMS-47XFT-ICR mass spectrometer, the values are: $\alpha = 2.8404$, $\gamma = 0.2787$, and a = cell length.

$$F = q \cdot U_{Trap} \cdot \left(\gamma + \frac{\alpha \cdot (2 \cdot z_{Pos}^2 - r^2)}{a^2} \right) \tag{2.7}$$

Though this has no influence on the centrifugal force, it affects the Lorentz force, so that Equation 2.5 has to be modified with a correction term (Equation 2.8):

$$m \cdot \omega^2 \cdot r = q \cdot r \cdot \omega \cdot \vec{B} - \frac{q \cdot U_{Trap} \cdot \alpha \cdot r}{a^2} \tag{2.8}$$

The solutions of this quadratic equation in ω give the perturbed cyclotron frequency ω_+ (Equation 2.9) and the so-called magnetron frequency ω_- (Equation 2.10) which belongs to a circular motion superimposed to the cyclotron motion.

$$\omega_+ = \frac{\omega_c}{2} + \sqrt{\left(\frac{\omega_c}{2}\right)^2 - \frac{\omega_z^2}{2}} \tag{2.9}$$

$$\omega_- = \frac{\omega_c}{2} - \sqrt{\left(\frac{\omega_c}{2}\right)^2 - \frac{\omega_z^2}{2}} \tag{2.10}$$

The additional frequency ω_z corresponds to a oscillation along the z-axis, induced by the trapping plates and superimposing both circular motions (Equation 2.11).

$$\omega_z = \sqrt{\frac{2 \cdot q \cdot V_{Trap} \cdot \alpha}{m \cdot a^2}} \tag{2.11}$$

Those three oscillations cause a rather complex ion motion, indicated in Figure 2.4b.

[ii] The position in the xy-plane is originally given as $x_{Pos}^2 + y_{Pos}^2$, which corresponds, according to the theorem of Pythagoras, to r^2 used in Equation 2.7

However, as the general relation $\omega_+ >> \omega_z >> \omega_-$ applies, only the perturbed cyclotron frequency ω_+ is recorded in terms of mass analysis. [160,162]

The orbital ion motion described above does not by itself generate an observable electrical signal at the detection plates [162] because the ions with the same frequency and radius enter the cell at different times and do thus not have the same phase. Hence, the statistical distribution of the ions phase angles for a given m/z value must be transformed into a coherent one to enable the detection of one characteristic cyclotron frequency. This is achieved by excitation via a radio-frequency pulse which brings all ions (with equal m/z) into a synchronous movement on a larger orbital radius (Figure 2.5a); this can be either a broadband or a single-frequency pulse to excite all or just the ions with a given m/z value, respectively. [162] After excitation, the detection is possible by measuring the induced image currents on the detector plates (Figure 2.5b). The transient free induction decay (FID) is recorded and converted from the time domain to the frequency domain by means of Fourier transformation, *i.e.* the complex FID caused by the superposition of many frequencies is deconvoluted to single contributing frequencies of the various ions. As frequencies can be measured with high accuracy, FT-ICR mass spectrometry offers the advantage of extremely high resolution and thus high mass accuracy; [163] however, the high resolution strongly depends of the magnetic strength of the ICR employed, which is disproportionate to the price of the machine, thus the disadvantage of FT-ICR mass spectrometry is the high cost in acquisition and maintenance. [158,160]

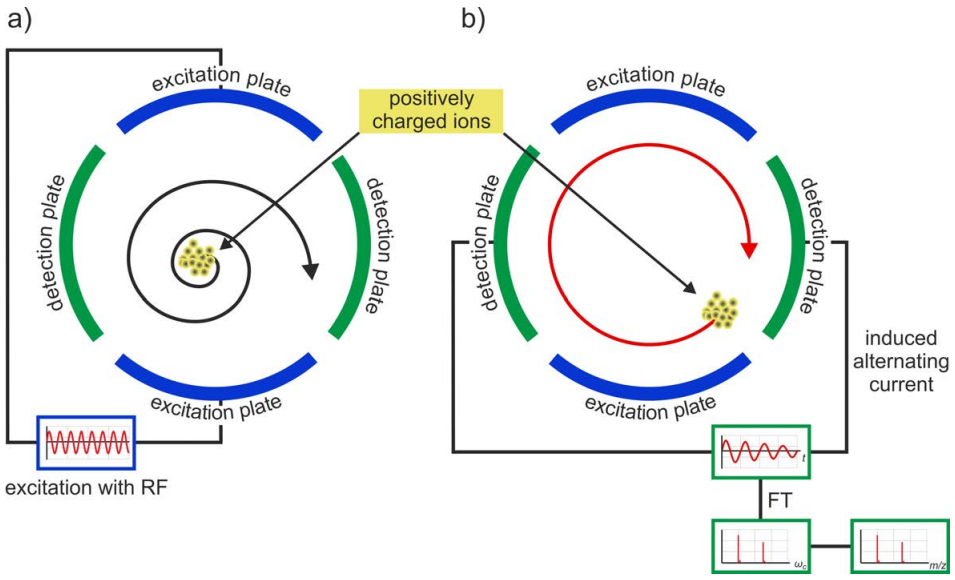

Figure 2.5: Schematic description of the excitation/detection process in the ICR cell: a) excitation with radio frequency RF to bring all ions with equal m/z into a coherent, larger orbital radius; b) measurement of the induced image currents on the detector plates and mass analysis via Fourier transformation (FT).

Ion excitation is not only indispensable for the detection process but also necessary for the mass selection of an ion; [164] if an unwanted ion is accelerated to an orbit larger than the cell geometry, it hits the wall and is neutralized. Therefore, similarly to the excitation preceding the ion detection, both broadband and single-frequency pulses can be used for mass selection of an ion; while broadband ejection covers a larger part of the m/z range, single-ion ejection can be used to very precisely remove selected ions from the cell. Furthermore, both excitation pulses are not strictly rectangular but have more or less broad flanks which might excite the ion that is supposed to be selected; this secondary effect is known as off-resonant excitation, *i.e.* a further thermalization of the ion is necessary to perform ion/molecule reactions at room temperature conditions. In general, broadband ejection should be avoided close to the m/z value of the ion of interest, because broadband ejection is presumed to promote off-resonant excitation easier, [164]; here, single-ion ejection should be favored. However, a reasonable relation between accuracy and time consumption of the ejection procedure should be considered, and the so-called FERETS (front-end-resolution enhancement using tailored sweeps) technique provides an acceptable trade-off, as is combines broadband and single-ion ejections. [165]

2.2.2.2 The instrumental setup for FT-ICR mass spectrometry

For the present work, several FT-ICR machines, located at the Universities in Berlin, Bonn, Kiel, and Rome, were used. While all of them are described in table form in the Experimental Details (Appendix B, Table B.1), details of the Kiel instrument, commonly employed for the acquisition of the presented data in this thesis, are described in the following. This FT-ICR machine consists of a modified Bruker/Spectroscopin CMS47X mass spectrometer, equipped with an Apex III data station and consists of three major parts, *i.e.* the ion source, the ion-transfer optics, and the FT-ICR cell (Figure 2.6); the latter is surrounded by a superconducting magnet (Oxford Instruments, 4.7 - 7.05 T). After plasma generation (see Section 2.1.2) and cooling by supersonic expansion, the atomic and cluster ions enter the ion-transfer optics. These optics comprise a complex system of electrostatic potentials and lenses, transferring the ions to the ICR cell and removing the neutral components by differential pumping. The pressure in the downstream source region is about 10^{-6} mbar, whereas a high vacuum of 10^{-11} mbar is reached in the ICR cell, in the following quoted as UHV (ultra-high vacuum) region. After transfer into the ICR cell, the isolated ions are exposed to neutral substrates to study their reactivity. The neutral reactants are introduced into the cell by a needle leak valve at stationary pressures on the order of 10^{-8} mbar; to avoid the introduction of impurities in the UHV region, liquid reactants were degassed by several freeze-pump-thaw cycles. The measurement of the pressure, relevant for the determination of the absolute rate constants (see Section 2.3.2) were achieved by means of a calibrated ion gauge (BALZERS IMG070) and acknowledgment of the ion gauge sensitivities for each neutral substrate. Pulsing-in of neutral reactants to the cell is generally also possible via

pulse valves to allow MS^n experiments using more than one substrate. As the targeted metal-oxide cluster ions are generated only in poor quantities, the spectra in all experiments were accumulated between 50-250 scans to improve the signal-to-noise ratio.

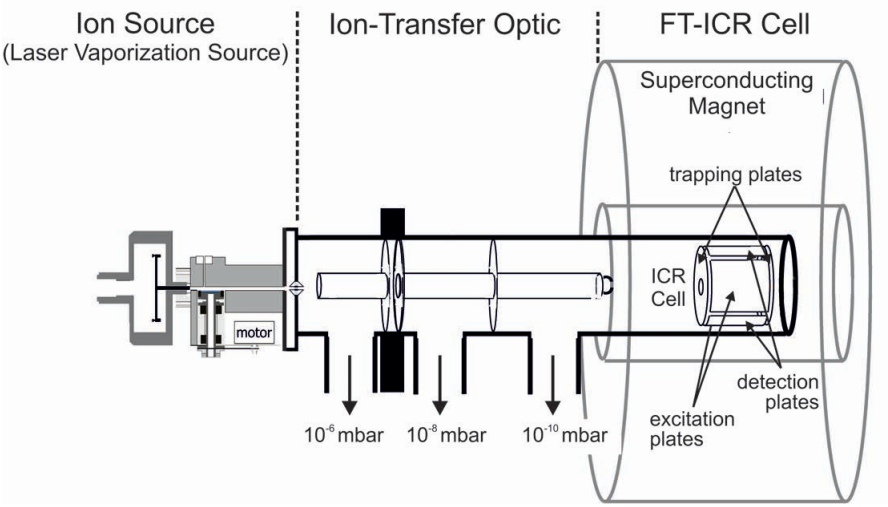

Figure 2.6: Technical draft of the modified Bruker/Spectrospin CMS47X FT-ICR mass spectrometer with the ion source.

2.2.3 Infrared photodissociation (IRPD) spectroscopy

Infrared photodissociation spectroscopy of mass selected cluster ions enables their structural characterization in the gas phase;[47,60–67] a rather small introduction into this method is presented in the following.

Spectroscopy techniques measuring the absorption of light are all based on the Beer-Lambert law (Equation 2.12).

$$\text{Transmission} = \frac{I}{I_0} = e^{-\sigma(\nu)\cdot l\cdot N} \tag{2.12}$$

The law states that there is a logarithmic dependence between the transmission of light, of a given wavenumber ν, with the absorption cross section $\sigma(\nu)$ of an analyte, as well as its density N and the length l the light has to pass through the absorber; I_0 and I are the intensity/power of the incident and the transmitted light, respectively. However, when working with mass-selected ions in the gas phase, the attainable ion number densities are rather small, typically below 10^8 ions per cubic centimeter,[67] due to space charge effects. Thus, this very low value for N impedes the practicability of the Beer-Lambert law as $\lim_{x\to 0} e^x = 1$, and the difference between I_0 and I becomes undetectable. Therefore, an alternative method for the infrared structural characterization of ions in the gas phase has been developed, in which the absorption of photons is measured indirectly.[60–62] The basic idea is to detect the response of the ion after photon absorption, which could be a change in

mass or charge, in conjunction with fragmentation, or photoelectron ejection, respectively; these methods are generally referred to as „action spectroscopy“. Thus, in analogy to the Beer-Lambert law, the quotient of the incident to the transmitted light $\frac{I}{I_0}$ is replaced by the ratio of responding ions n to the initially present ions n_0 (Equation 2.13); further, the product of length and density $N \cdot l$ is replaced by the so-called laser fluence F: [67]

$$\text{Transmission} = \frac{n}{n_0} = e^{-\sigma(\nu)\cdot F} \tag{2.13}$$

As a mass-selected ion only absorbs light of discrete wavenumbers according to its vibrational frequencies, the response or fragmentation of the parent ion can be detected as function of the wavenumber thus providing structur-specific informations. By using appropriate mass filters for the selection of the parent ion, the fragment ions can be detected background-free and with nearly 100 % detection efficiency. [65,67]

The most common IRPD technique is the so-called infrared multiphoton dissociation (IRMPD) spectroscopy, [63,65,66,166,167] which takes advantage of the absorption of multiple photons in order to induce fragmentations via the lowest dissociation threshold. The IRMPD mechanism is divided into three overlapping time domains: *i*) The cluster of interest is excited resonantly over discrete states into the quasi-continuum region; *ii*) the cluster continues to absorb photons resonantly, but this energy is quickly randomized among all vibrational degrees of freedom; and *iii*) once the internal energy reaches the dissociation limit, the molecule dissociates according to the statistical model of unimolecular fragmentations (see Section 2.3.1). [166] Due to the low ion density, a high brightness of the light source is necessary to trigger the multiple photon excitation, *i.e.* free-electron lasers are indispensable for IRMPD experiments.

A useful alternative to avoid IRMPD experiments is the so-called messenger atom technique, [168] employed in this thesis. Here, a rare-gas atom, *i.e.* helium or argon, is attached to the ionic cluster before exposition to IR radiation. As rare-gas atoms are generally only weakly bound to any clusters, the dissociation threshold of the respective system is considerably lowered and can be ideally overcome by single-photon excitation only. However, this technique can only be applied to systems in which the perturbation of the messenger atom can be neglected.

The experimental setup [169,170] of the IRPD experiments is depicted in Figure 2.7. The ions are generated in a commercial ESI source and the resulting beam of ions is collimated in a helium-filled, RF ion guide. Then, the ions of interest are mass selected in a quadrupole mass filter and deflected by 90° in an electrostatic quadrupole deflector. They are subsequently focused into a cryogenically-cooled ion trap, which consists of of a 22 cm long linear RF ion guide and two electrostatic ion lenses contained in a cylindrical housing; cooling is achieved by a cold head of a closed-cycle helium cryostat. Since helium works also as the messenger

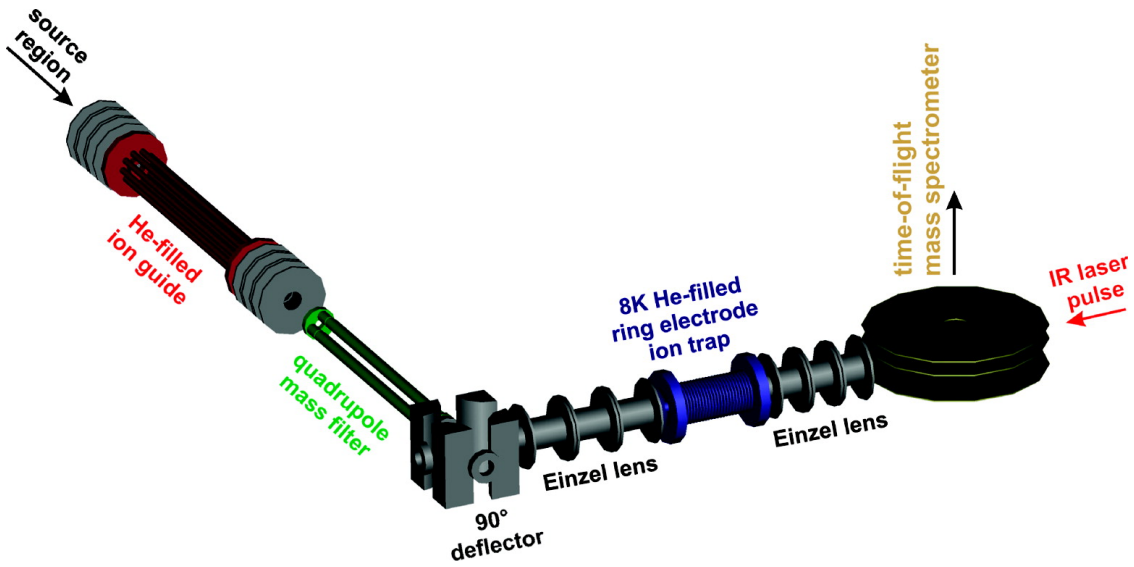

Figure 2.7: Schematic setup of the ion trap/tandem mass spectrometer used for the infrared photodissociation experiments.

atom, the [ion-He]-complex formation is realized as the trap is continuously filled with helium as a buffer gas at an ion trap temperature of 15 K; He-tagged complexes are further stabilized through three-body collisions. [171,172] After ion accumulation in the trap and ion tagging with the messenger atom, all ions are extracted from the ion trap and focused both temporally and spatially into the center of the extraction region of an orthogonally mounted linear time-of-flight (TOF) mass spectrometer. Here, the ion packet can be irradiated with the IR laser pulse and the depletion of the tagged parent ions as well as the formation of photofragment ions are simultaneously monitored by means of TOF mass spectrometry. In the framework of the present thesis, the laser radiation originates from a table-top setup and covers the wavenumber range of interest for the systems investigated in sufficient intensity; often, strong sources as free-electron lasers are also necessary for single photon measurements. Here, pulsed IR radiation is provided by a tabletop OPO/OPA/$AgGaSe_2$ IR laser system (LaserVision) [173] which is pumped by a pulsed, seeded Nd:YAG laser (Continuum, Powerlite P-8000). The pump laser operates at a repetition rate of 10 Hz and provides 7 ns long pulses. The IR laser system is operated in the spectral region from 800 cm^{-1} to 1500 cm^{-1}, where IR pulses with pulse energies 4 mJ and a spectral bandwidth of 1.8 cm^{-1} are typically produced.

2.3 Chemistry of ions in the gas phase - Theory of ion/molecule reactions

„When speaking about chemical reactivity, there is still a tendency to think primarily of molecule-molecule interactions. In fact, however, ion-molecule reactions frequently play an outstanding role." [174]

– Rudolf Zahradník

The following section gives a short overview about the chemistry of ions in the gas phase and the underlying theories. This includes the reaction of ions with neutral molecules at room temperature conditions, referred to as ion/molecule reactions, as well as the theory of dissociation processes of ions. Also the concept of isotopic labeling to uncover mechanistic details of an ion/molecule reaction is addressed.

2.3.1 Dissociation processes of ions

Despite the growing importance of mass spectrometry in analytical chemistry, structural information of the investigated systems are not directly accessible; only information about the composition can be obtained. Therefore, complementary experiments are necessary to provide further insight into the structure and energetics of ions, *e.g.* the examination of fragment pathways of an ionic species. After decades of rather intensive research, there are now numerous possibilities to excite the ions and induce the unimolecular dissociation, such as electron-capture dissociation (ECD) or collision-induced dissociation (CID). [158,175] Since all experiments are performed under high vacuum conditions, in the range between 10^{-4} and 10^{-10} mbar, single-collision conditions are assumed. Accordingly, in contrast to the condensed-phase chemistry, gaseous ions can only internally redistribute excessive energy, *e.g.* gained in a collision or in a photodissociation experiment, thus resulting in either radiative cooling, isomerization or fragmentation. The dissociative process can only occur, if the internal energy of the ion $[AB]^+$ exceeds the activation energy $\Delta E^{\neq}$ for the formation of ion $[A]^+$ and neutral B. In this context, a differentiation between two different fragmentation reaction is useful for further understanding of breakdown curves as shown in the lower part of Figure 2.8. The first kind of fragmentation represents simple bond-cleavage reactions, generally occurring via loose transition states (Figure 2.8a), while the second fragmentation constitutes more complex rearrangement reactions, resulting from transition states with a well-defined, often rigid structure (tight TS), *e.g.* via a six-membered ring,[iii] thus forming a new ion/neutral complex $[CD]^+$ (Figure 2.8b). In the latter scenario, the activation entropy ΔS gets significantly reduced, but the rearrangement still occurs if the internal energy of the ion is higher than that of the respective transition structure. Tight

[iii] The most prominent example is surely the well-known McLafferty rearrangement. [176]

transition structures are favorably involved at lower internal energies, while at higher internal energies the fragmentation via loose transitions structures prevails. In the following, a summary about the three employed dissociation techniques used in the present work is given, *i.e.* collision-induced dissociation, cone-voltage collision-induced dissociation and infrared photodissociation.

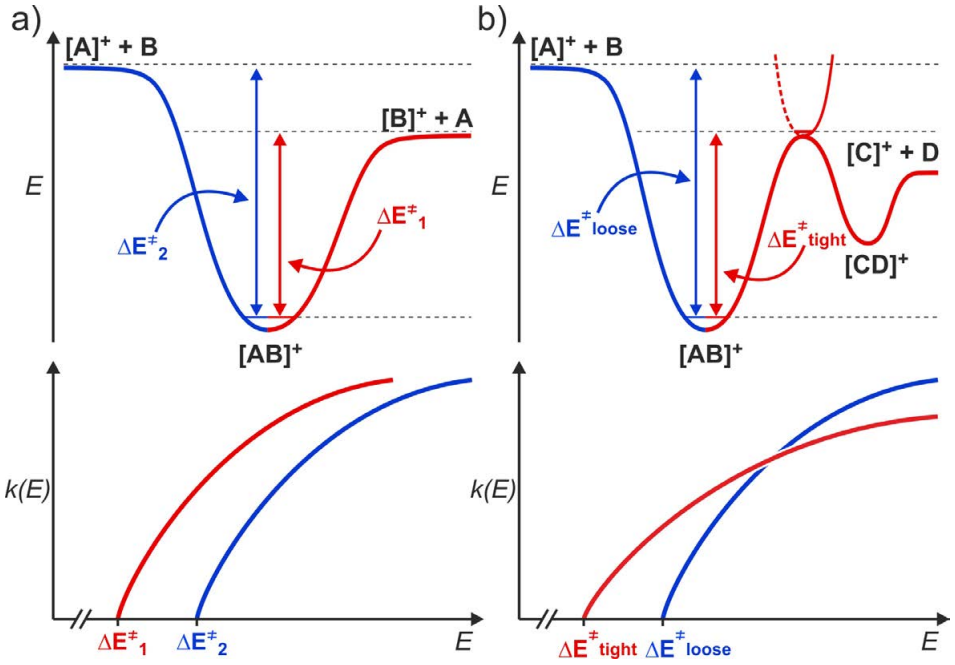

Figure 2.8: Schematic description of the energy dependence as well as of the resulting relative rates of competing fragmentation channels: a) Direct bond cleavage involving loose transition states with the different activation energies $E_1^{\neq}$ and $E_2^{\neq}$; b) direct bond cleavage $E_{loose}^{\neq}$ versus rearrangement and consecutive fragmentation $E_{tight}^{\neq}$.

The **collision-induced dissociation** [177–179] (CID) of ions with neutral gas atoms or molecules is still the most common ion activation method for dissociation experiments. [175] Briefly, a package of mass-selected ions is guided trough a collision cell, filled with the buffer gas (typically nitrogen, argon or xenon), and recording the fragments provides information about bond strengths, structural features, etc. Assuming an inelastic collision with the neutral, stationary gas atoms, the kinetic energy of the ions is converted into internal energy, leading to subsequent dissociation. The energy transferred is defined as *center-of-mass collision energy*[iv] E_{CM} which is a function of the mass of the neutral gas m_N, the mass of the

[iv] To simplify the description of such a process, it is more useful to work in the center-of-mass framework, assuming a moving particle (ion) and a static target (gas), instead of the laboratory reference frame. In the latter, a binary collision is described by the two separate particles involved with their individual position and velocity vectors, respectively. A conversion to the center-of-mass reference frame makes the situation easier to describe, because the center-of-mass momentum is always zero. [175]

ion m_I and the kinetic energy of the ion in the laboratory frame of reference E_{lab} (2.14):

$$E_{CM} = E_{lab}\frac{m_N}{m_N + m_I} \tag{2.14}$$

In other words, the E_{CM} value represents the maximum possible amount of energy which can be transferred during the collision incidence. Further, the overall CID process is assumed to occur by a two-step mechanism: The first step includes the collision process of the ion $[AB]^+$ with the neutral N and the energy transfer as described above, leading to the excited species $[AB]^{+*}$. After the redistribution of the internal energy, the second step occurs, *i.e.* the dissociation process, causing different fragmentation pathways according to the internal energy available.

$$[AB]^+ \xrightarrow[\text{with N}]{\text{collision}} [AB]^{+*} \xrightarrow{\text{dissociation}} [A]^+ + B \tag{2.15}$$

Experimentally, various collision conditions are achieved by changing the translational energy E_{lab} of the ions either by acceleration of the ions prior to the collision cell in a tandem mass spectrometer, or via the excitation time in a FT-ICR mass spectrometer. The pressure on the other hand should be kept under single collision conditions, because otherwise an ill-defined amount of energy is transferred in additional collisions.

Another type of collisional activation is the **in-source collision-induced dissociation** (ISCID), also often referred to as cone-voltage collision-induced dissociation in ESI sources. [149] Here, the application of a high cone voltage (for further details, see Chapter 2.2.1) causes a significant acceleration of the ions an multiple collisions between the accelerated ions and the nebulizing/drying gas at atmospheric pressure. As quoted above, lower cone voltages can be used for the removal of solvent molecules while higher cone voltages give access to highly fragmented species.

Finally, **infrared dissociation** [60,66,175] (IRPD) provides a powerful alternative to collision induced experiments, as shown previously in Section 2.2.3. Regarding Equation 2.15, activation of the ion $[AB]^+$ is achieved via absorption of one or more photons from a laser source instead of collisions with a neutral gas. With respect to the mechanism, the absorption of IR photons occurs by IR active modes in the ion, followed by rapid redistribution of the energy over all vibrational degrees of freedom. The energy gain by absorption of IR frequencies is remarkably smaller than in collision experiments and subsequent fragmentation takes place via the lowest energetic pathways accessible. However, there are several important criteria for photodissociation to occur: the precursor ion must be able to absorb energy in the form of photons thus producing vibrationally excited states, above the threshold of dissociation for the ion of interest. The energy gained by the absorption

of photons must consequently overcome the energy lost by photon emission from the excited ions as well as deactivation by collisions. [175] However, this technique enabled new possibilities for the structural characterization of cluster ions based on mass-selective gas phase vibrational spectroscopy, also applied in this work. [47,63–65]

2.3.2 Theory of ion/molecule reactions

Beginning from the middle of the last century, it was found that the collision of an ion and a neutral reactant must not always lead to simple fragmentation of the ion; instead, more complex reactions and rearrangements within the encounter complex can occur, referred to as ion/molecule reaction . [174,180,181] For example, the bimolecular reaction of the mass-selected ion $[A]^+$ with a molecule B can also lead to a newly formed ionic product $[C]^+$ and the neutral fragment D, also often referred to as neutral loss D (2.16).

$$[A]^+ + B \longrightarrow [C]^+ + D \tag{2.16}$$

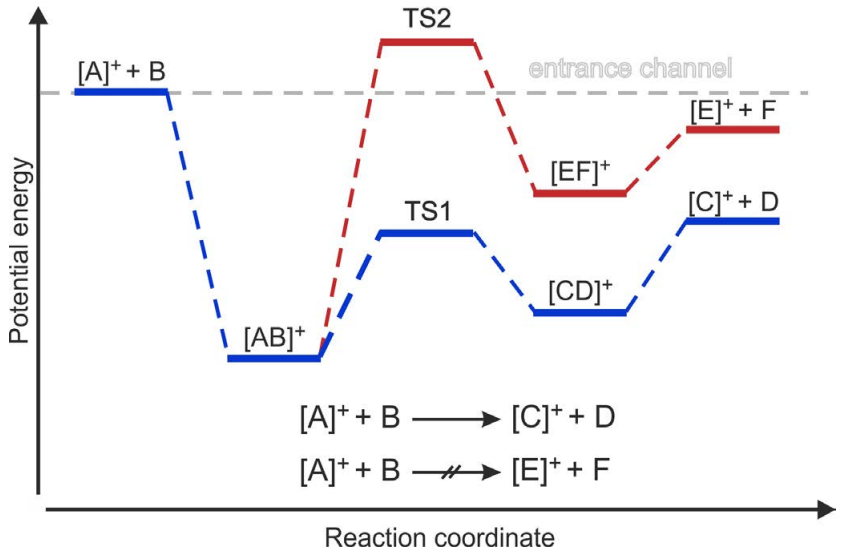

Figure 2.9: Schematic potential-energy surface for a thermally accessible (blue) and a non-accessible (red) bimolecular ion/molecule reaction in the gas phase.

These ion/molecule reactions are mostly performed under so-called thermal conditions, which means that the ions are cooled down (thermalized) to approximately room temperature, *e.g.* via low-energy collisions with an inert buffer gas. [88] Thus, prior to the reaction, the ions are in the electronic ground-state and only exothermic reactions are allowed. An ion/molecule reaction can be best explained by the three steps which define a "double-well" potential-energy surface, [182] as shown in Figure 2.9. The first step constitutes the adduct formation from the separated reactants to form the encounter complex $[AB]^+$;

this complexation process is always associated with a certain gain of energy, *e.g.* due to the attractive ion-dipole forces between the cation and the neutral molecule. As described before for the collision energy, under high-vacuum conditions this excessive energy can only be redistributed internally among the rotational and vibrational degrees of freedom and can be used to induce more complex rearrangement reactions, leading to the formation of a new species such as $[CD]^+$ via the respective transition structure **TS1** (Figure 2.9 - blue line). The reaction is completed with the loss of the neutral product D. If the transition state is too high in energy, *i.e.* above the entrance channel (**TS2** in Figure 2.9 - red line), re-dissociation to the initial reactants rather takes place. Thus, even though the formation of $[E]^+$ and F is exothermic and therefore thermodynamically allowed, the reaction is kinetically hindered in the gas phase and only formation of $[C]^+$ and D can be observed.

For a quantitative description of a bimolecular ion/molecule reaction $[A]^+ + B \rightarrow [C]^+ + D$, many methods have been developed. Experimentally, the kinetic parameters of a gas-phase reaction can be determined by assuming a pseudo-first order kinetic since the concentration of the neutral gas is so much larger compared to the concentration of the ions $[A^+]$ that the former's concentration can be viewed as constant. Therefore, the observed rate constant k_{obs} corresponds to the product of the actual rate constant k and the partial pressure p_B of reactant B:

$$\frac{d[A^+]}{dt} = -k_{exp} \cdot [A^+] \cdot p_B = -k_{obs} \cdot [A^+] \tag{2.17}$$

Taking into account that the intensity of the signal should be a reasonable indicator of concentration of the ions $I(A^+) = [A^+]$, the differential equation can be solved, with $I_0(A^+)$ representing the concentration at the beginning of the reaction delay ($t = 0$):

$$I(A^+) = I_0(A^+) \cdot e^{-k_{obs} \cdot t} \tag{2.18}$$

Linearization of the function leads to the following equation:

$$ln(\frac{I(A^+)}{I_0(A^+)}) = -k_{obs} \cdot t \tag{2.19}$$

Measuring the relative intensity $\frac{I(A^+)}{I_0(A^+)}$ as a function of the time t thus gives a linear plot, in which the gradient m parallels the observed rate constant, *i.e.* $m = -k_{obs}$. Thus, m can be employed to calculate the overall experimental rate constant k_{exp} according to Equation 2.20 in which F corresponds to an instrument-specific calibration factor and R is the relative ion-gauge sensitivity factor [183] which is applied to derive the real pressures of B relative to air. The relative errors for the absolute rate constant mainly result from the inaccuracy of the pressure measurement and are estimated to amount to ± 50 %: [88]

$$k_{exp} = -100 \cdot m \cdot R \cdot F^{-1} \cdot p_B^{-1} \tag{2.20}$$

The experimental rate constant can be related to the collision rate to quantify the efficiency ϕ of the ion/molecule reaction (Equation 2.21). ϕ corresponds to the percentage of collisions resulting in a reaction (including adduct formation); the remaining part of the collisions leads to re-dissociation of the encounter complex into the reactants.

$$\frac{k_{exp}}{k_{coll}} = \phi \tag{2.21}$$

Several theoretic models have been developed to derive a proper value for k_{coll}. The first model to quantify the collisions of ions and molecules was introduced by Langevin in 1905, using the kinetic theory of gases. [184] Treating the ion as a point charge q and the molecule as polarizable dielectric with the polarizability α, the collision rate can be expressed by Equation 2.22 (m_r is the reduced mass of the ion/molecule couple):

$$k_{coll} = k_L = 2 \cdot \pi \cdot q \cdot \sqrt{\frac{\alpha}{m_r}} \tag{2.22}$$

This approach has later been improved to the average-dipole orientation (ADO) theory, developed by Su and Bowers, which includes the dipole moment of the neutral substrate. [185,186] Finally, this model was further refined by Su, resulting in the capture theory, [187–189] in which the rate constant k_{cap} is defined as a function of the polarizability α, the permanent dipole moment μ_D, the elementary charge e, the number of elementary charges z and the temperature T. However, since μ_D is zero for all substrates used in the relevant experiments of the present work (methane, ethane, propane, ethene, etc.), all theories yield the same value for the collision rate, *i.e.* $k_L = k_{ADO} = k_{cap}$.

Contrary to the ICR experiments, allowing a direct measurement of the absolute rate constant, only relative rate constants k_{rel} are obtained in the triple quadrupole mass spectrometer (Chapter 2.2.1). Since the residence time in the hexapole of the tandem mass spectrometer, where the reaction takes place, is unknown, one can only use the approximation that the time to traverse the hexapole is equal for every ion, even though it rather corresponds to a Gaussian distribution. Therefore, the pressure of neutral reactant B (p_B) remains as only possible variable in Equation 2.18, while the time t becomes constant and thus included in k_{rel}:

$$I(A^+) = I_0(A^+) \cdot e^{-k_{obs} \cdot t} = I_0(A^+) \cdot e^{-k \cdot p_B \cdot t} = I_0(A^+) \cdot e^{-k_{rel} \cdot p_B} \tag{2.23}$$

$$\Leftrightarrow ln(\frac{I(A^+)}{I_0(A^+)}) = -k_{rel} \cdot p_B \tag{2.24}$$

Accordingly, k_{rel} is experimentally accessible by variation of the pressure of the neutral substrate. Further, the derivation of the absolute rate constant from k_{rel} is possible, by calibrating k_{rel} to a related reaction, *i.e.* with the same neutral substrate and a comparable ionic species, for which both k_{rel} and the absolute rate constant are known.

2.3.3 Labeling experiments and kinetic isotope effects

Isotopic labeling at a specific position in a molecule may provide a lot of valuable information about the mechanism of a chemical reaction. Apparently, the selective exchange of one atom in a molecule by one of its isotopes allows to distinguish one position from another in the molecule. Thus, first of all, isotopic labeling at specific positions within a molecule may provide insights in the regioselectivity of the ion/molecule reaction investigated. Moreover, isotopic substitutions can have an effect on the kinetic and thermodynamic properties of a selected process, known as isotope effects. The most pronounced isotope effects are observed for the substitution of hydrogen by deuterium due to the significant relative mass gain of 100 %. If isotopic substitution affects on the rate of the chemical reaction, this is referred to as a kinetic isotope effect (KIE), while any influence on the thermodynamical equilibrium of a chemical reaction is known as equilibrium isotope effect (EIE). The latter is usually much smaller and thus negligible for ion/molecule reactions in the gas phase, because substitution by a heavy isotope slows down forward as well as backward reactions such that the overall effects on the equilibrium constants are rather small. [190]

$$\mathrm{KIE} = \frac{k_H}{k_D} \tag{2.25}$$

In general, the kinetic isotope effect is defined as the quotient of the two independent rate constants for an unlabeled molecule compared to its deuterated analogue, respectively (Equation 2.25). The values of a KIE can be interpreted as follows: *i*) if k_H/k_D = 1, the substitution of H by D has no influence on the rate constant of the reaction, and the corresponding C−H/C−D bonds are most likely unaffected in the rate-determining step; *ii*) normal KIE: if $k_H/k_D > 1$, the reaction proceeds faster with the unlabeled compound and the activation of the particular C−H(D) bond is involved in the rate-determining step; finally, inverse KIE: if *iii*) $k_H/k_D < 1$, the rate constant increases with H → D exchange. The change in the rate constants originates from the different zero-point energies (ZPE) of the unlabeled and the labeled substrates, which is a function of m_r and the force constant k (Equation 2.26). Since $(\mathrm{ZPE}_{C-H}) > (\mathrm{ZPE}_{C-D})$, the activation energies $\Delta E^{\neq}_{\mathrm{C-H}}$ and $\Delta E^{\neq}_{\mathrm{C-D}}$ of the labeled and unlabeled compound are shifted and cause a KIE if the difference in ZPE is decreased in the transition structure of the respective reaction (Figure 2.10a). Further, the vibrational modes that have the largest force constants and those that undergo the largest changes in the course of the reaction have the greatest influence on the isotope effect. In the hypothetical scenario of a homolytic C−H bond cleavage as shown in Figure 2.10a, for instance, the C−H stretching vibration has completely been converted to a translational degree of freedom, thus causing the largest possible kinetic isotope effect.[v]

[v] Neglecting tunneling processes which are known to cause very large KIEs.

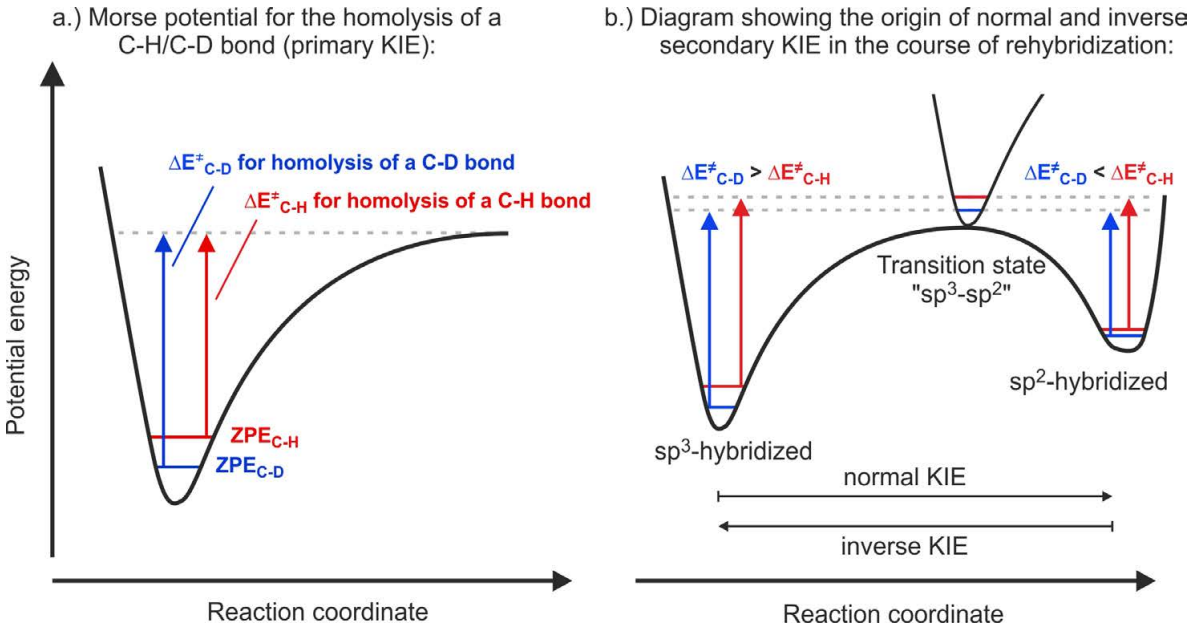

Figure 2.10: Origin of primary (a.) and secondary (b.) kinetic isotope effects.

$$\mathrm{ZPE} = \frac{1}{2} \cdot h\nu = \frac{h}{4\pi} \cdot \sqrt{\frac{k}{m_r}} \tag{2.26}$$

A further distinction of KIEs concerns the precise role of the substituted bond in the reaction mechanism. If the labeled bond is broken in the rate-determining step of the reaction, one refers to a primary KIE. Primary KIEs are usually limited to normal KIEs and depend mostly on the nature of the bond to be broken and on the extent of the transformation of the vibrational mode into translation in the transition structure.[vi] However, a KIE can also occur if the labeled bond is not broken in the course of the reaction; these effects are called secondary KIEs (Figure 2.10b). In general, they are smaller than primary KIEs and can be either normal or inverse. A well-known example in which a secondary KIE plays a role concerns rehybridization processes. Contrary to primary KIEs, they do not depend on the stretching-vibration modes, but rather on the bending vibrations. For example, the frequency of an *out-of-plane* bending vibration of a sp^3-hybridized C−H bond amounts to 1350 cm^{-1}, while the corresponding vibration of a sp^2-hybridized C−H bond is significantly smaller, amounting to only 800 cm^{-1}. On the other hand, the *in-plane* deformation mode is almost identical for both (1350 cm^{-1}). The smaller force constant of the *out-of-plane* deformation vibration of the sp^2-hybridized C−H bond implies a smaller ZPE, thus resulting in a smaller $(\mathrm{ZPE}_H)/(\mathrm{ZPE}_D)$ splitting than in the sp^3-hybridized ground state. As shown in Figure 2.10b, the respective transition state between sp^3 and sp^2 exhibits a force constants between the two ground states. Hence, the activation energy $\Delta E^{\neq}$ for a sp^3-hybridized C−D bond to form the sp^2-hybridized equivalent is larger than for the according C−H bond; a normal KIE

[vi] For further details, see [16, 191]

is observed. In contrast, the activation energy for a sp^2-hybridized C−D bond to form the sp^3-hybridized counterpart is smaller than for the respective C−H bond, thus, an inverse KIE is observed. Other examples where secondary KIEs might play a role are hyperconjugative or steric effects, directly affecting the rate-determining step.

Experimentally, intramolecular or intermolecular isotope effects can be measured. To measure an intramolecular KIE, at least two structurally identical C−H bonds must be present in the molecule of interest, and one of them has to be selectively deuterated, *e.g.* two C−H bonds in methane to give CH_2D_2. The isotopic pattern in the product ion provides directly reliable numbers of the involved isotopic effect. The determination of intermolecular KIEs, however, requires two separated experiments, one with the unlabeled and the other with the labeled compound, *e.g.* with CH_4 and CD_4 respectively, to determine k_{CH_4} and k_{CD_4} independently. Due to the relatively large error bars of 50 % for measuring rate constants, [88] the experimentally derived intermolecular KIEs are affected by the same error. Moreover, differences in collision rates and diffusion coefficients might interfere the determination of intermolecular KIEs. Thus, though the interpretation of intermolecular KIEs proved valuable, *e.g.* for mechanistic studies in the condensed phase, [192–195] intramolecular KIEs should be favored over intermolecular KIEs.

2.4 Modeling of ions in the gas phase - Computational methods

„Erwin with his psi can do
Calculations quite a few.
But one thing has not been seen:
Just what does psi really mean?“ [196]

– Erich Hückel (translated by Felix Bloch)

Quantum chemical calculations represent a powerful, complementary tool for mass-spectrometry based studies. [42,44,46,48–54,68,70] While isotopic-labeling and structural-characterization by CID or IRPD experiments can reveal some mechanistic features of an ion/molecule reaction, direct information about the electronic states or the discrimination between isomeric intermediates is rather difficult. Here, computational chemistry proved extremely helpful, as it allows the determination of structural, energetic and electronic details of the starting compounds, products, intermediates, and transition states involved. Further, the well defined systems in gas-phase experiments performed under solvent-free, low-pressure conditions are particularly close to the isolated systems which are the objects of electronic structure calculations. [68,69,197]

Many computational approaches have been developed in the past centuries, including density-functional theory (DFT), wave-function based ab-initio methods (*e.g.* HF),

Møller-Plesset pertubation theory (MP2, MP3, MP4), coupled-cluster (*e.g.* CCSD), or extrapolation methods (*e.g.* CBS). DFT calculations provide a reasonable compromise between time-consumption and accuracy and are thus used most frequently; however, as the performance of computers improved, more accurate calculations become also available for larger systems. In the following, the underlying theory of quantum chemical calculations is addressed briefly, with particular emphasis on the methods employed in the present thesis.

2.4.1 From basic quantum mechanics to density-functional theory

According to the classical formulation of quantum mechanics, the wavefunction Ψ contains all information necessary for the complete description of a chemical system, and fulfills the Schrödinger Equation 2.27 ($\hat{H}$ is the Hamiltonian operator, $\hbar$ the Planck constant and i the imaginary unit): [198,199]

$$i \cdot \hbar \cdot \frac{\partial}{\partial(t)} \Psi = \hat{H}\Psi \tag{2.27}$$

As $\Psi(x, R, t)$ is a function of the spatial and spin coordinates of the electrons x, the spatial coordinates of the nuclei R, and the time t, a fully analytical solution of the Schrödinger Equation 2.27 is only numerically possible for one-electron systems; for systems with two or more electrons, approximative methods become inevitable to reduce the number of free parameters. [199] Therefore, in a first approximation, the time-dependent system is treated as a time-independent one, thus resulting in the time-independent Schrödinger Equation 2.28. However, this simplification is only valid if the system does not experience any time-dependent external forces. The second and most important approximation concerns the famous Born-Oppenheimer approximation, [200] assuming that the electrons move considerably faster than the atomic nuclei due to their lower mass. This assumption simplifies the Hamiltonian operator significantly, as the kinetic-energy term of the nuclei can be neglected and their potential-energy can be considered as constant. Hence, only the electronic Hamiltonian operator $\hat{H}_{el}$ remains, whereas the nuclear positions R enter as fixed parameters (Equation 2.29).

$$\hat{H}\Psi(x, R) = \hat{E}\Psi(x, R) \tag{2.28}$$

$$\hat{H}_{el}\Psi(x, R) = \hat{E}_{el}\Psi(x, R) \tag{2.29}$$

The electronic energy operator $\hat{E}_{el}$ in Equation 2.29 is composed of four different operators, *i.e.* operators for the kinetic energy of the electrons $\hat{T}_e$, the electron-electron interaction $\hat{V}_{ee}$, the nuclear-electron interaction $\hat{V}_{ne}$ and, for the nuclear-nuclear interaction, $\hat{V}_{nn}$ (Equation 2.30);

the latter does not affect the electrons and corresponds to a constant as described above.

$$\hat{E}_{el} = \hat{T}_e + \hat{V}_{ee} + \hat{V}_{ne} + \underbrace{\hat{V}_{nn}}_{=const.} \tag{2.30}$$

Equation 2.30 represents the starting point for the conceptual idea behind density-functional theory (DFT), as postulated by Hohenberg and Kohn. In 1964, they published the so-called Hohenberg-Kohn theorem, [201] stating that the Hamiltonian operator, and thus all properties of the system including the ground-state electronic energy, is completely and uniquely determined by the electron density ρ (Equation 2.31). [201,202] Hence, DFT reduces the $3N$ (N = number of electrons) dimensional problem encountered in wave-function based *ab-initio* methods to a much simpler numerical problem that only requires the knowledge of the electron-density distribution ρ that is a three-dimensional function.[vii] As a further prerequisite, Hohenberg and Kohn assume that the functional that determines the ground-state energy of the system delivers the lowest energy only if it is applied to the true ground-state density ρ_0 of the system, while any other electronic density ρ will result in higher energies (Equation 2.32).

$$\hat{E}_{el}(\rho) = \hat{T}_e(\rho) + \underbrace{\hat{V}_{ee}(\rho)}_{J(\rho)+\hat{V}_{XC}(\rho)} + \hat{V}_{ne}(\rho) \tag{2.31}$$

$$\hat{E}_{el}(\rho_0) < \hat{E}_{el}(\rho) \tag{2.32}$$

In DFT, the electron-electron interaction $\hat{V}_{ee}$ is divided into a coulomb term $J(\rho)$ and an exchange-correlation functional $\hat{V}_{XC}(\rho)$ (Equation 2.31); [70,202] while exact formulations of J and $\hat{V}_{ne}$ can be made, $\hat{T}_e$ + $\hat{V}_{XC}$ includes everything that cannot be treated exactly. Hence, the search for appropriate approximations to a better description of the exchange-correlation functional is one of the main challenges in DFT research, and the difference between the various DFT methods originates from different exchange and correlation functionals. [70,204] As a result, DFT cannot systematically be improved like *e.g.* Møller-Plesset or coupled-cluster methods. Instead, many different functionals exists for many different systems, *e.g.* transition-metal complexes, surfaces or biomolecules. Therefore, the choice of the right functional for a certain task/system is important and a comparison with high-level *ab-initio* calculations or experimental results is indispensable in order to judge on the quality of the quantum-mechanical description. [70] Hence, many systematic studies have been performed to investigate the quality of various DFT approaches, [70,204–209] and it emerged that for gas-phase ion chemistry the B3LYP method brings about the best overall performance. [70] This hybrid-functional includes Becke's three-parameter non-local exchange potential with

[vii] The applicability of DFT to molecular systems was very much facilitated by the introduction of Kohn and Sham orbitals in 1965, by which the electron density can be written in terms of one-electron orbitals. [203]

the non-local correlation functional of Lee, Yang and Parr. [210–212] Therefore, B3LYP and the unrestricted method UB3LYP for *open-shell* systems [211,212] are mostly applied in this work to model and support the experimental results; for selected systems, also other functionals or high-level *ab-initio* calculations are employed.

2.4.2 Coupled-cluster and extrapolation methods

The *ab-initio* coupled cluster (CC) theory is based on an exponential approach of the wave function: [213,214]

$$\Psi = exp(T)\Psi_0 \tag{2.33}$$

Ψ_0 corresponds to the Hartree-Fock wave function, and the exponential factor T consists of the sum of the operators $T = T_1 + T_2 + T_3 + ...$ that generate linear combinations of single, double, triple, etc. excitations. However, only by applying single and double excitations to the wave function, *i.e.* CCSD, a complex term results, depicted in Equation 2.34, in which not only single and double excitations but also the so-called disconnected doubles ($\frac{1}{2}T_1^2$), disconnected triples (T_1T_2), or disconnected quadruples ($\frac{1}{2}T_2^2$), etc. are included.

$$\Psi_{CCSD} = exp(T_1 + T_2)\Psi_0 = (1 + T_1 + T_2 + \frac{1}{2}T_1^2 + T_1T_2 + \frac{1}{2}T_2^2 + \frac{1}{2}T_1^2T_2 + ...)\Psi_0 \tag{2.34}$$

The CCSD formalism is exact for a two-electron system; [70] yet, triple excitations of many-electron systems account for a not inconsiderable part to the correlation energy, *i.e.* the difference between the exact energy and the HF energy. CCSDT explicitly includes three-electron correlations; however, it scales with the number of electrons raised to the power of eight and is thus impractical even for systems of only moderate size. This complexity can be reduced by estimating the triple excitation in a perturbative manner as applied in the CCSD(T) method which is much cheaper with respect to computational resources. [215,216] Hence, the CCSD(T) method is used in the present work for selected systems. Furthermore, a diagnostic tool can be implemented in the coupled-cluster calculations, the so-called T_1 diagnostics by Lee and Taylor, [217] which gives an indication of the multireference character of the wave function; T_1 values below 0.02 suggest that the HF wave function is a good reference and the results of the CC calculations are considered to be reliable.

Another approach to accurate quantum chemical calculations consists of a series of additive approximations. [70] The goal of these methods is to achieve high accuracy by extrapolating the results of lower-level calculations to the performance of a higher level computation which itself is much too expensive to be practical. As an example, the Complete Basis Set (CBS) is a common and widely accepted method, originally developed by

Ochterski, Petersson and Montgomery. [218–220] As the largest errors in *ab-initio* calculations result from basis set truncations, the aim of CBS procedures is to extrapolate the results from calculations using a finite basis set to the complete basis set limit. Different types of CBS methods exist according to the level of theory employed. In this work, the CBS-Q (Q = quadratic) method has been used to calculate selected reaction paths, as it provides a reasonable trade-off between accuracy and time-consumption. [219,220]

Briefly, the CBS-Q model starts with a geometry optimization at the MP2 level of theory;[viii] the zero-point energy is computed at the HF level and scaled by a factor 0.91844. An MP2 calculation with a large basis set (6-311+G(3d,2f,2df,2p)) is then performed as well as a CBS extrapolation to correct the energy up to second order. Two additional calculations are used to include higher order contributions: MP4(SDQ)/6-31+G(d,p) (for the higher order correlation effects), and QCISD(T)/ 6-31+G(d')127 for even higher order effects. [221] This model also has empirical corrections for spin contamination and a size-consistent higher order correction.

Another, even more accurate extrapolation method is given by the Weizmann-1 (W1) theory; [222,223] it is considered to yield the most accurate results without empirical parametrization, at substantially increased computational expense. While it was shown that CBS methods provide on average an accuracy of 4 kJ mol^{-1}, W1 calculations predict thermochemical data with an average error of only 1 kJ mol^{-1}; [223] however, W1 calculations can only be applied to first-row and second-row compounds, while CBS also covers the third row, including the first row of the transition metals. The protocol of W1 theory is rather complex, as it involves many optimization, single-point and extrapolation steps. [222] Briefly, the initial geometry optimization is performed at the B3LYP/cc-pVTZ+1 level of theory, including scaled zero-point energies, followed by CCSD(T)/AVDZ+2d and CCSD(T)/AVTZ+2$d1f$ single-point calculations, *i.e.* extrapolation and correlation components are derived from alternating CCSD and CCSD(T) methods.

2.4.3 Basis sets and computational procedures

All calculations presented in this study were performed using the Gaussian03 or the Gaussian09 package. [224,225] Furthermore, basis sets of approximately triple-ζ quality were employed for all elements; those were in most cases the tripleζ plus polarization basis sets (TZVP) of Ahlrichs *et al.*, [226] as well as higher analogues, including diffusion (def2-TZVP) [227] or the correlation-consistent basis set aug-cc-pVTZ by Dunning and coworkers. [228] Vibrational frequency analyses have been carried out at the same level of theory to characterize the nature of stationary points as minima or transition structures,

[viii] MP stands for the Møller-Plesset perturbation theory, originally developed from many-body perturbation theory. It generally provides accurate results and especially MP2 has become the most often applied method for the treatment of electron-correlation effects. [70]

and to derive the zero-point energy (ZPE) corrections; the application of scaling factors is indicated in the respective chapters. All relative electronic and Gibbs free energies reported in this thesis are corrected for ZPE contributions and given in kJ mol^{-1}; Gibbs free energies values correspond to standard conditions for temperature and pressure (STP). Transition-states structures were generally localized by using the classical Berny algorithm,[229] or *the Synchronous Transit-Guided Quasi-Newton* (STQN) Method, developed by Schlegel and coworkers.[230] If appropriate, intrinsic reaction coordinate (IRC) calculations or manual displacements along the reaction trajectory of the imaginary frequency were performed to link the transition-state structures with the respective intermediates.[231–234]

3 Structure and Reactivity of Vanadium-Phosphorous Oxygen-Cluster Ions

„God made the bulk; the surface was invented by the devil!" [235]

– Wolfgang E. Pauli

As mentioned in the introduction, the selective oxidation of hydrocarbons continues to constitute one of the major challenges in contemporary chemistry to solve global problems, such as an environmentally benign and economically feasible conversion of natural gas into value-added products. [8,9,11,13,236] In this context, oxygen-based catalysts, especially metal oxides, play a particular role as powerful oxidation reagents. [25,237–240] Despite the apparently large number of different pathways and mechanistic scenarios, formation of the various oxidation products of hydrocarbons by metal oxides can be classified in terms of three general reaction types (Figure 3.1): *i*) Hydrogen-atom transfer (HAT) from the hydrocarbon to the metal oxide to bring about oxidative coupling, *ii*) oxygen-atom transfer (OAT) to the organic substrate, and *iii*) oxidative dehydrogenation (ODH) of the latter. While there exist numerous effective homogeneous and heterogeneous catalysts which cover this rather broad spectrum of oxidation reactivity, it is no exaggeration to state the paucity of detailed knowledge about the intrinsic properties of many of the catalysts which, after all, control also the chemoselectivity of the three competing oxidation processes depicted in Figure 3.1. [34–37,39] To further improve the understanding on how such complex systems, *e.g.* surfaces in real-life heterogeneous catalysis may operate, often model systems have been studied as they can provide insights at what happens at a molecular level. [51] For example, hydrogen-atom abstraction from CH_4 to generate $CH_3^\bullet$ is viewed as the decisive step in the oxidative dehydrogenation and dimerization of methane, [23,241–244] and many studies suggest the crucial role of oxygen-centered radicals to bring about homolytic C−H bond scission by (doped) metal oxides. [238,245–259] The perhaps most compelling experimental evidence for this concept has been provided by the reactions of free aluminum-oxide cluster ions with methane: [137] Aluminum-oxide cluster cations with an *odd* number of aluminum atoms, thus lacking an oxygen-centered radical, do not react with methane at ambient conditions, in spite of a substantial thermodynamic driving force; in distinct contrast,

oligomeric $[(Al_2O_3)_x]^{\bullet+}$ (x = 3, 4, 5) cluster ions possessing an *even* number of aluminum atoms and an oxygen-centered radical are remarkably reactive towards methane even at room temperature (for more details on the role of the spin see Chapter 4).

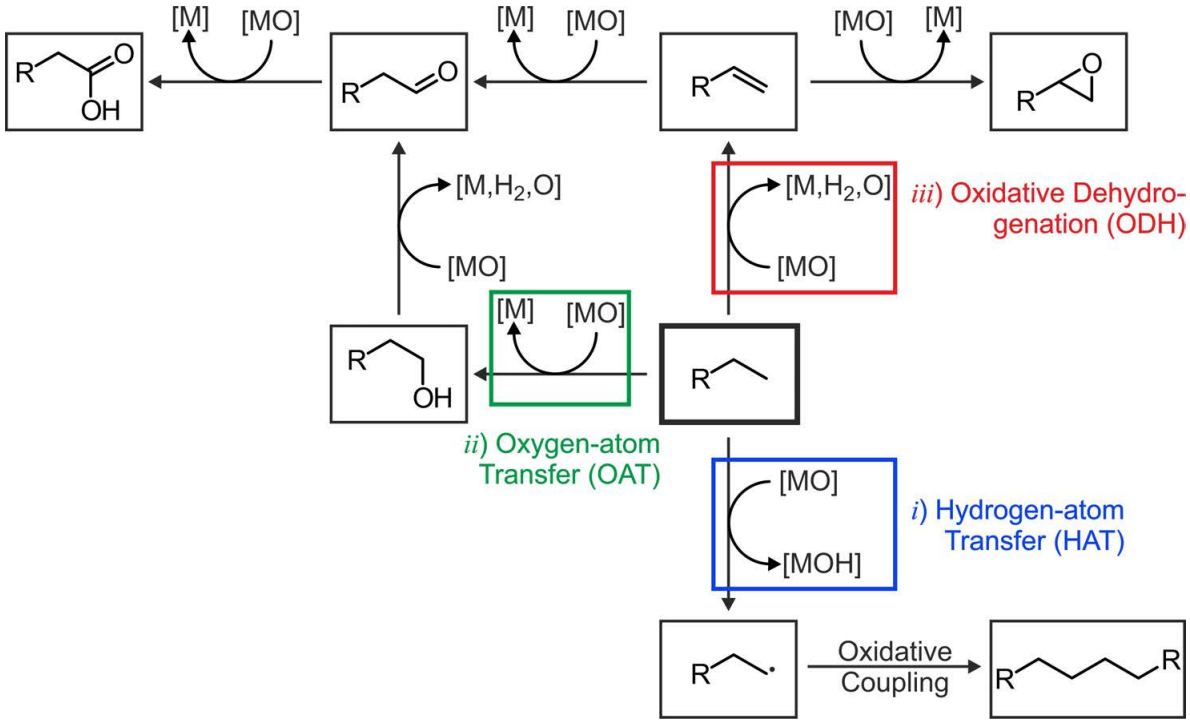

Figure 3.1: Schematic description of three basic oxidation processes of hydrocarbons by metal oxides [MO], all commencing with C−H bond activation.

Contemporary heterogeneous catalysts are often composed of multiple components, *i.e.* mixed-metal oxo-frameworks and doped materials, or employ non-innocent support materials.[40,260,261] Thus, in addition to the large number of homonuclear metal and non-metal oxides investigated,[139,142,144,262–271] more recently heteronuclear oxide clusters have been brought into focus, *e.g.* $[Al_xV_yO_z]^{+/-}$ ($x + y = 2, 3, 4$; $z = 3$ - 10),[272,273] $[Ce_xV_yO_z]^+$ ($x + y = 2, 3$; $z = 4, 5, 6$),[274] or $[(V_2O_5)_x(SiO_2)_y]^{+/-}$ ($x = 1, 2$; $y = 1$ - 4),[140,275] respectively, due to the chemically closer resemblance with „real world“ heterogeneous catalysts.

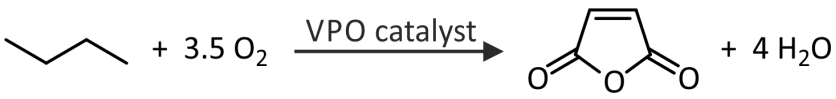

Figure 3.2: Industrial synthesis of maleic anhydride from *n*-butane.

As a well-known example for such a multi-component system in heterogeneous catalysis serves the efficient chemical transformation of *n*-butane to maleic anhydride by the so-called *VPO*-catalysts, Figure 3.2; this reaction involves the abstraction of eight hydrogen atoms from, as well as the transfer of three oxygen atoms to *n*-C_4H_{10}. Quite obviously, it is one of the most complex and yet highly selective oxidation reactions used in industry today.[276–281]

Since the first commercial use of *VPO* catalysts for the synthesis of maleic anhydride in the early 80s, many experimental and theoretical studies have been carried out to investigate this remarkable transformation. [282–290] However, the underlying reaction mechanisms are still only poorly understood and many different hypothesis exist. Reactivity studies of mixed vanadium-phosphorous oxygen-cluster ions with small hydrocarbons which are conducted under near single-collision conditions in the gas phase provide an promising approach in the elucidation of the mechanistic aspects of these systems and may help to characterize the reactive sites of such highly selective *VPO*-catalysts. The following chapter deals with the reactivity of selected *VPO*-cluster cations in terms of hydrocarbon oxidation and is divided into two parts: the first one discusses the reactivities of the adamantane-like heteronuclear vanadium-phosphorous oxygen cluster ions $[V_xP_{4-x}O_{10}]^{\bullet+}(x = 0, 2 - 4)$ towards methane, ethane, and ethene, including reactivity experiments as well as DFT-based calculations to study the rather complex mechanisms for the respective gas-phase reactions. The second part considers the structure and chemistry of the small, mixed oxo-cluster $[VPO_4]^{\bullet+}$ as a model system for the oxidation of small hydrocarbons in comparison to the long-time known and extensively studied homonuclear vanadium-oxide cation $[V_2O_4]^{\bullet+}$. In addition to reactivity studies and DFT calculations, advanced IR photodissociation spectroscopy is employed; the results underline the crucial role of phosphorous in terms of C−H bond activation of hydrocarbons by mixed *VPO*-clusters.

3.1 Reactivity of the vanadium-phosphorous oxygen-cluster ions $[V_xP_{4-x}O_{10}]^{\bullet+}$ ($x = 0 - 4$) towards small hydrocarbons

3.1.1 Generation and electronic structure of $[V_xP_{4-x}O_{10}]^{\bullet+}$ ($x = 0 - 4$)

With respect to the generation of the extensively studied vanadium cluster $[V_4O_{10}]^{\bullet+}$, [136,154,265,291–296] two different preparations are reported in the literature: the first method takes advantage of laser desorption/ionization of a suitable vanadium target with a mixture of O_2 seeded in the carrier gas helium, enabling the generation of this cluster in excellent yields. [291] However, this method also tends to generate structural isomers, *e.g.* the oxygen-bound $[V_4O_8(O_2)]^{\bullet+}$ complex, which affects the reactivity and kinetic analysis of $[V_4O_{10}]^{\bullet+}$. The second method uses a well-defined breakdown pathway from the precursor $V_6O_7(OCH_3)_{12}$ in the course of the electrospray-ionization process, [154] leading solely to the formation of the isomer of interest. The signal intensities of this method are relatively low but sufficient for ion/molecule reactions, and this method is considered as the method of choice.

For the homonuclear phosphorous cluster $[P_4O_{10}]^{\bullet+}$, neither laser desorption/ionization nor electrospray ionization are suitable for its generation. Instead, sublimation of solid

phosphorous pentoxide at 350 °C and subsequent electron ionization (electron impact) is necessary to generate the ion of interest in sufficient yields. [297,298] This method is generally referred to as *harsh* ionization method, since the electrons are accelerated to 70 eV before colliding with the neutral substrate molecules, thus often producing highly energetic radical cations. However, P_4O_{10} possesses a remarkably high ionization energy (*IE*), as will be discussed in detail below, and $[P_4O_{10}]^{\bullet+}$ is thus not accessible by soft ionization methods.

For the generation of the mixed *metal/non-metal* oxide cluster ions $[V_xP_{4-x}O_{10}]^{\bullet+}$ (x = 1 - 3), laser desorption/ionization is the method of choice. Using a relative simple preparation, the precursor $VOPO_4 \cdot 2H_2O$ can easily be synthesized (for details see Appendix B.2), subsequently dried and finally sintered to prepare small targets suitable for the laser-vaporization/ionization experiment conducted with an FT-ICR mass spectrometer; by this procedure two of the three clusters of interest, *i.e.* $[V_2P_2O_{10}]^{\bullet+}$ and $[V_3PO_{10}]^{\bullet+}$, are accessible in the gas phase. Furthermore, the formation of unwanted structural isomers, *i.e.* O_2-adducts, is rather unlikely, as no molecular oxygen is used in the generation process; all oxygen atoms originate from the sintered targets. However, despite numerous efforts of target modification and of optimizing the experimental parameters of the mass spectrometer, the remaining cluster $[VP_3O_{10}]^{\bullet+}$ could not be successfully generated. This most likely originates from the unfavorably high *IE*s for phosphorous-rich clusters. While the targets used in the experiments allow the generation of $[V_2P_2O_{10}]^{\bullet+}$, $[V_3PO_{10}]^{\bullet+}$, and $[V_4O_{10}]^{\bullet+}$, gaseous $[VP_3O_{10}]^{\bullet+}$ and $[P_4O_{10}]^{\bullet+}$, both requiring remarkably higher *IE*s, are not accessible by this method; the respective *IE*s were derived from DFT-calculations and amount to 1179 kJ mol^{-1} for P_4O_{10}, 1127 kJ mol^{-1} for VP_3O_{10}, 1081 kJ mol^{-1} for $V_2P_2O_{10}$, 1041 kJ mol^{-1} for V_3PO_{10}, and 1082 kJ mol^{-1} for V_4O_{10}. Nevertheless, it should be mentioned that also the generation process of $[V_2P_2O_{10}]^{\bullet+}$ and $[V_3PO_{10}]^{\bullet+}$ is highly sensitive towards the experimental parameters. Especially modifications of the targets or the pulse valve (see Section 2.1.2) can cause dramatic effects on the signal intensities.

Regarding the intrinsic features of these systems, further insight into the geometric and electronic structures are provided by density functional calculations. According to UB3LYP computations, all five clusters $[V_xP_{4-x}O_{10}]^{\bullet+}$ (x = 0 - 4) have surprisingly similar properties, concerning the structure and electron distribution. The most stable isomer of all five systems corresponds to a slightly Jahn-Teller distorted tetrahedral cage structure, with one terminal X=O bond (X = V, P) being significantly elongated compared to the neutral cluster due to the removal of an electron from the respective double bond. For example, one of the terminal P−O bonds in the homonuclear $[P_4O_{10}]^{\bullet+}$ cluster ion, thus possessing a cage structure with C_S symmetry, is elongated from 1.46 to 1.57 Å, caused by the removal of an electron from the P=O double bond of neutral P_4O_{10}. However, the most notable feature of all mixed clusters, *i.e.* $[V_3PO_{10}]^{\bullet+}$, $[V_2P_2O_{10}]^{\bullet+}$, and $[VP_3O_{10}]^{\bullet+}$, concerns the distribution of the spin density, indicated by the blue isosurfaces in Figure 3.3. For the corresponding neutral clusters, orbital

analysis showed that the HOMO in all these vanadium/phosphorous-containing clusters corresponds to the π-bonding orbital of the terminal P=O bond; removing an electron from this orbital in the laser-ionization process results in phosphorous-bound, oxygen-centered radicals as the most stable isomers, *i.e.* P−O$^{\bullet}$, respectively. An isomeric cluster with the spin located at the vanadium-bound oxygen atom V−O$^{\bullet}$ could only be located as a local minimum on PES in the case of $[V_3PO_{10}]^{\bullet+}$ with a relative energy of 74 kJ mol^{-1} compared to the P−O$^{\bullet}$ isomer. Due to the rather small or even non-existing barriers in the case of $[V_2P_2O_{10}]^{\bullet+}$ and $[VP_3O_{10}]^{\bullet+}$ structure optimization were only feasible by fixing the terminal V=O bond to 1.75 Å, as reported for the structure of $[V_4O_{10}]^{\bullet+}$. The resulting relative energies for isomers with V−O$^{\bullet}$ units amount to 92 kJ mol^{-1} for $[V_2P_2O_{10}]^{\bullet+}$ and 71 kJ mol^{-1} for $[VP_3O_{10}]^{\bullet+}$ above the P−O$^{\bullet}$ ground state, respectively.

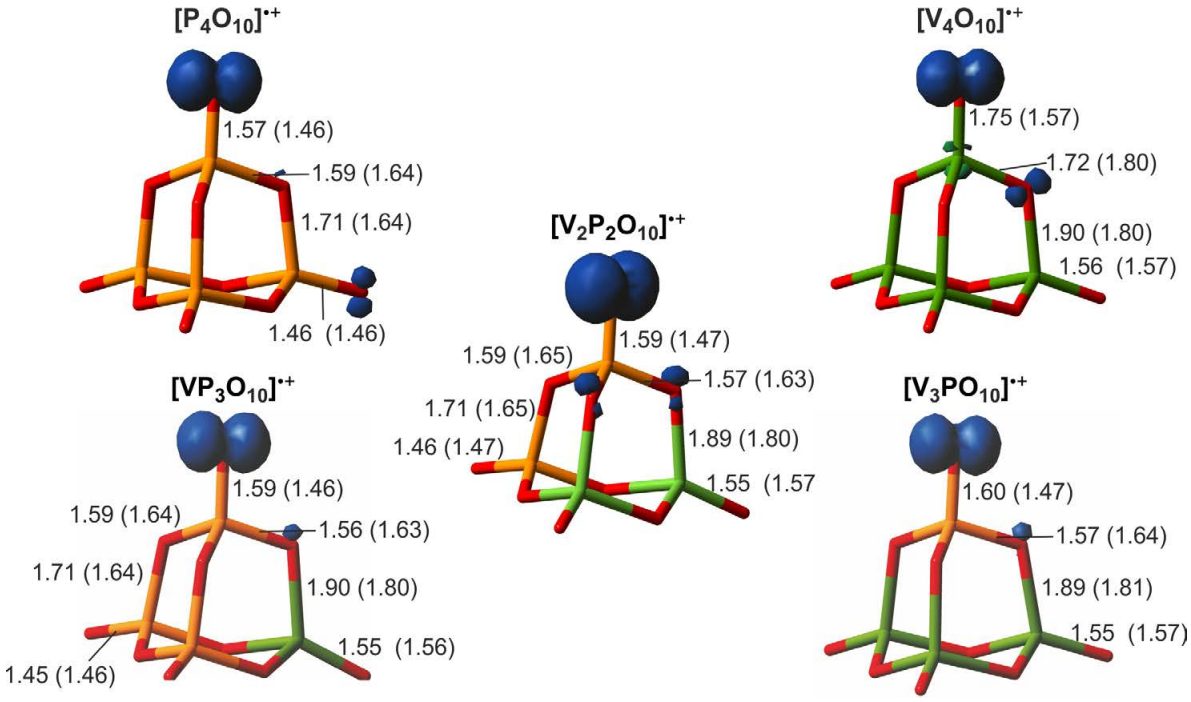

Figure 3.3: Lowest-energy structures calculated for $[V_xP_{4-x}O_{10}]^{\bullet+}$($x$ = 0 - 4) using DFT with the UB3LYP functional (green V, yellow P, red O). The blue isosurface indicates the spin density within the respective cluster. Bond lengths for the cationic and the according neutral cluster (in parentheses) are given in Å.

3.1.2 Reactivity of $[V_xP_{4-x}O_{10}]^{\bullet+}$ (x = 0, 2 - 4) towards methane

As mentioned previously, the pure vanadium cluster $[V_4O_{10}]^{\bullet+}$ has been addressed in many studies, including the reactivity towards methane at ambient conditions;[265] it was shown that $[V_4O_{10}]^{\bullet+}$ brings about efficient activation of methane (Equation 3.1) with a rate constant of $k = 5.5 \cdot 10^{-10}$ cm^3 s^{-1} molecule^{-1}; this corresponds to an efficiency of 60 % as compared to the collision rate.

$$[V_4O_{10}]^{\bullet+} + CH_4 \longrightarrow [V_4O_9(OH)]^+ + CH_3^{\bullet} \tag{3.1}$$

Based on the findings on various metal-oxide clusters, it was long-time assumed, that this kind of reactivity requires some kind of metal-species involved. For example, with respect to the *VPO*-catalysts it was conjectured from surface studies that structurally ill-defined phosphate species work as catalytically innocent, chemically inert linkers between the active vanadium-oxide sites in these mixed metal-oxide phosphates.[276] However, this general assumption was questioned by several gas-phase study, *e.g.* room-temperature hydrogen abstraction from methane by the metal-free radical cation oxide $[SO_2]^{\bullet+}$.[268] In the studies presented here, the tetranuclear phosphorous oxide cluster $[P_4O_{10}]^{\bullet+}$ serves as the first example for the thermal activation of methane by a polynuclear metal-free oxide radical cation. As shown in Figure 3.4, mass-selected $[P_4O_{10}]^{\bullet+}$ reacts with CH_4 at room temperature via hydrogen-atom transfer, Equation 3.2, with a rate constant of $k = 6.4 \cdot 10^{-10}$ cm^3 s^{-1} molecule^{-1}; this corresponds to an efficiency of 66 %. The intramolecular KIE, derived from the $[P_4O_{10}]^{\bullet+}/CH_2D_2$ couple (Figure 3.4c) amounts to KIE = 1.6 $\pm$ 0.1. The occurrence of reaction 3.2 implies that the newly formed O−H bond in the ionic cluster exceeds the C−H bond energy of methane (439 kJ mol^{-1}).[299]

$$[P_4O_{10}]^{\bullet+} + CH_4 \longrightarrow [P_4O_9(OH)]^+ + CH_3^{\bullet} \tag{3.2}$$

Regarding the mechanism of the reaction calculated with DFT and CCSD(T) methods, the coordination of methane to the $[P_4O_{10}]^{\bullet+}$ cluster and the smooth hydrogen-abstraction process are associated with a significant gain of energy, 162 kJ mol^{-1} for DFT and 168 kJ mol^{-1} for CCSD(T), respectively (Figure 3.5). It has to be noted that no stable encounter complexes of the type $[P_4O_{10}^{\bullet}\cdots CH_4]^+$ were found in the structure optimizations, suggesting that the reaction proceeds, without a noticeable reaction barrier, by direct hydrogen-atom abstraction to form the intermediate $[P_4O_9OH\cdots CH_3^{\bullet}]^+$. For the related $[V_4O_{10}]^{\bullet+}/CH_4$ system, molecular dynamics calculations suggested that forming the O−H and breaking the C−H bonds are completed after ca. 450 fs.[265] In view of the quite similar potential energy surfaces of the two couples $[X_4O_{10}]^{\bullet+}/CH_4$ (X = V, P), we assume

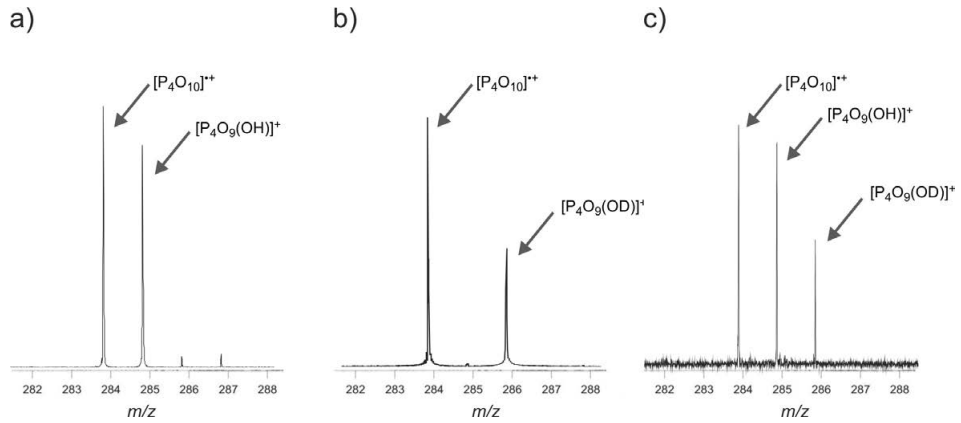

Figure 3.4: Ion/molecule reactions of mass-selected $[P_4O_{10}]^{\bullet+}$ with a) CH_4, b) CD_4, and c) CH_2D_2.

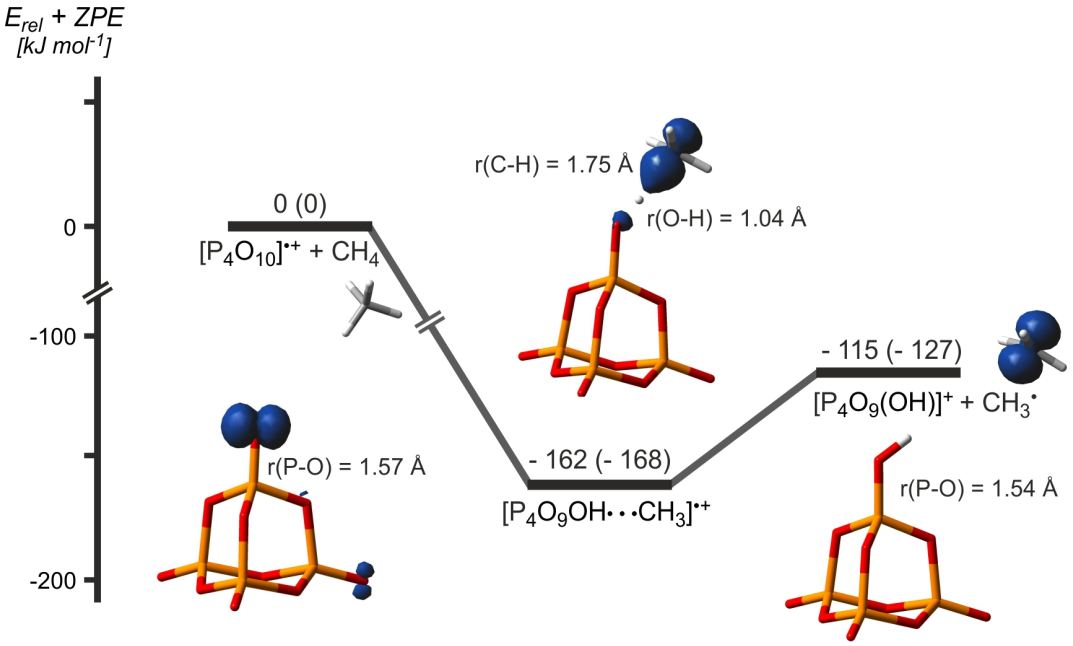

Figure 3.5: Energy diagram for the reaction of $[P_4O_{10}]^{\bullet+}$ with methane. The energy values are derived from DFT and the more accurate CCSD(T) (in parentheses) calculations; the blue isosurface indicates the spin density along the reaction pathway.

a comparable time scale of C−H bond activation for the $[P_4O_{10}]^{\bullet+}/CH_4$ system.[ix] In the intermediate complex $[P_4O_9OH\cdots CH_3^{\bullet}]^+$, the methyl group is very loosely coordinated to the hydrogen atom of the newly formed, phosphorous-bound hydroxyl group; the reaction is completed by loss of a $CH_3^{\bullet}$ radical concomitant with formation of $[P_4O_9(OH)]^+$. The computed exothermicity, which amounts to -115 kJ mol^{-1} for DFT and -127 kJ mol^{-1} for CCSD(T), together with the absence of kinetic barriers, are in full accordance with the experimentally observed occurrence of Reaction 3.2 at room temperature. Moreover, the higher exothermicites for the $[P_4O_{10}]^{\bullet+}/CH_4$, compared to the $[V_4O_{10}]^{\bullet+}/CH_4$ couple, in

[ix] For a detailed discussion on the direct HAT mechanism, including the $[V_4O_{10}]^{\bullet+}/CH_4$ system, see Chapter 4.1.1.

addition to the larger rate constant strongly emphasize the assumption that the metal-free $[P_4O_{10}]^{\bullet+}$ cluster cation is actually more reactive than the metallic, isostructural analogue $[V_4O_{10}]^{\bullet+}$. Thus, the enhanced reactivity of $[P_4O_{10}]^{\bullet+}$ may shed a new light on the common presumption of catalytically innocent phosphate linkers between catalytically active metal oxide sites in mixed metal oxide phosphates widely used as catalyst in industry.

In line with the structural similarities with their homonuclear analogues (see Page 39), also the mixed clusters $[V_2P_2O_{10}]^{\bullet+}$ and $[V_3PO_{10}]^{\bullet+}$ bring about efficient homolytic C−H bond cleavage of methane at room temperature (Figure 3.6) according to Equations 3.3 and 3.4. From the kinetic analysis, the rate constants of $k([V_2P_2O_{10}]^{\bullet+}) = 5.6 \cdot 10^{-10}$ cm^3 s^{-1} molecule^{-1} and $k([V_3PO_{10}]^{\bullet+}) = 5.6 \cdot 10^{-10}$ cm^3 s^{-1} molecule^{-1} were derived; these values correspond to reaction efficiencies of 57 % and 53 %, respectively, relative to the collision rate. Further, the intramolecular KIEs, derived from the $[V_2P_2O_{10}]^{\bullet+}/CH_2D_2$ and $[V_3PO_{10}]^{\bullet+}/CH_2D_2$ couples amount to KIE = 1.3 ± 0.1 for $[V_2P_2O_{10}]^{\bullet+}$ and to KIE = 1.2 ± 0.1 for $[V_3PO_{10}]^{\bullet+}$. These values are in the same order of magnitude as for the homonuclear clusters, thus in excellent agreement with the previous findings.

$$[V_2P_2O_{10}]^{\bullet+} + CH_4 \longrightarrow [V_2P_2O_9(OH)]^+ + CH_3^{\bullet} \tag{3.3}$$

$$[V_3PO_{10}]^{\bullet+} + CH_4 \longrightarrow [V_3PO_9(OH)]^+ + CH_3^{\bullet} \tag{3.4}$$

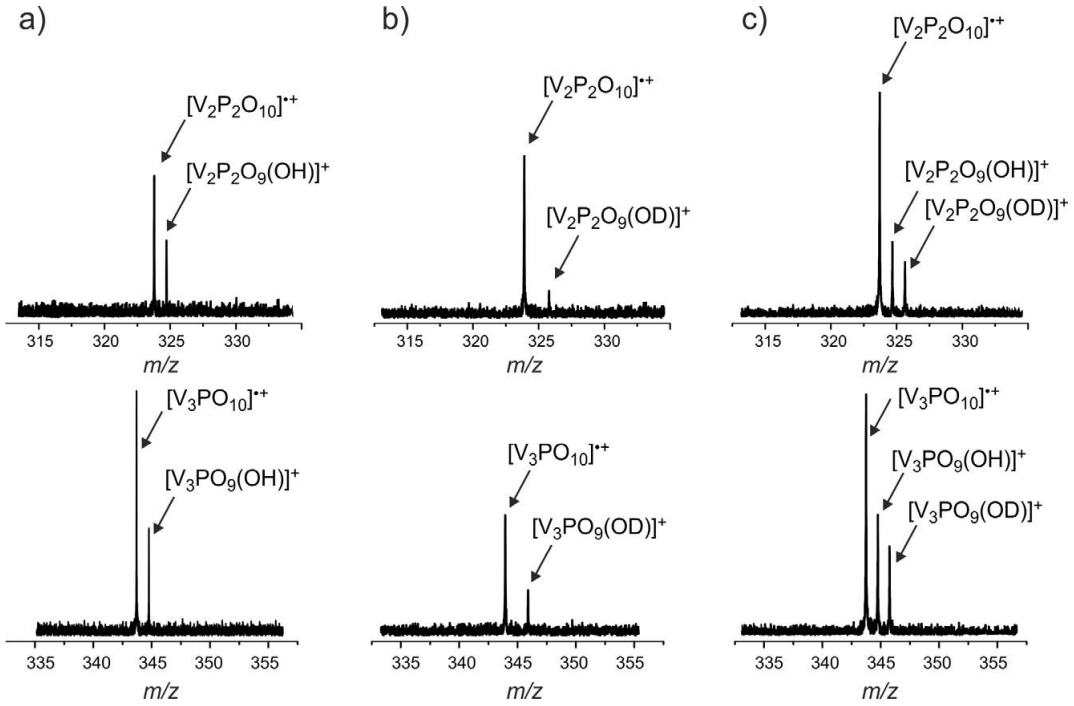

Figure 3.6: Ion/molecule reactions of mass-selected $[V_2P_2O_{10}]^{\bullet+}$ and $[V_3PO_{10}]^{\bullet+}$ with a) CH_4, b) CD_4, and c) CH_2D_2.

Not entirely unexpected, also the PESs of $[V_2P_2O_{10}]^{\bullet+}$ and $[V_3PO_{10}]^{\bullet+}$ in their reactions with methane resemble strongly the reaction mechanisms reported earlier for $[P_4O_{10}]^{\bullet+}$ and $[V_4O_{10}]^{\bullet+}$, as shown in Figure 3.7. Smooth, barrier-free hydrogen-atom abstraction from methane to the cluster leads to an intermediate in which the methyl group is only loosely coordinated to the hydrogen atom of the newly formed phosphorous-bound hydroxyl group. For both systems, the formation of this intermediate is associated with a significant energy gain of -137 kJ mol^{-1} for $[V_2P_2O_9OH\cdots CH_3]^{\bullet+}$ and -127 kJ mol^{-1} for $[V_3PO_9OH\cdots CH_3]^{\bullet+}$. The reactions are completed by liberating the methyl radical $CH_3^{\bullet}$ concomitant with the formation of $[V_2P_2O_9(OH)]^+$ and $[V_3PO_9(OH)]^+$, respectively; the computed exothermicities amount to -102 kJ mol^{-1} for $[V_2P_2O_9(OH)]^+$ and to -97 kJ mol^{-1} for $[V_3PO_9(OH)]^+$. As already mentioned with respect to the electronic structure, this reaction proceeds at room temperature due to kinetic reasons only at the radical P$-$O$^{\bullet}$ unit. As shown by He and coworkers in a detailed DFT study on the $[V_3PO_{10}]^{\bullet+}/[V_4O_{10}]^{\bullet+}$ systems in their HAT reactions with methane, the reaction is thermochemically possible also at a V=O unit of either $[V_3PO_{10}]^{\bullet+}$ or $[V_4O_{10}]^{\bullet+}$ bearing no spin density at the oxygen atom; however, in the course of the reaction the unpaired electron has to be transferred to the reactive site, *i.e.* a so-called intramolecular spin-density transfer is necessary. [300] For $[V_3PO_{10}]^{\bullet+}$, the resulting transition state lies significantly above the entrance channel, exhibiting an endothermic barrier of + 21 kJ mol^{-1} and this reaction pathway is thus not possible for this cluster under thermal conditions which is most likely also the case for $[V_2P_2O_{10}]^{\bullet+}$.

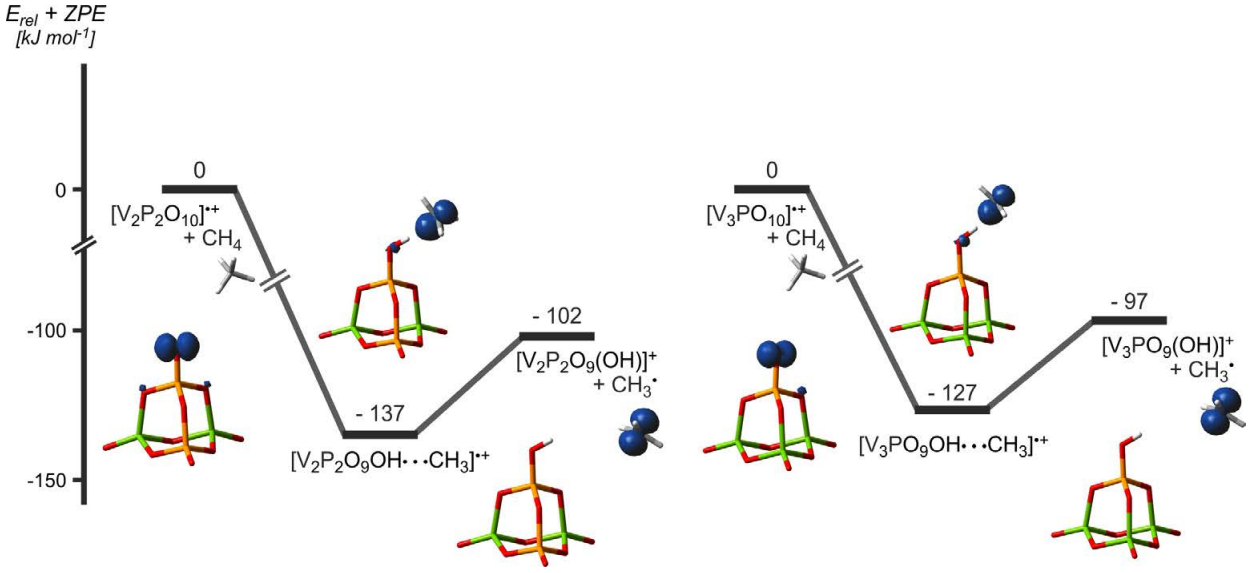

Figure 3.7: Energy diagram for the reaction of $[V_2P_2O_{10}]^{\bullet+}$ (left) and $[V_3PO_{10}]^{\bullet+}$ (right) with methane (green V, yellow P, red O, gray C, white H); the blue isosurface indicates the spin density along the reaction pathway, respectively.

3.1.3 Reactivity of $[V_xP_{4-x}O_{10}]^{\bullet+}$ (x = 0, 2 - 4) towards ethane and ethene

In contrast to the observed, more or less uniform reactivity of $[V_xP_{4-x}O_{10}]^{\bullet+}$($x$ = 0, 2 - 4) towards methane, the reactivity patterns with ethane and ethene differ quite dramatically. With respect to the homonuclear metal cluster $[V_4O_{10}]^{\bullet+}$, recent results for the reactivity towards ethane reported by different laboratories are somewhat contradictory: Castleman and co-workers describe oxygen-atom transfer in the reaction of $[V_4O_{10}]^{\bullet+}$ with ethane as the only reaction channel (Equation 3.5), [136] while the couple $[V_4O_{10}]^{\bullet+}$/propane, in two different experimental setups, gives rise to the dehydrogenation product; here, OAT is either non-existing [301] or forms only a minor product. [294] Repeating the experiment of $[V_4O_{10}]^{\bullet+}$ with ethane in the triple quadrupole mass spectrometer, only the dehydrogenation product $[V_4O_{10}H_2]^{\bullet+}$ is detected according to Equation 3.6; oxygen-atom transfer was not observed at the detection limit. In view of the rather poor signal intensities, we cannot rigorously rule out the minor presence of oxygen-atom transfer; yet, oxidative dehydrogenation is clearly the main product. The calculated energetics, reported in Chapter 3.2, further support the notion that oxidative dehydrogenation is favored over oxygen-atom transfer.

$$[V_4O_{10}]^{\bullet+} + C_2H_6 \longrightarrow [V_4O_9]^{\bullet+} + C_2H_6O \tag{3.5}$$

$$[V_4O_{10}]^{\bullet+} + C_2H_6 \longrightarrow [V_4O_{10}H_2]^{\bullet+} + C_2H_4 \tag{3.6}$$

$$[V_4O_{10}]^{\bullet+} + C_2H_4 \longrightarrow [V_4O_9]^{\bullet+} + CH_3CHO \tag{3.7}$$

Regarding the reactivity towards ethene, $[V_4O_{10}]^{\bullet+}$ brings about oxygen-atom transfer to the hydrocarbon according to Equation 3.7 as shown in a combined experimental/theoretical study. [292] DFT calculations revealed that the resulting neutral product corresponds to acetaldehyde CH_3CHO rather than ethenol C_2H_3OH or ethylene oxide C_2H_4O.

For the isostructural, tetranuclear phosphorous oxide cluster $[P_4O_{10}]^{\bullet+}$, neither oxidative dehydrogenation of, nor oxygen-atom transfer transfer to C_2H_6 take place; instead, hydrogen-atom transfer dominates, thus producing the cationic *closed-shell* species $[P_4O_9(OH)]^+$ (Equation 3.8). This preference towards homolytic C−H bond activation also prevails in the ion/molecule reaction with ethene. Here, two different reaction channels occur at room temperature, one corresponds to hydrogen-atom abstraction (Equation 3.9) and the other to a single-electron transfer (SET) according to Equation 3.10, respectively, with a branching ratio of approximately 1 : 1 (Figure 3.8); the charge-exchange pathway is due to the rather high ionization energy of P_4O_{10} (*IE* = 12.2 eV) as compared to C_2H_4 (*IE* = 10.3 kJ mol^{-1}). [302]

$$[P_4O_{10}]^{\bullet+} + C_2H_6 \longrightarrow [P_4O_9(OH)]^+ + C_2H_5^{\bullet} \quad (3.8)$$

$$[P_4O_{10}]^{\bullet+} + C_2H_4 \longrightarrow [P_4O_9(OH)]^+ + C_2H_3^{\bullet} \quad (3.9)$$

$$[P_4O_{10}]^{\bullet+} + C_2H_4 \longrightarrow P_4O_{10} + [C_2H_4]^{\bullet+} \quad (3.10)$$

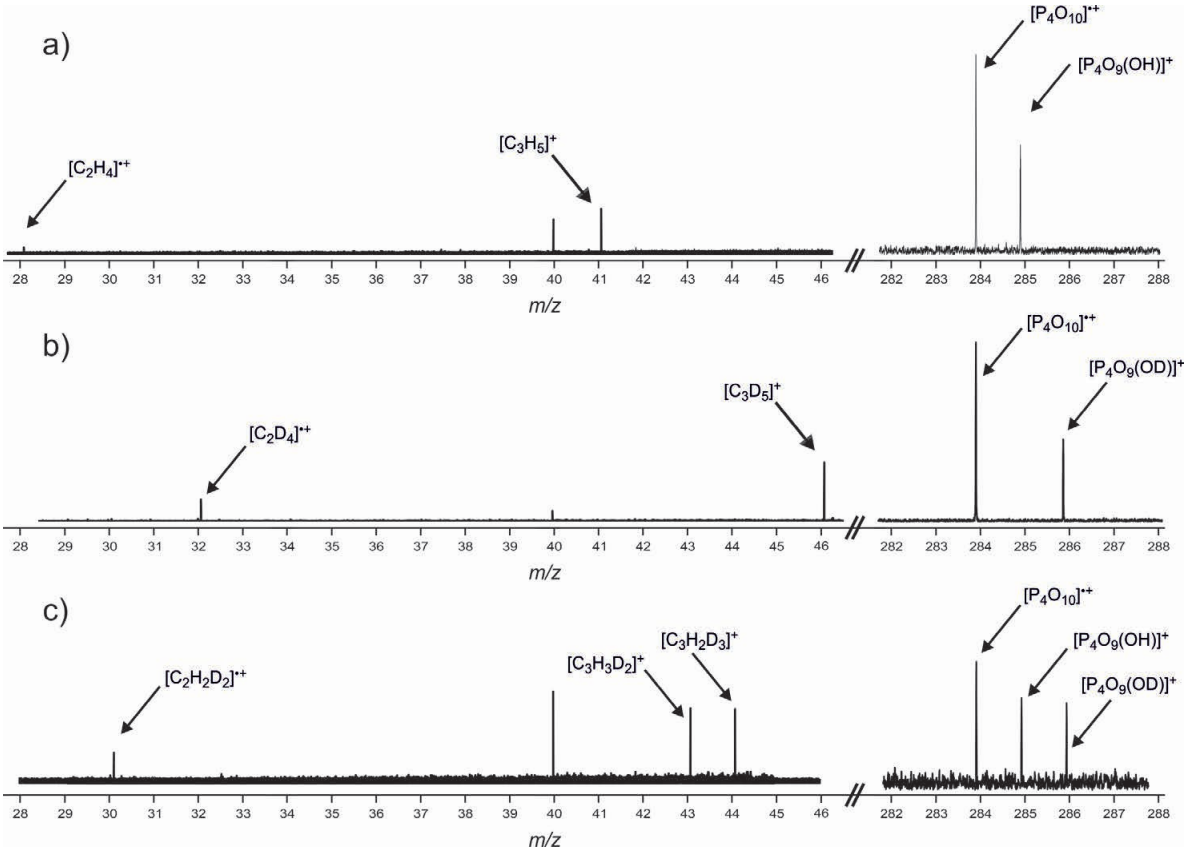

Figure 3.8: Ion/molecule reactions of mass-selected $[P_4O_{10}]^{\bullet+}$ with a) C_2H_4, b) C_2D_4, and c) CH_2CD_2. The signal at m/z = 39.9 is attributed to ionized argon, which was used as buffer gas to thermalize the hot ions.

From a kinetic analysis, a rate constant of $k = 2.0 \cdot 10^{-9}$ cm^3 s^{-1} molecule^{-1} was derived, corresponding to an efficiency of 100 % in terms of the collision rate. When C_2D_4 and CH_2CD_2 are used (Figure 3.8b, c) no significant kinetic isotope effect (KIE = 1.05) was found for the homolytic C−H(D) bond cleavage. The formation of the *closed-shell* ion $[C_3H_5]^+$ can be traced back to an efficient secondary reaction of $[C_2H_4]^{\bullet+}$ with another neutral molecule of ethene (Euqation 3.11), resulting in the formation of an allyl cation and a methyl radical, as studied in detail quite some time ago. [303–306] The rate constant $k = 0.9 \cdot 10^{-9}$ cm^3 s^{-1} molecule^{-1} for this secondary reaction is of the same order of magnitude as the primary reaction. [306]

$$[C_2H_4]^{\bullet+} + C_2H_4 \longrightarrow [C_3H_5]^+ + CH_3^{\bullet} \tag{3.11}$$

Accordingly, even though the two homonuclear, cationic radical clusters have similar geometries, comparable spin densities and the same reactivity pattern in the reaction with methane, for the higher hydrocarbons, the reactivities are completely different, Equations 3.5 - 3.10; thus, a more detailed comparison of $[P_4O_{10}]^{\bullet+}$ with $[V_4O_{10}]^{\bullet+}$ is quite instructive. While an in-depth theoretical analysis is given Chapter 3.2, a short comparison concerning the energetics of the oxygen-atom and electron transfers is presented here. Based on the DFT calculations, the following pictures emerge: oxygen-atom transfer is by 119 kJ mol^{-1} more favored from the terminal V=O bond in $[V_4O_{10}]^{\bullet+}$ as compared with the terminal P=O bond in $[P_4O_{10}]^{\bullet+}$; this reflects the significantly higher oxygen-atom affinity of $[P_4O_9]^{\bullet+}$ and explains the non-occurrence of OAT for $[P_4O_{10}]^{\bullet+}$ in contrast to $[V_4O_{10}]^{\bullet+}$. As to the single-electron transfer, the DFT calculated *IE* of P_4O_{10} amounts to 1179 kJ mol^{-1} and that of V_4O_{10} to only 1080 kJ mol^{-1} compared with $IE(C_2H_4)$ = 993 kJ mol^{-1}. While for the $[P_4O_{10}]^{\bullet+}/C_2H_4$ couple SET takes place, it has not been observed for the related $[V_4O_{10}]^{\bullet+}/C_2H_4$ system at room temperature; this may be a consequence of the substantial difference of the recombination energies of the two cluster ions $[X_4O_{10}]^{\bullet+}$ (X = P, V).

The reaction of $[V_4O_{10}]^{\bullet+}$ with C_2H_4 has also been studied in the triple quadrupole mass spectrometer. At collision energies nominally set to o eV, oxygen-atom transfer is observed exclusively as reported previously;[292] SET to give rise to $[C_2H_4]^{\bullet+}$ occurs only at elevated collision energies. Further, homolytic C−H bond activation of C_2H_4 by $[V_4O_{10}]^{\bullet+}$ does not even occur at higher collision energies, as shown in Figure 3.9. This illustrate once more the lower ionization energy of $[V_4O_{10}]^{\bullet+}$, as well as the lower reactivity in terms of homolytic C−H bond activation of hydrocarbons.

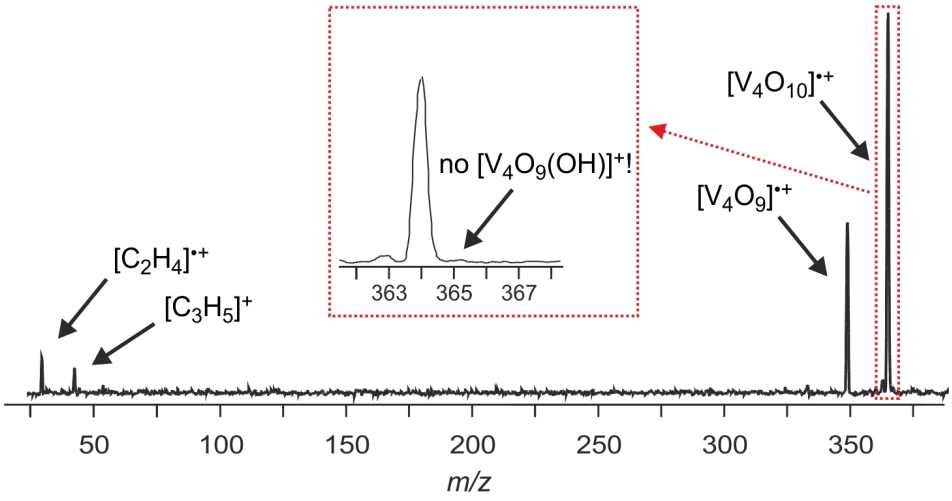

Figure 3.9: Ion/molecule reactions of mass-selected $[V_4O_{10}]^{\bullet+}$ with ethene at a collision energy of E_{CM} = 3.0 eV.

However, with respect to the remarkably differing reactivity patterns of $[V_4O_{10}]^{\bullet+}$ and $[P_4O_{10}]^{\bullet+}$ with ethane and ethene, it deems of interest to study the reactivity of the heteronuclear clusters with the C_2-hydrocarbons, respectively. Quite unexpectedly, the reactions of $[V_2P_2O_{10}]^{\bullet+}$ and $[V_3PO_{10}]^{\bullet+}$ with ethane and ethene give rise to completely new product distributions, as shown in Figure 3.10 and 3.11, for the couples $[V_2P_2O_{10}]^{\bullet+}/C_2H_x$ and $[V_3PO_{10}]^{\bullet+}/C_2H_x$ (x = 4, 6), respectively. While homolytic C−H bond scission,

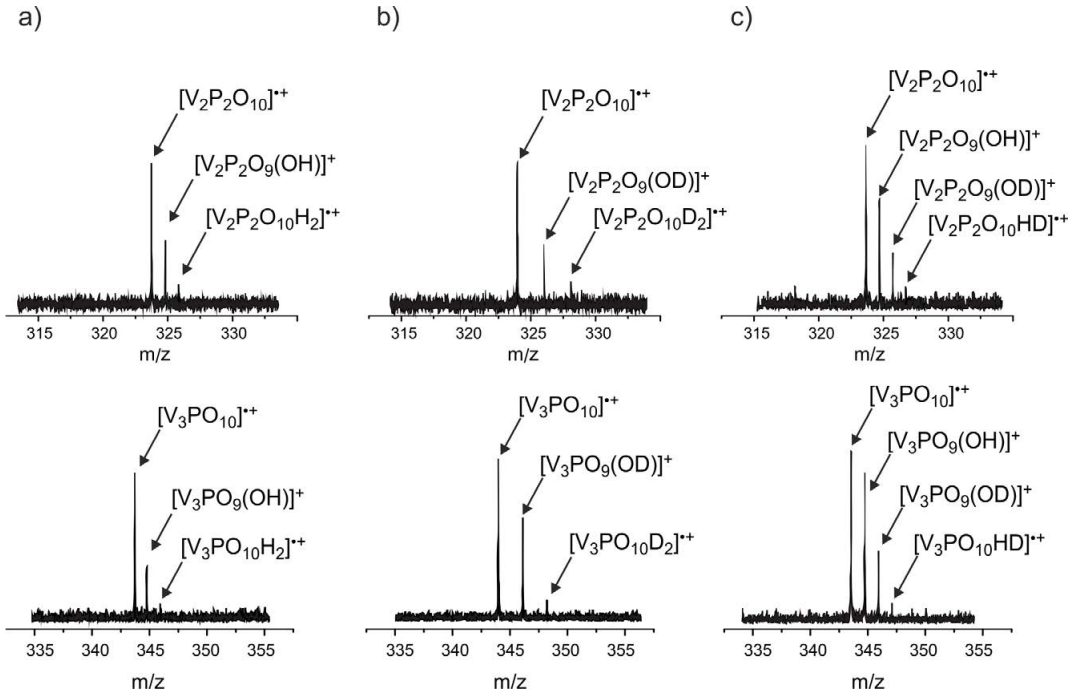

Figure 3.10: Ion/molecule reactions of mass-selected $[V_2P_2O_{10}]^{\bullet+}$ and $[V_3PO_{10}]^{\bullet+}$ with a) C_2H_6, b) C_2D_6, and c) CH_3CD_3.

according to Equations 3.12 and 3.15, prevails for all four educt couples, oxygen-atom transfer does not take place, Equations 3.13 and 3.16. The occurrence of Reaction 3.12 and 3.15 and the lack of an oxygen-atom transfer suggest once more that the radical site is located at the phosphorous-bound oxygen atom, based on the distinctly different reactivity pattern of $[P_4O_{10}]^{\bullet+}$ versus $[V_4O_{10}]^{\bullet+}$. More surprisingly, double C−H bond activation, *i.e.* dehydrogenation of ethane and ethene, according to Equations 3.14 and 3.17 takes place as a new reaction channel; this reaction has not been observed in the reactions of C_2H_x (x = 4, 6) with $[P_4O_{10}]^{\bullet+}$ and $[V_4O_{10}]^{\bullet+}$, respectively.

$$[V_2P_2O_{10}]^{\bullet+} + C_2H_x \longrightarrow [V_2P_2O_9(OH)]^{+} + C_2H_{x-1}^{\bullet} \quad (3.12)$$

$$[V_2P_2O_{10}]^{\bullet+} + C_2H_x \not\longrightarrow [V_2P_2O_9]^{\bullet+} + C_2H_xO \quad (3.13)$$

$$[V_2P_2O_{10}]^{\bullet+} + C_2H_x \longrightarrow [V_2P_2O_{10}H_2]^{\bullet+} + C_2H_{x-2} \quad (3.14)$$

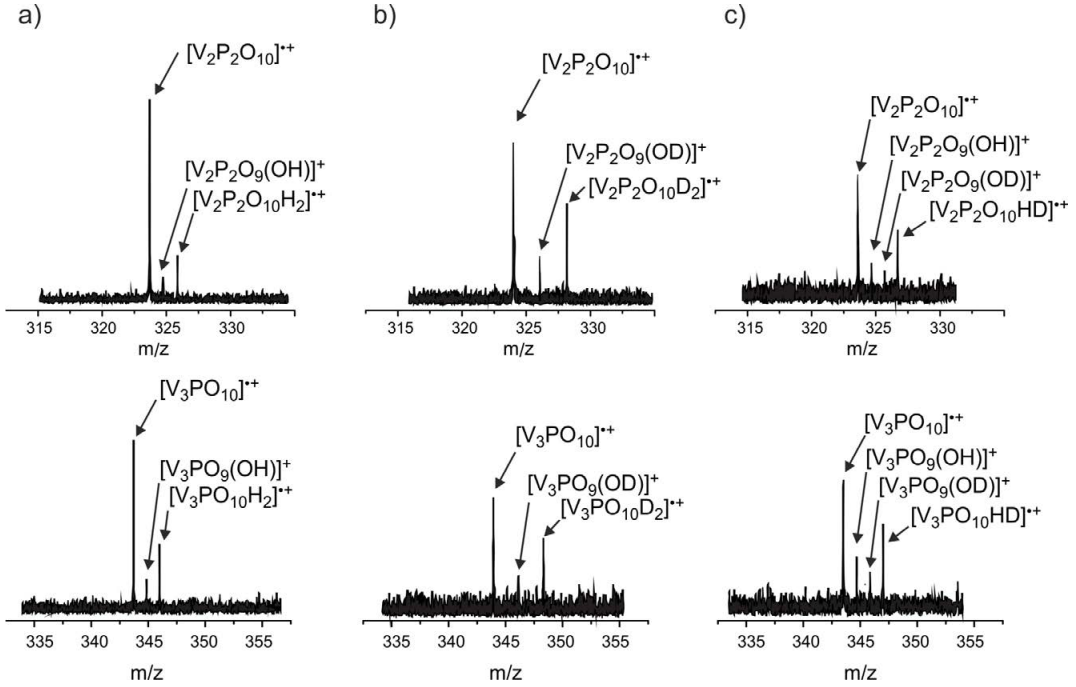

Figure 3.11: Ion/molecule reactions of mass-selected $[V_2P_2O_{10}]^{\bullet+}$ and $[V_3PO_{10}]^{\bullet+}$ with a) C_2H_4, b) C_2D_4, and c) CH_2CD_2.

$$[V_3PO_{10}]^{\bullet+} + C_2H_x \longrightarrow [V_3PO_9(OH)]^+ + C_2H_{x-1}{}^{\bullet} \quad (3.15)$$

$$[V_3PO_{10}]^{\bullet+} + C_2H_x \not\longrightarrow [V_3PO_9]^{\bullet+} + C_2H_xO \quad (3.16)$$

$$[V_3PO_{10}]^{\bullet+} + C_2H_x \longrightarrow [V_3PO_{10}H_2]^{\bullet+} + C_2H_{x-2} \quad (3.17)$$

Based on the reactions with the selectively deuterated ethane CH_3CD_3 and ethene CH_2CD_2, double hydrogen (deuterium) transfer proceeds for both substrates in a clean [1,2]-fashion which is not preceded by H/D scrambling, as indicated by the lack of signals corresponding to the transfer of either two hydrogen or two deuterium atoms to the respective cluster ion. However, despite many attempts, the stereoselectivity of the dehydrogenation of *cis*- and *trans* CHD=CHD could not be studied. These experiments had to be carried out employing another set of targets and a replaced pulse valve as compared to previous measurements, and it turned out that $[V_2P_2O_{10}]^{\bullet+}$ and $[V_3PO_{10}]^{\bullet+}$ could not be generated in sufficient intensities. However, though the intensities of the product ions are very weak, the isotopic pattern points to a statistical distribution with a slight *cis*-preference thus indicating a rather stereounselective elimination.[x]

The rate constants for the individual reaction couples amount to $k([V_2P_2O_{10}]^{\bullet+}/C_2H_6)$ = 5.9 · 10^{-10} cm^3 s^{-1} molecule^{-1}, $k([V_3PO_{10}]^{\bullet+}/C_2H_6)$ = 8.7 · 10^{-10} cm^3 s^{-1} molecule^{-1},

[x] This finding is in agreement with theory, as the rotational barrier of the C−C bond in the respective adduct complexes of $[V_2P_2O_{10}]^{\bullet+}$ and $[V_3PO_{10}]^{\bullet+}$ (Chapter 3.2) amounts to only +4 kJ mol^{-1} and +9 kJ mol^{-1} respectively, similar to the rotational barrier of the single C−C bond in ethane; thus, the stereochemical integrity of the C−C unit of C_2H_4 most likely is not preserved in the course of the reaction.

$k([V_2P_2O_{10}]^{\bullet+}/C_2H_4)$ = 5.5 · 10^{-10} cm^3 s^{-1} $molecule^{-1}$, and $k([V_3PO_{10}]^{\bullet+}/C_2H_4)$ = 7.1 · 10^{-10} cm^3 s^{-1} $molecule^{-1}$, corresponding to reaction efficiencies of 62 %, 93 %, 58 %, and 76 %, respectively. The KIEs for each reaction were derived from the respective couples $[V_xP_{4-x}O_{10}]^{\bullet+}/CH_3CD_3$ and $[V_xP_{4-x}O_{10}]^{\bullet+}/CH_2CD_2$ (x = 2, 3), amounting to KIE($[V_2P_2O_{10}]^{\bullet+}/C_2H_6$) = 2.2, KIE($[V_3PO_{10}]^{\bullet+}/C_2H_6$) = 1.9, KIE($[V_2P_2O_{10}]^{\bullet+}/C_2H_4$) = 1.3, and KIE($[V_3PO_{10}]^{\bullet+}/C_2H_4$) = 1.4. The rate constants and efficiencies are slightly larger compared to the previously reported findings on $[P_4O_{10}]^{\bullet+}$ and $[V_4O_{10}]^{\bullet+}$, in line with the trend observed for the efficiencies in the reaction with methane. The larger KIEs observed for the mixed clusters may suggest a mechanistically more complex homolytic C−H bond activation step instead of a direct hydrogen-atom abstraction which will be discussed in the following section.

3.2 Reactivity of $[V_xP_{4-x}O_{10}]^{\bullet+}$ (x = 0, 2 - 4) towards ethane and ethene: A DFT-based analysis of puzzling reactivity patterns

3.2.1 Intrinsic properties of the $[V_xP_{4-x}O_{10}]^{\bullet+}$clusters (x = 0, 2 - 4)

Before discussing the relative energies of the intermediates and transition structures as well as the mechanistic details of the three reaction channels for the individual $[V_xP_{4-x}O_{10}]^{\bullet+}/C_2H_4$ and $[V_xP_{4-x}O_{10}]^{\bullet+}/C_2H_6$ systems (x = 0, 2 - 4), *i.e.* hydrogen-atom transfer, oxygen-atom transfer, and oxidative dehydrogenation, some of the intrinsic properties of the individual clusters are addressed; this may be helpful in the discussion of the experimentally observed reactivity patterns. Therefore, the discussion is restricted to the experimentally observed clusters; as $[VP_3O_{10}]^{\bullet+}$ could not yet be generated, this cluster is excluded from the upcoming analysis.

To explain the preference for OAT observed in the reaction of $[V_4O_{10}]^{\bullet+}$ with ethene and its complete absence for the phosphorous-containing systems, a closer look at the bond-dissociation energies (BDEs) for the terminal V−O_t and P−O_t bonds, respectively, is instructive (O_t = terminal oxygen atom).[xi]

Table 3.1: BDEs (kJ mol^{-1}) of the terminal V−O_t and P−O_t bonds in $[V_xP_{4-x}O_{10}]^{\bullet+}$($x$ = 0, 2 - 4), calculated at the B3LYP/aug-cc-pVTZ // B3LYP/TZVP level of theory.

	$[V_4O_{10}]^{\bullet+}$ (**1$_{V4}$**)	$[V_3PO_{10}]^{\bullet+}$ (**1$_{V3P}$**)	$[V_2P_2O_{10}]^{\bullet+}$ (**1$_{V2P2}$**)	$[P_4O_{10}]^{\bullet+}$ (**1$_{P4}$**)
BDE(V−O_t)	280	356	351	-
BDE(P−O_t)	-	397	396	399

As shown in Table 3.1, BDE(V−O_t) increases when phosphorous atoms are present in the cluster: In $[V_4O_{10}]^{\bullet+}$ (**1$_{V4}$**), BDE(V−O_t) amounts to only 280 kJ mol^{-1} which is 76

[xi] For similar chemoselective processes in the $[MO]^+/C_2H_4$ couple (M = Ge, Sn, Pb), see Ref. [271].

kJ mol^{-1} and 71 kJ mol^{-1} lower compared to the values obtained for the $[V_3PO_{10}]^{\bullet+}$ (**1$_{V3P}$**) and $[V_2P_2O_{10}]^{\bullet+}$ (**1$_{V2P2}$**) clusters, respectively.[xii] In contrast, the BDEs of the terminal BDE(P$-$O$_t$) bonds for all phosphorous-containing clusters investigated are not affected by the vanadium/phosphorous ratio and lie around 400 kJ mol^{-1}. These features can be explained by the fact that the most stable structures of all phosphorous-containing clusters possess a P$-$O$_t^{\bullet}$ bond as discussed above; a V$-$O$_t^{\bullet}$ bond is only present in $[V_4O_{10}]^{\bullet+}$. Thus, energy in addition to BDE(V$-$O$_t$) = 280 kJ mol^{-1} as determined for $[V_4O_{10}]^{\bullet+}$ is necessary to cleave the inert V=O double bond for $[V_3PO_{10}]^{\bullet+}$ and $[V_2P_2O_{10}]^{\bullet+}$, respectively. As described in Chapter 3.1.1, the ground-state energies for the V$-$O$_t^{\bullet}$ isomers of the mixed clusters could only be estimated by fixing the length of the terminal V=O bond; recapturing the values of +74 kJ mol^{-1} for $[V_3PO_{10}]^{\bullet+}$ and +92 kJ mol^{-1} for $[V_2P_2O_{10}]^{\bullet+}$, relative to the P$-O_t^{\bullet}$ isomer, respectively, these energies are in good agreement with the additional V=O dissociation energies for $[V_3PO_{10}]^{\bullet+}$ and $[V_2P_2O_{10}]^{\bullet+}$, compared to $[V_4O_{10}]^{\bullet+}$, respectively (Table 3.1).[xiii] Thus, while for the heteronuclear clusters it is energetically favored to remove an electron from the P=O double bond, generating a P$-$O$_t^{\bullet}$ instead of a V$-$O$_t^{\bullet}$ unit, the binding energy of the P$-$O$_t^{\bullet}$ vs. the V$-$O$_t^{\bullet}$ single bond is significantly higher. An analysis of the nature of the singly occupied molecular orbitals (SOMOs) of the dissociation products $[V_xP4-xO_9]^{\bullet+}$ (x = 2, 3) is quite instructive to understand the origin of these thermochemical differences; these SOMOs are utilized to form a single bond to oxygen in the respective $[V_xP_{4-x}O_{10}]^{\bullet+}$cluster ions. As exemplified in Figure 3.12 for $[V_2P_2O_{10}]^{\bullet+}$, loss of a terminal oxygen atom from vanadium leads to a vanadium-centered radical having a dz^2 orbital as a SOMO. In contrast, cleavage of the P$-$O$_t^{\bullet}$ bond in $[V_2P_2O_{10}]^{\bullet+}$ gives rise to a phosphorous-centered SOMO possessing s/p character (Figure 3.12); the latter is, in comparison to the d orbital of the vanadium atom, more suited to form a single bond to the oxygen atom due to the better overlap with its sp^x orbital; similar properties of the SOMO were obtained for all phosphorous-containing cluster ions.

In general, the thermochemistry of the competing HAT and ODH reaction channels depends on the relative energies of the $[V_xP_{4-x}O_9(OH)]^+$ and $[V_xP_{4-x}O_{10}H_2]^{\bullet+}$ product ions, respectively. While the first hydrogen-atom abstraction results in the formation of *closed-shell* product ions concomitant with spin transfer to the emerging hydrocarbon radicals, respectively, *open-shell* systems are regenerated in the course of the second hydrogen-atom transfer under reduction of a vanadium or phosphorous atom, respectively, to the formal oxidation state $+IV$. As it will be discussed later, the reduction to the oxidation state $+IV$ is disfavored for phosphorous. Thus, $[P_4O_{10}]^{\bullet+}$ gives rise to the *closed-shell* HAT product $[P_4O_9(OH)]^+$ without changing the formal oxidation state of

[xii] The BDE(V=O) of $[VO]^+$ calculated at a similar level of theory amounts to 541 kJ mol^{-1}, [307] the experimental number to 564 kJ mol^{-1}. [308]

[xiii] Note that both computational methods slightly differ, as the latter values on BDEs include single-point calculations on UB3LYP/aug-cc-pVTZ level of theory; further, the larger gap for $[V_2P_2O_{10}]^{\bullet+}$ (21 kJ mol^{-1}) is most likely given by the fact, that structural optimization for the V$-$O$_t^{\bullet}$ isomer was only feasible by fixing the terminal V=O bond as described above in chapter 3.1.1.

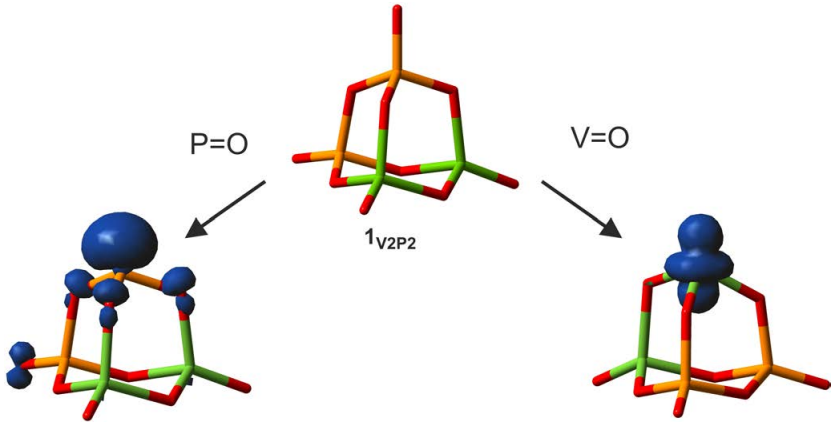

Figure 3.12: Two possible DFT-derived $[V_2P_2O_9]^{\bullet+}$ isomers resulting from dissociation of a $P-O_t^{\bullet}$ or $V-O_t^{\bullet}$ bond of $[V_2P_2O_{10}]^{\bullet+}$ (green V, yellow P, red O). The blue isosurfaces indicate the spin density within the respective cluster.

phosphorous; formation of the *open-shell* product $[P_4O_{10}H_2]^{\bullet+}$ via ODH is not possible due to thermochemical constraints. In contrast, the presence of redox-active vanadium opens up the latter reaction channel. The relative stabilities of the *open-* vs. the *closed-shell* cations are indicated by the adiabatic ionization energies (*IE*s) of the respective neutral clusters (Table 3.2). The formation of *open-shell* cluster cations, *i.e.* $[V_xP_{4-x}O_{10}]^{\bullet+}$, $[V_xP_{4-x}O_9]^{\bullet+}$, and $[V_xP_{4-x}O_{10}H_2]^{\bullet+}$, is rather energy demanding in the case of the homonuclear phosphorous systems (x = 0, Table 3.2); in contrast, the ionization energy required to produce a *closed-shell* cluster cation, *i.e.* $[P_4O_9(OH)]^+$, is significantly lower (7.2 eV) as compared to the *IE*s of the respective vanadium-containing systems (> 8.5 eV).

Table 3.2: Adiabatic ionization energies (in eV) of $V_xP_{4-x}O_{10}$, $V_xP_{4-x}O_9$, $V_xP_{4-x}O_9(OH)$ and $V_xP_{4-x}O_{10}H_2$ as calculated at the B3LYP/aug-cc-pVTZ // B3LYP/TZVP level of theory.

	$x = 4$	$x = 3$	$x = 2$	$x = 0$
$V_xP_{4-x}O_{10}$	11.2	10.7	11.1	12.2
$V_xP_{4-x}O_9$	8.6[a]	9.7	10.2	11.4
$V_xP_{4-x}O_9(OH)$	8.7	8.5	8.8	7.2
$V_xP_{4-x}O_{10}H_2$	8.2[a]	8.0	7.9	9.7

[a] The ground state of the neutral cluster is a triplet, while the ground states of all other neutral clusters in the respective row are *closed-shell* singlets.

3.2.2 Mechanism for the ion/molecule reactions of $[V_xP_{4-x}O_{10}]^{\bullet+}$clusters ($x$ = 0, 2 - 4) with C_2H_4

Having discussed some of the thermochemical properties of the educt and product ions, the mechanistic details for the reactions of the $[V_2P_2O_{10}]^{\bullet+}$/ethene system will be outlined in the following; this may serve as a representative example for all the *VPO*-cluster ions investigated, and the corresponding potential-energy profile is shown in

Figure 3.13. The potential-energy profiles of the other reaction couples, *i.e.* $[P_4O_{10}]^{\bullet+}/C_2H_4$, $[V_3PO_{10}]^{\bullet+}/C_2H_4$, and $[V_4O_{10}]^{\bullet+}/C_2H_4$, are given in the supplementary information (Appendix C); the electronic energies and the relative free energies of all systems investigated are summarized in Table 3.3.[xiv]

Table 3.3: Relative energies and free energies (in parentheses), given in kJ mol^{-1}, of the transition states and intermediates for oxygen-atom transfer (OAT), hydrogen-atom transfer (HAT), and oxidative dehydrogenation (ODH) for the reactions of $[V_xP_{4-x}O_{10}]^{\bullet+}$($x$ = 0, 2 - 4) with C_2H_4, respectively, calculated at the B3LYP/aug-cc-pVTZ//B3LYP/TZVP level of theory.

	$[V_4O_{10}]^{\bullet+}$		$[V_3PO_{10}]^{\bullet+}$		$[V_2P_2O_{10}]^{\bullet+}$		$[P_4O_{10}]^{\bullet+}$	
2	-203	(-167)	-192	(-152)	-206	(-165)	-244	(-207)
TS2-3	-190	(-148)	-134	(-92)	-145	(-101)	-102	(-70)
3	-342	(-330)	-279	(-237)	-291	(-249)	-191	(-189)
4	-176	(-179)	-59	(-64)	-61	(-66)	-57	(-60)
2	-203	(-167)	-192	(-152)	-206	(-165)	-244	(-207)
TS2-5	-125	(-90)	-127	(-92)	-145	(-108)		-
5	-123	(-90)	-129	(-92)	-142	(-106)	-224	(-193)
6	-68	(-71)	-82	(-83)	-87	(-87)	-100	(-101)
7	-292	(-249)	-180	(-140)	-190	(-149)	-92	(-58)
TS7-8	-119	(-72)	-96	(-57)	-115	(-76)		-
8	-310	(-268)	-236	(-190)	-244	(-205)		-
TS8-9	-159	(-109)	-148	(-105)	-160	(-115)	-33[a]	(+5)
9	-268	(-236)	-262	(-232)	-266	(-235)	-146	(-119)
10	-239	(-234)	-239	(-236)	-148	(-147)	-105	(-103)

[a] Directly linking intermediates $\mathbf{7_{P4}}$ and $\mathbf{9_{P4}}$.

In the first step, a carbon atom of the ethene molecule coordinates in a radicophilic fashion to the terminal phosphorous-bound oxygen atom of the cluster, carrying the high spin density, to form intermediate **2** in which the spin density then is mainly transferred to the terminal carbon atom for all of the vanadium containing intermediates $\mathbf{2_{V4}}$, $\mathbf{2_{V3P}}$, and $\mathbf{2_{V2P2}}$ (0.866, 0.893, and 0.866, respectively); in contrast, the spin is distributed over the two carbon atoms in $\mathbf{2_{P4}}$ (0.310 at the proximal and 0.608 at the terminal carbon atom). A comparison of the C−O, C−C, and P−O bond lengths in **2** for the individual clusters also reveals a notable effect due to the presence of vanadium. For all systems investigated, r(C−O) in **2** is longer compared to a C−O single bond in *e.g.* ethanol (1.431 Å); however, while a smooth increase of r(C−O) is observed in going from $\mathbf{2_{V4}}$ via $\mathbf{2_{V3P}}$ to $\mathbf{2_{V2P2}}$ (1.517 Å, 1.583 Å, and 1.619 Å, respectively), r(C−O) in the pure phosphorous intermediate $\mathbf{2_{V4}}$ is with 2.021 Å much more elongated.

[xiv] Free energies are included into the discussion as they support the mechanistic picture, even though the reactions described are not in a chemical equilibrium. However, as shown in previous studies on vanadium-oxygen clusters, it might be of importance to consider also free energies. [264, 309]

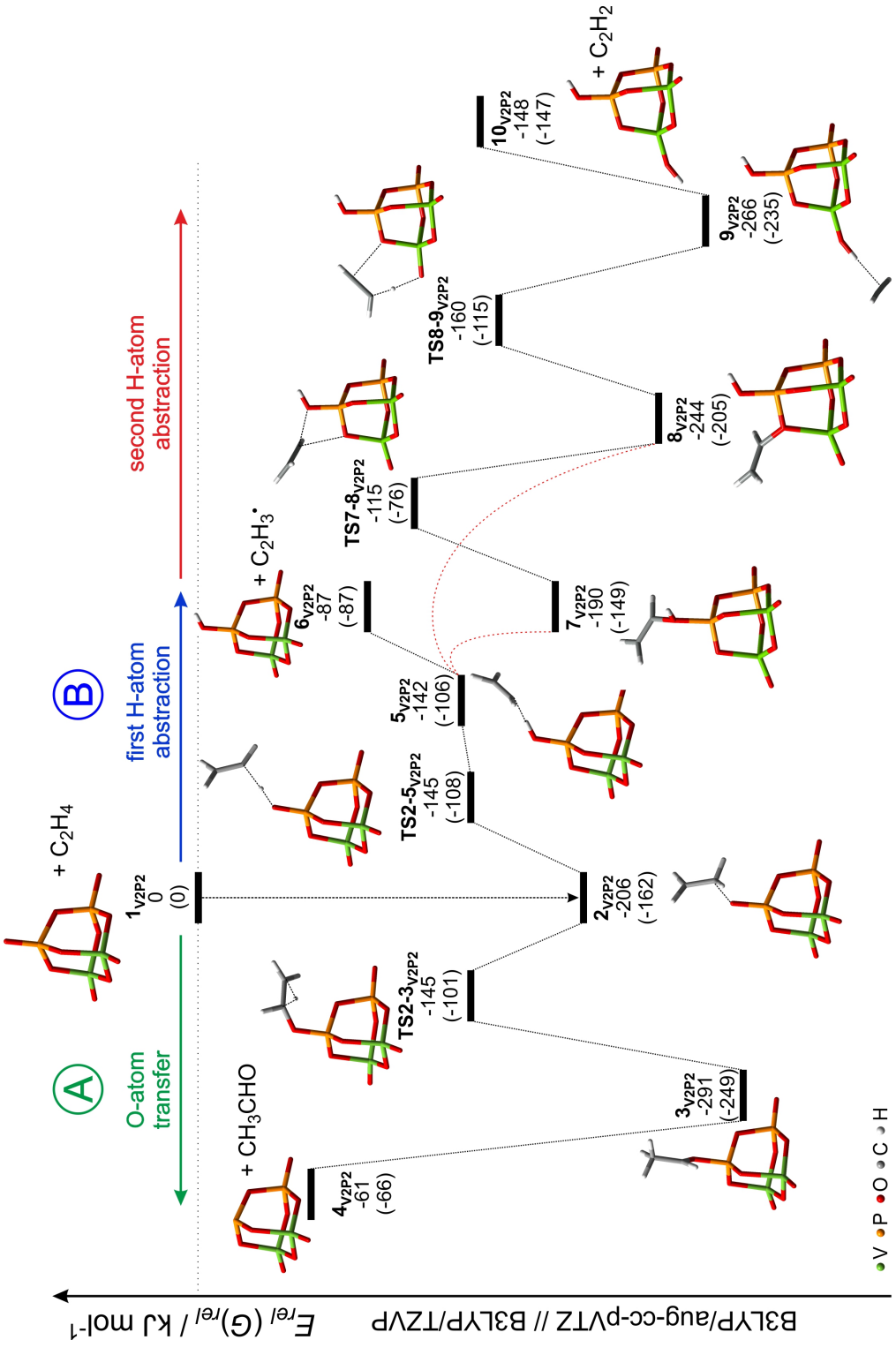

Figure 3.13: PES for the reactions of $[V_2P_2O_{10}]^{\bullet+}$ with C_2H_4, calculated at the B3LYP/aug-cc-pVTZ//B3LYP/TZVP level of theory (green V, yellow P, red O, gray C, white H). The electronic energies and relative Gibbs free energies (in parentheses) are given in kJ mol^{-1} and corrected for unscaled zero-point energy contributions.

Though less pronounced, decreasing trends in the same direction are observed for the C−C and P−O bond lengths of the four systems. The addition of ethene to the cluster shortens the P−O bond from 1.599 Å in $\mathbf{1_{V3P}}$ to 1.539 Å in $\mathbf{2_{V3P}}$, and from 1.593 Å in $\mathbf{1_{V2P2}}$ to 1.530 Å in $\mathbf{2_{V2P2}}$, respectively; the C−C bonds of **2** are lengthened from 1.326 Å in free C_2H_4 to 1.461 Å in $\mathbf{2_{V4}}$, 1.455 Å in $\mathbf{2_{V3P}}$, and 1.449 Å in $\mathbf{2_{V2P2}}$, respectively. In contrast, the shortening of the P−O bond is the highest for the $[P_4O_{10}]^{\bullet+}/C_2H_4$ cluster (from 1.569 Å in $\mathbf{1_{P4}}$ to 1.493 Å in $\mathbf{2_{P4}}$) while the elongation of the C−C bond is the smallest for this particular system (from 1.326 Å in free ethene to 1.408 Å, respectively); thus, the P−O and the C−C bonds are the shortest for the vanadium-free intermediate $\mathbf{2_{P4}}$.

Starting from intermediate **2**, two different reactions channels *A* (OAT) and *B* (HAT and ODH) are accessible (Figure 3.13). In pathway *A*, which has already been identified by Castleman and co-workers for the reaction of $[V_4O_{10}]^{\bullet+}$ with C_2H_4,[292] a hydrogen atom from the oxygen-bound methylene unit undergoes a [1,2]-migration to the terminal carbon atom via transition structure **TS2-3** to form intermediate **3**. The binding situation of the newly generated acetaldehyde building block to the cationic cluster fragment in **3** differs significantly for the pure phosphorous cluster as compared with the vanadium-containing systems: While the C−O bond lengths in $\mathbf{3_{V4}}$, $\mathbf{3_{V3P}}$, and $\mathbf{3_{V2P2}}$ (1.242 Å, 1.262 Å, and 1.266 Å, respectively) are similar to that of *r*(C−O) in free acetaldehyde (1.205 Å), *r*(C−O) in $\mathbf{3_{P4}}$ is with 1.472 Å relatively long; these structural characteristics are inversely mirrored in the shortening of the P−O bond lengths to 1.745 Å, 1.733 Å, and 1.526 Å in $\mathbf{3_{V3P}}$, $\mathbf{3_{V2P2}}$, and $\mathbf{3_{P4}}$, respectively. Remarkable differences among the individual clusters also concern the spin distributions of the intermediates and transition structures for the intramolecular hydrogen migration, *i.e.* **2** → **TS2-3** → **3**. In line with avoiding a high spin density at a phosphorous atom and the energetic disadvantage of an associated reduction to the formal oxidation state $P^{+V} \rightarrow P^{+IV}$ as described above, the spin in $\mathbf{3_{P4}}$ is located at the C_2 unit, *i.e.* at the proximal carbon atom of the ligand (Figure 3.14); here, the transfer of the unpaired electron takes place only during the reductive elimination of acetaldehyde, $\mathbf{3_{P4}} \rightarrow \mathbf{4_{P4}}$. The bonding situation is different for the vanadium-containing couples $[V_xP_{4-x}O_{10}]^{\bullet+}/C_2H_4$ (x = 2 - 4): In **TS2-3** the spin density has already been shifted to a vanadium atom of the cluster; thus, the actual hydrogen transfer **2** → **TS2-3** → **3** corresponds rather to a [1,2]-hydride shift within a cationic, *closed-shell* C_2 unit (the C_2 units in transition structures **TS2-3** possess a positive charge for all systems investigated), as exemplified for $\mathbf{TS2\text{-}3_{V4}}$ in Figure 3.14; this process is energetically favored as compared to the energy-demanding [1,2]-hydrogen-atom migration within the radical-cation C_2 unit in $\mathbf{TS2\text{-}3_{P4}}$.

The alternative to the OAT pathway shown in Figure 3.13, *i.e.* the transfer of an oxygen atom from a vanadium-bound oxygen of $[V_2P_2O_{10}]^{\bullet+}$ (Appendix C, Figure C.1) is thermodynamically favored; the same holds true for $[V_3PO_{10}]^{\bullet+}$ (Table 3.3 and Appendix C, Figure C.1). Formation of the resulting products $\mathbf{4_{V2P2}\text{-}VO}$ and $\mathbf{4_{V3P}\text{-}VO}$ are more

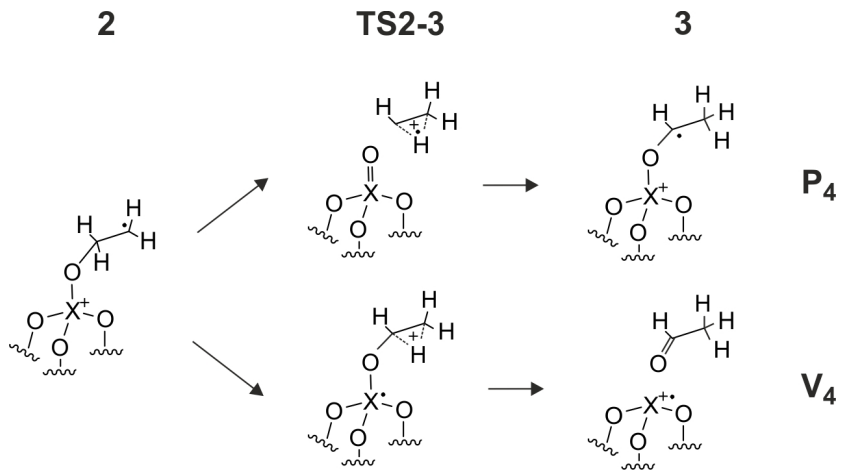

Figure 3.14: Schematic description of the process **2** → **TS2-3** → **3** for the homonuclear $[X_4O_{10}]^{\bullet+}/C_2H_4$ couples (*X* = P, V).

exothermic (exergonic) by 45 (-43) kJ mol^{-1} and -41 (-41) kJ mol^{-1} respectively, than the corresponding product ions of the OAT mechanism depicted in Figure 3.13. However, a rather energy demanding intramolecular spin-density transfer from the P=O to the V=O site is required, [300] and the associated adduct complexes **2$_{V2P2}$-VO** and **2$_{V3P}$-VO**, in which ethene is coordinated to the V=O side of the cluster, are 59 (56) kJ mol^{-1} (**2$_{V2P2}$-VO**) and 59 (54) kJ mol^{-1} (**2$_{V3P}$-VO**) less stable than the P=O-bound isomers **2$_{V2P2}$** and **2$_{V3P}$**, respectively. The transition structures **TS2-3$_{V2P2}$-VO** and **TS2-3$_{V3P}$-VO** are with -139 (-88) kJ mol^{-1} and -116 (-67) kJ mol^{-1} (relative to the reactants, respectively) comparable in energy to the barriers of the OAT pathway A depicted in Figure 3.13. Regarding the electronic structure of the two transition states **TS2-3$_{V2P2}$-VO** and **TS2-3$_{V3P}$-VO**, the depicted situation in Figure 3.14 for the **TS2-3$_{V4}$** holds true also for these systems; rather the process corresponds to a [1,2]-hydride shift within the cationic hydrocarbon fragment as the spin is mainly localized at the proximate vanadium atom. Thus, both OAT variants are accessible at thermal conditions for the mixed clusters; note, however, that a kinetic barrier caused by the intramolecular spin-density transfer might be involved in the initial coordination of C_2H_4 to a non-radical V=O site of the cluster, as reported for the reaction of $[V_3PO_{10}]^{\bullet+}$ with methane. [300]

Pathway *B* results either in HAT or ODH and commences with a hydrogen-atom transfer from the oxygen-bound methylene unit in **2** to this very oxygen atom (**TS2-5**), thus generating a oxo-hydroxo cluster with an ethenyl radical ligand; the latter is loosely bound to the cluster via the hydrogen atom of the newly generated hydroxy group. In the energy profile, Figure 3.13, the energy of **TS2-5$_{V2P2}$** is slightly lower than the energy of the resulting intermediate **5$_{V2P2}$**; this is due to zero-point energy and free-energy corrections. The fact that transition state **TS2-5** and intermediate **5** are very close in energy is reasonable, since the only structural reorganization in this step corresponds to the widening of the binding angle of the C_2H_3-fragment to the cluster. This HAT-reaction path has

been located for all vanadium-containing clusters, while **TS2-5$_{P4}$** could not be located for the $[P_4O_{10}]^{\bullet+}/C_2H_4$-couple on the potential-energy surface (Appendix C, Figure C.2). Furthermore, the nature of intermediate **5$_{P4}$** differs remarkably from the structures of **5$_{V2P2}$**, **5$_{V3P}$**, and **5$_{V4}$**. In the latter intermediates, the C−H bond is already strongly elongated (r(C−H) 1.675 Å for **5$_{V2P2}$**, 1.756 Å for **5$_{V3P}$**, and 1.643 Å for **5$_{V4}$**) and the newly formed O−H bond is rather short (r(O−H) 1.053 Å for **5$_{V2P2}$**, 1.030 Å for **5$_{V3P}$**, and 1.051 Å for **5$_{V4}$**). In **5$_{P4}$**, however, the C−H bond is only slightly elongated (r(C−H) = 1.102 Å) and the O−H distance amounts to 1.858 Å. Thus, **5$_{P4}$** rather corresponds to a hydrogen-bridged [310] adduct complex $[P_4O_{10}\cdots H\cdots C_2H_3]^{\bullet+}$ directly generated from the educts instead of being formed via **2$_{P4}$** → **TS2-5$_{P4}$** → **5$_{P4}$**; similar adduct complexes could not be located for the vanadium-containing clusters with ethene. According to a relaxed scan of the C−H bond, the ethenyl radical $C_2H_3^{\bullet}$ is liberated from **5$_{P4}$** without the involvement of any further intermediates or transition structures. In addition to the structural differences of **5$_{P4}$** as compared with **5$_{V2P2}$**, **5$_{V3P}$**, and **5$_{V4}$**, also the formation of **5$_{P4}$** is with 224 kJ mol^{-1} significantly more exothermic than that of the other HAT-intermediates (-142 kJ mol^{-1} for **5$_{V2P2}$**, 129 kJ mol^{-1} for **5$_{V3P}$**, and -123 kJ mol^{-1} for **5$_{V4}$**). In line with these findings, the energy necessary for the liberation of the $C_2H_3^{\bullet}$ radical from **5** to form the hydrogen-atom transfer (HAT) product **6** amounts to 124 kJ mol^{-1} for $[P_4O_9(OH)]^+$ (**6$_{P4}$**), compared to only 55 kJ mol^{-1} for both $[V_2P_2O_9(OH)]^+$ (**6$_{V2P2}$**) and $[V_4O_9(OH)]^+$ (**6$_{V4}$**), and 47 kJ mol^{-1} for $[V_3PO_9(OH)]^+$ (**6$_{V3P}$**), respectively.

Structure **5$_{V2P2}$** in Figure 3.13 constitutes to a common intermediate for both the HAT and the ODH pathways. In competition with the formation of the HAT product **6**, the incipient $C_2H_3^{\bullet}$ radical can rebind to the oxygen atom of the newly formed hydroxyl group thus producing structure **7**; due to the rather shallow nature of the PES in this region, a transition state **TS5-7** could not be located on the PES. However, the unsuccessful attempts to locate this transition state suggest that the barrier for this rebound step is lower than the liberation of the hydrocarbon fragment resulting in the HAT product **6**. Regarding the structure of clusters **7**, all vanadium-containing cations **7$_{V2P2}$**, **7$_{V3P}$**, and **7$_{V4}$** possess the bonding pattern depicted in Figure 3.13 with the spin density exclusively located at one of the vanadium atoms within the cluster skeleton. For the pure phosphorous system instead, the rebound step is associated with an opening of the cluster cage thus leading to a distorted structure of **7$_{P4}$** (See Appendix C, Figure C.2). For the vanadium-containing clusters the reaction continuous via transfer of the C_2H_3 fragment to a bridging, vanadium-bound oxygen atom. In the case of $[V_2P_2O_{10}]^{\bullet+}$, the C_2H_3 fragment can alternatively be transferred to the bridging, phosphorous-bound oxygen atom; this pathway is described further below. Note also that starting from **5** the direct migration of the $C_2H_3^{\bullet}$ radical to a bridging oxygen atom also results in the formation of **8** and represents an alternative mechanistic scenario; however, locating the corresponding transition structure was not successful either. From **5**, transfer of a hydrogen atom from the terminal CH_2 unit to the adjacent V=O site, thus generating

a V−OH group, completes the ODH process. The barrier height of the step **8** → **TS8-9** → **9** depends strongly on the system, ranging from 84 and 88 kJ mol^{-1} for $[V_2P_2O_{10}]^{\bullet+}$ and $[V_3PO_{10}]^{\bullet+}$, respectively, to 151 kJ mol^{-1} for $[V_4O_{10}]^{\bullet+}$. For the latter, the high intrinsic barrier is due to the relative low energy of intermediate $\mathbf{8_{V4}}$ in which the bond length of bridging μ-$OCHCH_2$ ligand to the V(OH) and VO_t units, respectively, are quite similar (r((HO)V−$OCHCH_2$) = 2.003 Å, r(O_tV−$OCHCH_2$) = 1.918 Å); in contrast, the μ-$OCHCH_2$ ligand in $\mathbf{8_{V2P2}}$ and $\mathbf{8_{V3P}}$ is more strongly bound to the (HO)P unit at the expense of the CH_2CHO−VO_t bond, respectively ($\mathbf{8_{V2P2}}$: r((HO)P−$OCHCH_2$) = 1.691 Å, r(O_tV−$OCHCH_2$) = 2.069 Å; $\mathbf{8_{V3P}}$: r((HO)P−$OCHCH_2$) = 1.708 Å, r(O_tV−$OCHCH_2$) = 2.071 Å). The relative energies of the respective transition structures **TS8-9** are however comparable (within a range of 12 kJ mol^{-1}) when related to the entrance channel, respectively. As to the homonuclear phosphorous cluster $[P_4O_{10}]^{\bullet+}$, intermediates **7** and **9** are linked via a single transition state; here, the second hydrogen atom is transferred directly to a terminal P=O unit (See Appendix C, Figure C.2); however, this process is 67 kJ mol^{-1} higher in energy compared to the generation of the HAT product $\mathbf{6_{P4}}$. For all vanadium-containing clusters, the spin distribution remains by and large unchanged along the reaction sequence **7** → **TS7-8** → **8** → **TS8-9** → **9**, carrying most of the spin density by a vanadium atom which is remote from the reactive sites. From **9**, the weakly bound acetylene ligand can easily be liberated to yield the experimentally observed oxidative-dehydrogenation (ODH) product $[V_2P_2O_{10}H_2]^{\bullet+}$ (**10**).

As already mentioned above, an alternative reaction pathway has been identified for the ODH-process of the $[V_2P_2O_{10}]^{\bullet+}$ cluster in which a structural isomer of $\mathbf{10_{V2P2}}$, *i.e.* $\mathbf{10_{V2P2}}$**-2** in Figure 3.15, is generated bearing two P−OH moieties instead of the P−OH/V−OH groups as in $\mathbf{10_{V2P2}}$. The relative energy (free energy) of $\mathbf{10_{V2P2}}$**-2** is 153 (150) kJ mol^{-1} lower compared to the one of $\mathbf{10_{V2P2}}$; however, the corresponding reaction mechanism generating the former product ion (Figure 3.15) is kinetically more demanding than the HAT exit channel as well as the ODH pathway shown in Figure 3.13, *i.e.* the hydrocarbon migration from the terminal- to the bridging oxygen atom (**TS7-8**$_{\mathbf{V2P2}}$**-2**) is 8 (42) kJ mol^{-1} and 36 (31) kJ mol^{-1} higher in (free) energy compared to the HAT product $\mathbf{6_{V2P2}}$ and to **TS7-8**$_{\mathbf{V2P2}}$**-2**, respectively. Alternatively, starting from $\mathbf{6_{V2P2}}$ with a direct rebound of the C_2 fragment to the bridging oxygen atom of the P−O−P unit via $\mathbf{5_{V2P2}}$ → $\mathbf{8_{V2P2}}$**-2** might be possible but also here the PES is rather flat and the respective transition structure could not be located. Intermediate $\mathbf{8_{V2P2}}$**-2** corresponds to an open-cage cluster with a planar PO_3 unit generated by the cleavage of the internal P−O−P bond. Next, the transfer of a second hydrogen atom completes the ODH reaction, and the process is accompanied with the regeneration of the closed-cage structure $\mathbf{9_{V2P2}}$**-2**; the intrinsic barrier $\mathbf{8_{V2P2}}$**-2** → **TS8-9**$_{\mathbf{V2P2}}$**-2** is about 40 kJ mol^{-1} lower than the related barrier $\mathbf{8_{V2P2}}$→ **TS8-9**$_{\mathbf{V2P2}}$ shown in Figure 3.13.

As to the well-studied homonuclear clusters $[V_4O_{10}]^{\bullet+}$ and $[P_4O_{10}]^{\bullet+}$, the reactivity

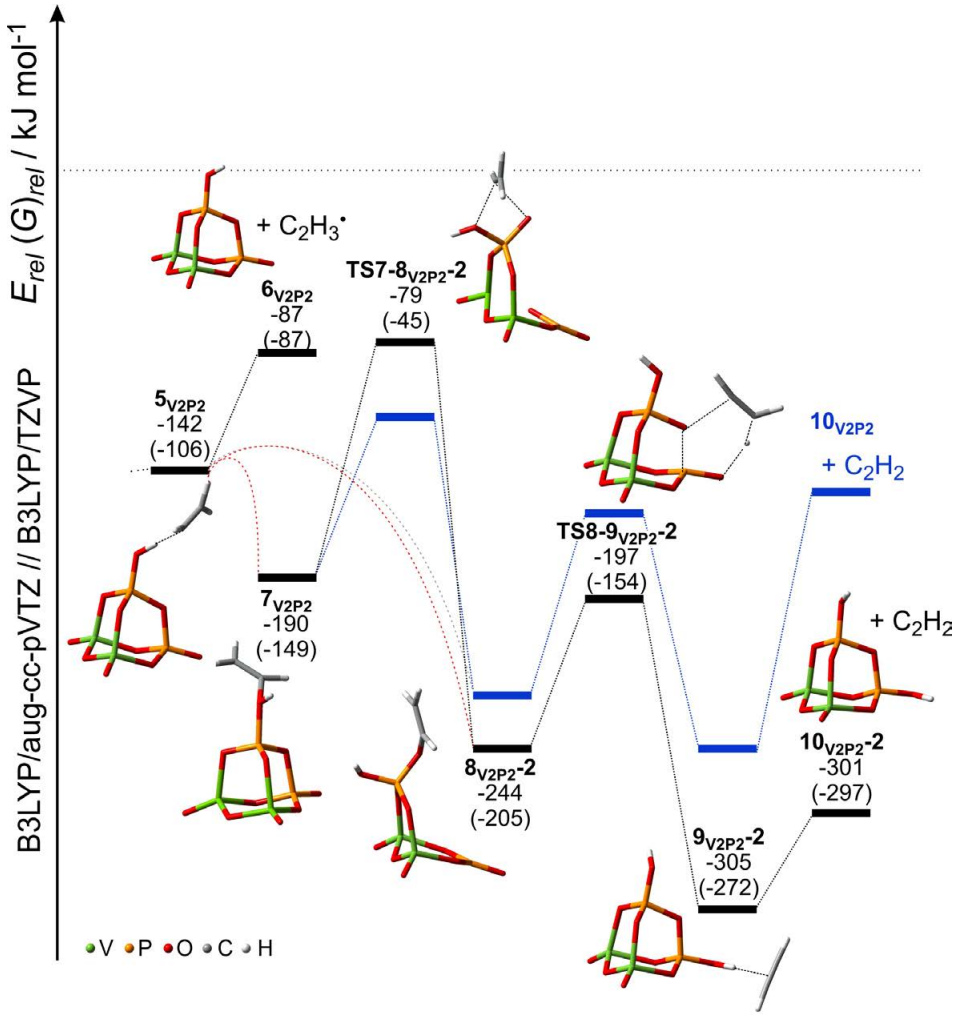

Figure 3.15: Alternative mechanism for the ODH-reaction of $[V_2P_2O_{10}]^{\bullet+}$ with C_2H_4, calculated at the B3LYP/aug-cc-pVTZ//B3LYP/TZVP level of theory (green V, yellow P, red O, gray C, white H). The electronic energies and relative Gibbs free energies (in parentheses) are given in kJ mol^{-1} and corrected for unscaled zero-point energy contributions. The blue line shows the pathway from Figure 3.13.

patterns observed in their reactions with ethene are consistent with the relative energies of the competing pathways calculated in this study. For $[V_4O_{10}]^{\bullet+}$, OAT is kinetically and thermochemically favored; the same holds true for the HAT pathway in the case of $[P_4O_{10}]^{\bullet+}$ for which no barrier exists along the reaction path. The latter process gains in importance in going from $[V_4O_{10}]^{\bullet+}$ via $[V_3PO_{10}]^{\bullet+}$ and $[V_2P_2O_{10}]^{\bullet+}$ to $[P_4O_{10}]^{\bullet+}$, indicating that *i*) the hydrogen-atom affinity of the P$-$O$_t^{\bullet}$ unit in $[P_4O_{10}]^{\bullet+}$ is higher compared to that of the V$-$O$_t^{\bullet}$ entity in $[V_4O_{10}]^{\bullet+}$ and that *ii*) the newly generated PO$_t-$H bond increases in strength with the number of phosphorous atoms being present in the cluster. In contrast, the reaction energies for an oxygen-atom transfer from $[V_3PO_{10}]^{\bullet+}$, $[V_2P_2O_{10}]^{\bullet+}$, and $[P_4O_{10}]^{\bullet+}$ to C_2H_4 are similar and OAT is most exothermic for $[V_4O_{10}]^{\bullet+}$ (Table 3.3). Note that the HAT and

OAT reaction channels are different with respect to the redox chemistry: While in the OAT process $[V_xP_{4-x}O_{10}]^{\bullet+} + C_2H_4 \rightarrow [V_xP_{4-x}O_9]^{\bullet+} + C_2H_4O$ a reduction from $+V$ to $+IV$ takes place for V (x = 4) and P (x = 0, 2, 3), respectively, the formal oxidation states of the vanadium and phosphorous atoms do not change in the course of the HAT reaction.

The branching ratio of OAT versus HAT/ODH is mainly determined by the relative energies of the barriers **TS2-3** vs. **TS2-5** in Figure 3.13, respectively; both are lower in energy compared to the entrance channel for all clusters investigated (Table 3.3). As mentioned above, the number of phosphorous atoms in the $[V_xP_{4-x}O_{10}]^{\bullet+}$ (x = 0, 2, 3) clusters has a negligible effect on the strength of the corresponding BDEs($P-O_t^{\bullet}$) and thus affects the energies of the OAT products $[V_xP_{4-x}O_9]^{\bullet+}$ (x = 0,2,3) only marginally. However, the relative energies of the corresponding OAT transition structures **TS2-3** increase discontinuously with the number of phosphorous atoms (Table 3.3). With respect to the HAT channel, the replacement of one vanadium atom by phosphor, *i.e.* $[V_4O_{10}]^{\bullet+}$ vs. $[V_3PO_{10}]^{\bullet+}$, has only a minor effect on the relative energies of the corresponding **TS2-5** while the increasing thermochemical preference for HAT in going from $[V_2P_2O_{10}]^{\bullet+}$ to $[P_4O_{10}]^{\bullet+}$ is even more pronounced when looking at the respective transition structures. As a result, the difference between the relative energies (free energies) of **TS2-3** and **TS2-5** amount to -65 (-58) kJ mol^{-1}, -7 (0) kJ mol^{-1}, and 0 (7) kJ mol^{-1}, for the $[V_4O_{10}]^{\bullet+}/C_2H_4$, $[V_3PO_{10}]^{\bullet+}/C_2H_4$, and $[V_2P_2O_{10}]^{\bullet+}/C_2H_4$ systems, respectively; for the $[P_4O_{10}]^{\bullet+}/C_2H_4$ system there is no barrier for the HAT process. Thus, the calculations are consistent with the experimentally observed selectivities for OAT and HAT in the gas-phase reactions of $[V_4O_{10}]^{\bullet+}$ and $[P_4O_{10}]^{\bullet+}$ with C_2H_4, respectively. Although OAT in the reaction of $[V_3PO_{10}]^{\bullet+}$ and $[V_2P_2O_{10}]^{\bullet+}$ with C_2H_4 is exergonic and kinetically allowed at room temperature, the thermodynamic preference of the HAT and ODH products may account for the absence of OAT in the experiments. The non-observation of the second hydrogen transfer leading to ODH in the case of the homonuclear system $[P_4O_{10}]^{\bullet+}/C_2H_4$, however, is in line with the calculations since the corresponding transition structure **TS7-9$_{P4}$** is much higher in energy compared to the HAT exit channel so that ODH cannot compete and is thus not observable under the experimental conditions.

3.2.3 Mechanism for the ion/molecule reactions of $[V_xP_{4-x}O_{10}]^{\bullet+}$clusters ($x$ = 0, 2 - 4) with C_2H_6

After discussing the intrinsic features of the $[V_xP_{4-x}O_{10}]^{\bullet+}$/ethene systems, $[V_2P_2O_{10}]^{\bullet+}$ has also been chosen as a cluster prototype to demonstrate the reactions of the various cluster ions $[V_xP_{4-x}O_{10}]^{\bullet+}$ (x = 0, 2-4) with ethane; the potential-energy profile is shown in Figure 3.16. The PESs of the other reaction couples, *i.e.* $[P_4O_{10}]^{\bullet+}/C_2H_6$, $[V_3PO_{10}]^{\bullet+}/C_2H_6$, and $[V_4O_{10}]^{\bullet+}/C_2H_6$, are given in the supplementary information (Section C); the electronic energies and the relative free energies of all systems investigated are summarized in Table 3.4.

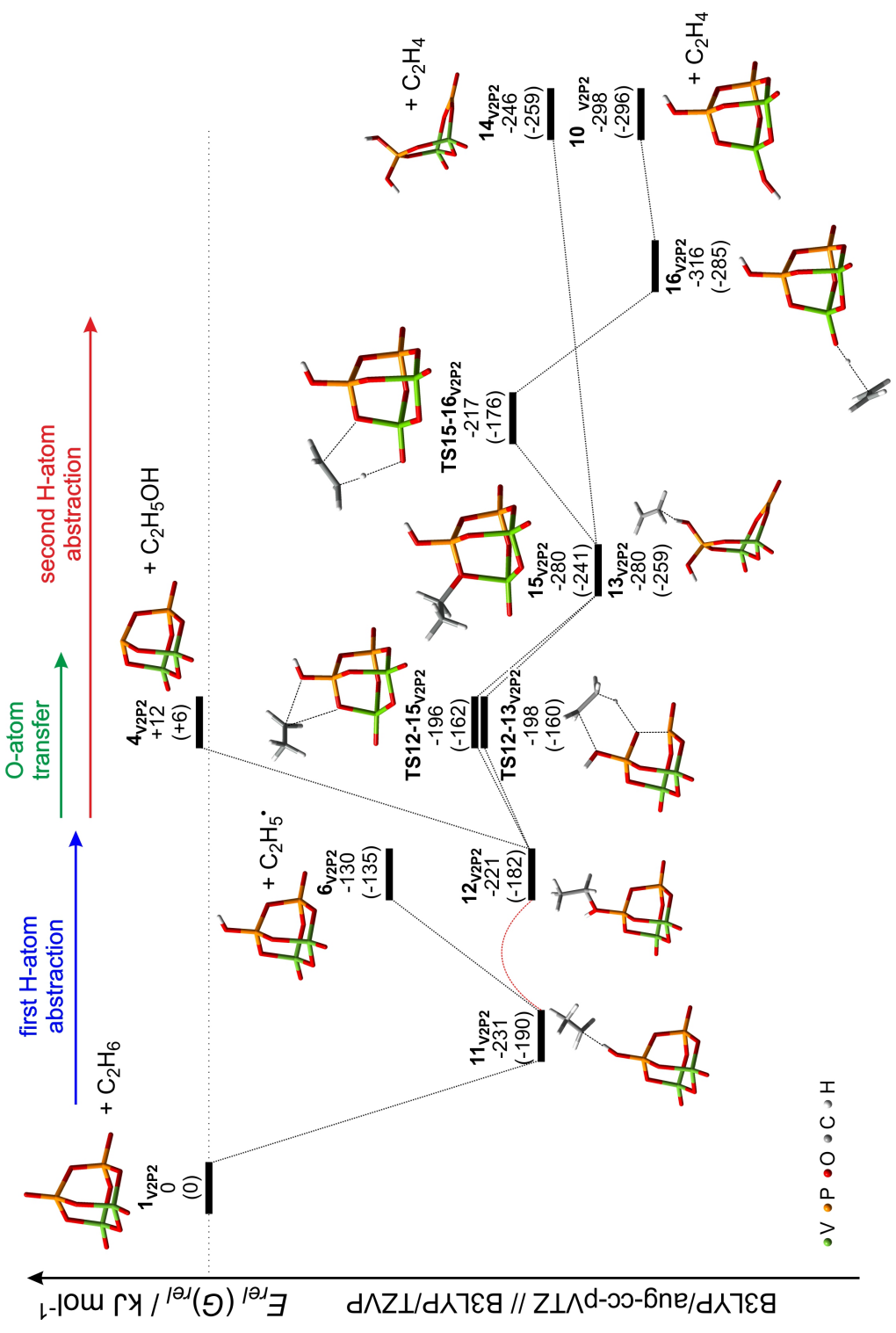

Figure 3.16: PES for the reaction of $[V_2P_2O_{10}]^{\bullet+}$ with C_2H_6 (green V, yellow P, red O, gray C, white H). The electronic energies and relative Gibbs free energies (in parentheses) are given in kJ mol^{-1} and corrected for unscaled zero-point energy contributions.

Table 3.4: Relative energies and free energies (in parentheses), given in kJ mol^{-1}, of the transition states and intermediates for oxygen-atom transfer (OAT), hydrogen-atom transfer (HAT), and oxidative dehydrogenation (ODH) for the reactions of $[V_xP_{4-x}O_{10}]^{\bullet+}$($x$ = 0, 2 - 4) with C_2H_6, respectively, calculated at the B3LYP/aug-cc-pVTZ//B3LYP/TZVP level of theory.

	$[V_4O_{10}]^{\bullet+}$		$[V_3PO_{10}]^{\bullet+}$		$[V_2P_2O_{10}]^{\bullet+}$		$[P_4O_{10}]^{\bullet+}$	
11		-	-171	(-141)	-231	(-190)	-213	(-185)
6	-112	(-118)	-124	(-130)	-130	(-135)	-143	(-148)
12	-272	(-235)	-209	(-171)	-221	(-182)	-111	(-78)
4	-103	(-108)	+14	(+7)	+12	(+6)	+16	(+11)
12	-272	(-235)	-209	(-171)	-221	(-182)	-111	(-78)
TS12-13	-158	(-115)	-169	(-129)	-198	(-160)	+23	(+50)
13	-163	(-141)	-180	(-159)	-280	(-259)	-81	(-62)
14	-133	(-144)	-149	(-105)	-246	(-259)	-35	(-51)
12	-272	(-235)	-209	(-171)	-221	(-182)	-111	(-78)
TS12-15	-186	(-146)	-168	(-132)	-196	(-162)		-
15	-312	(-270)	-251	(-214)	-280	(-241)		-
TS15-16	-211	(-167)	-204	(-162)	-217	(-176)	-87[a]	(-53)
16	-318	(-286)	-312	(-282)	-316	(-285)	-195	(-170)
10	-287	(-289)	-287	(-291)	-298	(-296)	-153	(-158)

[a] Directly linking intermediates $\mathbf{12_{P4}}$ and $\mathbf{16_{P4}}$.

Similar to the reactions of these cluster-cation radicals with methane, coordination of C_2H_6 to the clusters $[V_xP_{4-x}O_{10}]^{\bullet+}$ (x = 0, 2, 3) also results in a barrierless generation of the intermediates $\mathbf{11_{P4}}$, $\mathbf{11_{V2P2}}$, and $\mathbf{11_{V3P}}$, respectively; once more, the $P-O_t^{\bullet}$ unit constitutes the reactive site for the hydrogen-atom transfer; in contrast to the reactions with ethene, no encounter complex has been located on the potential-energy surface. With respect to the homonuclear $[V_4O_{10}]^{\bullet+}$ cluster, the corresponding intermediate $\mathbf{11_{V4}}$ could not be located as a local minimum on the PES; instead, the hydrocarbon fragment migrates in the course of the HAT reaction around the terminal oxygen atom and rebinds to it thus forming directly intermediate $\mathbf{12_{V4}}$, bearing an intact ethanol ligand.

For the phosphorous-containing clusters, the species $\mathbf{11_{P4}}$, $\mathbf{11_{V2P2}}$, and $\mathbf{11_{V3P}}$ serve as common intermediates to branch out in three different reaction paths: Firstly, the weakly-bound ethyl group can be eliminated yielding the cationic HAT product **6** and the ethyl radical $C_2H_5^{\bullet}$; the computed exothermicity decreases with increasing number of vanadium atoms within the cluster, amounting to -143 kJ mol^{-1} for $[P_4O_{10}]^{\bullet+}$, -130 kJ mol^{-1} for $[V_2P_2O_{10}]^{\bullet+}$, and -124 kJ mol^{-1} for $[V_3PO_{10}]^{\bullet+}$, respectively. As an alternative, rebound of the ethyl group to the newly generated OH group may occur to form ethanol C_2H_5OH which upon liberation of the alcohol gives rise to the OAT product **4**. Here too, the transition state could not be located, the smooth PES in this region and the non-existing barrier for the $\mathbf{11_{V4}} \rightarrow \mathbf{12_{V4}}$ process indicate, however, a low activation energy for the rebound step. The C−O bond lengths in $\mathbf{12_{V4}}$, $\mathbf{12_{V3P}}$, and $\mathbf{12_{V2P2}}$ increase with the number of phosphorous

atoms (1.517 Å, 1.567 Å, and 1.588 Å, respectively) and all three are elongated compared to free ethanol (1.430 Å); the C−O bond length in $\mathbf{12_{P4}}$ amounts to 1.559 Å. While $\mathbf{12_{V4}}$, $\mathbf{12_{V3P}}$, and $\mathbf{12_{V2P2}}$ correspond to closed-cage structures, a distorted open-cage structure was found for $\mathbf{12_{P4}}$ as the local minimum with one $(C_2H_5OH)PO-P$ being broken, thus forming a bent PO_3 moiety with a threefold coordinated phosphorous atom at which 50 % of the spin is located.

Finally, the third reaction path starting from phosphorous-containing intermediates **12** comprises two variants of ODH reactions. In the first scenario, the open-cage structure **13** can be formed from intermediate **12** via **TS12-13**; this transition state corresponds to the second HAT from the terminal methyl group to the bridging $P-O_b$ unit thus leading to a $(O_b)_2P(OH)_2$ moiety to which the newly generated ethene molecule is only weakly coordinated. Regarding the electronic structures of the vanadium-containing clusters, the spin density is located at one of the vanadium atoms throughout the whole reaction sequence. In contrast, the spin in $\mathbf{TS12\text{-}13_{P4}}$ is transferred from the bent PO_3 unit to an adjacent phosphorous atom which is accompanied with a second P−O bond scission (r(P−O) = 1.607 Å and 2.943 Å in $\mathbf{12_{P4}}$ and $\mathbf{TS12\text{-}13_{P4}}$, respectively), thus resulting in a planar PO_3 unit possessing two terminal oxygen atoms (Appendix C, Figure C.5). The latter process requires 138 kJ mol^{-1} activation energy and is thus 23 kJ mol^{-1} higher in energy compared to the entrance channel. In all transition structures, one hydrogen atom of the terminal CH_3 group is transferred to the oxygen-atom and the respective C−H bond is elongated (r(C−H) 1.125 Å for $\mathbf{TS12\text{-}13_{P4}}$, 1.118 Å for $\mathbf{TS12\text{-}13_{V2P2}}$, 1.130 Å for $\mathbf{TS12\text{-}13_{V3P}}$, and 1.191 Å for $\mathbf{TS12\text{-}13_{V4}}$, respectively). Finally, liberation of C_2H_4 yields the product ion **14**.

In the second ODH-mechanism, the reaction sequence **12** → **TS12-15** → **15** → **TS15-16** → **16** → **10** parallels the pathway for the oxidative dehydrogenation of ethene as discussed above (Figure 3.13). Briefly, for all vanadium-containing clusters the hydrocarbon fragment is first transferred to a bridging oxygen atom via the isomerization sequence **12** → **TS12-15** → **15**; the barrier of this process is almost isoenergetic to the alternative transition state **TS12-13** for $[V_2P_2O_{10}]^{\bullet+}$ (+2 kJ mol^{-1}) and $[V_3PO_{10}]^{\bullet+}$ (+1 kJ mol^{-1}), respectively, while it is distinctly lower for $[V_4O_{10}]^{\bullet+}$ (-28 kJ mol^{-1}). Subsequently, the second HAT process occurs from intermediate **15** via **TS15-16** in which the hydrogen atom is transferred to the adjacent $V-O_t$ unit. Again, the homonuclear phosphorous cluster represents an exception in that the second C−H bond activation occurs directly from $\mathbf{12_{P4}}$ at one of the terminal $P-O_t$ units, without a prior migration of the hydrocarbon to a bridging oxygen atom. From **16**, the ethene molecule is easily liberated, leading to the formation of the thermochemically preferred closed-cage product **10** (Table 3.4).

Similar to the $[V_2P_2O_{10}]^{\bullet+}/C_2H_4$ couple, an alternative pathway for the oxidative dehydrogenation in the reaction of $[V_2P_2O_{10}]^{\bullet+}$ with C_2H_6 has been found in which the more stable product ion $\mathbf{10_{V2P2}\text{-}2}$ (Figure 3.17) is generated bearing two P−OH units instead

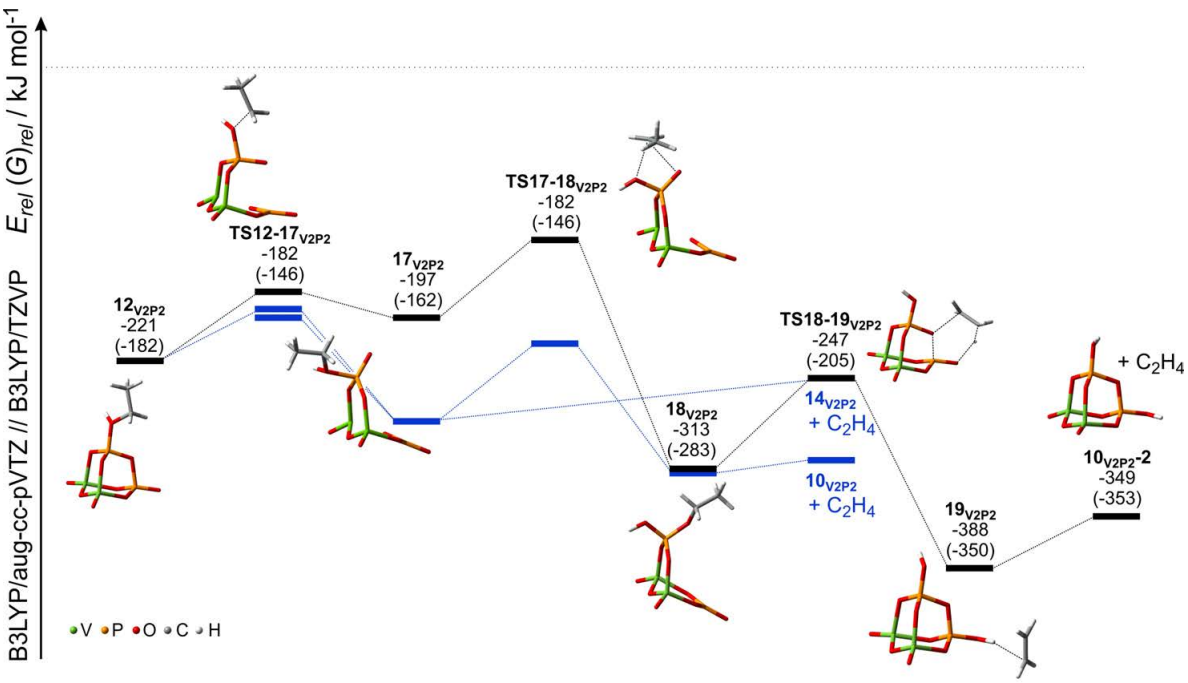

Figure 3.17: Alternative mechanism for the ODH-reaction of $[V_2P_2O_{10}]^{\bullet+}$ with C_2H_6 (green V, yellow P, red O, gray C, white H). The electronic energies and relative Gibbs free energies (in parentheses) are given in kJ mol^{-1} and corrected for unscaled zero-point energy contributions. The blue lines show the pathway from Figure 3.16.

of one V−OH and one P−OH group. However, this process is kinetically more demanding compared to the two ODH pathways described above. Starting from intermediate **12$_{V2P2}$**, the cage structure is opened via **TS12-17$_{V2P2}$**before the transfer of the ethyl radical to the newly formed P−O$_t$ unit via **TS17-18$_{V2P2}$** takes place; the latter corresponds to the transition structure with the highest relative energy (-182 kJ mol^{-1}). The second C−H bond activation of the oxidative dehydrogenation concomitant with the regeneration of the closed-cage structure **19$_{V2P2}$** occurs in the sequence **18$_{V2P2}$** → **TS18-19$_{V2P2}$** → **19$_{V2P2}$**. Finally, elimination of the weakly-bound ethene brings about formation of **10$_{V2P2}$-2**; the overall process is associated with a significant thermochemical driving force of -349 kJ mol^{-1}, being 53 kJ mol^{-1} more exothermic than the formation of the comparable **10$_{V2P2}$** product.

While the reaction channels discussed so far represent the energetically favored pathways for ODH, many other isomeric intermediates are conceivable as well, depending on the coordination of the hydrocarbon, the hydrogen atom, etc. However, the rate-determining activation barriers of the two ODH pathways determined for the $[V_3PO_{10}]^{\bullet+}/C_2H_6$ couple are **TS12-13$_{V3P}$** and **TS12-15$_{V3P}$**. While these transition structures with relative energies of -169 and -168 kJ mol^{-1}, respectively, are almost isoenergetic, the associated product ions are quite different from an energetic point-of-view with the formation of **10$_{V3P}$** being significantly more exothermic, *i.e.* 138 kJ mol^{-1}, compared to **14$_{V3P}$**. For the $[V_4O_{10}]^{\bullet+}/C_2H_6$

system, $\mathbf{10_{V4}}$ is not only thermochemically favored by ca. 154 kJ mol^{-1}, but also the transition state **TS12-15$_{V4}$** is 28 kJ mol^{-1} lower in energy than the alternative transition state **TS12-13$_{V4}$** leading to the formation of $\mathbf{14_{V4}}$. Moreover, formation of $\mathbf{14_{V4}}$ has been demonstrated in the reaction of $[V_4O_{10}]^{\bullet+}$ with C_3H_8 in an elegant combined experimental/computational study including infrared spectroscopic characterization of the ionic species. [301]

With respect to the process of oxygen-atom transfer, formation of the corresponding product **4** has been calculated to be endothermic by 14, 12, and 16 kJ mol^{-1} for heteronuclear $[V_3PO_{10}]^{\bullet+}$ and $[V_2P_2O_{10}]^{\bullet+}$ and homonuclear $[P_4O_{10}]^{\bullet+}$, respectively. In contrast, OAT is exothermic by -103 kJ mol^{-1} and thus accessible for the homonuclear vanadium $[V_4O_{10}]^{\bullet+}/C_2H_6$ system under thermal conditions. However, the ODH reaction channel for this system is even more exothermic by 183 kJ mol^{-1}, and the highest barrier of this pathway, *i.e.* **TS12-15$_{V4}$**, has been calculated to be about 83 kJ mol^{-1} lower in energy compared to the exit channel of the oxygen-atom transfer. Accordingly, consistent with theory and our experimental results described above, oxidative dehydrogenation corresponds to the main process in the reaction of $[V_4O_{10}]^{\bullet+}$ with C_2H_6.

3.3 Structure and chemistry of the oxo-cluster $[VPO_4]^{\bullet+}$ in comparison with $[V_2O_4]^{\bullet+}$

„Everything should be made as simple as possible, but not simpler." [311]

– Albert Einstein

In view of the fact that the „real world" *VPO*-catalysts consist of multiple components, including fully oxidized VPO_5 as well as lower oxidized $V_2P_2O_7$ phases, [276] it further deems of interest to expand the scope of the reactivity studies to not fully but only partially oxidized systems. Concerning the first part of this chapter, the targeted, mixed cluster ions $[V_xP_{4-x}O_{10}]^{\bullet+}$ (x = 2 - 3) are made up of phosphorous and vanadium atoms that are oxidized to the highest oxidation state of 5 considering a terminal $O^{\bullet-}$ unit in the cluster. As an example for lower oxidized metal-oxides, the small vanadium(IV/V)-oxide cation $[V_2O_4]^{\bullet+}$ has been studied extensively, including a structural characterization, [65] and it has been shown that this oxide cation exhibits no or just minor reactivity towards small hydrocarbons such as CH_4, C_2H_6, C_3H_8, $n-C_4H_{10}$, and C_2H_4. [291] Regarding its electronic structure, $[V_2O_4]^{\bullet+}$ possesses no spin density at one of the oxygen atoms; instead, the unpaired electron in $[V_2O_4]^{\bullet+}$ is centered at one vanadium atom, thus corresponding to a mixed valence cluster $[V^{IV}V^{V}O_4]^{\bullet+}$.

The following section reports on the ESI generation of the small, mixed-oxo cluster $[VPO_4]^{\bullet+}$, its electronic structure in the gas phase as well as its reactivity towards small hydrocarbons. As a further example of an only partially oxidized systems, the results are compared to the reactivity and structure of the gaseous vanadium-oxide cation $[V_2O_4]^{\bullet+}$ to uncover the underlying substitution effects in terms of C−H bond activation of small hydrocarbons; as shown recently, there is ample evidence that replacements of an atom by another element significantly affects the gas-phase ion chemistry of various cluster systems. [272,312–314]

3.3.1 Generation and electronic structure of $[VPO_4]^{\bullet+}$

With respect to the generation of $[VPO_4]^{\bullet+}$, it was already mentioned (Chapter 2.2.1) that by choosing the right precursor, larger metal-oxide clusters are also accessible by ESI, as shown previously for various vanadium systems; [154,155] these clusters are otherwise only accessible in the gas phase by use of LDI sources. However, the generation of mixed, cationic oxo-clusters by ESI is rather unique.

Nevertheless, upon spraying a millimolar solution of commercially available vanadyl trichloride $VOCl_3$ and triethyl phosphate $PO(OC_2H_5)_3$ in methanol or acetonitrile, the cluster cation $[VPO_4]^{\bullet+}$ (m/z 146) is generated in excellent yields (Figure 3.18); the maximum intensity is achieved at U_C = 160 V. Regarding the genesis of $[VPO_4]^{\bullet+}$, a stepwise

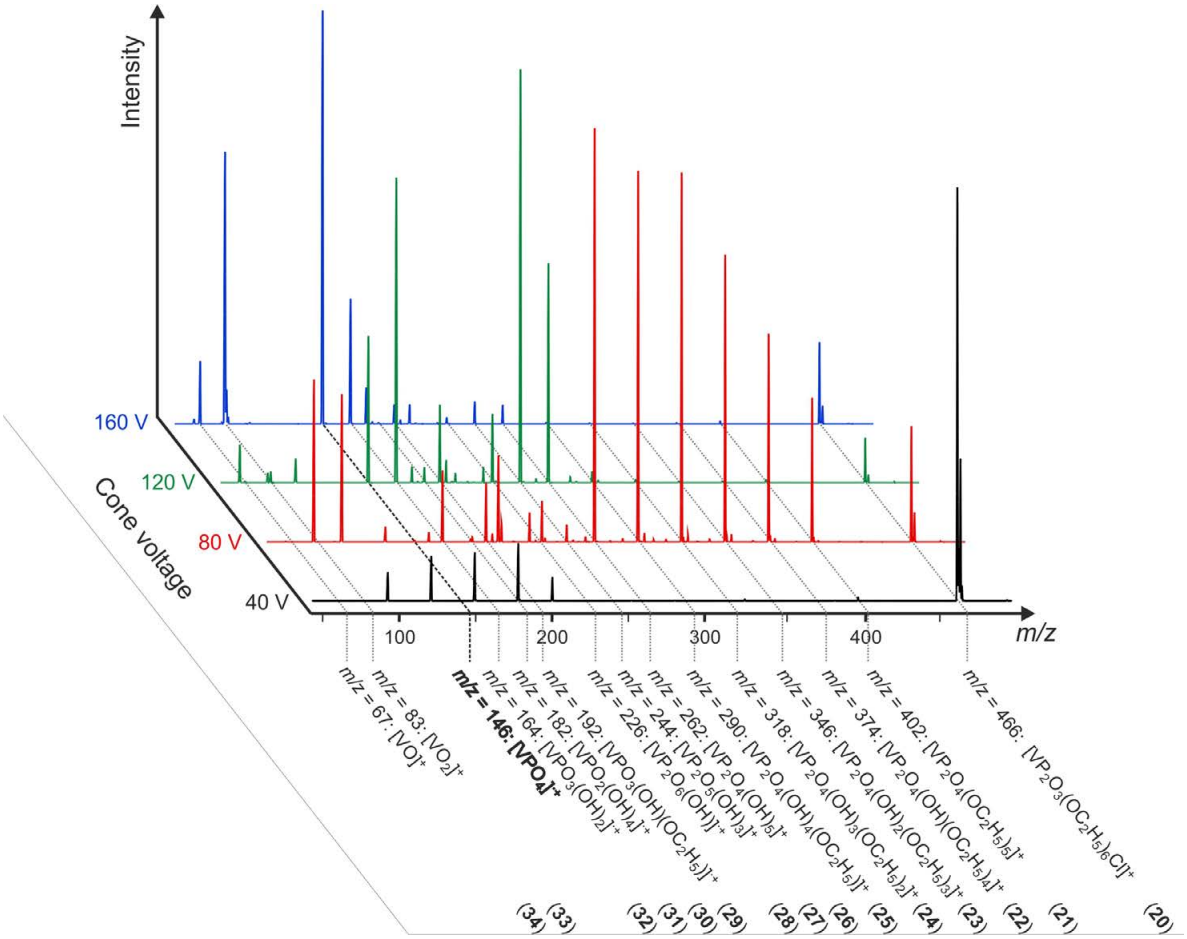

Figure 3.18: Ion-source spectra of a solution of $VOCl_3$ and $PO(OEt)_3$ in methanol at various cone voltages. Structural assignments are based on the postulated breakdown processes depicted in Figure 3.19.

fragmentation from an *in-situ* formed complex in solution is likely to occur. Based on CID experiments of the individual species involved, a fragmentation pathway for the generation of $[VPO_4]^{\bullet+}$can be derived (Figure 3.19). The ion $[VP_2O_3(OC_2H_5)_6Cl]^{\bullet+}$ (**20**) at m/z 466 serves as the parent ion; most likely, it contains a Cl−V−O moiety with two triethyl-phosphate groups coordinated to the metal core (Figure 3.19). Such hexa-coordinated structural motives are very common for vanadium centers in the oxidation state +IV, *e.g.* in aqueous $[VO(OH_2)_5]^{2+}$ or $[VO(OH)(OH_2)_4]^{+}$. In general, five- and six-coordinated vanadium cores prevail as dominant species in organometallic complexes of V^{IV} and V^{V}.[xv] Hence, increasing the cone voltage to values larger than 40 V initiates the breakdown of **20** (Figure 3.18), resulting first in the loss of neutral C_2H_5Cl and the formation of the vanadium complex $[VP_2O_4(OC_2H_5)_5]^{\bullet+}$ (**21**); further fragmentations involve the consecutive elimination of C_2H_4 (Δm = 28) via **21** → $[VP_2O_4(OH)(OC_2H_5)_4]^{\bullet+}$ (**22**) → $[VP_2O_4(OH)_2(OC_2H_5)_3]^{\bullet+}$ (**23**) → $[VP_2O_4(OH)_3(OC_2H_5)_2]^{\bullet+}$ (**24**) → $[VP_2O_4(OH)_4(OC_2H_5)]^{\bullet+}$ (**25**). From the latter, the

[xv] For more details of the chemistry and structural features of vanadium complexes, see [315].

fragmentation pattern bifurcates into two different pathways (Figure 3.19): The first one continues with the loss of C_2H_4 from the remaining ethoxy side-chain, thus forming the oxo-/hydroxyl-complex ion $[VP_2O_4(OH)_5]^{\bullet+}$ (**26**) from which $[VP_2O_5(OH)_3]^{\bullet+}$ (**27**) and $[VP_2O_6(OH)]^{\bullet+}$ (**28**) are generated upon the stepwise expulsions of H_2O, respectively. In the final step, one of the remaining phosphate fragments in **28** is liberated as neutral HPO_3 (metaphosphoric acid) to form the ion of interest $[VPO_4]^{\bullet+}$(**32**, m/z 146). The second pathway commences with the elimination of phosphorous acid H_3PO_4 from **25**, which then leads to the formation of $[VPO_3(OH)(OC_2H_5)]^{\bullet+}$ (**29**). Upon further collisional activation, expulsion of C_2H_4 to form $[VPO_3(OH)_2]^{\bullet+}$ (**31**) occurs and finally, loss of H_2O produces the target ion **32**. Moreover, structures **26** and **27** have been identified as direct precursors for **31** via losses of neutral H_3PO_4 and HPO_3, respectively. In addition, collision-induced elimination of HPO_3 from **26** gives rise to the formation of $[VPO_2(OH)_4]^{\bullet+}$ (**30**) which can consecutively undergo further dehydration to also produce **31**.

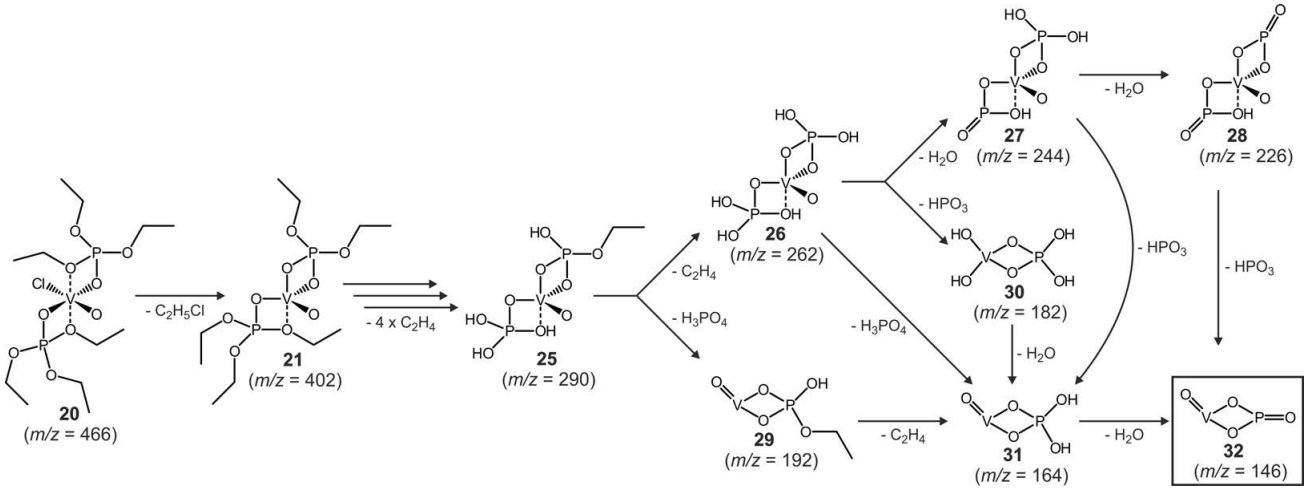

Figure 3.19: Postulated fragmentation mechanism for the generation of $[VPO_4]^{\bullet+}$ (**32**) from precursors $VOCl_3$ and $PO(OEt)_3$. The observed cone-voltage induced in-source dissociation has been verified with further CID experiments of the respective ions. For the sake of clarity, the positive charge for all species is omitted.

At cone voltages exceeding 160 V, the signal intensity of $[VPO_4]^{\bullet+}$ decreases again due to the dissociation of **32** into $[VO_2]^+$ (**33**) and $[VO]^+$ (**34**) (Figure 3.18), concomitant with the expulsion of open-shell oxides $PO_2^{\bullet}$ and $PO_3^{\bullet}$, respectively.

With respect to the structural assignment of cluster **32**, Figure 3.20 (top panel) shows the experimental IRPD spectrum of the $[VPO_4]^{\bullet+}\cdot$He complex (For details, see Appendix B). It exhibits four absorption bands (labeled **a**-**d**) in the spectral region from 800 cm^{-1} to 1500 cm^{-1}: The most intense band is observed at 1445 cm^{-1} (**a**) and three bands appear below 1100 cm^{-1}, *i.e.* at 1064 (**b**), 1038 (**c**) and 953 cm^{-1} (**d**). Addition of a second helium atom only affects the position of bands **c** and **d**, which are shifted to higher energies by 5 and 4 cm^{-1}, respectively (Figure 3.20 (second panel)).

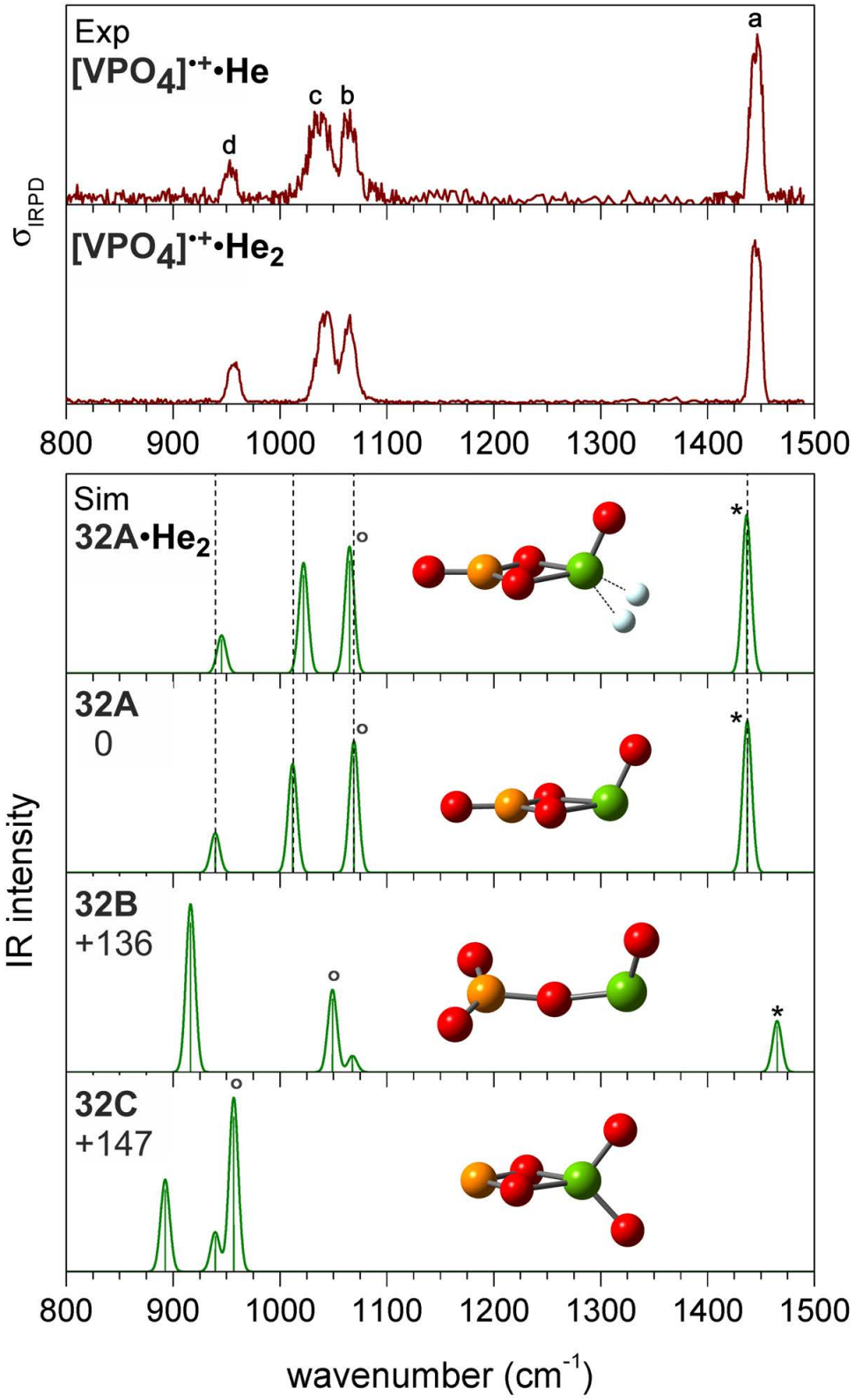

Figure 3.20: Experimental IRPD spectra (top) of the ion-He complex $[VPO_4]^{\bullet+}\cdot He_{1,2}$ compared to simulated B3LYP+D/TZVPP linear absorption spectra of three bare isomers (**32A** - **C**) and the helium-tagged isomer **32A**$\cdot He_{1,2}$. Given values indicate the relative energies (in kJ mol^{-1}) of the optimized structures **32A** - **C** (yellow P, green V, red O, grey He). The V=O stretching modes are marked with a circle, and P=O modes with an asterisk. Harmonic frequencies of the V=O modes are scaled by 0.9167 and all other modes by 0.9832.

A preliminary assignment of bands **a** - **d** can be made based on a comparison to the IRPD spectra of $[V_2O_4]^{\bullet+}\cdot He_3$, [316] and $[CeVO_4]^{\bullet+}\cdot He$, [274] which both were found to have $M-(O)_2-M$ ring structures containing two terminal M=O bonds in *trans* configuration. Both IRPD spectra exhibit bands only below 1050 cm^{-1}; the characteristic vanadyl (V=O) stretching modes are observed above ($[V_2O_4]^{\bullet+}\cdot He_3$: 1029 cm^{-1}, 1049 cm^{-1}; $[CeVO_4]^{\bullet+}\cdot He$: 1017 cm^{-1}) and the $M-(O)_2-M$ ring modes below 1000 cm^{-1}. Thus, the bands **b** and **c** fall in the spectral region where vanadyl (V=O) stretching vibrations are typically located. [65] Band **a** is attributed to a P=O stretching vibration; due to the 1.65-times lower mass of phosphorous compared to that of vanadium, all corresponding modes are expected to be significantly shifted to higher wavenumbers. For example, the P=O stretching vibrations of the phosphonate group ($-PO_3H_2$) are typically located in the spectral range from 1150 to 1270 cm^{-1}. [317,318] Furthermore, the observation that upon addition of a second helium atom only bands **c** and **d** are affected suggest that the helium atom binds to one of the ring atoms, most probably the vanadium atom, and therefore, as a result of a cage-like effect, blue-shifts mainly those bands (bands **c** and **d**).

To allow for a structural assignment, the experimental IRPD spectrum of $[VPO_4]^{\bullet+}\cdot He_{1,2}$ is compared to simulated B3LYP+D/TZVPP linear absorption spectra of three stable structures (**A** - **C**, Figure 3.20). The lowest energy structure found for $[VPO_4]^{\bullet+}$ is characterized by a four-membered $V-(O)_2-P$ ring containing terminal V=O and P=O bonds (**32A**, Figure 3.20); this bonding pattern is similar to the previously reported structures for $[Zr_2O_4]^{\bullet+}$, [319] $[V_2O_4]^{\bullet+}$, [316] or $[CeVO_4]^{\bullet+}$. [274] The calculations strongly favor structure **32A**, because the other isomers considered are predicted to lie more than 100 kJ mol^{-1} higher in energy, ruling these out as possible candidates purely for energetic reasons. This includes the isomer with a chain-like structure (**32B**, +136 kJ mol^{-1}) or the cyclic structure containing a terminal VO_2 group (**32C**, +147 kJ mol^{-1}). The experimental spectrum shows an excellent agreement with the simulated spectrum of the lowest energy structure **32A**, both for the band positions (exp/sim: 1445/1437 cm^{-1} (**a**), 1064/1069 cm^{-1} (**b**), 1043/1012 cm^{-1} (**c**), 957/939 cm^{-1} (**d**)) as well as their relative intensities, respectively. On the other hand, non-satisfactory agreement with the experimentally determined spectrum is found for isomers **32B** and **32C**. The observed bands **a**-**d** are thus assigned as follows: **a** and **b** are attributed to terminal P=O and V=O stretching vibrations, respectively, while the bands **c** and **d** correspond to the in-plane deformation modes of a $V-(O)_2-P$ ring. Moreover, an even better agreement between the experimental and simulated vibrational frequencies is obtained, when the interactions of the ion and helium are taken into account. Both helium atoms are predicted to bind to the vanadium atom in isomer **32A**, each with a binding energy of 14 kJ mol^{-1} (structure **32A**$\cdot He_2$, Figure 3.20). Normal mode analysis confirms that the presence of the helium atoms particularly affects the vibrational frequencies of the ring vibrations. In contrast, the position of the P=O and V=O stretching bands (**a** and **b**) are predicted to remain unchanged upon tagging, confirming the experimental observation.

These effects are also reflected in the experimental line widths of the vibrational transitions observed in the IRPD spectrum of $[VPO_4]^{\bullet+}\cdot He_2$. The P=O stretching band **a** has a width of 11 cm^{-1} (fwhm) representing the narrowest feature in the spectrum. The remaining bands **b**-**d** are broadened by 15, 18 and 12 cm^{-1}, respectively. All line widths exceed the spectral bandwidth of the laser (1.8 cm^{-1}) and are thus limited by dynamical effects or rotational broadening. The observed variations may (in part) indicate different coupling strengths between the vibrational modes and the dissociation channel, *i.e.* loss of helium atoms. Since the P=O stretching vibration is least influenced upon He-tagging (Figure 3.20), this mode is expected to couple rather weakly to the dissociation channel. In this case, intramolecular vibrational relaxation (IVR) is slow, thus resulting in a small line width. The situation is different for the ring vibration band **c**, which is most strongly affected upon tagging. This suggests that band **c** couples stronger to the dissociation channel, leading to faster IVR; thus, this band becomes noticeably broadened compared to band **a**. However, if IVR is predominantly responsible for the broadening of the spectral bands, one would expect a more significant difference between $[VPO_4]^{\bullet+}\cdot He$ and $[VPO_4]^{\bullet+}\cdot He_2$. Thus, the mobility of the vanadium-bound helium atoms might also account for a further broadening of the bands; though, here it remains ambiguous why this effect is more pronounced for band **c** compared to band **d**.

3.3.2 Reactivity of $[VPO_4]^{\bullet+}$towards small hydrocarbons

As mentioned previously, the homonuclear cationic cluster $[V_2O_4]^{\bullet+}$ was found to be rather inert towards small hydrocarbons, *e.g.* CH_4, C_2H_6, C_3H_8, *n*-C_4H_{10}, and C_2H_4.[291][xvi] However, the reactivity patterns changes significantly when one of the vanadium atoms is replaced by phosphorous (Equations 3.18 - 3.24, Figure 3.21).

$$[VPO_4]^{\bullet+} + CH_4 \longrightarrow \text{no reaction} \tag{3.18}$$

$$[VPO_4]^{\bullet+} + C_2H_6 \longrightarrow [VPO_4C_2H_4]^{\bullet+} + H_2 \tag{3.19}$$

$$[VPO_4]^{\bullet+} + C_3H_8 \longrightarrow [VPO_4H_2]^{\bullet+} + C_3H_6 \tag{3.20}$$

$$[VPO_4]^{\bullet+} + C_3H_8 \longrightarrow VPO_4H^{\bullet} + [C_3H_7]^{+} \tag{3.21}$$

$$[VPO_4]^{\bullet+} + n\text{-}C_4H_{10} \longrightarrow [VPO_4H_2]^{\bullet+} + C_4H_8 \tag{3.22}$$

$$[VPO_4]^{\bullet+} + n\text{-}C_4H_{10} \longrightarrow VPO_4H^{\bullet} + [C_4H_9]^{+} \tag{3.23}$$

$$[VPO_4]^{\bullet+} + C_2H_6 \longrightarrow [VPO_3]^{\bullet+} + C_2H_4O \tag{3.24}$$

[xvi] We confirmed these results in experiments performed exemplarily for the $[V_2O_4]^{\bullet+}/n\text{-}C_4H_{10}$ couple in our experimental setup; here, no bond activation of n-butane serving as least inert substrate investigated occurs, and only adduct formation can be observed.

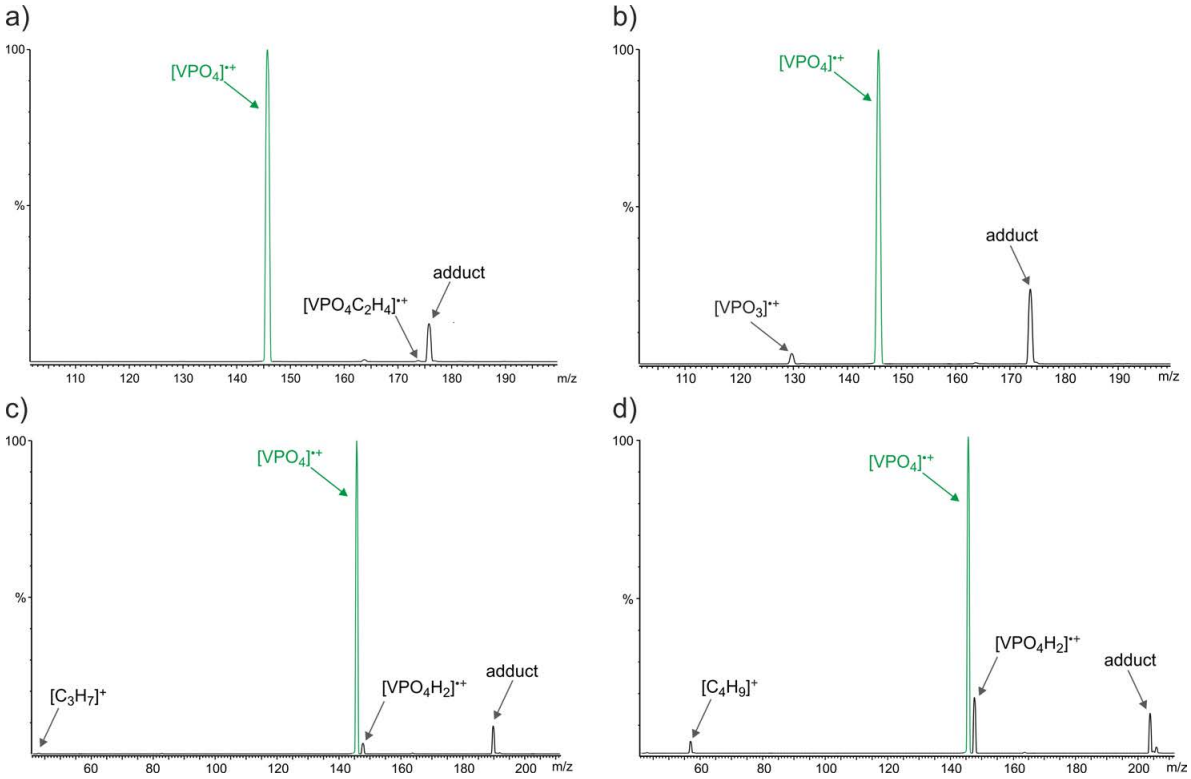

Figure 3.21: Ion/molecule reactions of mass-selected $[VPO_4]^{\bullet+}$ with a) C_2H_6, b) C_2H_4, c) C_3H_8 and d) *n*-C_4H_{10}. The weak signal at m/z 164 observed in all four spectra is due to adduct formation of the parent ion with residual water molecules present as impurity within the vacuum region.

As found for $[V_2O_4]^{\bullet+}$, also $[VPO_4]^{\bullet+}$ does not react with methane, and only very inefficient H_2 elimination is observed beside adduct formation in the thermal reaction with ethane (Figure 3.21a and Table 3.5). In the reactions with the higher homologues propane or *n*-butane, however, oxidative dehydrogenation takes place with increasing reaction rates (Table 3.5), resulting in the formation of the reduced cluster ion $[VPO_4H_2]^{\bullet+}$ and neutral C_3H_6 or C_4H_8, respectively, Equations 3.20 and 3.22. In addition, hydride abstraction is observed for both couples $[VPO_4]^{\bullet+}/C_3H_8$ and $[VPO_4]^{\bullet+}/n$-C_4H_{10}, leading to the formation of the neutral radical $VPO_4H^{\bullet}$ and the carbenium ions $[C_3H_7]^+$ and $[C_4H_9]^+$, respectively, Equations 3.21 and 3.23. Further, reaction with unsaturated hydrocarbons, *e.g.* ethene, gives rise to oxygen-atom transfer to the hydrocarbon with $[VPO_3]^{\bullet+}$ being formed as ionic product, Equation 3.24. Regarding the relative rate constants for bond activation, the reaction proceeds most efficiently with *n*-butane and decreases when proceeding from propane via ethene to ethane (Table 3.5).

Mechanistic insights into the oxidative dehydrogenation can be obtained from deuterium-labeling experiments. For the oxidation of propane, the reaction of $[VPO_4]^{\bullet+}$ with $CH_3CD_2CH_3$ gives rise exclusively to the ionic cluster $[VPO_4HD]^{\bullet+}$; $[VPO_4H_2]^{\bullet+}$ and

Table 3.5: Relative rate constants for the overall reactions, k_{rel}, and neglecting adduct formation, k^*_{rel} as well as the product distribution for the ion/molecule reactions of $[VPO_4]^{\bullet+}$ with small hydrocarbons.[a]

			Product channel				
Neutral reactant	k_{rel}	k^*_{rel}	ODH	OAT	H^- transfer	H_2 loss	adduct formation
C_2H_4	98	23	-	21	-	-	79
C_2H_6	46	2	-	-	-	3	97
C_3H_8	79	26	39	-	3	-	58
n-C_4H_{10}	100	100	56	-	9	-	35

[a] Relative rate constant values are normalized to k_{rel} = 100 for the reaction of $[VPO_4]^{\bullet+}$ with n-C_4H_{10}. Product distribution values are normalized to $\sum$ = 100; branching ratio is obtained via linear regression ($p_{reactant}$ = 0). ODH: oxidative dehydrogenation; and OAT: oxygen-atom transfer.

$[VPO_4D_2]^{\bullet+}$ are not observed. Hence, the elimination proceeds in a clean [1,2]-fashion without any H/D-scrambling involved. This holds presumably also true for the reaction with deuterium-labeled *n*-butane, *i.e.* $CD_3(CH_2)_2CD_3$; here, $[VPO_4HD]^{\bullet+}$ and $[VPO_4H_2]^{\bullet+}$ are the only product ions generated with a branching ratio of $1_{HD} : 1.4_{H_2}$. With respect to the hydride transfer, the abstraction from the secondary position is favored. The product distributions of $VPO_4H^{\bullet}$ versus $VPO_4D^{\bullet}$ amount to 11:1 and >20:1 (1:>20) for the reaction of $[VPO_4]^{\bullet+}$with $CD_3(CH_2)_2CD_3$ and $CD_3CH_2CD_3$ ($CH_3CD_2CH_3$), respectively; for the deuterated propanes, the small branching ratio for the hydride abstraction does not permit to accurately determine the site-selectivity.

To obtain further information on the corresponding reaction mechanisms, quantum-chemical calculations have been carried out once more; here, the couples $[VPO_4]^{\bullet+}/C_2H_4$ and $[VPO_4]^{\bullet+}/C_3H_8$ serve as suitable examples to uncover the intrinsic requirements for OAT and ODH, respectively.

Chemically reasonable structures for C_2H_4O, generated according to Equation 3.24, are oxirane, vinyl alcohol, and acetaldehyde. Among them, acetaldehyde corresponds to the thermochemically most favored neutral product and has been shown to be generated in many OAT reactions of oxo-clusters with ethene.[138,267,271,292,320] This holds true for the reaction of $[VPO_4]^{\bullet+}$towards ethene as well; while the generation of acetaldehyde is with -38 kJ mol^{-1} exothermic, both epoxidation of C_2H_4 to ethylene oxide as well as the formation of vinyl alcohol are endothermic by +85 kJ mol^{-1} and +14 kJ mol^{-1}, respectively. Furthermore, the reaction takes place solely at the P=O moiety; transfer of an oxygen-atom from the V=O site to generate acetaldehyde is +175 kJ mol^{-1} above the entrance channel and thus not accessible under thermal conditions.

The computed PES for the reaction of $[VPO_4]^{\bullet+}$with C_2H_4 is given in Figure 3.22a. In the first step, a carbon atom of ethene coordinates to the phosphorous atom of the cluster ion to form intermediate **35**; as a consequence, the C=C double bond of the incoming ligand gets elongated from 1.32 Å in free ethene to 1.36 Å, and the coordinating carbon atom of C_2H_4

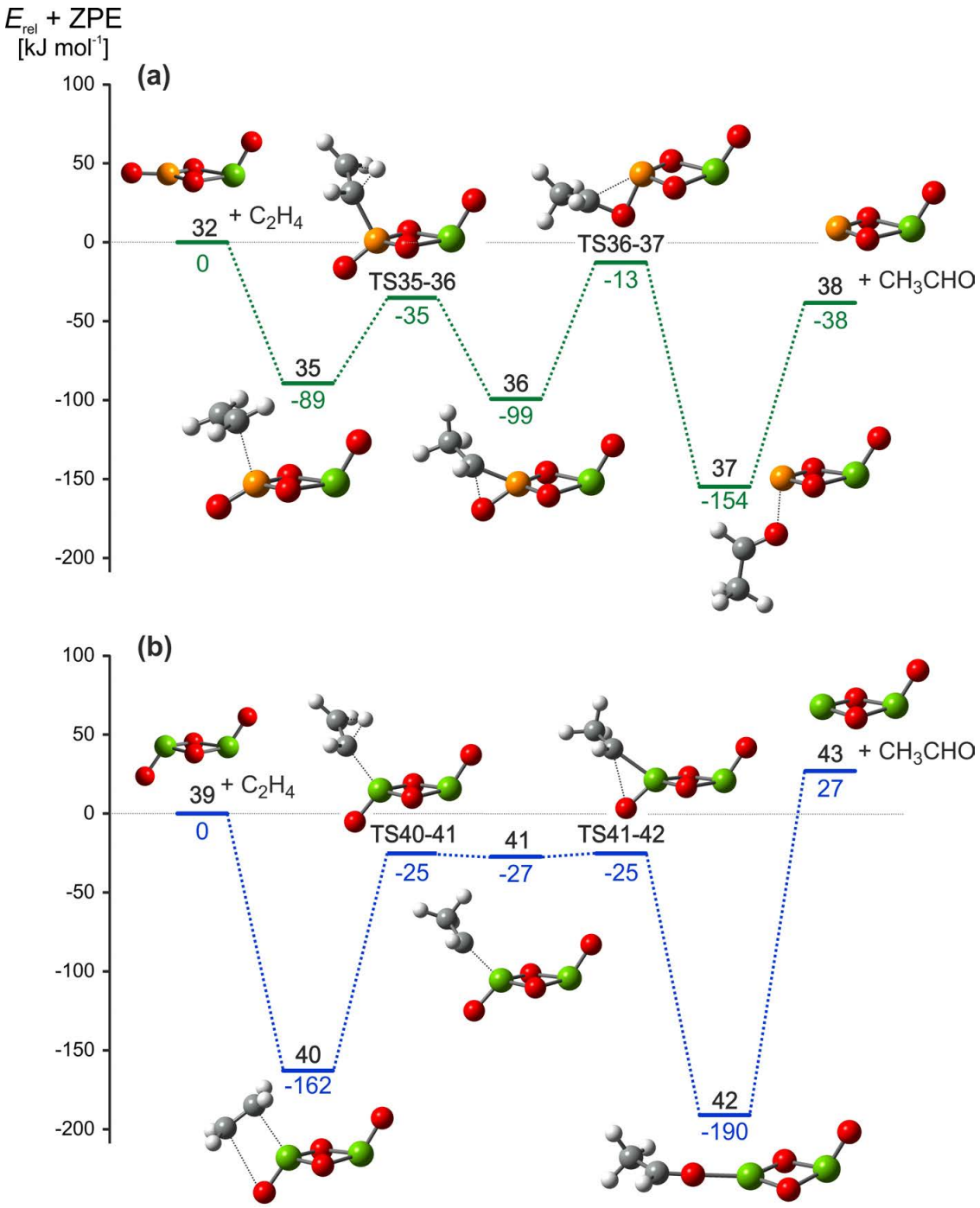

Figure 3.22: PES for the reactions of a) $[VPO_4]^{\bullet+}$ and b) $[V_2O_4]^{\bullet+}$ with C_2H_4, calculated at the B3LYP/def2-TZVP level of theory (green V, yellow P, red O, gray C, white H). The relative energies are given in kJ mol^{-1} and corrected for unscaled zero-point energy contributions.

is slightly pyramidalized with dihedral angles D_{HCCH} of 9° and 11°. Also the phosphorous atom loses its planar coordination sphere initially present in structure **32**; the terminal P=O bond in **35** is bent by 31° out of the P(μ−O)$_2$V ring plane. The reaction proceeds with a [1,2]-hydrogen migration from the proximal to the terminal carbon atom via transition

structure **TS35-36**. Concomitantly, the carbon and oxygen atoms approach each other, and the resulting intermediate **36** contains a hypervalent, four-coordinated phosphorous atom, forming a phospha-oxa cyclopropane analogue. The C−O distance of 1.66 Å in **36** is longer as expected for a C−O single bond (*e.g.* 1.431 Å in free ethanol or 1.425 Å in free ethylene oxide [302]); a further approach of both atoms is only achieved in **TS36-37** and is accompanied with a substantial elongation of the P−C bond. The resulting transfer of the hydrocarbon fragment to the terminal oxygen atom is associated with an intrinsic activation barrier of 86 kJ mol^{-1} and constitutes the energetically most demanding step in the course of the reaction. In **37**, the newly formed acetaldehyde molecule coordinates almost rectangularly to the plane of the four-membered ring P(μ−O)$_2$V ($\sphericalangle$VPO = 98°, r(P−O) = 2.03 Å). Finally, liberation of acetaldehyde requires 116 kJ mol^{-1} and completes the reaction with an overall exothermicity of -38 kJ mol^{-1}. The spin density of the various *open-shell* intermediates remains on the vanadium atom throughout the whole reaction.

To explain the different reactivity of $[V_2O_4]^{\bullet+}$ versus $[VPO_4]^{\bullet+}$, the potential-energy surface of $[V_2O_4]^{\bullet+}$ with C_2H_4 has been computed and studied as well (Figure 3.22b). Here, the ethylene molecule coordinates via its carbon atoms simultaneously to both the terminal oxygen and the vanadium (V^V) atom carrying no spin density; formation of the encounter complex **40** is much more exothermic (-162 kJ mol^{-1}) compared to the generation of the phosphorous-containing analogue **35** (-89 kJ mol^{-1}). An adduct complex, structurally similar to **40**, has also been located for the $[VPO_4]^{\bullet+}/C_2H_4$ couple at a relative energy of -143 kJ mol^{-1} with the ethene molecule coordinating to the vanadium and not to the phosphorous site; however, the subsequent activation barrier for the [1,2]-hydrogen migration is with 5 kJ mol^{-1} energetically higher and also entropically disfavored compared to the entrance channel $[VPO_4]^{\bullet+}$ + C_2H_4; thus, this pathway is not accessible under ambient conditions. The analogous intrinsic barrier for the pure vanadium system is also relatively high in energy and amounts to 137 kJ mol^{-1}; however, the associated transition structure **TS40-41** is in this case 25 kJ mol^{-1} lower in energy compared to the entrance channel and is accessible. The so-formed intermediate **41** is only 2 kJ mol^{-1} lower in energy compared to the two associated transition structures **TS40-41** and **TS41-42**; in the latter, acetaldehyde is generated by reductive elimination thus forming complex **42**. In contrast to the phosphorous-containing system **37**, the acetaldehyde ligand in **42** coordinates in an *in-plane* fashion to the vanadium atom, and the bond-dissociation energy of acetaldehyde to the $[V_2O_3]^{\bullet+}$ cluster is much higher compared to the respective BDE of the phosphorous-containing species (BDE($[V_2O_3]^{\bullet+}$−acetaldehyde) = 217 kJ mol^{-1}, BDE($[VPO_3]^{\bullet+}$−(acetaldehyde) = 116 kJ mol^{-1}). Although the relative energies of structures **42** and **43** have to be considered with care due to a broken spin character,[xvii] the qualitative

[xvii] All given ionic reactants, intermediates and transition states have been located on the ground state doublet potential energy surface; selected structures optimized in the quartet state are 200 kJ mol^{-1} and more higher in energy; however, for **42** and **43** (Figure 3.22), the splitting is with 7 kJ mol^{-1} and 26 kJ mol^{-1} relatively small.

picture of an endothermic OAT reaction from $[V_2O_4]^{\bullet+}$ to ethene does not change. In contrast, the overall reaction is by 38 kJ mol^{-1} exothermic for the mixed $[VPO_4]^{\bullet+}$ cluster, *i.e.* the origin for the different reactivities of $[V_2O_4]^{\bullet+}$ and $[VPO_4]^{\bullet+}$ with ethene is due to thermochemical reasons. This conclusion contrasts with the results of the previous findings on the reactions of the larger cluster ions $[V_xP_{4-x}O_{10}]^{\bullet+}$ (x = 0, 2 - 4) with ethene (Chapter 3.2.2), where OAT from a V−O group is energetically less demanding compared to the transfer of an oxygen atom from the P−O moiety. A closer look at the product ion explains these differences: the cleavage of the P−$O_t^{\bullet}$ bond in the larger clusters gives rise to a phosphorous-centered radical and results in the reduction of the phosphorous atom to a formal oxidation state of +IV; for $[VPO_4]^{\bullet+}$ described in this section, the spin remains located at the vanadium atom, and OAT from P−O corresponds to the more favored reduction $P^{+V} \rightarrow P^{+III}$.

For the mechanism of oxidative dehydrogenation, in the initial step of the reaction of $[VPO_4]^{\bullet+}$ with C_3H_8, an intermediate is generated which indicates an incipient hydride transfer from the alkane to the phosphorous atom of the cluster (**44**, Figure 3.23a); the overall Mulliken atomic charge of the C(3) unit in **44** amounts to 0.46 while the spin density is located at the remote vanadium atom. The C−H bond is remarkably elongated from 1.09 Å in free propane to 1.24 Å in intermediate **44** and the P−H bond amounts to 1.63 Å; the originally planar PO_3-unit of the cluster is bent by about 26° and the dihedral angle D_{CCCH} is slightly bent to 137°. The carbocationic character becomes even more pronounced in the subsequent transition structure **TS44-45** in which the Mulliken atomic charge at the C(3) unit amounts to 0.80 and D_{CCCH} to 167°. Concomitant with the hydride transfer, the carbocation unit migrates via **TS44-45** to the terminal oxygen atom of the P−O unit, thus forming intermediate **45**; the P−H bond in the latter corresponds to that of typical P−H single bond (r(P−H)$[PH_4]^+$ = 1.42 Å).[321] From intermediate **45**, a proton from one of the methyl group is transferred to the oxygen atom via **TS45-46**, thus forming the hydrogenated product ion $[VPO_4H_2]^{\bullet+}$ to which neutral propene is loosely coordinated via the hydrogen atom of the newly formed hydroxyl group. Finally, the reaction is completed by liberation of propene and generating the product ion **47**; the computed exothermicity of the overall reaction amounts to -97 kJ mol^{-1}.

As an alternative to the oxidative dehydrogenation, simple hydride transfer can occur as a competing pathway. The loss of the isopropyl cation $[C_3H_7]^+$ from intermediate **44** leads to the formation of the neutral, *open-shell* cluster $VPO_4H^{\bullet}$, and formation of $[i\text{-}C_3H_7]^+$ ion is associated with an overall exothermicity of -15 kJ mol^{-1}; a corner-protonated cyclopropane isomer is 52 kJ mol^{-1} higher in energy and the primary $[n\text{-}C_3H_7]^+$ ion does not exist in the gas phase[322] but rearranges to either one of the two isomers.[323–326] The remarkably high selectivity towards activation of the secondary C−H bond is in agreement with the

This further results in significant spin contamination for **42** ($<S^2>$ = 1.72) and **43** ($<S^2>$ = 1.73), while for all other structures spin contamination is, with a typical value of $<S^2>$ = 0.76, not a problem.

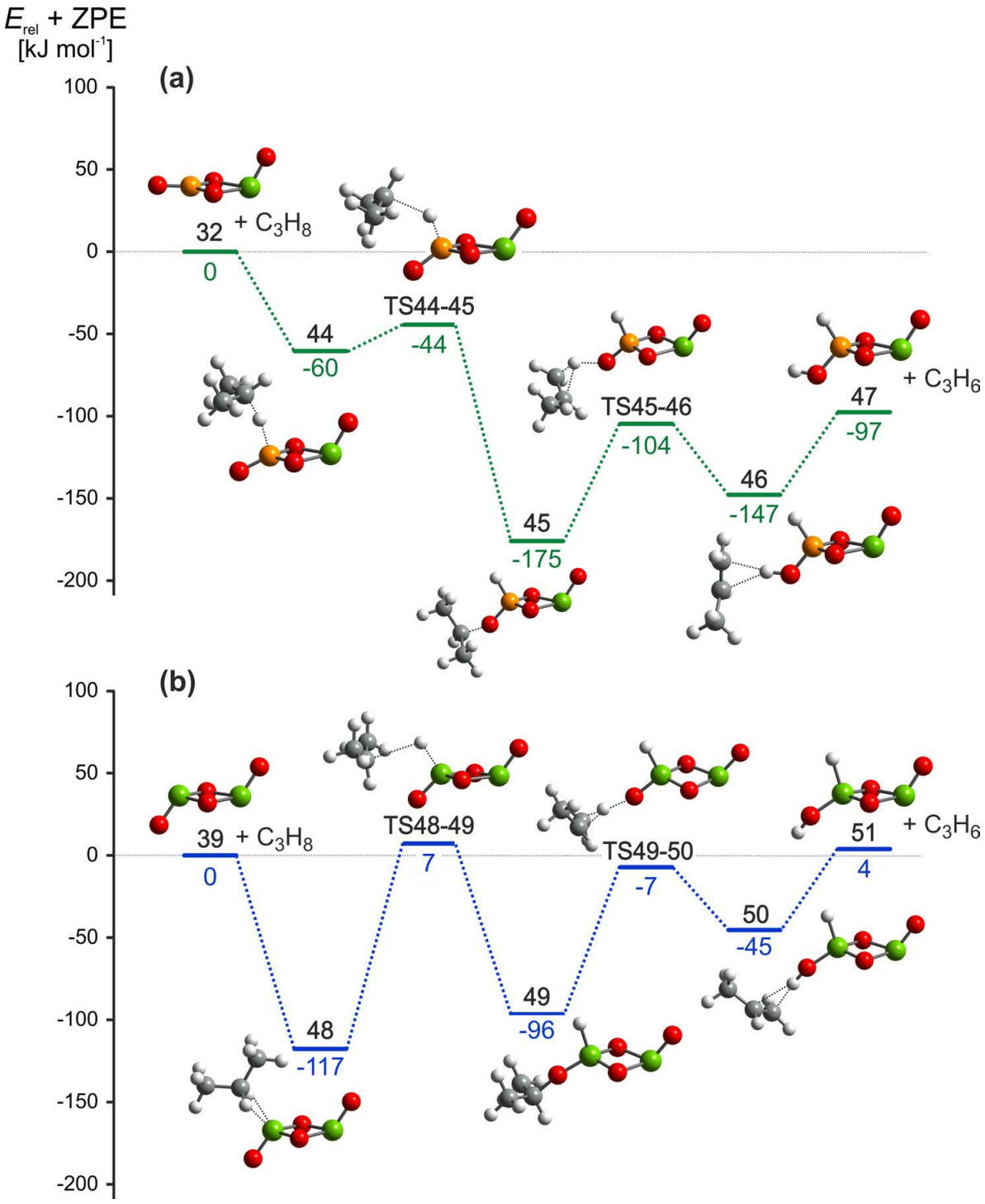

Figure 3.23: PES for the reactions of a) $[VPO_4]^{\bullet+}$ and b) $[V_2O_4]^{\bullet+}$ with C_3H_8, calculated at the B3LYP/def2-TZVP level of theory (green V, yellow P, red O, gray C, white H). The relative energies are given in kJ mol^{-1} and corrected for unscaled zero-point energy contributions.

hydride-ion affinities (HIAs) of primary carbocations (derived experimentally) which are about 75 - 84 kJ mol^{-1} higher than for secondary carbocations. [16]

Again, a comparison of the reaction of $[V_2O_4]^{\bullet+}$ with C_3H_8 deems of interest to analyze the structure-reactivity relationship in more detail; the suggested mechanism is given in Figure 3.23b. Here, the mode of coordination is distinctly different compared to the $[VPO_4]^{\bullet+}/C_3H_8$ couple; instead of forming one hydrogen bond as described above for **44**, the C_3H_8 molecule coordinates to $[V_2O_4]^{\bullet+}$ via both $C_{sec}-H$ bonds, thus forming a five-coordinated vanadium center (**48**, Figure 3.23b). Both C−H bonds are only slightly elongated to 1.12 Å, while the H−C−H angle is bent to ◁HCH = 113°. As found for **TS44-45** of the mixed vanadium-phosphorous system, a hydride transfer together with the migration of a carbocationic C(3) unit to the terminal oxygen takes place via **TS48-49**; the intrinsic barrier amounts to 124 kJ mol^{-1}; this is 7 kJ mol^{-1} above the entrance channel and thus not accessible under thermal conditions. Furthermore, the intrinsic barrier for the subsequent proton transfer via **TS49-50** is about 20 kJ mol^{-1} higher compared to the corresponding barrier of the $[VPO_4]^{\bullet+}/C_3H_8$ system. In addition to the kinetic barrier, also the formation of the reaction products $[V_2O_4H_2]^{\bullet+}$(**51**)$/C_3H_6$ is more energy demanding compared to $[VPO_4H_2]^{\bullet+}$(**47**)$/C_3H_6$ resulting in an overall endothermicity of 4 kJ mol^{-1} for the ODH reaction. This holds true as well for the competing hydride-abstraction yielding neutral $V_2O_4H^{\bullet}$ and $[i\text{-}C_3H_7]^+$; this reaction path is endothermic by 50 kJ mol^{-1} and not accessible under thermal conditions.

With respect to the selectivity of the initial C−H bond activation step, we calculated the analogous reaction pathway for the $[VPO_4]^{\bullet+}/C_3H_8$ couple, in which the initial C−H bond scission takes place at a primary C−H bond (Figure 3.24). However, the lowest transition structure for the C−H bond scission differs from the analogous **TS44-45** structure; after coordination of the hydrocarbon via the primary C−H bond (**52**, -41 kJ mol^{-1}), the transition structure **TS52-53** involves not only the hydride transfer to the phosphorous atom but also a [1,2]-hydrogen migration from the secondary to the primary position in the propane fragment thus reflecting the intrinsic instability of a primary carbocation. As in intermediate **45**, the C(3) unit is bound via a secondary carbon atom to the cluster, *i.e.* intermediates **53** and **45** correspond to rotational isomers along the C−O bond. As expected, the subsequent process **53** → **TS53-54** → **54** → **55** is almost identical to the analogous reaction described above (Figure 3.23a), and the overall exothermicities forming the two isomeric products **47** and **55** are the same. However, the activation of a primary C−H bond in the first step is endothermic by 8 kJ mol^{-1} and accordingly not accessible under thermal conditions; thus, the reaction exhibits a high chemoselectivity towards the secondary position.

In addition to the two-step mechanism presented in Figures 3.23 and 3.24, an alternative one-step reaction pathway has been located as well (Figure 3.25); for example, the simultaneous activation of two C−H bonds via a six-membered ring is feasible. This process can be considered as a combined hydride/proton transfer from the hydrocarbon to the cluster unit; the Mulliken charges at the transferred hydrogen atoms H1/H2 in

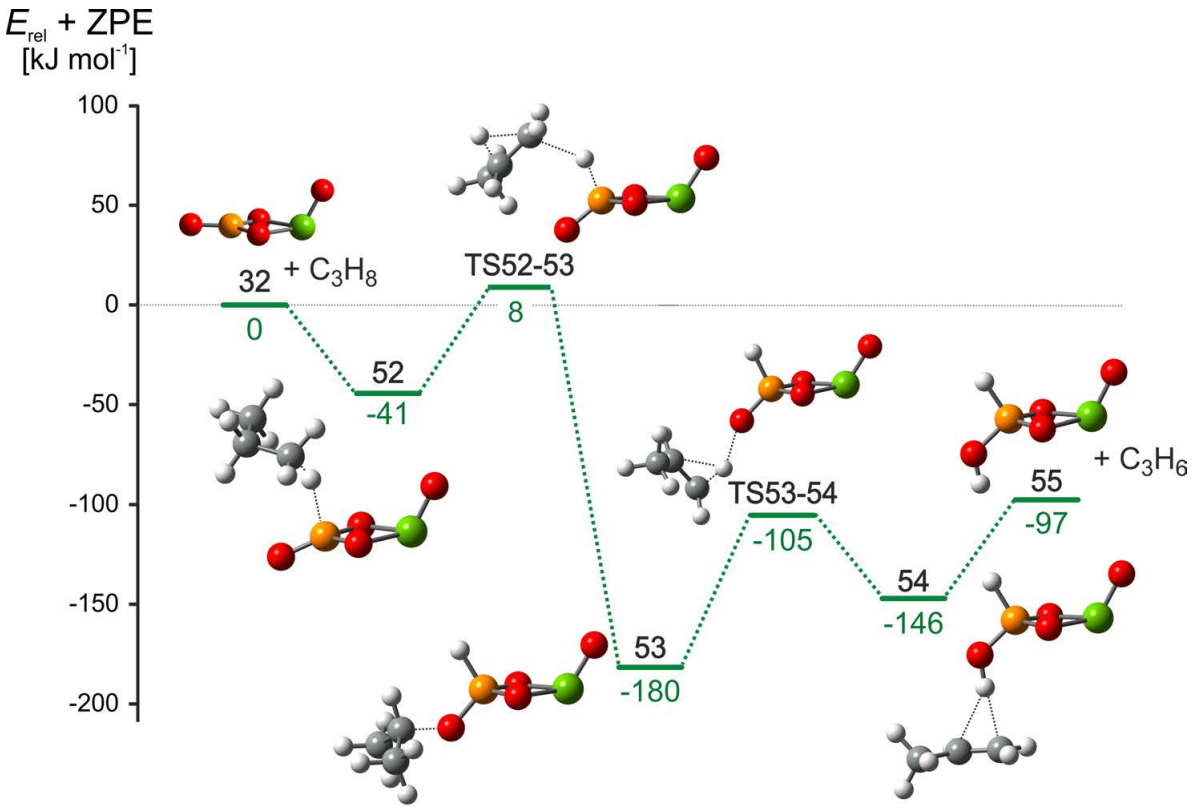

Figure 3.24: PES for the reactions of $[VPO_4]^{\bullet+}$ with C_3H_8 in which initial hydride transfer occurs from the primary position, calculated at the B3LYP/def2-TZVP level of theory (green V, yellow P, red O, gray C, white H). The relative energies are given in kJ mol^{-1} and corrected for unscaled zero-point energy contributions.

the corresponding transition structures **TS56-46** and **TS48-57** amount to -0.57/+0.21 and -0.45/+0.25 for the mixed vanadium-phosphorous system (Figure 3.25a) and the pure vanadium system (Figure 3.25b), respectively, and the spin density remains in both cases at the remote vanadium atom. Furthermore, the progress of the hydride transfer in **TS56-46** and **TS48-57** is much more pronounced compared to the proton migration as indicated by the respective C−H bond lengths (Figure 3.25), and the hydride transfer takes place preferably from the secondary position of C_3H_8. The barrier for the coupled hydride/proton transfer from a primary/secondary C−H bond is 50 kJ mol^{-1} higher in energy compared to **TS56-46**; thus, only the reaction path starting with the hydride transfer from a secondary position is considered. For $[VPO_4]^{\bullet+}$, the rate-determining step of the one-step process of Figure 3.25a is only 2 kJ mol^{-1} less energy demanding than the one shown in Figure 3.23a; thus, both mechanisms of ODH are likely to occur. In contrast, for the $[V_2O_4]^{\bullet+}/C_3H_8$ couple, both transition structures **TS48-57** and **TS48-49** of the one- and two-step mechanisms, Figures 3.25b and 3.23b, respectively, are higher in energy compared to the entrance channel, in line with the experimental results.

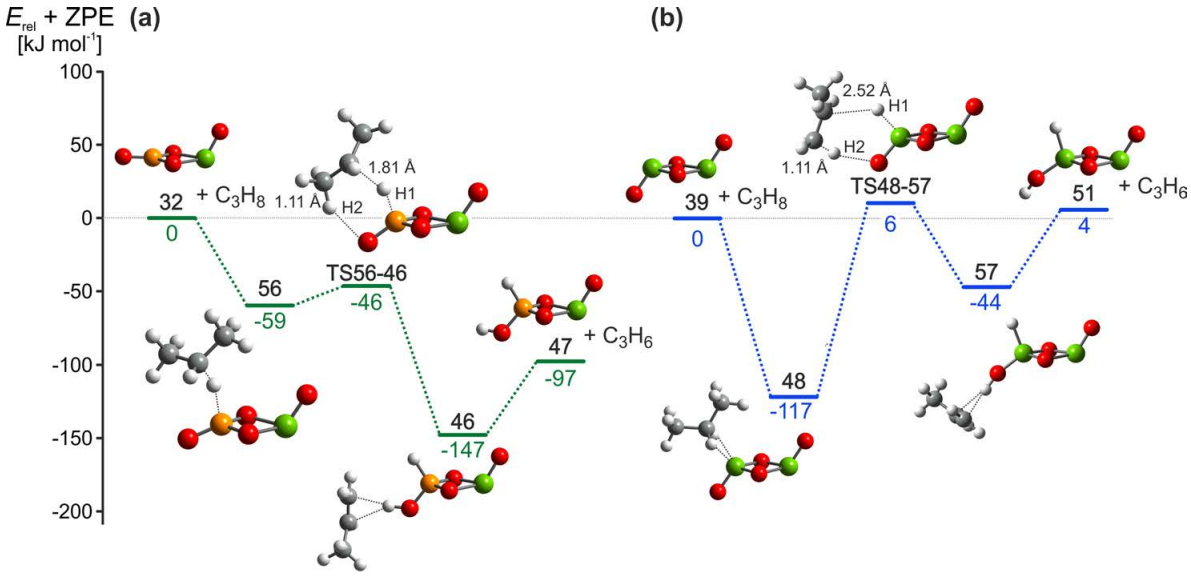

Figure 3.25: Alternative „one-step" PES for the reactions of a) $[VPO_4]^{\bullet+}$ and b) $[V_2O_4]^{\bullet+}$ with C_3H_8. All structures are calculated at the B3LYP/def2-TZVP level of theory (green V, yellow P, red O, gray C, white H) and the relative energies are given in kJ mol^{-1} and corrected for unscaled zero-point energy contributions; the relevant C−H bond lengths are given in Å.

Summarizing the mechanisms of both reaction couples $[VPO_4]^{\bullet+}/C_3H_8$ and $[V_2O_4]^{\bullet+}/C_3H_8$, it is the presence of phosphorous in the heteronuclear cluster that provides the intrinsic prerequisites to enable the C−H bond activation of small hydrocarbons. However, the mechanistic details of the C−H bond fission described here are different compared to the hydrogen-atom transfer observed for *e.g.* $[V_xP_{4-x}O_{10}]^{\bullet+}$ in their reactions with small hydrocarbons. For the latter process, a high spin density at the abstracting atom is required [258,259] (see also Chapter 4) while in the reaction of $[VPO_4]^{\bullet+}$ and $[V_2O_4]^{\bullet+}$ with propane no unpaired spin density is located at the reactive site, and hydride instead of hydrogen-atom abstraction takes place with $[VPO_4]^{\bullet+}$ being the stronger hydride abstractor compared to $[V_2O_4]^{\bullet+}$.

3.4 Summary

In conjunction with other recent studies on mixed oxo-clusters, the present chapter emphasizes once more the critical role of cluster ion compositions in C−H bond activation processes. Therefore, not only transition metals may have an impact on the oxidative reactivity towards hydrocarbons, but also main-group elements such as phosphorous can significantly affect the reactivity in terms of C−H bond activation, as shown *e.g.* by the increased reactivity of $[P_4O_{10}]^{\bullet+}$ in comparison to $[V_4O_{10}]^{\bullet+}$. Moreover, if vanadium and phosphorous are both present in the cluster, their cooperative effects can facilitate the formation of completely new product channels as shown in the reactions of $[V_2P_2O_{10}]^{\bullet+}$ and $[V_3PO_{10}]^{\bullet+}$ with ethane and ethene.

With respect to the analysis of the corresponding potential-energy surfaces, $[V_4O_{10}]^{\bullet+}$ reacts with ethene exclusively in terms of oxygen-atom transfer to the hydrocarbon, while the presence of already one phosphorous atom inhibits this pathway due to the strong $P-O_t^{\bullet}$ single bond. In contrast, $[P_4O_{10}]^{\bullet+}$ is much more reactive with respect to homolytic C−H cleavage to form the *closed-shell* HAT product $[P_4O_9(OH)]^+$. Further, while the first C−H bond scission is initiated by an active $P-O_t^{\bullet}$ site, the presence of a vanadium atom in the cluster is essential to enable the second hydrogen-atom transfer from the hydrocarbon, *i.e.* oxidative dehydrogenation. Obviously, while the presence of vanadium is crucial, a direct interaction of the redox-active transition metal with the hydrocarbon is not required to bring about ODH reactivity under thermal conditions. Thus, cooperative effects of vanadium and phosphorous atoms in the cluster are crucial to bring about ODH; neither $[V_4O_{10}]^{\bullet+}$ nor $[P_4O_{10}]^{\bullet+}$ alone possess the electronic properties necessary to facilitate the oxidative dehydrogenation of ethene.

The redox-activity of the phosphorous and vanadium atoms, *i.e.* accessibility of the oxidation state $+IV$, is also of importance in the reaction of the ionic cluster with ethane. Due to the preferred oxidation state $+V$, $[P_4O_{10}]^{\bullet+}$ is much more reactive in terms of homolytic C−H bond activation during which the formal oxidation state does not change, in contrast to OAT in which a phosphorous atom is necessarily reduced. On the other hand, vanadium can be reduced from $+V$ to $+IV$ and can therefore easier stabilize the radical site formed in the course of reductive processes. Furthermore, the $+V \rightarrow +IV$ reduction of vanadium is associated with rather small structural rearrangements, causing only a insignificant elongation of the internal V−O bonds of the cluster; accordingly, $[V_4O_{10}]^{\bullet+}$ favors the formation of the *open-shell* products $[V_4O_9]^{\bullet+}$ and $[V_4O_{10}H_2]^{\bullet+}$. Thus, the combination of both elements gives rise to new product distributions and illustrates the cooperative effects between different metals and non-metals in complex oxo-frameworks.

Similar observation hold true by comparison of the previously reported $[V_2O_4]^{\bullet+}$ ion and the newly generated $[VPO_4]^{\bullet+}$ cluster, investigated both experimentally and computationally. The latter cluster ion is generated by means of electrospray ionization of a mixed solution containing the two precursor compounds $VOCl_3$ and $PO(OC_2H_5)_3$; CID studies suggest a fragmentation pathway of the observed V/P precursor ion all the way down to $[VPO_4]^{\bullet+}$. State-of-the-art IR photodissociation spectroscopy reveals that the cluster exhibits a four-membered ring structure with a terminal oxygen atom at each of the vanadium and the phosphorous centers, respectively; the P=O-moiety is in plane with the four-membered ring, thus corresponding to a classical PO_3-unit. While $[V_2O_4]^{\bullet+}$ was found to be rather unreactive toward saturated and unsaturated hydrocarbons at thermal conditions, the $[VPO_4]^{\bullet+}$ ion brings about oxidative dehydrogenation and hydride abstraction from propane and *n*-butane, as well as oxygen-atom transfer to ethene. Contrary to the larger cluster ions $[V_xP_{4-x}O_{10}]^{\bullet+}$ (x = 0, 2 - 4), the reactive site of the $[VPO_4]^{\bullet+}$cluster

in the OAT reaction with ethene corresponds to the P−O and not to the V−O unit, *i.e.* the transfer of an oxygen atom from the former to C_2H_4 is preferred; this can also explain the higher OAT reactivity of $[VPO_4]^{\bullet+}$ versus $[V_2O_4]^{\bullet+}$ possessing only V−O units. The presence of phosphorous in $[VPO_4]^{\bullet+}$is also crucial in the oxidative dehydrogenation and hydride abstraction from propane. Again, the phosphorous site of the cluster constitutes the reactive site in that the phosphorous atom is the better hydride acceptor compared to vanadium; this advantage is also of importance for the ODH reaction. While vanadium rather promotes the one electron reduction as shown in the first section of this chapter, the intrinsic property of phosphorous favors two-electron reduction processes, thus causing a tremendous effect on the reactivity of these systems. Accordingly, these intrinsic features of both elements should be considered in upcoming investigation on gas-phase, condensed-phase, and surface-mediated bond activation processes, in which *VPO* and related heteronuclear oxide systems are being employed.

4 The Nature of Hydrogen-Atom Transfer: The Role of Radicals and Spin States in Oxo-Cluster Chemistry with Methane

„The presence of unpaired spin density at the abstracting atom is not a requirement for, or a predictor of, HAT reactivity." [327]

– James. M. Mayer

J. M. Mayer's rather controversial comment initiated the recent discussion on the nature of hydrogen-atom transfer (HAT) which has been regarded [327] as a special class of proton-coupled electron transfer (PCET), playing an important role in a broad range of chemical reactions, covering heterogeneous, homogeneous and enzymatic reactivity. [328–330] Based on numerous studies, HAT itself has been characterized both in terms of the timing of the elementary steps and the site of proton and electron transfer as typically described in free-radical chemistry. In contrast, in PCET the actual timing and the location to where $[H]^+$ and e^- are transferred might differ; for example, in the homolytic C−H bond scission of saturated and unsaturated hydrocarbons mediated by terminal oxo-ligands in high-valent transition-metal complexes, [237–240,331] the electron is accepted by the metal center and the proton transferred to the basic ligand. As to the actual sequence of events, the proton or the electron can be transferred first to different acceptor orbitals, respectively. However, this HAT/PCET classification is not rigorously defined, and the assignment becomes less meaningful the smaller the differences between the energies of different HOMOs in the donor or LUMOs in the acceptor are. [329] In other, more recent studies, the differentiation between HAT and PCET has been described in terms of an electronically adiabatic and a non-adiabatic proton transfer, respectively. [332–334]

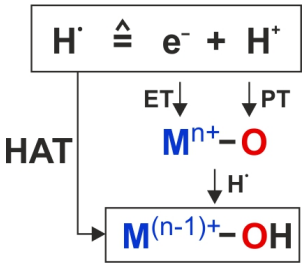

Figure 4.1: Schematic description of HAT versus proton-coupled electron transfer.

Mayer's controversial comment [327], based on the reactions of hydrocarbons R−H with organic radicals and transition-metal complexes, contradicts past and present observations in gas-phase (ion) chemistry in which the presence of a spin density at an oxygen atom of various metal and main-group element oxides *is* a requirement for and a predictor of efficient HAT reactivity at ambient conditions, provided the process is exothermic. The following part will give a short introduction and summary about the state of knowledge in gas-phase HAT reactions. In this context, recent results presented in this thesis further emphasize the crucial role of spin density with respect to HAT reactivity; the focus of these studies concern the thermal activation of methane as the most inert of all hydrocarbons.

4.1 HAT in the gas phase: An introduction

Briefly, Mayer's conclusion is based on a Polanyi correlation, [335] *i.e.* a correlation between $log(k)$ and ΔH, for the reactions of a particular substrate with different oxidants including oxyl radicals with doublet spin states, an S = 5/2 iron (III) complex, antiferromagnetically coupled Mn dimers as well as diamagnetic (d^0) permanganate $[MnO_4]^-$, [327,330,336,337] and cleavage of the C−H bond is assumed as the rate determining step for all systems investigated. Further, Marcus theory - originally developed for electron transfer processes [338] - has been applied, and the Polanyi correlation has then been analyzed using self-exchange rate constants which have been measured for the individual systems to estimate the intrinsic barrier of the Marcus equation. Thus, this intrinsic barrier of the Marcus equation for a HAT reaction R′−*H* + R$^\bullet$ → R′$^\bullet$ + R−H can by determined by the barriers for the self-exchange reactions R−H + R$^\bullet$ → R$^\bullet$ + R−H and R′−*H* + R′$^\bullet$ → R′$^\bullet$ + R′−*H* having no thermodynamic driving force ($\Delta G = 0$), and it corresponds to the reorganization energies of the reactants to accept and donate the hydrogen atom, respectively. [327,337] The need to generate a so-called *prepared state* has already been discussed at great length in the analysis of many organic reactions using valence bond (VB) theory. [339] If the reacting substrate is not prepared for the bonding changes in the course of the reaction, higher activation barriers will result. Consequently, the smallest intrinsic barrier is expected for those reactants that do not need to rearrange to a substantial degree to accept or donate the hydrogen atom, respectively. This requirement is fulfilled for complexes with oxygen-centered radicals which already possess the ideal properties to accept H$^\bullet$, and are thus *prepared* to undergo efficient HAT reactions. Of course, with substrates having rather weak C−H bonds, HAT reactions by non-radical reactive sites might as well be possible; however, in these cases energy is nevertheless necessary to access a suitable electronic structure to form a bond to the incoming hydrogen atom. For example, it has been shown by detailed DFT calculations that an oxyl-radical character of the Mn=O group of a manganese-porphyrine complex is necessary for the efficient C−H bond cleavage; this requirement is not provided by the

unreactive singlet ground state.[256,340] Further, VB modeling for the reaction of CrO_2Cl_2 with alkanes in solution revealed that the bonding pair of the *closed-shell* reactant, *i.e.* two electrons of the Cr=O bond, must be decoupled prior to the reaction in order to exhibit HAT reactivity.[339] In fact, many observations gathered in the last decades in gas-phase (ion) chemistry support the conjecture of the importance of a radical site for the efficient, thermal activation of methane as the most inert and challenging substrate.[42,49,52–54,57] As verified by state-of-the-art quantum chemical calculations, all of the numerous examples of thermal HAT from methane observed in gas-phase experiments are achieved by metal or non-metal oxide species which possess a high spin density at an oxygen atom to which the hydrogen is transferred to; they include the previously discussed $[V_xP_{4-x}O_{10}]^{\bullet+}$ clusters (x = 0, 2 - 4), $[(Al_2O_3)_x]^{\bullet+}$ (x = 3 - 5),[137] $[FeO]^{\bullet+}$,[87] $[VAlO_4]^{\bullet+}$,[272] and many more. Furthermore, oxide species lacking this property are not reactive or only activate much weaker C−H bonds of *e.g.* higher alkanes or those at allylic, benzylic, or otherwise activated positions. A comparison of the cationic dioxides $[MO_2]^+$ (M = Ti, V, Zr, Nb) may serve as an instructive example.[341] The ionization of TiO_2 and ZrO_2 corresponds to the removal of an electron from the strong M=O double bond leaving an unpaired electron at the oxygen in cationic $[TiO_2]^{\bullet+}$ and $[ZrO_2]^{\bullet+}$; both dioxides are capable of HAT from methane at ambient conditions. In contrast, the *closed-shell* , singlet species $[VO_2]^+$ and $[NbO_2]^+$ are unreactive with regard to C−H bond activation of methane (Figure 4.2a). A similar reasoning holds true for $[MoO_x]^{\bullet+}$ (x = 2, 3);[342] while two strong Mo=O bonds (BDE = 542 kJ mol^{-1}) are present in $[MoO_2]^{\bullet+}$ with the additional electron being located at the metal, the bonding situation of $[MoO_3]^{\bullet+}$ allows the formation of only two Mo=O double bonds and one weak Mo−O$^{\bullet}$ bond (BDE = 257 kJ mol^{-1}). Accordingly, $[MoO_3]^{\bullet+}$ is capable of hydrogen-atom abstraction from methane, while $[MoO_2]^{\bullet+}$ is inert under these conditions (Figure 4.2b).[342] Also in comparative studies of polynuclear oxide species which are composed of the same elements with the only difference being the presence or absence of M−O$^{\bullet}$ radicals, the former exhibit a much higher reactivity towards methane; examples of aluminum-containing oxide clusters will be discussed in more detail further below.

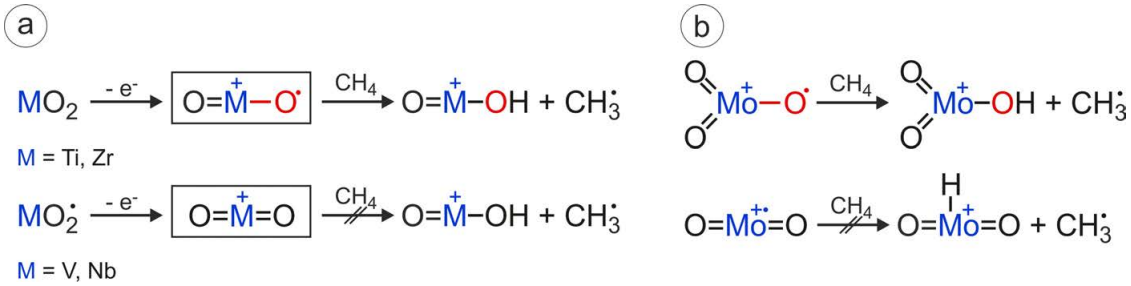

Figure 4.2: Schematic description of spin criteria for the selected examples a) $[MO_2]^+$ (M = Ti, V, Zr, Nb) and b) $[MoO_x]^{\bullet+}$ (x = 2, 3) in their reactions with methane.

4.1.1 Two mechanistic scenarios for HAT in the gas phase

Regarding mechanistic details of the HAT process, two variants of gas-phase hydrogen-atom abstraction by oxo-species are reported in the literature. The first one corresponds to a direct HAT pathway from the hydrocarbon to the abstracting oxygen atom; the alternative mode involves a metal-mediated activation step for which an empty coordination site at the metal atom is required. Numerous examples are known for either scenario, and details of the two variants are presented in the following.

The direct HAT process prevails predominantly for *open-shell* oxide clusters mostly with metal centers in relatively high oxidation states and with coordination numbers that prevent the indirect pathway to occur. Examples exhibiting this pattern include the non-metal system $[SO_2]^{\bullet+}$,[268] as well as the metal-containing clusters $[Ce_2O_4]^{\bullet+}$,[270] $[V_xP_{4-x}O_{10}]^{\bullet+}$ (x = 0, 2 - 4),[xviii] $[(Al_2O_3)_x]^{\bullet+}$ (x = 3 - 5),[137] $[VAlO_4]^{\bullet+}$,[272] or $[(V_2O_5)_x(SiO_2)_y]^{\bullet+}$ (x = 1, 2; y = 1 - 4).[140] The polynuclear oxide cluster $[V_4O_{10}]^{\bullet+}$ was studied at great length to reveal the mechanistic features of the direct HAT process.[265] It has been shown that the reaction proceeds barrier-free, without the formation of a long-lived encounter complex $[V_4O_{10}^{\bullet}\cdots CH_4]^+$, directly to the intermediate $[V_4O_9OH\cdots CH_3^{\bullet}]^+$; in the latter the methyl group is loosely coordinated to the hydrogen atom of the newly formed hydroxyl group. The rather exothermic reaction is completed by loss of the $CH_3^{\bullet}$ radical, resulting in the formation of $[V_4O_9(OH)]^+$. The absence of any barrier along the reaction pathway is consistent with the high reaction efficiency of 60 % relative to the collision rate (k = $5.5 \cdot 10^{-10}$ cm^3 s^{-1} molecule^{-1}).[265] Finally, HAT from the $[V_4O_{10}]^{\bullet+}/CH_2D_2$ couple is associated with a small intramolecular KIE of 1.35. In addition to the experimental results, detailed molecular dynamics (MD) simulations provide further evidence for a fast and barrier-free HAT pathway as depicted in Figure 4.3. According to the simulations, the potential energy decreases continuously in the first 450 fs due to the attractive forces between the incoming neutral methane and the ionic cluster; once more, no barrier has been located. Simultaneously, the O−H (red line) and V−C (green line) distances shrink steadily, while the C−H distance (blue line) slowly increases. After 450 fs, the system has lost ca. 102 kJ mol^{-1} of potential energy which is then channeled into the C−H and O−H stretching modes resulting in the oscillations of the hydrogen atom between the vanadyl oxygen and the methyl carbon atoms. Further, while the V−C distance decreases until t = 470 fs afterwards it slowly increases, thus indicating the beginning of the expulsion of the $CH_3^{\bullet}$ radical; this step is completed only after significantly longer simulation times.

The indirect, metal-mediated pathway is generally limited to small, mostly diatomic metal-oxides, such as $[MnO]^+$,[343] $[FeO]^{\bullet+}$,[87] $[MgO]^{\bullet+}$,[266] $[PbO]^{\bullet+}$,[269] $[SnO]^{\bullet+}$, or

[xviii] For details, see Chapter 3

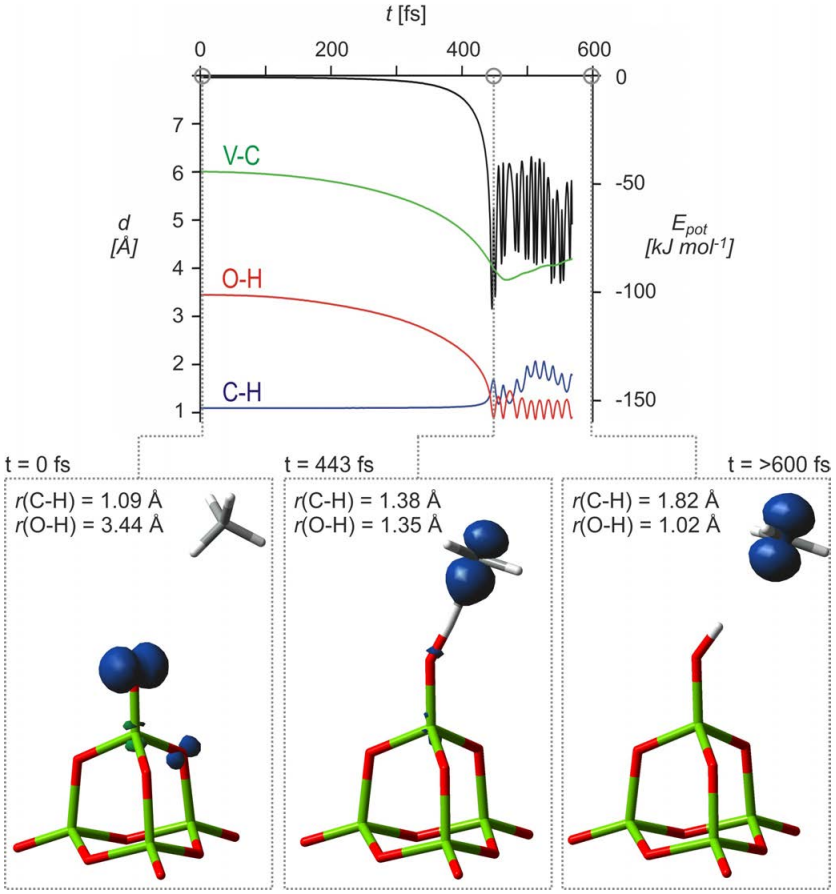

Figure 4.3: Evolution of the potential energy, bond lengths in the MD simulation and the relevant structures (green V, red O) for the thermal reaction of $[V_4O_{10}]^{\bullet+}$ with methane. The energy is shown in black and given in kJ mol^{-1}, d(C−H) in blue, d(O−H) in red, and d(V−C) in green. The fluctuations after 450 fs result from vibrational motions, mainly of the OH group. The blue isosurface indicates the spin density within the respective intermediate (adapted from Ref. [265]).

$[SnO]^{\bullet+}$.[271] These systems possess a vacant coordination site at the metal atom; thus, an encounter complex $[CH_4\cdots M{-}O^{\bullet}]^+$ and an intermediate $[CH_3^{\bullet}\cdots M{-}OH]^+$ are generated in the course of the reaction path. The $[MgO]^{\bullet+}/CH_4$ couple may serve as a good example without being further complicated by more complex reactivity scenarios, e.g. two-state reactivity[76,78–81,83],[xix] which matters for, e.g. $[FeO]^{\bullet+}$ or $[CuO]^+$; the simplified potential energy surface is shown in Figure 4.4. The initially generated adduct complex has gained enough internal energy for the hydrocarbon to migrate around the metal center towards the reactive oxo-site at which the C−H bond fission occurs. Subsequently, the newly-formed methyl group, in a metal-controlled fashion, returns back to the linear coordination thus forming the intermediate $[CH_3^{\bullet}\cdots Mg{-}OH]^+$; the latter represents a complex between a protonated magnesium-oxide unit and a loosely bound methyl radical which now carries more than 98 % of the spin. The overall exothermic reaction is completed by loss

[xix] For more details on two-state reactivity, see Chapter 4.2.2

of a $CH_3^\bullet$ radical from this intermediate. While the alternative rebound mechanism to generate methanol is thermochemically even more favorable than HAT, it is kinetically and entropically less attractive.

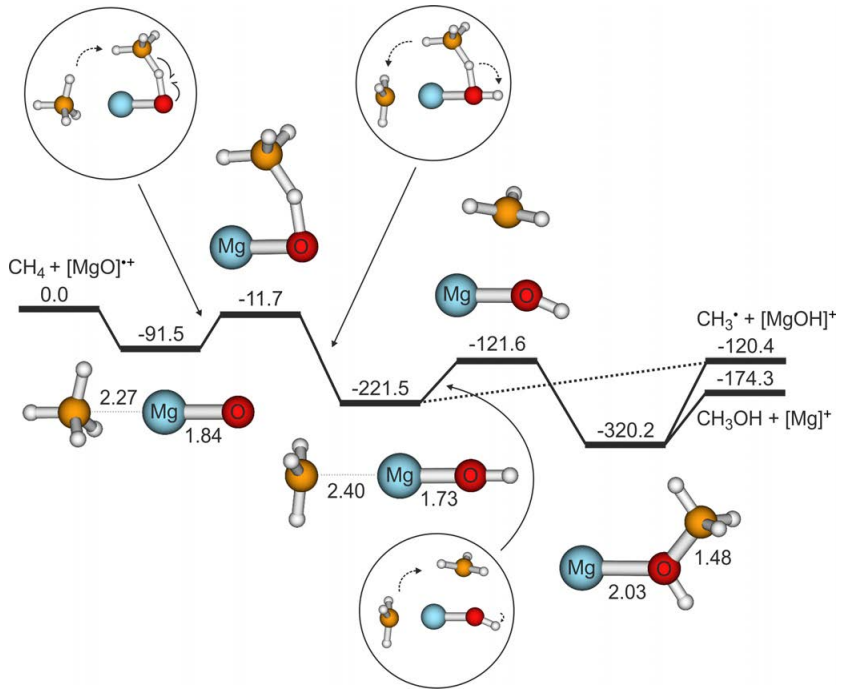

Figure 4.4: Potential-energy surface (in kJ mol^{-1}) for the reaction of $[MgO]^{\bullet+}$ with CH_4 calculated at the MP2/6-311+G(2d,2p) level of theory; selected bond lengths are given in Å. The encircled structures depict the rearrangements occurring along the reaction coordinate (adapted from Ref. [266]).

Contrary to the direct hydrogen-atom abstraction from CH_4 which is generally characterized by rather small KIEs, metal-mediated homolytic C−H bond cleavages exhibit larger KIEs, typically >2.0. Further, it has been noted that there exists, for a given reaction type, a relationship between the size of the KIEs and the overall rate coefficients of the hydrogen-atom abstraction from methane.[151] For example, the intermolecular KIEs, derived from the reactions of various diatomic $[MO]^{\bullet+}$ with CH_4 and CD_4, increase from about 1.3 for $[MgO]^{\bullet+}$, via 2.1 and 2.4 for $[CaO]^{\bullet+}$ and $[SrO]^{\bullet+}$, respectively, to 3.2 for $[BaO]^{\bullet+}$.[151,344] This trend of increasing KIEs is paralleled with a decrease of the overall rate coefficients for the activation of methane, from $3.9 \cdot 10^{-10}$ cm^3 s^{-1} $molecule^{-1}$ for $[MgO]^{\bullet+}$ and $2.9 \cdot 10^{-10}$ for $[CaO]^{\bullet+}$ to $9.8 \cdot 10^{-11}$ and $1.1 \cdot 10^{-11}$ for $[SrO]^{\bullet+}$ and $[BaO]^{\bullet+}$, respectively, thus reflecting an increasingly late TS and thereby an increasing KIE. With regard to catalysis, this observation implies that the less reactive oxidants exhibit higher selectivities in terms of the associated KIEs, apparently in line with the time-honored Bell-Evans-Polanyi principle.[335,345,346]

4.2 *Open-shell* vs. *closed-shell* systems and the role of the spin state

4.2.1 Activation of methane by aluminum-oxide clusters

The propably most compelling arguments for the importance of spin for hydrogen-atom transfer in gas-phase HAT processes are provided by the reactions of various aluminum-oxide clusters with methane mentioned above; some of these main-group metal clusters are indeed capable to bring about efficient C−H bond scission of methane at room temperature. [137] However, only those clusters having an *even* number of aluminum atoms $[(Al_2O_3)_x]^{\bullet+}$ (x = 3 - 5) are reactive, *e.g.* $[Al_8O_{12}]^{\bullet+}$, given in Equation 4.1, while clusters with an *odd* number of aluminum atoms do not react with CH_4, *e.g.* $[Al_7O_{11}]^+$, Equation 4.2.

$$[Al_8O_{12}]^{\bullet+} + CH_4 \longrightarrow [Al_8O_{11}(OH)]^+ + CH_3^{\bullet} \quad (4.1)$$

$$[Al_7O_{11}]^+ + CH_4 \not\longrightarrow [Al_7O_{10}(OH)]^{\bullet+} + CH_3^{\bullet} \quad (4.2)$$

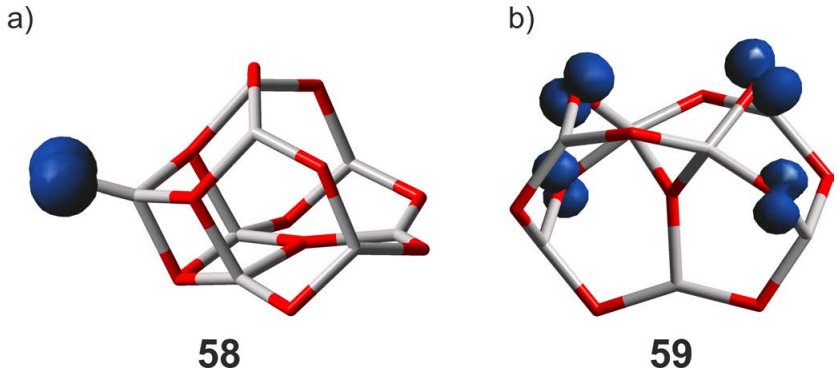

Figure 4.5: Lowest-lying doublet ground-state of a) $[Al_8O_{12}]^{\bullet+}$ (**58**) and b) triplet ground-state of $[Al_7O_{11}]^+$ (**59**), derived from DFT/UB3LYP calculations (gray Al, red O). The spin density is indicated by the blue isosurface.

One of the crucial differences between these two systems concerns the distribution of the spin within the respective cluster. While in the doublet ground-state of $[Al_8O_{12}]^{\bullet+}$ the spin is exclusively localized at one terminal oxygen atom, thus representing an oxygen-centered radical, in the triplet ground-state of $[Al_7O_{11}]^+$ the unpaired electrons are distributed among four oxygen atoms, each one carrying approximately 0.5 units of the spin, respectively (Figure 4.5). Thus, this cluster is lacking an unpaired electron localized at one oxygen atom, and its non-reactivity underlines once more the importance of oxygen-centered radicals to bring about thermal hydrogen-atom abstraction from methane.

With regard to the reaction mechanism, the reaction of $[Al_8O_{12}]^{\bullet+}$ with CH_4 (Figure 4.6a) follows a slightly differing direct HAT pathway. Methane coordinates to the cluster **58** via

the terminal oxygen atom, thus forming the encounter complex **60**. In the following, the reaction proceeds via transition structure **TS60-61** in a quasi barrier-free process to generate intermediate **61** which corresponds to a classical intermediate for the direct HAT process. Dissociation of the product fragments leads finally to the generation of the ionic cluster product **62**, *i.e.* $[Al_8O_{11}(OH)]^+$, and a methyl radical $CH_3^\bullet$. In contrast, in the reaction of $[Al_7O_{11}]^+$ (**59**) with CH_4 (Figure 4.6b), a significantly more stable adduct complex **63** is generated in the first step via coordination of the organic substrate to the vacant site of an aluminum atom. Next, from **63**, HAT can only proceed via the energetically demanding transition state **TS63-64** to form **64**. Again, liberation of the methyl radical $CH_3^\bullet$ from the *open-shell* cluster cation $[Al_7O_{10}(OH)]^{\bullet+}$ **64** completes the reaction, to generate **65**.

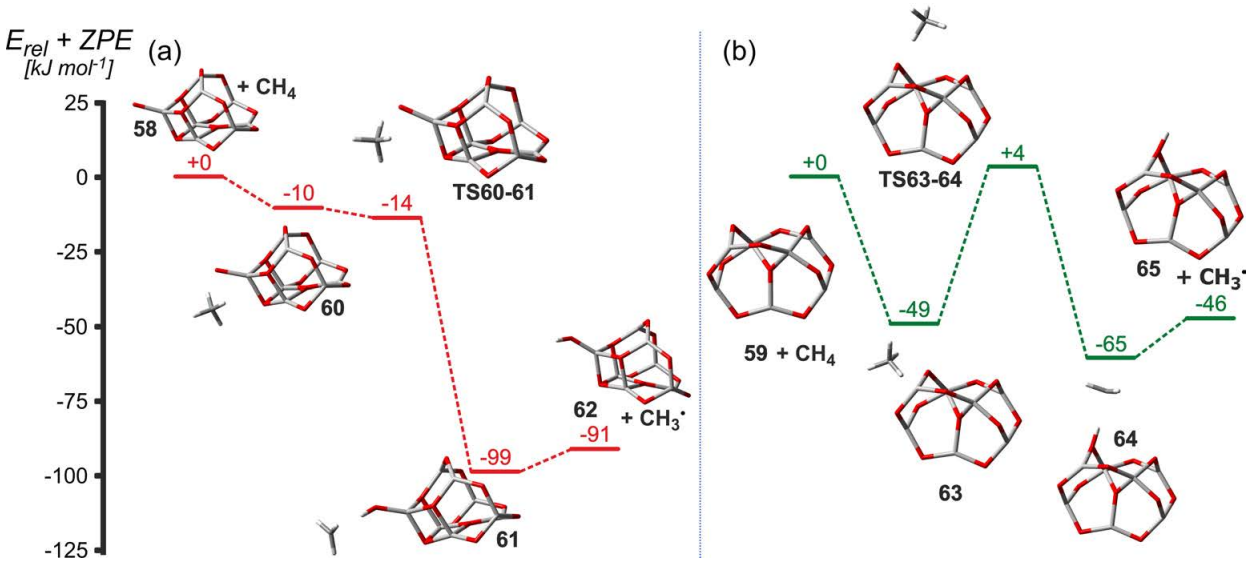

Figure 4.6: Potential energy surfaces for the reactions of $[Al_8O_{12}]^{\bullet+}$ (a) and $[Al_7O_{11}]^+$ (b) with CH_4 and the associated structures of the intermediates and transition structures, at the UB3LYP/TZVP level of theory. Relative energies, corrected for zero-point energy contributions, are given in kJ mol^{-1}(PES in (a) is adapted from Ref. [137]).

A further comparison of these two PESs is quite revealing: First, both reactions are exothermic and therefore thermochemically allowed. Not entirely unexpected, HAT to the terminal oxygen atom of $[Al_8O_{12}]^{\bullet+}$ is energetically favored by ca. 45 kJ mol^{-1} as compared with the couple $[Al_7O_{11}]^+/CH_4$; nevertheless, HAT to a bridging oxygen-atom to $[Al_7O_{11}]^+$ is also energetically feasible and significantly exothermic. Second, and more importantly, although both HAT processes are exothermic, the kinetic barriers differ strongly. In the doublet $[Al_8O_{12}]^{\bullet+}/CH_4$ system, the initial interaction between the oxygen-centered radical in the cluster and the C−H bond of methane enables a barrier-free C−H bond scission; in contrast, HAT to an oxygen atom of $[Al_7O_{11}]^+$ is not kinetically favored. Thus, the heights of the two intrinsic barriers **TS60-61** and **TS63-64** for HAT starting from the intermediates **60** and **63**, respectively, are negligible only for the $[Al_8O_{12}]^{\bullet+}/CH_4$ system but substantial for

the $[Al_7O_{11}]^+/CH_4$ couple. The significantly lower spin density at a particular oxygen atom of the latter oxide, as well as the fact that the reactive site constitutes a bridging oxygen-atom, increase the activation barrier for the C−H bond cleavage such that the respective transition state **TS63-64** is higher in energy than the entrance channel and therefore not accessible in a thermal ion/molecule reaction as observed experimentally in the gas phase.

Similar observations have been made for the reactivity of the main-group $[(MgO)_x]^{\bullet+}$ (x = 1 - 7) clusters towards methane and other small hydrocarbons; while $[MgO]^{\bullet+}$ brings about HAT from CH_4, the larger clusters are completely inert towards methane, even though the reactions are exothermic. [266] For example, in $[(MgO)_2]^{\bullet+}$ the spin is equally distributed over the two oxygen atoms of the cluster; intra-cluster spin density transfer and the associated kinetic barrier for the C−H bond activation of methane are too high in energy to be accessible under thermal conditions, resulting in a barrier of 20 kJ mol^{-1} above the entrance channel. Further, the $[(MgO)_7]^{\bullet+}$ cluster is the only species among the larger magnesium-oxide cations $[MgO]_x^{\bullet+}$ (x = 2 - 7) investigated in which the radical is located at only one of the bridging oxygen atoms; compared to the other magnesium-oxide clusters, $[(MgO)_7]^{\bullet+}$ has to overcome the lowest computed barrier in the reaction with methane which is reduced to -0.5 kJ mol^{-1} including the zero-point energy correction. [347] Thus, although bridging oxygen atoms are not as reactive as terminal oxygen-atoms, the presence of spin density also counts in these systems. For example, HAT reactions mediated by $[(MgO)_2]^{\bullet+}$ are only observed with those substrates that possess C−H bonds which are much weaker compared to the one of methane, e.g. propane or butane, [266] while the silver-oxide cluster $[Ag_2O]^{\bullet+}$, carrying a truly oxygen-centered radical at the bridging oxygen atom, enables the efficient activation of ethane at ambient conditions. [267] Additional spectroscopic and reactivity studies on larger $[(MgO)_x]^{\bullet+}$ cluster (x = 2 - 7) support these findings. [142]

4.2.2 Diatomic $[CuO]^+$ and its role in the spin-selective hydrogen- and oxygen-atom transfers in the thermal activation of methane

With respect to the activation of methane and its subsequent conversion into more valuable feedstocks at ambient conditions, hydrogen-atom transfer is not only important for the oxidative coupling of methane (OCM) to the C_2-hydrocarbons ethane and ethylene using metal-oxide based catalysts in heterogeneous catalysis, it also plays a significant role in the selective oxidation of methane to methanol, which is catalyzed in nature by the metalloenzymes methane monoxygenases (MMOs). [348–350] Soluble MMO (sMMO) contains a well-characterized doubly oxygen-bridged di-iron cluster; in contrast, the reactivity of particulate MMO (pMMO), after a long controversy about the nature of its active site, has been shown to depend on copper. [351,352]

Thus, with respect to this biological relevance, it was demonstrated already twenty years ago that bare $[FeO]^{\bullet+}$ is capable to activate methane at room temperature. [87] The by

now well-established concept of two-state reactivity (TSR),[76–85] which proved important also in the context of describing the mechanisms of metalloenzyme-mediated reactions, is in fact based on a detailed analysis of the gas-phase reactions of this simple, diatomic reagent $[FeO]^{\bullet+}$. Yet, only recently a complete description of the gas-phase conversion of methane to methanol by $[FeO]^{\bullet+}$ has been achieved; this has been based on advanced gas-phase spectroscopy combined with rather high-level calculations.[95] Further, while the detailed nature of the active copper-oxide species in pMMO had been under debate for quite some time,[348–357] bare $[CuO]^+$ was predicted already a decade ago to be a suitable, if not extremely powerful candidate to mediate the methane/methanol conversion.[358][xx] However, no gas-phase experiments with bare $[CuO]^+$ have been reported so far. The ligated cation $[Cu(O)(phen)]^+$ (*phen* = 1.10-phenanthroline) brings about activation of small hydrocarbons, *i.e.* propane or butane, but it is not powerful enough to attack the thermodynamically strong and kinetically inert C−H bond of methane.[362] The general problem with the generation of bare $[CuO]^+$ is the relatively small dissociation energy $D_0(Cu^+{-}O)$ = 130 kJ mol^{-1};[42,363,364] in a more recent investigation, using multi-reference theory, $D_0(Cu^+{-}O)$ = 106 kJ mol^{-1} was even suggested as the more accurate value.[365,366] Thus, it proved rather difficult to produce sufficient amounts of $[CuO]^+$ to probe its reactivity in bond-activation processes, and various attempts to generate this cationic metal oxide by *e.g.* electrospray ionization mass spectrometry failed;[53,362] thus, for a long time $[CuO]^+$ was the only bare transition-metal oxide cation of the first row whose reactivity towards methane had not been experimentally investigated.

Its generation in sufficient yields was finally achieved by laser desorption/ionization from isotopically pure copper ^{63}Cu targets, suitable for the laser-vaporization/ionization source of an FT-ICR mass spectrometer in the presence of a He/N_2O plasma.[xxi] As shown in Figure 4.7, $[CuO]^+$ brings about efficient activation of methane at room temperature, Equation 4.3 and 4.4. Further, the *open-shell* product cation $[CuOH]^{\bullet+}$ itself also homolytically cleaves the C−H bond from a second methane molecule, thus giving rise to the formation of a *closed-shell* water complex (Equation 4.5). The latter reaction was verified by the reaction of $[CuO]^+$ with a mixture of CH_4/CD_4 in which the formation of $[Cu(OHD)]^+$ clearly proves the occurrence of a secondary reaction, and this is further supported by theory;[367] moreover, it exclusively affects the branching ratio of the hydrogen-atom abstraction channel.

[xx] For the role of CuO-doped zeolites in the context of methane activation, see [359–361].

[xxi] Again, the generation is highly sensitive to the experimental parameters; *e.g.* initially, the ion of interest was generated with an He/N_2O ratio of approximately 5:1, while after replacement of the pulse valve, $[CuO]^+$ could only be generated in weaker yields and only by a drastically changed ratio of the carrier gas, amounting to approximately 100:1.

$$[CuO]^+ + CH_4 \longrightarrow [CuOH]^{\bullet+} + CH_3^{\bullet} \quad (40\%) \tag{4.3}$$

$$[CuO]^+ + CH_4 \longrightarrow [Cu]^+ + CH_3OH \quad (60\%) \tag{4.4}$$

$$[CuOH]^{\bullet+} + CH_4 \longrightarrow [Cu(OH_2)]^+ + CH_3^{\bullet} \tag{4.5}$$

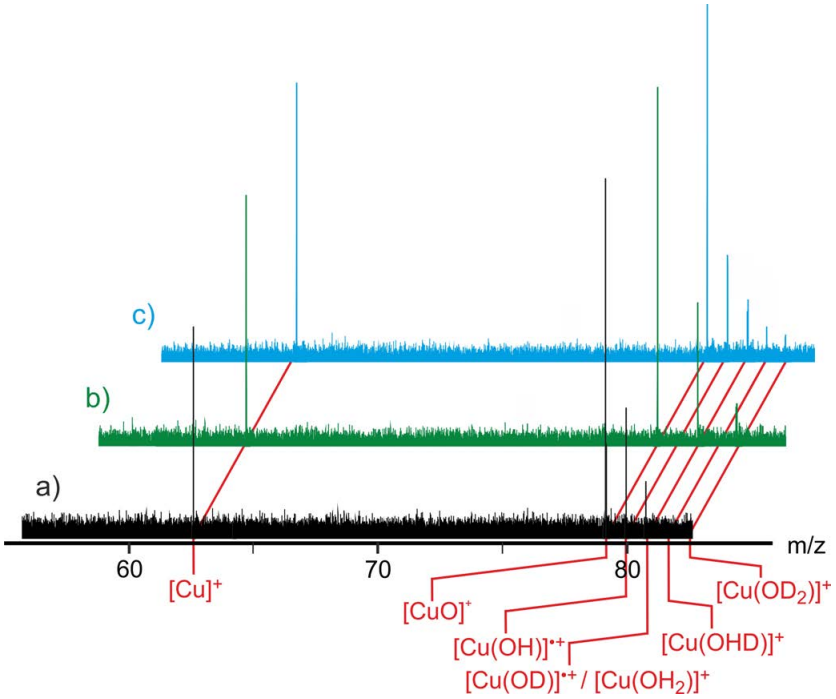

Figure 4.7: Ion/molecule reactions of mass-selected $[CuO]^+$ with a) CH_4, b) CD_4, and c) CH_2D_2.

From a kinetic analysis, a rate coefficient of $k = 5.3 \cdot 10^{-10}$ cm^3 s^{-1} molecule^{-1} was derived; this corresponds to an overall efficiency of 51 %, *i.e.* 20 % for reaction 4.3 and 31 % for reaction 4.4, respectively. Based on labeling experiments with CH_2D_2, an intramolecular KIE of 2.6 has been obtained for the hydrogen-abstraction process. For the hydrogen abstraction in the related $[FeO]^{\bullet+}/CH_4$ system, an efficiency of 11 % and a KIE of 4.6 have been reported. [87] As discussed by Schröder *et al.* [368] and mentioned above, decreasing KIEs are often associated with increasing reaction efficiencies for a given type of reaction, *i.e.* the hydrogen-atom abstraction from methane. Moreover and quite remarkably, the two metal-oxides that bring about HAT as well as OAT in the thermal ion/molecule reaction with methane, *i.e.* $[FeO]^{\bullet+}$ and $[CuO]^+$, are composed of the same metals that are also responsible for the biological oxidation of methane to methanol by the two different MMOs. Thus, there is a beautiful agreement between the gas-phase chemistry of these systems with observation in biological chemistry, which is quite remarkable in terms of modeling these rather complex, *real-life* metalloenzymes.

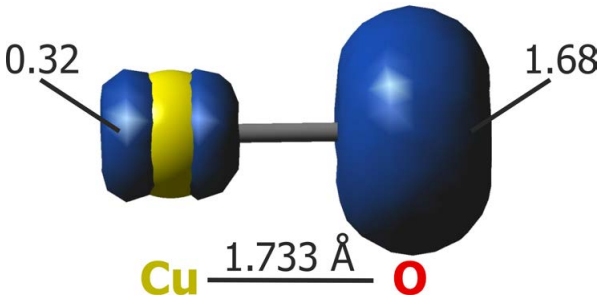

Figure 4.8: Triplet ground-state of $[CuO]^+$. The spin density is given in numbers and indicated by the blue isosurface.

For the copper system, further mechanistic insights into the details of the reaction are provided by quantum-chemical calculations. A DFT study of reactions 4.3 and 4.4 using the B3LYP functional is already known from the literature; [358] however, the high-spin/low-spin splitting of $[Cu]^+$ reported in this study (156 kJ mol^{-1}) is largely underestimated, compared to the experimental value of 271 kJ mol^{-1}. [369] A much better value of 281 kJ mol^{-1} has been obtained in a different context using also the B3LYP functional but different basis sets; [370] thus, a recalculation of the PES of the reaction $[CuO]^+ + CH_4$ was performed in the hope to provide an improved picture of the reaction mechanism, including more reliable energetic values. However, calculations with the otherwise accurate CCSD(T) method employing moderately sized basis sets are not suited for the $[CuO]^+/CH_4$ system. Thus, we employed the complete basis set procedure CBS-QB3 to study the reactivity of $[CuO]^+$ towards methane, which implies predominantly calculations on the Möller-Plesset perturbation level of theory.

With respect to the electronic structure, the high-spin, O_2-like state (triplet) corresponds to the ground state of $[CuO]^+$, as has been found also for other late transition-metal oxides; [42,53,358] the bonding situation in $[MO]^+$ (M = late 3d metal) has been described earlier in analogy to the dioxygen molecule having a biradicaloid π bonding. [76,371,372] This holds true also for $[CuO]^+$ with degenerate singly-occupied π orbitals which correspond to the antibonding π^* of $[CuO]^+$. However, these orbitals possess a relatively strong character of the $2p_\pi$ orbital of oxygen, thus resulting in a spin density of 1.68 at oxygen and of only 0.32 at copper (Figure 4.8). In other words, cationic copper-oxide can be regarded as $[Cu^{II}-O^\bullet]^+$, rather than the formally higher oxidized Cu^{III} species $[Cu^{III}-O]^+$.[xxii]

Both reaction profiles and the respective structures for the triplet and the singlet PES are given in Figure 4.9, respectively. With respect to the high-spin/low-spin splitting of $[CuO]^+$ (**66**) single-reference methods are reliable to describe properly the electronic structure of the triplet state of $[CuO]^+$ (^{3}**66**). [366] In contrast, multi-reference methods might be necessary to provide a more realistic picture of the singlet states. A $\langle S^2 \rangle$ value of approximately 1.0 has been calculated for the *open-shell* $^1\Delta$ state of $[CuO]^+$ which is 60 kJ mol^{-1} lower in energy

[xxii] For solution-phase studies on the electronic state of active copper centers, see [357,373–375].

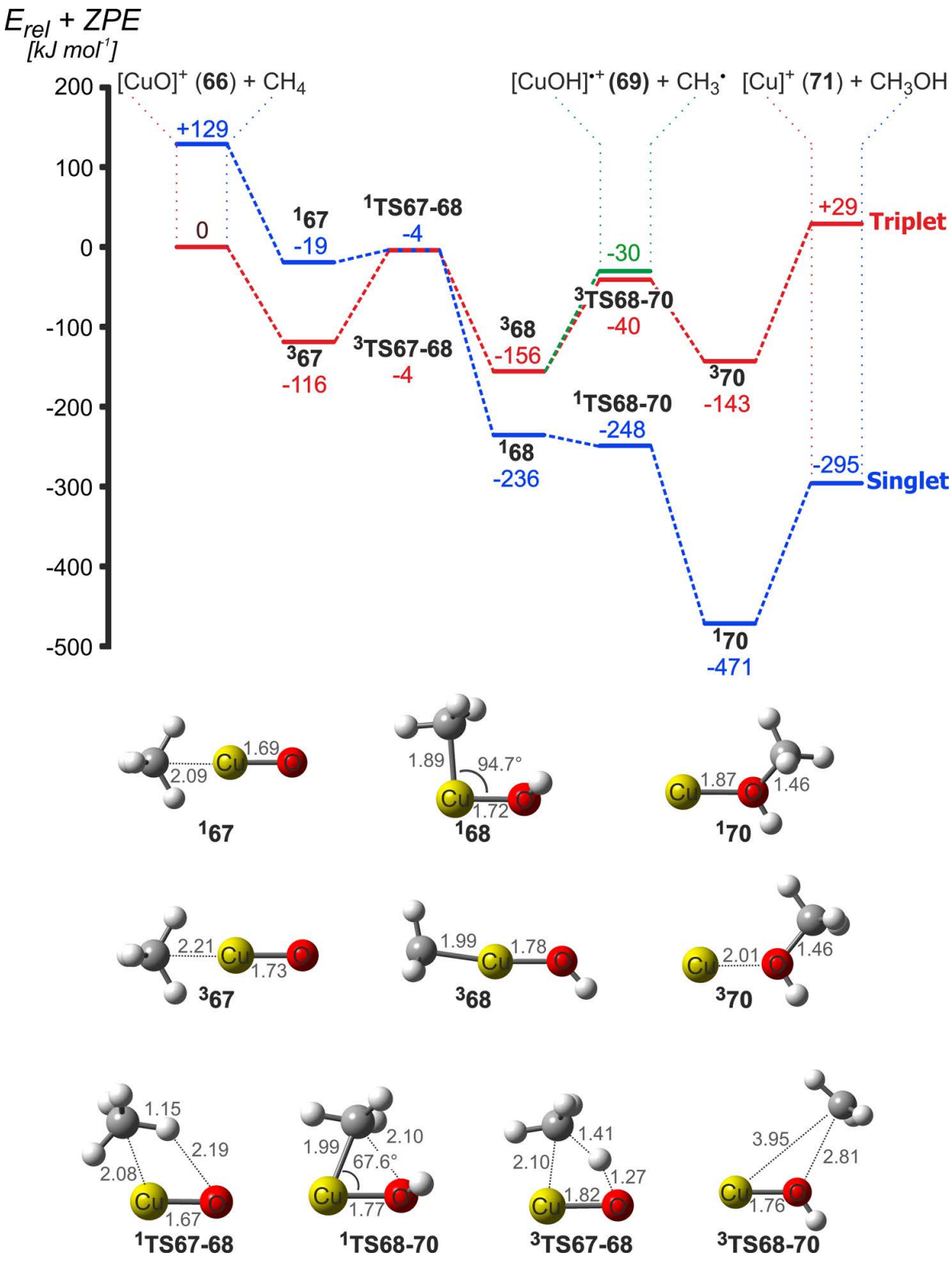

Figure 4.9: PES for the reaction of $[CuO]^+$ with CH_4 (blue = singlet, red = triplet) and the associated structures of the intermediates and transition structures, calculated at the CBS-QB3 level of theory. Relative energies, corrected for zero-point energy contributions are given in kJ mol^{-1} and relevant bond lengths in Å.

compared to the *closed-shell* singlet $^1\sum$ state of $[CuO]^+$. Thus, the energies of ^{1}**66** as well as the initial encounter-complex ^{1}**67** are most likely overestimated. Nevertheless, the triplet state of $[CuO]^+$ was clearly proven to be the ground state and is therefore assumed to be the only state species generated in the mass spectrometer under thermal conditions.

With respect to the reaction of $[CuO]^+$ with methane, this process can be classified in terms of an indirect HAT pathway: After coordination of the carbon atom to the copper-site of the ground-state cation to form the adduct complex ^{3}**67**, the reactions proceeds via **TS67-68**, delivering the hydrocarbon atom to the oxygen where C−H bond activation occurs, thus resulting in the formation of an O−H bond, and pulling back the methyl ligand to form ^{3}**68**. Next, the methyl group can either be liberated to give the spin-allowed HAT product **69**, or in a rebound-step is transferred to the oxygen atom, leading to the formation of $^3[Cu(CH_3OH)]^+$ (^{3}**70**); however, formation of free CH_3OH in a spin-allowed process ^{3}**70** $\rightarrow$ $^3[Cu]^+$ (^{3}**71**) + CH_3OH is endothermic by 29 kJ mol^{-1}. Rather, formation of CH_3OH requires an intersystem crossing (ISC) to the singlet surface, because only this path has an exothermicity of 295 kJ mol^{-1}; thus, a TSR scenario is indeed involved in the formation of methanol and $[Cu]^+$ as has been found for the $[FeO]^{\bullet+}/CH_4$ system. Since the two geometrically quite different transition structures ^{1,3}**TS67-68** are almost isoenergetic, the ISC to the singlet-surface occurs either closely before or directly after passing through **TS67-68**. Interestingly, the rate-determining step for both pathways corresponds to the initial cleavage of the inert C−H bond of methane for which the spin density at the abstracting atom is crucial, while for the oxygen-atom transfer to form methanol in a rebound-step, a spin-flip to the singlet is essential in the course of the reaction. A minimal-energy crossing point [75,376,377] has not been located in this study; however, the remarkable branching ratio of 60 % for the formation of methanol in the experiment indicates a rather efficient ISC at the crossing seam of the two PESs.

4.2.3 Comparison of $[CO]^{\bullet+}$ and $[SiO]^{\bullet+}$ in their reactions with methane

As shown in previous studies, group 14 metal-oxide cations $[MO]^+$ (M = Ge, Sn, Pb) are excellent reagents of HAT reactivity towards methane. [269,271] Further, in the context of interstellar chemistry, also the reactivity of cationic carbon monoxide $[CO]^{\bullet+}$ towards CH_4 was studied quite some time ago by the groups of Smith and Anicich. In addition to electron transfer (61 %) and $H^\bullet$ expulsion (4 %), $[CO]^{\bullet+}$ was shown to bring about hydrogen-atom transfer (35 %) in the reaction with methane under thermal conditions; [378,379] however, mechanistic details have not been addressed in this experimental study. Also silicon oxide species are relevant in the chemistry of interstellar clouds as well as of the Earth's upper atmosphere, [380–384] and HAT has also been observed for isosteric $[SiO]^{\bullet+}$ in the reaction with H_2 (and D_2). [385] Thus, it deems of interest to further probe the reactivities of $[CO]^{\bullet+}$ and $[SiO]^{\bullet+}$ towards methane, aiming to uncover the underlying reaction mechanisms of these non-metallic systems.

Contrary to the previous ICR-studies described in this thesis, the FT-ICR experiments with $[CO]^{\bullet+}$ were performed with the help of Prof. de Petris and Dr. Angelini in Rome, using an EXTREL FTMS 2001 double-cell mass spectrometer (for more details, see Appendix B). Briefly, CO was admitted into the „source cell" at a pressure of $2.9 \cdot 10^{-7}$ mbar, and $[CO]^{\bullet+}$ ions were generated upon electron impact. Then, the $[CO]^{\bullet+}$ ions were isolated and transferred into the „analyzer cell" containing CH_4 (or CD_4, CH_2D_2). These gases were admitted into the analyzer cell at stationary pressures ranging from 3.2 to $8.7 \cdot 10^{-8}$ mbar. Thus, in line with the previous findings on the $[CO]^{\bullet+}/CH_4$ system using the SIFT technique,[386] the present FT-ICR experiments demonstrate that thermalized $[CO]^{\bullet+}$ ions react with CH_4 to give rise to the following primary products (Equations 4.6 - 4.8). For the sake of clarity, the HAT product in the reaction of $[CO]^{\bullet+}$ with CH_4 (Equation 4.7) will be denoted in the upcoming discussion as $[HCO]^+$, even though based on calculations, the formation of the isomer $[COH]^+$ is also thermochemically feasible.

$$[CO]^{\bullet+} + CH_4 \longrightarrow [CH_4]^{\bullet+} + CO \quad (4.6)$$

$$[CO]^{\bullet+} + CH_4 \longrightarrow [HCO]^+ + CH_3^{\bullet} \quad (4.7)$$

$$[CO]^{\bullet+} + CH_4 \longrightarrow [CH_3CO]^+ + H^{\bullet} \quad (4.8)$$

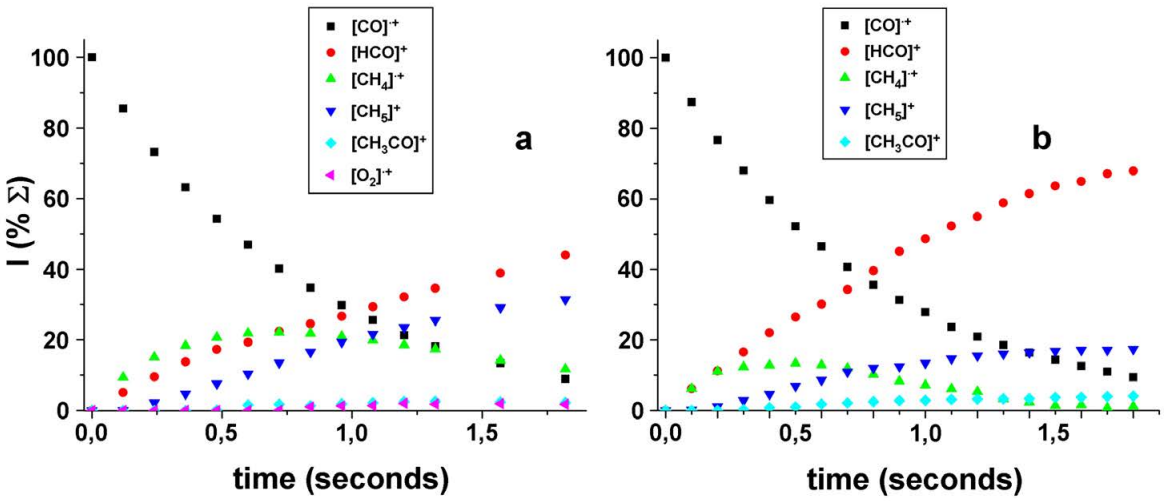

Figure 4.10: Time dependence for the product distribution in the reaction of thermalized $[CO]^{\bullet+}$ with CH_4 ($p(CH_4) = 5.3 \cdot 10^{-8}$ mbar; $p_{source}(CO)$: (a) $p = 2.9 \cdot 10^{-7}$, (b) $p = 5.3 \cdot 10^{-7}$.

With respect to thermochemistry, the exothermicities amount to $\Delta_r H° = -135.0$ kJ mol^{-1} for reaction 4.6, $\Delta_r H° = -186.4$ kJ mol^{-1} for reaction 4.7, and $\Delta_r H° = -284.2.0$ kJ mol^{-1} for reaction 4.8, respectively. However, the branching ratios of reactions 4.6 - 4.8 depend on the CO pressures in the ion source ($p_{source}(CO)$), Figure 4.10. This effect is due to the diffusion of neutral CO into the reaction cell followed by ion/molecule reactions with the primary and

secondary product ions $[CH_4]^{\bullet+}$ and $[CH_5]^+$ to generate $[HCO]^+$, Equations 4.9 and 4.11. The product ion $[CH_5]^+$ is generated in a secondary reaction of $[CH_4]^{\bullet+}$ with CH_4, Equation 4.10, and reacts in turn also with CH_4 according to Equation 4.12. Thus, as these subsequent ion/molecule reactions occur with an ill-defined mixture of CH_4 and CO, an unambiguous determination of the primary branching ratio of reactions 4.6 - 4.8 renders difficult. To resolve these problems various control experiments were conducted.

$$[CH_4]^{\bullet+} + CO \longrightarrow [HCO]^+ + CH_3^{\bullet} \quad (4.9)$$

$$[CH_4]^{\bullet+} + CH_4 \longrightarrow [CH_5]^+ + CH_3^{\bullet} \quad (4.10)$$

$$[CH_5]^+ + CO \longrightarrow [HCO]^+ + CH_4 \quad (4.11)$$

$$[CH_5]^+ + CH_4 \longrightarrow [C_2H_5]^+ + 2H_2 \quad (4.12)$$

First, independent experiments under the same conditions were performed by isolating the $[CH_4]^{\bullet+}$ ion after its formation via reaction 4.6; the products generated are $[CH_5]^+$, $[HCO]^+$, and $[C_2H_5]^+$ with the latter only being observed at the lowest CO pressure investigated (p_{source}(CO) $\approx 10^{-7}$ mbar). Different from earlier reports,[386] $[CH_3CO]^+$ is not generated in the reaction of $[CH_4]^{\bullet+}$ with CO; thus, formation of $[CH_3CO]^+$ can be traced back exclusively to Equation 4.8. Finally, rather small amounts of $[O_2]^{\bullet+}$ are formed by charge transfer from $[CH_4]^{\bullet+}$ to the O_2 background; this indicates also that the low $[O_2]^{\bullet+}$ intensity (< 1.5 %) occasionally observed in the reaction of thermalized $[CO]^{\bullet+}$ ions with CH_4 is due to the secondary reaction of the product ion $[CH_4]^{\bullet+}$ with O_2 (see Figure 4.10a). At the lowest CO pressure that still provides sufficient signal intensity, the diffusion of CO from the source to the reaction cell is minimized though not completely suppressed. Therefore, in order to obtain an accurate branching ratio, the $[HCO]^+$ and $[CH_4]^{\bullet+}$ intensities have been corrected as described in the following; the experimental conditions chosen (p_{source}(CO) = 2.9 $\cdot 10^{-7}$ mbar) represent the best compromise between a sufficient intensity of $[CO]^{\bullet+}$ and a minimum of unwanted side reactions.

Since the product ions $[CH_5]^+$ and $[C_2H_5]^+$ are exclusively generated in consecutive reactions of $[CH_4]^{\bullet+}$, their intensities are directly linked to the formation of the latter in Equation 4.6 and can simply be added to its intensity. In contrast, $[HCO]^+$ is formed in the primary reaction 4.7 as well as in secondary and higher-order reactions, including Equations 4.9 and 4.11, respectively, as well as self-protonation. Thus, the fractions of $[HCO]^+$ formed in these three reactions have to be evaluated to determine a proper branching ratio. To this end, experiments with a CO/^{13}CO mixture (1:1) have been performed; here, the $[CO]^{\bullet+}$ ion at m/z 28 is isolated and reacted with methane; the resulting $[CH_4]^{\bullet+}$ product ion subsequently reacts with both CO and ^{13}CO diffusing from the ion source into the ICR cell. While reaction 4.7 gives only rise to the formation of $[HCO]^+$ (m/z 29), reactions 4.9 and 4.11 bring about the formation of both $[HCO]^+$ and $[H^{13}CO]^+$ (m/z 30), respectively. The intensity of the $[H^{13}CO]^+$

ions thus equals the contribution of these secondary reactions; subtracting them from the total intensity of the $[HCO]^+$ ions then determines the amount of those $[HCO]^+$ ions which are exclusively formed by reaction 4.7. The so-obtained branching ratio amounts to $[CH_4]^{\bullet+}$ = 62 %, $[HCO]^+$ = 36 %, $[CH_3CO]^+$ = 2 %. However, a possible drawback of this protocol arises from self-protonation of ^{13}CO by the $[HCO]^+$ ions formed initially in reaction 4.7, thus possibly overestimating this correction. The results obtained by a second, independent procedure, however, indicate that the contribution of this self-protonation is negligible (see below). Likewise, $[^{13}CO]^{\bullet+}$ ions, formed by charge exchange, are not formed in appreciable abundance at the detection limit.

In the second correction procedure, CO and CH_4 are introduced as before in the ion source and analyzer cell, respectively. Under identical conditions, the reaction between $[CO]^{\bullet+}$ and CH_4 is performed while continuously ejecting the $[CH_4]^{\bullet+}$ product ion in a double-resonance experiment.[387] The difference in the intensity of $[HCO]^+$ ions generated in the double-resonance experiment and in the unperturbed experiment as well as the intensities of the $[CH_5]^+$ and $[O_2]^{\bullet+}$ ions are then assigned to reaction 4.6 (Figure 4.11); the intensity of $[HCO]^+$, derived from the double-resonance experiment, can then be assigned to reaction 4.7. The so-obtained results amount to $[CH_4]^{\bullet+}$ = 63 %, $[HCO]^+$ = 34 %, and $[CH_3CO]^+$ = 3 % (Figure 4.11), in very good agreement with the branching ratio obtained by the experiments using a $CO/^{13}CO$ mixture (See also C, Figures C.8 and C.9).

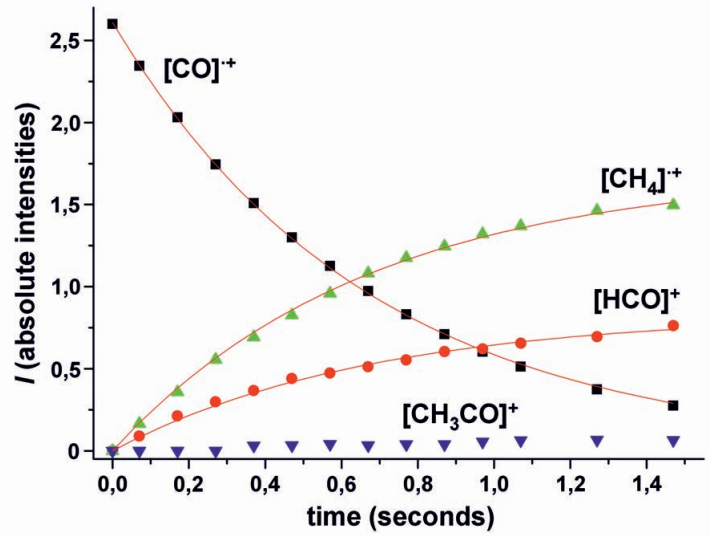

Figure 4.11: Kinetic plots and best-fit lines for the reaction between $[CO]^{\bullet+}$ and CH_4 ($p_{source}(CO) = 2.9 \cdot 10^{-7}$ mbar; $p(CH_4) = 6.3 \cdot 10^{-8}$ mbar). The $[HCO]^+$ profile has been recorded by continuous ejection of the $[CH_4]^{\bullet+}$ ion. The intensities are normalized with respect to the absolute intensity of the parent ion.

Finally, based on labeling experiments with CH_2D_2, an intramolecular KIE of 1.2 has been derived for the hydrogen-atom abstraction; for the hydrogen-atom expulsion, Equation 4.8, the KIE amounts to 1.1. The measured rate constant of the reaction between $[CO]^{\bullet+}$ and CH_4

amounts to $k = 9.1 \cdot 10^{-10}$ cm^3 s^{-1} molecule^{-1},[xxiii] corresponding to a reaction efficiency of 80 %, relative to the collision rate.

In contrast to $[CO]^{\bullet+}$, the experiments with $[SiO]^{\bullet+}$ are much more straightforward and hence more simple to analyze. Briefly, $[SiO]^{\bullet+}$ ions are formed in the reaction of N_2O with $[Si]^{\bullet+}$; the latter can be generated by laser desorption/ionization of a silicon target. After subsequent thermalization of the hot $[SiO]^{\bullet+}$ ions, they are reacted with CH_4 in the Berlin FT-ICR instrument. Not entirely unexpected, $[SiO]^{\bullet+}$ brings about efficient activation of methane at room temperature, Equation 4.13; hydrogen-atom transfer constitutes the only reaction channel and more complex by-products are not formed (Figure 4.12). The kinetic analysis reveals a rate coefficient of $k = 6.6 \cdot 10^{-10}$ cm^3 s^{-1} molecule^{-1}, corresponding to a reaction efficiency of 60 %. The intramolecular KIE, derived from the $[SiO]^{\bullet+}/CH_2D_2$ couple, amounts to 1.6.

$$[SiO]^{\bullet+} + CH_4 \longrightarrow [SiOH]^+ + CH_3^{\bullet} \qquad (4.13)$$

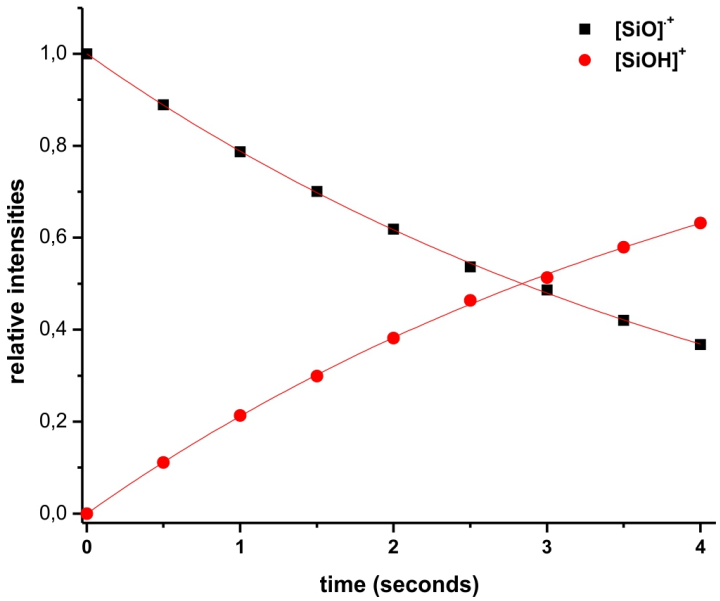

Figure 4.12: Kinetic plot of the ion/molecule reaction between $[SiO]^{\bullet+}$ and CH_4 ($p(CH_4) = 3.0 \cdot 10^{-9}$ mbar). The intensities are normalized with respect to the absolute intensity of the parent ion.

Mechanistic insights into the details of the HAT with the two hydrogen acceptors $[CO]^{\bullet+}$ and $[SiO]^{\bullet+}$ have been obtained by quantum-chemical calculations. To this end, the unrestricted W1 (Weizmann-1) theory is used, as this method provides reliable data in the calculation of thermochemical values.[xxiv] As shown in Figure 4.13, the reactions of

[xxiii] The rate constant differs from the data reported in [378,379,386] (k = 1.3 - 1.36 $\cdot 10^{-9}$ cm^3 s^{-1} molecule^{-1}.)

[xxiv] Calculations were also performed at the MP2/aug-cc-pVTZ level of theory. However, the energies obtained with W1 compare better with the experimental findings on *e.g.* the energy difference between $[HCO]^+$ versus $[COH]^+$; hence, the discussion is restricted to the W1 values.

$[CO]^{\bullet+}$ and $[SiO]^{\bullet+}$ with CH_4 proceed via distinctly different mechanistic scenarios; while $[CO]^{\bullet+}$ reacts according to a direct HAT pathway, it is the indirect process that matters for $[SiO]^{\bullet+}$. Moreover, HAT from methane to $[CO]^{\bullet+}$ can occur at both the carbon as well as the oxygen sites of the radical cation, as shown in Figure 4.13, while the formation of $[HSiO]^+$ is 98 kJ mol^{-1} higher in energy, relative to the entrance channel and can thus not take place at thermal conditions;[382] thus, $[SiOH]^+$ is exclusively generated in the HAT reaction of $[SiO]^{\bullet+}$ with CH_4. A closer look at the electronic structures of the two reactive species $[CO]^{\bullet+}$ and $[SiO]^{\bullet+}$ reveals an explanation for the unexpectedly different mechanistic scenarios. In $[SiO]^{\bullet+}$, the spin is mainly localized at the oxygen atom (Si = 0.11 μ_B; O = 0.89 μ_B) while the radical site in $[CO]^{\bullet+}$ corresponds mainly to the carbon atom (C = 1.60 μ_B; O = -0.60 μ_B). Furthermore, the $[CO]^{\bullet+}$ and $[SiO]^{\bullet+}$ ions possess also different properties when compared to their neutral counterparts CO and SiO. The calculated bond length of $[SiO]^{\bullet+}$ amounts to 1.521 Å and is 0.01 Å longer than that of neutral SiO, in good agreement with experimental data (1.510 Å).[302] In contrast, the CO bond length decreases upon the removal of an electron, from r(C−O) = 1.128 Å (exp.: 1.126 Å[302]) in neutral CO to 1.110 (exp.: 1.115 Å[302]) for $[CO]^{\bullet+}$. As described previously,[388–390] adding a proton or a point charge to the carbon (oxygen) atom of CO results in a shortening (or an elongation) of the C−O bond, *i.e.* the higher stability of $[HCO]^+$ versus $[COH]^+$ can be partly traced back in part to the stronger C−O bond in the former species. The strengthening of the C−O bond upon protonation at the carbon atom of CO has previously been assigned to an anti-bonding character of the 5σ orbital of CO that is located at the carbon atom and forms the bond to the proton;[391] however, according to more recent studies the strengthening is due mostly to an electrostatic effect:[388–390] the bonding orbitals in free CO are polarized towards oxygen, and adding a proton at the carbon atom is expected to oppose this polarization and thus to enhance the covalent character of the CO bond.

With respect to the actual mechanism, the approach of methane at the O-site of $[CO]^{\bullet+}$ triggers a so-called intramolecular spin-density transfer[300] and leads to the barrier-free transfer of hydrogen to the oxygen atom; in the process **72** → **74**, O−H bond formation occurs at the expense of weakening the C−O bond. However, in the resulting intermediate **73** the spin is not yet completely transferred to the CH_3 fragment as is usually typical for a direct HAT;[53,258] actually, only 64 % of the spin density is located at the carbon atom of the methyl fragment and 34 % on the migrating hydrogen atom. In intermediate **73**, the C−H bond to be broken is with r(C−H) = 1.360 Å still quite short and the C−O bond is not as elongated as in the product ion **74** (r(C−O) = 1.144 Å in **73** versus r(C−O) = 1.155 Å in **74**). An incomplete HAT process in **73** is also indicated by the relatively large energy demand of 128 kJ mol^{-1} required for the liberation of the methyl radical to form the $[COH]^+$ cation; nevertheless, this process is overall slightly exothermic by about -40 kJ mol^{-1} and can thus occur even at room temperature. On the other hand, this pathway has to compete with the thermochemically much more preferred abstraction of the hydrogen atom by the C-site of

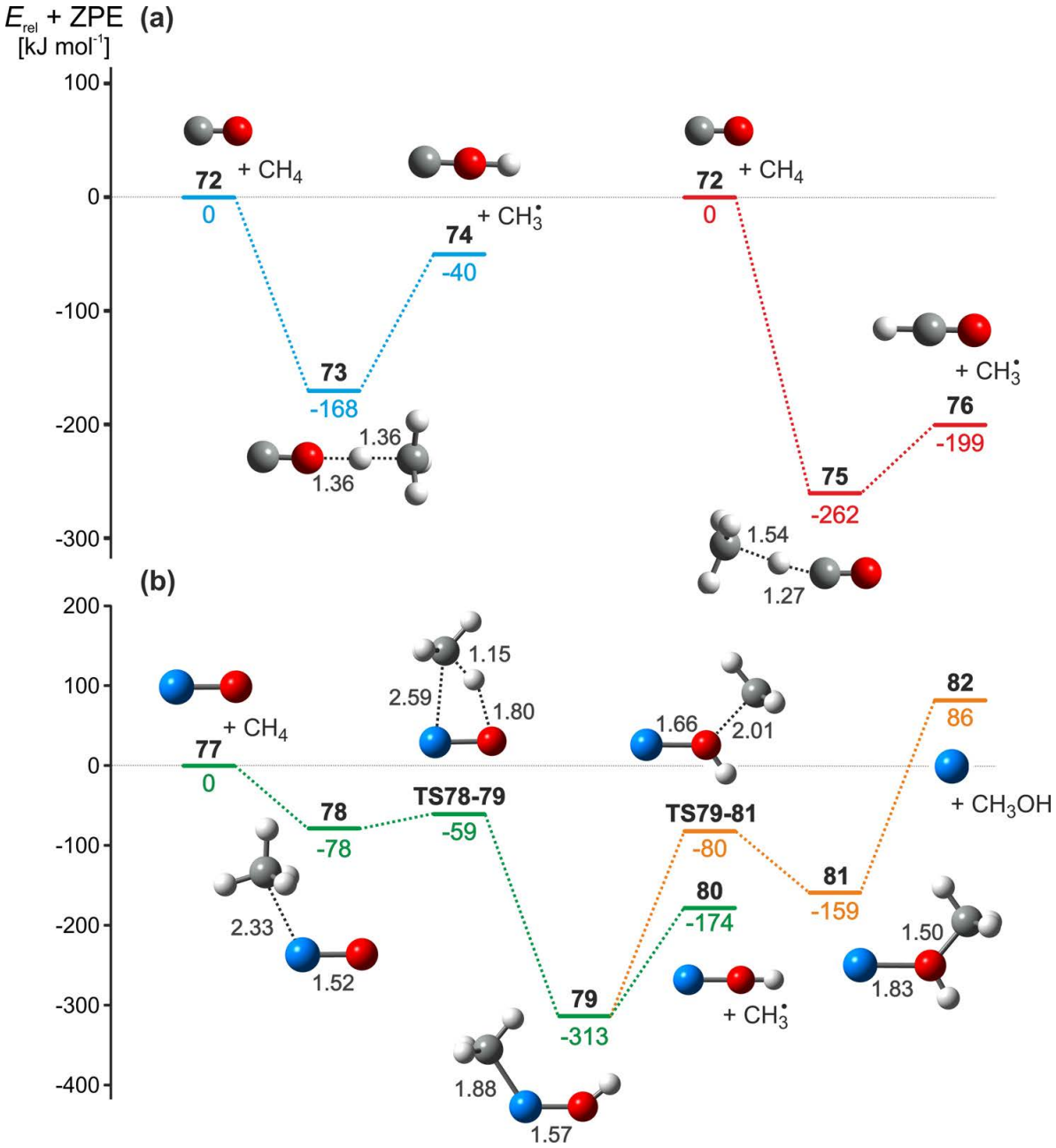

Figure 4.13: Potential energy surfaces for the reactions of (a) $[CO]^{\bullet+}$ and (b) $[SiO]^{\bullet+}$ with CH_4 and the associated structures of the intermediates and transition structures, calculated at the W1U level of theory (gray C, white H, red O, blue Si). Relative energies, corrected for scaled, zero-point energy contributions (scaling factor: 0.986) are given in kJ mol^{-1}, and relevant bond lengths in Å.

$[CO]^{\bullet+}$, for which no intramolecular spin-density transfer is required. In intermediate **75**, the spin is almost completely transferred to the carbon atom of the methyl group (83 %) with the remaining spin localized at the carbon atom of the CO fragment. Furthermore, the cleavage of the C−H bond of methane is with r(C−H) = 1.539 Å much more advanced compared to the one in intermediate **73**. Finally, while **75** is about 94 kJ mol^{-1} lower in energy than

73, the expulsion of the methyl radical to complete the reaction is with 63 kJ mol^{-1} much less energy-demanding than the alternative route. The energy of $[COH]^+$ **74** relative to the $[HCO]^+$ cation **76** amounts to 159 kJ mol^{-1}; this value is in good agreement with previous experimental (168 kJ mol^{-1}) [392–394] and theoretical findings (158 - 169 kJ mol^{-1}). [395,396] For the $[SiO]^{\bullet+}/CH_4$ couple, the reaction proceeds as it has been reported for almost all diatomic metal-oxide cations. Adduct formation occurs via coordination of the hydrocarbon to the silicon-site of the cluster, with a favorable angle ◁CSiO = 114° for intermediate **78**; hence, the barrier for the migration of the hydrocarbon around the silicon atom amounts to only 19 kJ mol^{-1}; this is significantly less than for *e.g.* the $[MgO]^{\bullet+}/CH_4$ couple (◁CMgO = 180°; 80 kJ mol^{-1}) [266] but still higher compared to the other group 14 $[XO]^{\bullet+}/CH_4$ couples (X = Ge, Sn, Pb; ◁CXO < 90°; 1 - 6 kJ mol^{-1}). [271] In the subsequent transition state **TS78-79**, the C−H bond scission occurs at the reactive oxo-site, followed by a recoil of the newly-formed methyl group, thus forming the intermediate $[CH_3^{\bullet}\cdots Si{-}OH]^+$ (**79**). Again, the angle ◁CSiO = 123° is slightly larger in this intermediate compared to the other group 14 metal-oxide systems, and the relative energy of intermediate **79** (-313 kJ mol^{-1}) is in line with the increasing relative energies obtained for the corresponding intermediates of the Ge, Sn, and Pb systems, respectively (-252 kJ mol^{-1}, -210 kJ mol^{-1}, and -193 kJ mol^{-1}). [271] The overall HAT reaction is completed by the liberation of the $CH_3^{\bullet}$ radical from **79** to form oxygen-protonated silicon-oxide **80**; the computed exothermicity amounts to -174 kJ mol^{-1}. The alternative rebound mechanism to generate methanol and bare $[Si]^{\bullet+}$ (Figure 4.13b, orange line) is kinetically and entropically much less attractive (about 94 kJ mol^{-1}); moreover, the overall process is endothermic by about 80 kJ mol^{-1}, and can thus not compete with HAT to $[SiO]^{\bullet+}$.

A comparison of the thermochemistry of the reactions of $[XO]^{\bullet+}$ with CH_4 (X = C, Si, Ge, Sn, Pb), [271] reveals decreasing exothermicities for the HAT processes down the periodic table; the opposite situation prevails with respect to the formation of methanol. The latter observation is related to the $X^+{-}O$ BDEs which decrease with increasing atomic numbers. Here, the differences of BDE($C^+{-}O$) and that of the BDEs of the oxides of higher rows are especially pronounced; while for metal- and metalloid oxides the BDEs range between 242 and 459 kJ mol^{-1}, the BDE for $[CO]^{\bullet+}$ is with 803 kJ mol^{-1} extremely high. Also the ionization energy of neutral CO is distinguished from that of the other p element oxides (Table 4.1). The different chemistry of the p elements of the second row, which is manifested *e.g.* in higher ionization energies of the elements as well as in high electronegativities, is due to similar sizes of the 2s and 2p (n < 2) orbitals in contrast to np (n > 2) orbitals which are much more radially extended than the corresponding ns orbitals. [397,398] As pointed out previously, this difference is due to the fact that the 2p orbitals do not possess a centrifugal term in the radial term of the effective potential of the Schrödinger equation. [397,398] Based on these fundamental differences in orbital properties between n = 2 and n > 2 , the distinction of

the p block elements of the second row is also reflected in the reactivity of $[CO]^{\bullet+}$ toward methane.

Table 4.1: Adiabatic IE of XO, as well as the reaction enthalpies for hydrogen-atom transfer and methanol formation (OAT) in the reaction with CH_4, respectively (all numbers are given in kJ mol^{-1}). X = C, Si were calculated at the W1U level of theory, while for X = Ge, Sn, Pb the UB3LYP/def2-QZVP method was employed.

	BDE	IE_{XO}	$\Delta_r H°_{HAT}$	$\Delta_r H°_{OAT}$
$[CO]^{\bullet+}$	803	1356	-199	431
$[SiO]^{\bullet+}$	459	1122	-174	86
$[GeO]^{\bullet+}$	346[a]	1068	-164[a]	-16
$[SnO]^{\bullet+}$	285[a]	954	-146[a]	-77
$[PbO]^{\bullet+}$	242[a]	909	-137[a]	-120

[a] Values taken from Ref. [271].

4.3 Summary

The examples highlighted in this chapter provide further arguments for the importance of spin density in gas-phase (ion) chemistry with respect to the homolytic C−H bond cleavage of methane at ambient conditions. Basically, all reactive species capable of an efficient hydrogen-atom abstraction from methane at room temperature possess a high spin density at the abstracting atom; on the other hand, if the radical is delocalized over a few centers, or when the abstracting atom bears no unpaired spin density, significantly higher activation barriers exist. Especially in the comparison of polynuclear aluminum-oxide clusters with the only difference being the presence, *i.e.* $[Al_8O_{12}]^{\bullet+}$, or absence ,*i.e.* $[Al_7O_{11}]^{+}$, of a M−O$^{\bullet}$ radical, the former exhibit a much higher reactivity towards methane. In the latter, the spin of the triplet state is distributed among multiple, bridging oxygen atoms; this electronic feature causes an higher activation barrier for the C−H bond cleavage. Moreover, spin density counts also for small, diatomic systems as the $[CuO]^+$ ion. Here, with respect to hydrogen-atom transfer, the electronic structure of $[CuO]^+$ certainly represents a key issue for the remarkable reactivity towards methane, permitting it to bring about thermal HAT from methane in the gas phase. In detail, the rather high spin density at the oxygen atom in the ($^3\Sigma^-$) triplet-ground state results in a radical functionality, *i.e.* $[Cu^{II}-O^{\bullet}]^+$, triggering the kinetically demanding, homolytic C−H bond activation step; further, a two-state reactivity scenario in combination with the low bond energy of $[Cu^+-O]$ enables the $CH_4 \rightarrow CH_3OH$ conversion. Finally, the last gap in the group 14 metal-oxide cations was closed by generating the carbon and silicon system and probing their reactivity towards methane. With respect to the nature of HAT, $[CO]^{\bullet+}$ represents the very first cationic system which is able to react at two reactive sites, *i.e.* the oxygen- as well as the carbon-site, thus resulting in

two HAT processes. These reactions are, however, quite different with respect to both thermochemistry and reaction mechanism. The generation of $[HCO]^+$ is significantly favored due to a shorter and thus stronger C−O bond as compared to the one leading to $[COH]^+$, and HAT proceeds via a direct pathway. $[SiO]^{\bullet+}$ on the other hand is shown to react according to a metal-mediated scenario, bringing about efficient HAT only at the oxygen site as previously reported for other diatomic metal-oxide cations.

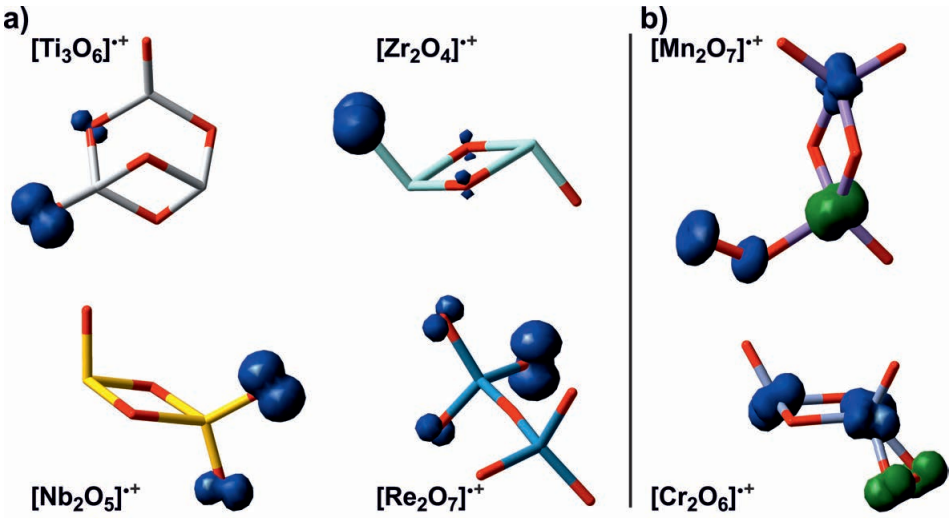

Figure 4.14: Lowest-energy structures calculated for selected early transition-metal oxide clusters with Δ = 1 (see Equation 4.14; white Ti, cyan Zr, violet Mn, yellow Nb, dark teal Re, silver Cr, red O). The blue isosurfaces indicate the spin density (green with opposite algebraic sign). Clusters (a) possessing an oxygen-centered radical are reactive towards methane, while (b) those with an intact O-O bond lacking an oxygen-centered radical do not bring about HAT from methane under thermal conditions.

These results find also support in other recent studies, where the presence of an oxygen-centered radical in various transition-metal oxide (TMO) clusters has been suggested to be responsible for their reactivity towards methane.[54,399] Based on experimental and theoretical studies on various larger TMO clusters, it was found that clusters of $M_xO_y^q$ stoichiometry contain oxygen-centered radicals if they satisfy the general equation 4.14, in which n is the number of valence electrons of the metal M:

$$\Delta \equiv 2y - nx + q = 1 \tag{4.14}$$

According to theory, the prediction of an oxygen-centered radical holds true for a large number of early transition-metal oxides clusters (Figure 4.14a), and several series of these stoichiometric early transition-metal oxide clusters fulfilling the Δ = 1 criteria were successfully probed with respect to their HAT reactivity towards methane, including $[(TiO_2)_{1-5}]^{\bullet+}$, $[(ZrO_2)_{1-4}]^{\bullet+}$, $[(HfO_2)_{1-2}]^{\bullet+}$, $[(MoO_3)_{1-2}]^{\bullet+}$, $[(WO_3)_{1-3}]^{\bullet+}$, $[(V_2O_5)_{1-5}]^{\bullet+}$,

$[(Nb_2O_5)_{1-3}]^{\bullet+}$, $[(Ta_2O_5)_{1-2}]^{\bullet+}$ and $[Re_2O_7]^{\bullet+}$.[139,341,342] In contrast, the oxide clusters with $\Delta \neq 1$ were completely inert in their thermal reactions with methane. However, a few exceptions are known which, while satisfying Equation 4.14, do not possess oxygen centered radicals, *i.e.* oxide clusters of chromium and manganese, *e.g.* $[(CrO_3)_{1-3}]^{\bullet+}$ or $[Mn_2O_7]^{\bullet+}$. As revealed by DFT calculations, these clusters exhibit a different bonding pattern; in fact, super-oxide or molecular oxygen units with intact O−O bonds are present in these clusters instead of terminal bound oxides as found for the early TMOs (Figure 4.14b). Accordingly, these clusters do not possess an oxygen-centered radical, thus being completely inert towards methane.

Finally, taking all these results into account, the general statement[327] at the beginning of this chapter about the unimportance of unpaired spin density at the hydrogen-abstracting atom finds no support by the numerous experimental/computational studies in the framework of the present thesis and in the associated literature; rather, it is quite misleading.

5 Remote Functionalization by Metal-Oxide Cations: A Proof-of-Principle Study

„It is by logic that we prove, but by intuition that we discover." [400]

– J. Henri Poincaré

The regioselective activation of non-activated C−H and C−C bonds *e.g.* at a defined position of an alkane chain constitutes an ongoing challenge in current research activities, particularly in the field of homogeneous and heterogeneous catalysis. [401–404] In this context, enzymatic reactions provide compelling evidence for the beauty and efficiency of directed attacks at a specific site remote from a functional group X. Breslow *et al.* introduced the concept of *remote functionalization* in the early seventies by mimicking enzymatic oxidation processes, [96–99] and selective functionalization of C−H bonds has been realized in the ensuing years for a growing number of examples in homogeneous catalysis. [402, 403, 405–411]

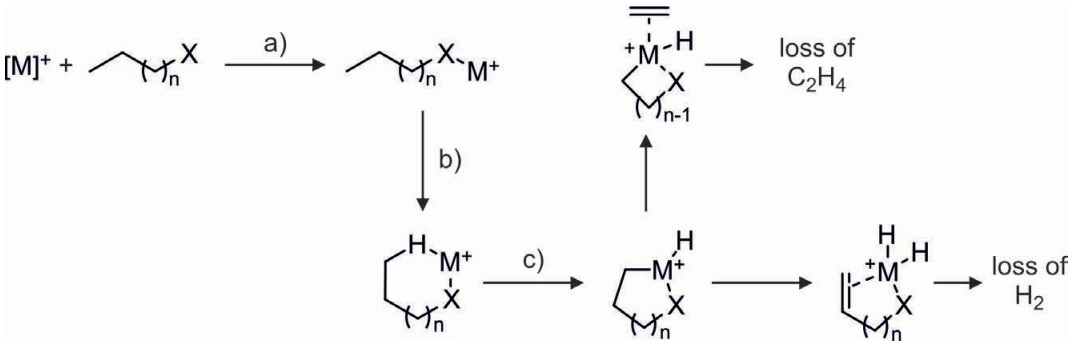

Figure 5.1: Schematic, general mechanism for the *remote functionalization*of a metal cation $[M]^+$ and a organic substrate R−X, including a) coordination to the functional group, b) *internal solvation*, and c) regioselective C−H bond activation.

While in liquid phase this concept is mostly limited to the directed activation of sp^2 C−H bonds in functionalized, aromatic systems, *i.e. ortho-*, *meta-*, or *para*-functionalization, the regioselective activation of saturated hydrocarbons is much more demanding. However, in analogy to Breslow's biomimetic systems, numerous examples of *remote functionalization*, mainly by "naked" metal cations $[M]^+$, have been described and investigated in detail in the gas phase. [100, 101] With respect to the mechanism (Figure 5.1), $[M]^+$ is first anchored

at the functional group X of the substrate R−X, followed by a recoil of the alkyl chain towards the cationic metal center (*internal solvation*) and *remote functionalization* is finally realized by a regioselective C−H activation at positions remote from the functional group X. As revealed by deuterium-labeling experiments and computational studies, amazingly regio- and stereoselective gas-phase bond activation has been observed for a large variety of functionalized alkanes, including nitriles, [412–418] alcohols, [419–421] ketones, [422–426] amines, [421,427,428] and alkynes. [429–432]

However, while there exists now a broad spectrum on the reactivity of all kind of bare metal cations with various organic substrates, the knowledge about the reactivity of metal oxides in terms of *remote functionalization* is rather scarce. Since only early examples of *remote functionalization* by $[FeO]^+$ are known, [433,434] it was noted that „*... a key aspect of future work would be to provide a sufficient thermochemical driving force by inclusion of an oxidation step (e.g., remote functionalization by $[MO]^+$ rather than $[M]^+$ ions)*“. [52] Hence, in the present thesis the scope of *remote functionalization* in the gas phase has been extended to metal oxides $[MO]^+$.

With respect to regioselectivity, different preferences for primary vs. secondary C−H bond activations of unfunctionalized alkanes by bare $[MO]^+$ were reported. Bond activation in favor of the methylene group of propane due to the weaker secondary C−H bonds has been described in the reactions with the ligated copper cation $[L{-}CuO]^+$ (L = 1,10-phenanthroline), [362] silver oxide $[Ag_2O]^{\bullet+}$, [267] and with the metal-free cluster ion $[P_4O_{10}]^{\bullet+}$. [435] In contrast, predominance for activation of the primary C−H bond of propane, *e.g.* in the reaction with the $[VO_2]^+$ cation, [436] has been attributed to the stabilizing effect in the transition structure due to a simultaneous interaction of the metal center with both methyl groups. [347] A strong preference for primary C−H bond activation of propane by $[MgO]^{\bullet+}$ has also been observed experimentally, as reported by Schröder et al., [368] and dynamic effects have been invoked to account for these findings. In contrast, C−H bond activation of propane by bare $[FeO]^+$ and $[MnO]^+$ occurs almost indiscriminately. [343,437]

5.1 Remote functionalization of valeronitrile (*n*-C_4H_9CN) by the bare metal oxides $[MO]^+$ (M = Mn, Mg, Ca)

The oxides $[MgO]^{\bullet+}$, $[CaO]^{\bullet+}$, and $[MnO]^+$ have been shown to be very reactive in ion/molecule reactions with respect to homolytic C−H bond cleavage of alkanes, [266,343,344] and are thus perfectly suitable as reactive species to study the concept *remote functionalization* in bond activations by metal-oxide cations. Further, valeronitrile (*n*-C_4H_9CN) was chosen as model substrate, as nitrile groups already showed with bare metal ions a very efficient steering effect. [412–418]

First, the dramatic effect on „anchoring“ the reagent becomes already obvious when comparing the reactions of $[MO]^+$ with *n*-C_4H_9CN versus *n*-C_4H_{10}; for $[MnO]^+$, the

introduction of the nitrile group causes a significant change in the product distribution (Figure 5.2). Certain reaction channels become strongly disfavored, including the oxygen-atom transfer to *n*-C_4H_9CN (Figure 5.2, *m/z* 55), as well as the hydrogen-atom abstraction from *n*-C_4H_9CN (Figure 5.2, *m/z* 72). Moreover, the reaction channel of oxidative dehydrogenation to form C_4H_8 from *n*-C_4H_{10} (Figure 5.2a, *m/z* 73), vanishes completely. On the other hand, other product channels increase remarkably in their relative intensities; in the reaction with *n*-C_4H_9CN for example, while the loss of propene in the reaction of $[MnO]^+$ with *n*-C_4H_{10} takes place only with a very low branching ratio of less than 2 % (Figure 5.2a, *m/z* 87), introduction of the nitrile function results in a significant increase of this reaction channel to 33 % (Figure 5.2b, *m/z* 112).

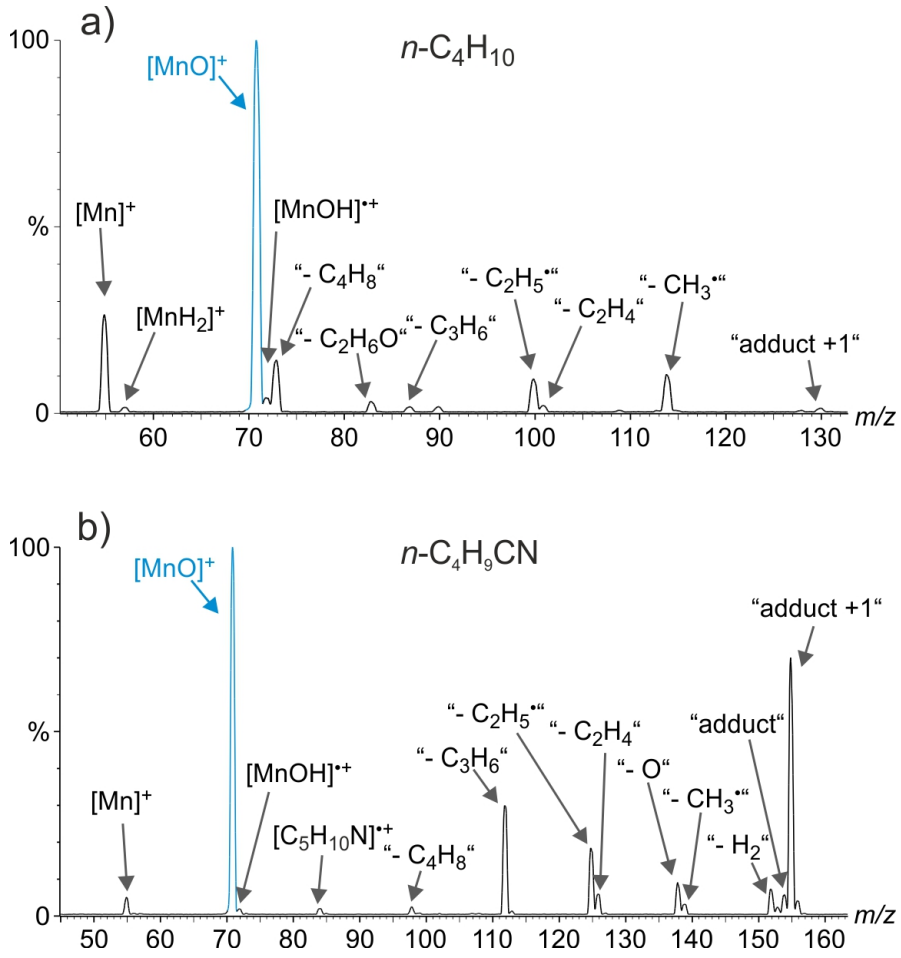

Figure 5.2: Ion/molecule reactions of mass-selected $[MnO]^+$ with a) *n*-C_4H_{10} and b) *n*-C_4H_9CN.

Similar observations hold true for the $[MgO]^{\bullet+}$/*n*-C_4H_9X couples (X = H, CN); while for these systems the branching ratio for the hydrogen-atom transfer decreases significantly from 42 % for X = H [151] to 17 % for X = CN, loss of propene increases from 1 % to 29 %, respectively. For the $[CaO]^{\bullet+}$/*n*-C_4H_9CN couple, hydrogen-atom transfer prevails as the main reaction channel, and thus the intensities of HAT are for both reactive species $[MgO]^{\bullet+}$

Table 5.1: Intensities of product ions (expressed in % of $\sum \mathrm{Int}_i$ = 100) together with the corresponding neutral losses for the reactions of mass selected $[MO]^+$ (M = Mn, Mg, Ca) with *n*-C_4H_9CN.

Reaction	Product ion	Neutral loss	$[MnO]^+$	$[MgO]^{\bullet+}$	$[CaO]^{\bullet+}$
oxygen-atom transfer	$[M]^+$	C_5H_9NO	7.4	-	-
hydrogen-atom transfer	$[M(OH)]^+$	C_5H_8N	2.7	17.0	59.3
loss of butene	$[M,O,C,H,N]^+$	C_4H_8	3.1	-	3.2
loss of propene	$[M,O,C_2,H_3,N]^+$	C_3H_6	33.0	37.0	23.4
loss of ethyl radical	$[M,O,C_3,H_4,N]^+$	C_2H_5	23.4	36.1	6.3
loss of ethene	$[M,O,C_3,H_5,N]^+$	C_2H_4	7.2	6.6	2.8
loss of methyl radical	$[M,O,C_4,H_6,N]^+$	CH_3	4.4	3.3	5.0
dehydrogenation	$[M,O,C_5,H_7,N]^+$	H_2	10.2	-	-
adduct formation	$[M,O,C_5,H_9,N]^+$	-	8.6	-	-

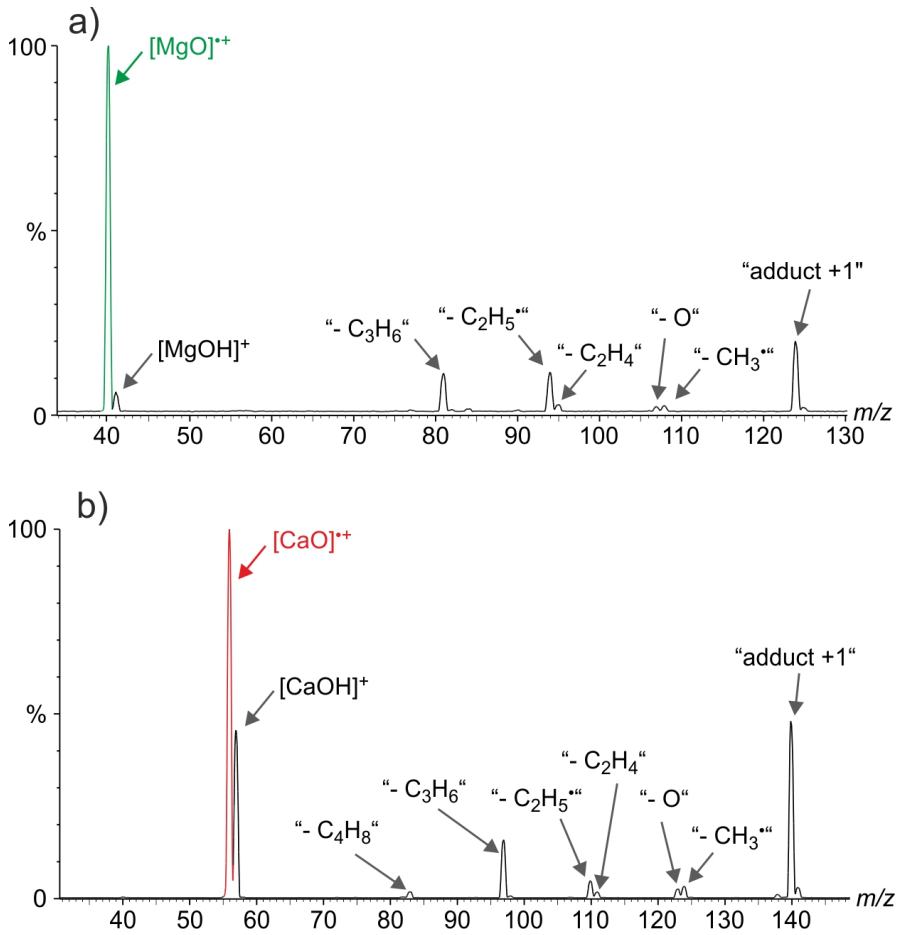

Figure 5.3: Ion/molecule reactions of mass-selected a) $[MgO]^{\bullet+}$ and b) $[CaO]^{\bullet+}$ with *n*-C_4H_9CN.

and $[CaO]^{\bullet+}$ sufficient (Figure 5.3, Table 5.1) to study the regioselectivity of HAT from valeronitrile.

To study the regioselectivities of the HAT reactions by performing labeling experiments, the selectively deuterated isotopomers of *n*-valeronitrile **83b - e** (Figure 5.4) were synthesized

according to established laboratory procedures (see Appendix B.2). The resulting isotope patterns in the ion/molecule reactions of $[MO]^+$ (M = Mn, Mg, Ca) with **83b** - **e** are given in Table 5.2.

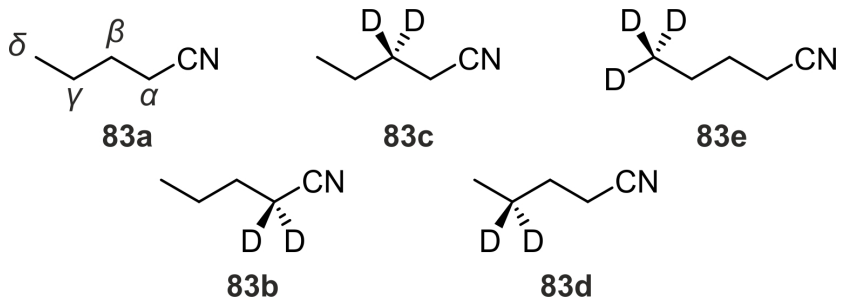

Figure 5.4: Isotopomers of *n*-C_4H_9CN employed in the labeling experiments.

However, before discussing the observed regioselectivities, it should be mentioned, that quite efficient secondary reactions (Equations 5.1 - 5.3) take place which, to some extent, may affect the analysis. For example, the formal loss of an oxygen-atom, Equation 5.2, has been assigned to a secondary reaction since a primary ligand-exchange reaction is highly endothermic on the ground that the upper bond-dissociation energies (BDEs) of $[Fe]^+$-nonanitrile and $[Co]^+$-nonanitrile have been estimated to 201 kJ mol^{-1} and 234 kJ mol^{-1},[418] respectively, as compared to BDE(Fe^+-O) = 339 kJ mol^{-1} and BDE(Co^+-O) = 314 kJ mol^{-1}, respectively. Thus, the product ion $[M-C_5H_9N]^+$ is rather formed by an oxygen-atom transfer to the hydrocarbon, followed by adduct formation of the bare metal ion with a second nitrile. Note that, based on the labeling experiments, loss of CH_4 rather than an oxygen atom can be ruled out. Similarly, the formal *adduct+1* reaction product from Equation 5.1 corresponds to a hydrogen-atom transfer, followed by adduct formation with another nitrile or vice versa, *i.e.* the initially formed adduct complex brings about intermolecular HAT from a second substrate molecule. Thus, as the C−H bond activation step can occur intra- or intermolecular, no preferential activation site is observed.

$$[MO]^+ + 2\,C_5H_9N \longrightarrow [M, C_5, H_{10}, N, O]^+ + C_5H_8N^\bullet \quad (5.1)$$

$$[MO]^+ + 2\,C_5H_9N \longrightarrow [M, C_5, H_9, N]^+ + [C_5, H_9, N, O] \quad (5.2)$$

$$[MO]^+ + 2\,C_5H_9N \longrightarrow C_5H_{10}N^+ + [M, C_5, H_8, N, O] \quad (5.3)$$

With this remarks, the regioselectivities of C−H and C−C bond activations are described in the following.

Table 5.2: Isotope pattern in the reactions of $[MO]^+$ (M = Mn, Mg, Ca) with **83b - e** (Intensities are normalized to $\sum$ = 100 % for each class of neutral molecules generated).

Metal oxide		**[MnO]$^+$**				**[MgO]$^{\bullet+}$**				**[CaO]$^{\bullet+}$**			
Isotopomers → Neutral Losses ↓		**83b**	**83c**	**83d**	**83e**	**83b**	**83c**	**83d**	**83e**	**83b**	**83c**	**83d**	**83e**
H_2		[a]	95	100	95								
HD			5		5								
D_2													
CH_3		100	100	100		100	100	100		100	100	100	
CH_2D[b]													
CHD_2					2								
CD_3					98				100				100
C_2H_4		15	13	11	12	9	11	16	2	13	15	15	6
C_2H_3D	C_2H_5	17	41	31	5	41	56	20	11	36	56	19	3
$C_2H_2D_2$	C_2H_4D	35	16	27	27	25	11	29	19	36	12	41	9
C_2HD_3	$C_2H_3D_2$	33	30	31	32	25	22	35	33	15	17	25	41
	$C_2H_2D_3$				24				35				41
C_3H_6		100				100				100			
C_3H_5D				97				100				99	
$C_3H_4D_2$			100	3			100				100	1	
$C_3H_3D_3$					100				100				100
C_4H_7D			95								100		
$C_4H_6D_2$		100	5	100						100		100	
$C_4H_5D_3$					100								100
$[MOH]^+$		95	76	65	91	89	83	61	85	91	77	73	91
$[MOD]^+$		5	24	35	9	11	17	39	15	9	23	27	9

[a] Very small intensities are observed, most likely due to incomplete deuteration of the starting material CD_3CN (99.8 % D_3).

[b] Channel overlaps with secondary reaction 5.2 and it can therefore not completely be ruled out, that very small amounts of CH_2D are formed.

Hydrogen-atom transfer provides the most simple method to determine the regioselectivity for C−H bond activation, as no further, more complicated bond activation processes are involved. Thus, the isotopic distribution for HAT given in Table 5.2, corresponding to the formation of $[MOH]^+$ and $[MOD]^+$, respectively, enables a straight-forward analysis of the regioselectivity operative for the homolytic C−H bond fissions. Hence, in distinct contrast to the preference of primary C−H bond activation of C_3H_8 and *n*-C_4H_{10} by $[MgO]^{\bullet+}$ [267] and the near statistical H-atom abstraction from C_3H_8 by $[MnO]^+$ and $[FeO]^+$, [343,437] homolytic C−H bond activation of valeronitrile **83a** by all three metal oxides $[MO]^+$ (M = Mn, Mg, Ca) to form $[MOH]^+$ follows the concept of *remote functionalization*. As shown in Table 5.3, kinetic modeling [437] of the isotope pattern for the hydrogen-atom abstraction by $[MnO]^+$, $[MgO]^{\bullet+}$, and $[CaO]^{\bullet+}$ from **83b** - **e**, taking into account a KIE and corrected for the statistical contribution of C−H and C−D bonds, reveals that the homolytic C−H bond activation strongly favors the γ position. This preference amounts to 50 % for the $[MgO]^{\bullet+}$/*n*-C_4H_9CN couple, *i.e.* one of two C−H bond activation steps along the chain occurs at the γ position; also the β position is with 23 % slightly favored compared to the α and δ positions. The $[MnO]^+$/*n*-C_4H_9CN couple reacts with the same preference at the γ position (49 %); the preference for the β position is with 35 % higher compared to the $[MgO]^{\bullet+}$ system. Finally, similar preferences of the γ and β positions (38 % and 33 %, respectively) are found for the $[CaO]^{\bullet+}$/*n*-C_4H_9CN couple. Thus, introduction of a functional group brings about remote C−H bond functionalisation by metal-oxide cations. This concurs with previous findings, *e.g.* on the dehydration of 4-heptanone by bare $[FeO]^+$; [433] here the δ and γ positions serve as hydrogen sources to produce H_2O.

Table 5.3: Regioselectivities ($\sum$ = 100 %) and KIEs for the homolytic C−H bond scission in *n*-C_4H_9CN by $[MO]^+$ (M = Mn, Mg, Ca).

Metal oxide	α position	β position	γ position	δ position	*KIE*
$[MnO]^+$	8 %	35 %	49 %	8 %	1.6
$[MgO]^{\bullet+}$	14 %	23 %	50 %	13 %	1.4
$[CaO]^{\bullet+}$	15 %	33 %	38 %	14 %	1.6

Next to the hydrogen-atom transfer, reaction channels involving more complex C−C bond activation of **83a** by $[MO]^+$ support this interpretation (Table 5.2), *e.g.* propene elimination: In contrast to the reactions of $[MO]^+$ (M = Mg, Mn) with *n*-butane, loss of propene C_3H_6 dominates the ion/molecule reaction of $[MO]^+$ with *n*-C_4H_9CN; the branching ratios amount to 33 %, 37 %, and 23 % for $[MnO]^+$, $[MgO]^{\bullet+}$, and $[CaO]^{\bullet+}$ (Table 5.1), respectively. Moreover, this process is initiated by a selective activation of the γ C−H bond as indicated by the clean labeling distributions obtained for the isotopologues **83b** - **e** (Table 5.2, *i.e.* only in the ion/molecule reaction of $[MO]^+$ with the isotopomer **83d** the fission of a labeled C−D bond occurs, leading to the formal loss of neutral C_3H_5D; for the other labeled

substrates **83b**, **83c**, and **83e**, no C−D bond activation at the respective positions is observed. Thus, after abstraction of a hydrogen atom from the γ position (Figure 5.5 **83a** $\rightarrow$ **84a**), homolytic C−C bond cleavage occurs which, for all three metal oxides, is not proceeded by any exchange processes. Consequently, for instance, at least 33 % (br) of the reactive collisions of $[MnO]^+$ with *n*-C_4H_9CN lead to a regioselective activation of the γ C−H bond, not taking into account yet possible addiotional activation of this positions from HAT or other C−C bond activation processes, discussed in the following. Noteworthy, the branching ratios for $[MnO]^+$ (33 %), $[MgO]^{\bullet+}$ (37 %), and $[CaO]^{\bullet+}$ (23 %) parallel nicely the relative regioselectivities for homolytic C−H bond activation, dervived from the hydrogen-abstraction process (Table 5.3), *i.e.* being rather high for $[MnO]^+$ and $[MgO]^{\bullet+}$ and somewhat lower for $[CaO]^{\bullet+}$.

The preference of the C−H bond fission at the β position can be found in the more complex reaction pathways, including C−C bond activation, *i.e.* the loss of a methyl radical, as well as the elimination of C_4H_8; the H/D distributions (Table 5.2) observed for the formation of these two neutral products also points to highly specific processes. For the generation of C_4H_8, presumably butene, the exclusive loss of C_4H_7D in the reaction of $[MO]^+$ (M = Mn, Ca) with **83c** (Table 5.2) indicates an initial β C−H bond activation to trigger the consecutive cleavage of the C−C bond which occurs most likely between the α- and the nitrile-carbon atom, thus resulting in the formation of 1-butene. Further, specific loss of $CH_3^{\bullet}$ from the terminal part of the alkyl chain is proven by the exclusive expulsion of $CD_3^{\bullet}$ in the reaction of $[MO]^+$ (M = Mn, Mg, Ca) with **83e**, while the ion/molecule reactions of all other isotopomers **83b** - **d** result solely in the liberation of $CH_3^{\bullet}$ (Table 5.2). Mechanistically, this isotopic pattern points to an initial hydrogen-atom abstraction from C_β followed by β alkyl scission from structure **84b** (Figure 5.5), leading to the formation of a carbon-carbon double bond between C_β and C_γ.

With respect to the formation of ethene and the expulsion of the ethyl radical, the simultaneous loss of both neutral molecules impedes an unambiguous analysis of the respective isotope patterns of the individual reaction channels for the substrates **83b** - **e**; the isobaric overlap, in combination with the limited mass resolution of the mass spectrometer, makes a proper discrimination between the various reaction products and the respective isotopomers impossible. Nevertheless, inspection of the data in Table 5.2 clearly reveals that neither a statistical nor a specific, initial activation of the terminal methyl group can account for the observed H/D distributions. Thus, a more complex reaction sequence seems to exist.

Finally, the labeling distribution for the dehydrogenation of valeronitrile by $[MnO]^+$ is quite remarkable. For the nitriles **83c**, **83d**, and **83e** H_2 elimination is observed almost exclusively with an approximate ratio of H_2:HD of around 20:1; this points to a [1,1]-elimination from C_α (Table 5.2). However, deuterium labeling at C_α suppresses the dehydrogenation channel nearly completely; this may point to the operation of isotopically

sensitive branching. [420,438–443] Contrary to expectations, formation of the H_2 does not occur in the ion/molecule reactions of $[MnO]^+$ with CH_3CN and CH_3CH_2CN; accordingly, the intermediacy of a metal-carbene species as a result of a [1,1]-elimination is not very likely. Thus, the actual mechanism of dehydrogenation of **83a** is rather complex and despite many attempts not clarified yet.

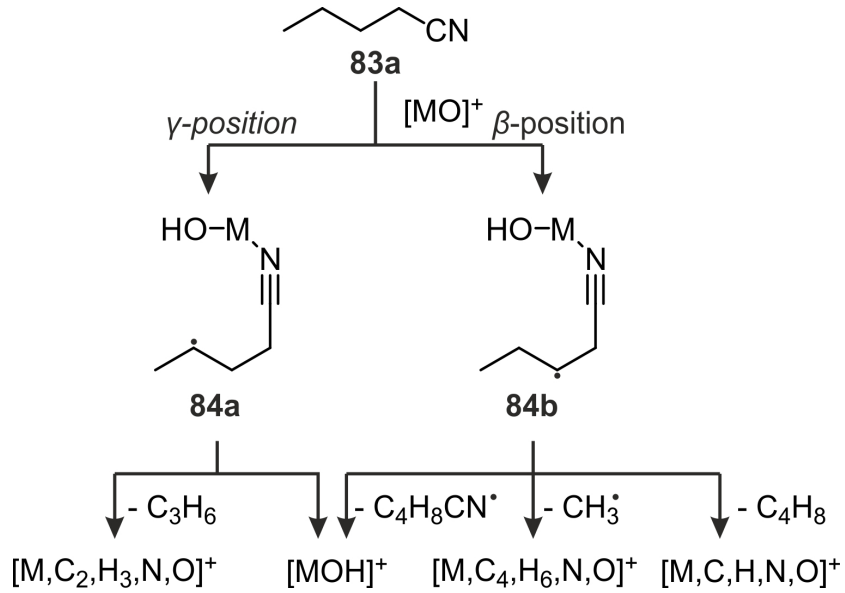

Figure 5.5: Initial C−H bond activation of valeronitrile **83a** in the β and γ positions by bare metal oxide cations $[MO]^+$ (M = Mn, Mg, Ca) and subsequent reactions, including C−C bond cleavage.

Next to these experimental findings, there is also computational support for a directed C−H bond activation of **83a** by $[MO]^+$ (M = Mn, Mg, Ca) in the gas phase. Generally, the concept of *remote functionalization* of nitriles in the gas phase assumes a quasi-linear coordination of the functional group to the metal center, *i.e.* initial formation of an *end-on* coordinated complex. As a consequence, bond activation near the functional group is hampered while remote positions become accessible by recoil of the carbon backbone. This internal solvation is facilitated by a bending of the linear M−N−C arrangement, which has been assessed previously by computational studies. [418] To study this internal solvation of the experimentally studied $[MO]^+$/**83a** couple, model calculations employing coordination of acetonitrile as a simple substrate to $[MO]^+$ have been conducted. In all three cases, according to the calculations on the UB3LYP/TZVP level of theory, the *end-on* coordination of CH_3CN to the metal in $[MO]^+$ is significantly preferred. Starting structures with a side−on bonded nitrile group rearrange to a linear coordination mode; thus, all $[(CH_3CN)MO]^+$ complexes located as local minimum on the potential energy surface possess an angle $\sphericalangle$(C,N,M) close to 180°. The bending potentials of the *end-on* complexes in the angle regime

180 - 70° are shown in Figure 5.6,[xxv] and the following conclusions can be drawn: *i*) The potential energy increases with similar gradients for all three types of metal oxide/nitrile clusters, and does in no case exceed a barrier of 200 kJ mol^{-1}. *ii*) This barrier is rather small, compared to the energy gained in the formation of the coordination adducts, exceeding for all three couples significantly the value of 200 kJ mol^{-1}, respectively, *e.g.* amounting to -293 kJ mol^{-1}for $[MgO]^{\bullet+}$; due to the absence of an energy bath, this complexation energy is accessible for the hot $[RCN{-}MO]^{+}$ complexes. *iii*) As a consequence, recoil of the alkyl chain and C−H bond activation by the bent $[RCN{-}MO]^{+}$ complexes becomes feasible.

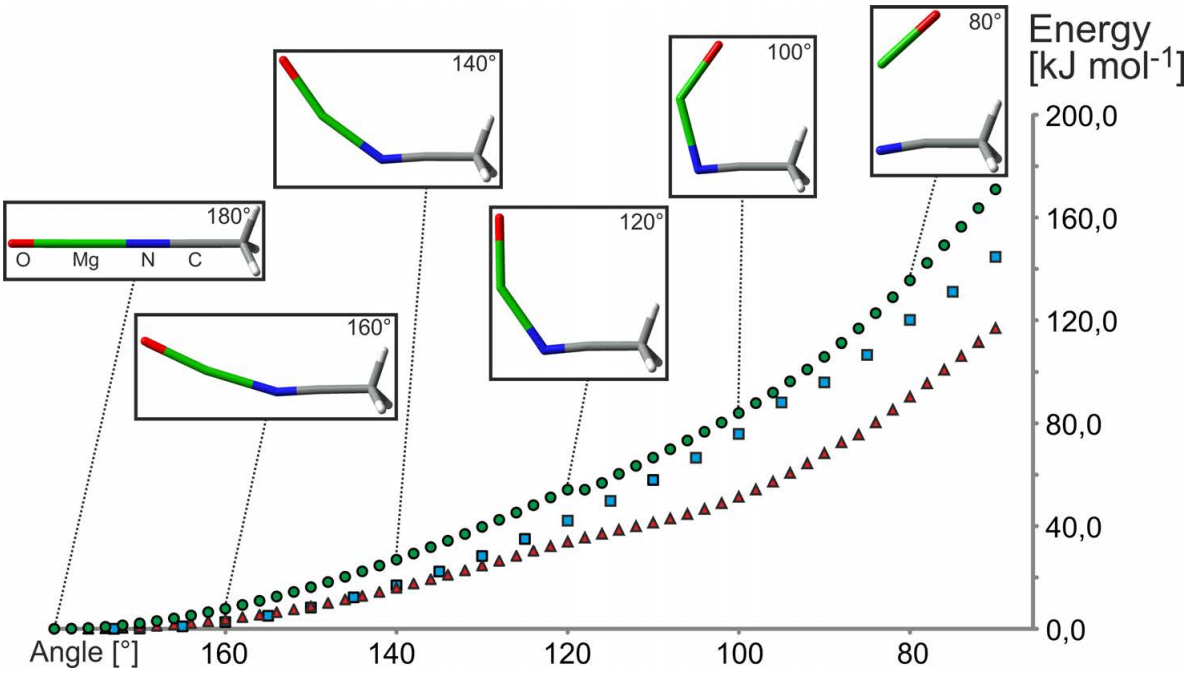

Figure 5.6: Schematic potential energy surfaces for the bending potential of $[CH_3CN{-}MO]^{+}$ as a function of the angle ◁(C,N,M) for the range 180 to 70 degrees, obtained by UB3LYP (for M = Mn, Ca) and CCSD (for M = Mg) (green = Mg, blue = Mn, and red = Ca). The UB3LYP energies for M = Mg (not shown) are in excellent agreement with the one obtained by the more precise CCSD method.

More precisely, geometric analysis of the according transition states show that the required bending values for the hydrogen abstraction in all four position are significantly lower than 70°; for example, for the $[MgO]^{\bullet+}/n\text{-}C_4H_9CN$ couple, the bending angles amount to 96° for the α-, 110° for the β-, 125° for the γ-, and 135° for the δ-position, respectively. Similar values have been obtained for the $[CaO]^{\bullet+}/n\text{-}C_4H_9CN$ and $[MnO]^{+}/n\text{-}C_4H_9CN$ couples.

In line with the experiments, homolytic C−H bond activation at the γ positions prevails as the kinetically most favored step for all three reaction couples; the thermochemical data from DFT calculations of the respective transition states are shown in Table 5.4 and depicted for the $[MgO]^{\bullet+}/n\text{-}C_4H_9CN$ system in Figure 5.7. However, also the transition structure for

[xxv] In addition to the UB3LYP/TZVP calculations, the scanning of the angle regime has for $[MgO]^{\bullet+}$/acetonitrile also been computed with the coupled cluster method CCSD using the same basis set TZVP.

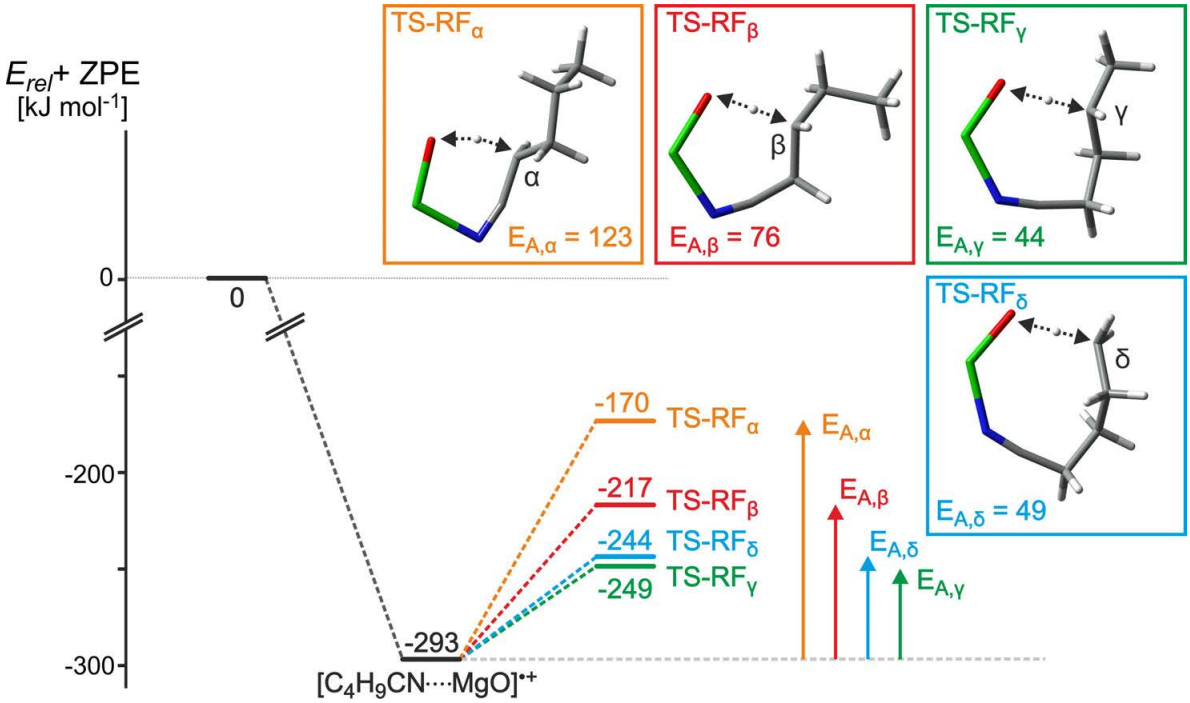

Figure 5.7: Schematic potential energy surface for the apparent activation barriers $E_{A,x}$ ($x = \alpha, \beta, \gamma, \delta$) for hydrogen-atom transfer from the respective position in the $[MgO]^{\bullet+}/n$-C_4H_9CN couple (values are given in kJ mol^{-1}); the black arrows indicate the trajectory of the imaginary frequency of the respective transition state.

homolytic C−H bond fission from the δ position is relatively low in energy, contradictory to the rather poor regioselectivity of the δ position observed in the experiments, amounting to 8 % for $[MnO]^+$, 13 % for $[MgO]^{\bullet+}$, and 14 % for $[CaO]^{\bullet+}$ (Table 5.3), respectively. Therefore, the regioselectivity is not only a product of the ring strain, but rather a combination of ring strain and the steering effect of the nitrile group; apparently, the latter favors the approach of the oxygen-atom towards the γ-position over the δ-position due to spatial, rather than energetic reasons.

Besides this disagreement, the order of the experimentally observed regioselectivities for the homolytic C−H bond activation at the α, β, and γ position are in reasonable agreement

Table 5.4: Apparent activation barriers $E_{A,x}$ ($x = \alpha, \beta, \gamma, \delta$) for hydrogen-atom transfer from the adduct complex $[n$-$C_4H_9CN\cdots MO]^+$ (M = Mn, Mg, Ca), as well as the relative energy of each transition state $TS_{rel,x}$, normalized to the lowest-lying transition structure ($TS_{rel,\gamma} = 0$) for each system, respectively (all values are given in kJ mol^{-1}).

Metal oxide	$E_{A,\alpha}$	$E_{A,\beta}$	$E_{A,\gamma}$	$E_{A,\delta}$	$TS_{rel,\alpha}$	$TS_{rel,\beta}$	$TS_{rel,\gamma}$	$TS_{rel,\delta}$
$[MnO]^+$	196	115	68	69	128	47	0	1
$[MgO]^{\bullet+}$	123	76	44	49	79	32	0	5
$[CaO]^{\bullet+}$	69	47	29	38	40	18	0	9

with the calculations. Due to the increasing ring strain, the activation barrier increases when going from $\gamma \rightarrow \alpha$ for all systems investigated (Table 5.4); for the latter scenario, a four-member ring like structure is necessary to bring about the geometrical prerequisites for hydrogen-atom transfer from this very position; abstraction from the γ position occurs via a more favorable six-membered ring.[xxvi] With respect to the $[CaO]^{\bullet+}/n\text{-}C_4H_9CN$ couple, the low regioselectivities for this system correlate quite well with the lowest difference in relative energies of the respective transitions states; $TS_{rel,\beta}$ is only 18 kJ mol^{-1} above $TS_{rel,\gamma}$, while $TS_{rel,\alpha}$ is by 40 kJ mol^{-1} higher in energy compared to $TS_{rel,\gamma}$.

5.2 Summary

In summary, the present chapter, combined with the previously reported findings on $[FeO]^+$,[433,434] clearly suggests the potential of *remote functionalization* of C−H bonds by bare metal oxides in the gas phase.[xxvii] Finally, this work may stimulate prospective research to realize and improve regioselective functionalization of remote C−H bonds by the growing number of recently reported metal-oxo-species in the condensed phase.[25,239,240]

[xxvi] Note that the C−C−N-, as well as the O−H−C moiety are linear, thus resulting in a formal six-membered ring structure, composed of eight atoms.

[xxvii] Note that similar studies have been carried on the reactivity of the metal-oxides $[FeO]^+$, $[CoO]^+$, and $[NiO]^+$ towards valeronitrile, further supporting the concept of *remote functionalization*. Here, no direct hydrogen-atom transfer product is observed, impeding direct determination of regioselectivities for homolytic C−H bond activation; nevertheless, regioselective C−C bond activation processes take place in the reactions with isotopomers of $n\text{-}C_4H_9CN$. Thus, the concept of *remote functionalization* in the gas phase is also operative in these systems.

6 Conclusions and Outlook

„The ability to simplify means to eliminate the unnecessary so that the necessary may speak." [444]

– Hans Hofmann

The present work explores selected, gaseous oxo-clusters in their reactivity towards small hydrocarbons by means of mass-spectrometric experiments in conjunction with isotope-labeling studies as well as quantum-chemical calculations. Key reactions like hydrogen-atom transfer, oxygen-atom transfer, as well as oxidative dehydrogenation constitute the focus of these studies which aim at a better understanding of fundamental properties of selected systems in all fields of catalysis.

By comparing the structure and reactivity of mixed vanadium-phosphorous oxygen-cluster ions $[V_xP_{4-x}O_{10}]^{\bullet+}$ (x = 0, 2 - 4) it is obvious that the metal does not necessarily represent the key factor in terms of homolytic C−H bond activation. In fact, it turned out that the metal-free $[P_4O_{10}]^{\bullet+}$ cluster ion exhibits a similar reactivity towards the C−H bond of methane as the previously studied metallic analogue $[V_4O_{10}]^{\bullet+}$. Further, $[P_4O_{10}]^{\bullet+}$ is not less reactive in the reaction with ethene in which $[P_4O_{10}]^{\bullet+}$ gives again rise to HAT from the hydrocarbon while $[V_4O_{10}]^{\bullet+}$ only brings about exclusive formation of the OAT product. The combination of both elements in the mixed clusters $[V_2P_2O_{10}]^{\bullet+}$and $[V_3PO_{10}]^{\bullet+}$leads to the observation that a third reaction pathway occurs with small hydrocarbons, *i.e.* ODH of ethane and ethene. DFT calculations reveal that the intrinsic properties of both elements have a crucial effect on the reactivity of the clusters. Based on a better overlap of the bonding orbitals, a stronger P−$O_t^{\bullet}$ bond results for the phosphorous-containing cluster, while the relatively weak V−$O_t^{\bullet}$ bond in $[V_4O_{10}]^{\bullet+}$ enables the OAT pathway. In contrast, $[P_4O_{10}]^{\bullet+}$ is much more reactive with respect to homolytic C−H cleavage to form the *closed-shell* HAT product $[P_4O_9(OH)]^+$ without changing the formal oxidation state of phosphorous. The combination of both elements in the mixed clusters illustrates their cooperative effects, facilitating the formation of new products such as double hydrogen-atom transfer (*i.e.* ODH). The first C−H bond scission is initiated by the significant driving force of the active P−$O_t^{\bullet}$ site; the second hydrogen-atom transfer to the cluster then crucially depends on the presence of a vanadium atom in the cluster. The key issue for the second HAT as well as OAT concerns the redox activity of the elements present in the cluster. Both reactions correspond to a one-electron reduction of the cluster, *i.e.* the accessibility of the formal oxidation state $+IV$ of vanadium and phosphorous determines

the PESs of these reactions. While vanadium can be reduced easily from $+V$ to $+IV$ and therefore stabilize the radical site formed in the course of reductive processes, phosphorous strongly disfavors oxidation state $+IV$; however, a direct interaction of the redox-active transition metal with the hydrocarbon is not required to bring about ODH reactivity under thermal conditions.

Even more pronounced substitution or „doping“ effects are observed in the comparative study of the small $[VPO_4]^{\bullet+}$ and $[V_2O_4]^{\bullet+}$clusters. While $[V_2O_4]^{\bullet+}$ was found to be rather unreactive, the $[VPO_4]^{\bullet+}$ ion brings about ODH and hydride abstraction from saturated hydrocarbons, *i.e.* propane and *n*-butane, as well as oxygen-atom transfer to unsaturated hydrocarbons, *i.e.* ethene, at thermal conditions. With respect to the electronic structure, the situation is comparable for both clusters in that the spin is in both systems completely localized on the vanadium atom, corresponding to a formal oxidation state of $+IV$; thus, because the bonding and electronic properties of the vanadium atoms are similar in $[V_2O_4]^{\bullet+}$ and $[VPO_4]^{\bullet+}$, the phosphorous atom in the latter is most likely directly involved in the reactions. In fact, a P−C bond is formed along the reaction mechanism of the OAT process and the actual C−H bond activation step in the ODH occurs at the phosphorous atom. However, the latter reaction corresponds to a coupled hydride/proton transfer rather than an HAT process with intermediates possessing a radical character. To conclude, the intrinsic properties of phosphorous cause a significant impact on the reactivity and thus should be considered in upcoming investigation on gas-phase, condensed-phase, and surface-mediated bond activation processes.

With respect to understanding of processes on surfaces, especially for *VPO*-catalysts which have been synthesized and applied in industry for many years with little understanding of the underlying mechanisms that are responsible for their excellent selectivity towards hydrocarbon oxidation, the results on *VPO*-clusters provide a model system for chemical understanding at a molecular scale. Although the charge of the gas-phase clusters certainly affects the energetics of the investigated processes compared to the neutral systems, further investigation of these model systems can help to elucidate reaction mechanisms and provide hints with respect to the structure of reactive intermediates in heterogeneous catalysis; these insights should be considered relevant for designing real catalytic systems. Nevertheless, a recent study on the electronic structure of $[V_3O_{6\text{-}8}]^+$ in the gas phase brings into mind that gas-phase structures can be highly sensible to their surrounding. [445] As shown by the elegant combination of theory and experiment, it is revealed that the structure of $[V_3O_7]^+$ can vary depending on the rare-gas atom attached to it; while the attachment of a neon atom results in the formation of a cage structure, the substitution with argon decreases the isomerization barrier, resulting in the formation of a ring structure. Thus, even a rare-gas atom can have an remarkable effect on the structure of a gas-phase cluster. Nevertheless, while the conclusions derived from gas-phase studies cannot directly be transferred to bulk

chemistry, insights at a molecular level from gas-phase (ion) chemistry find support in many surface and solution-phase studies.

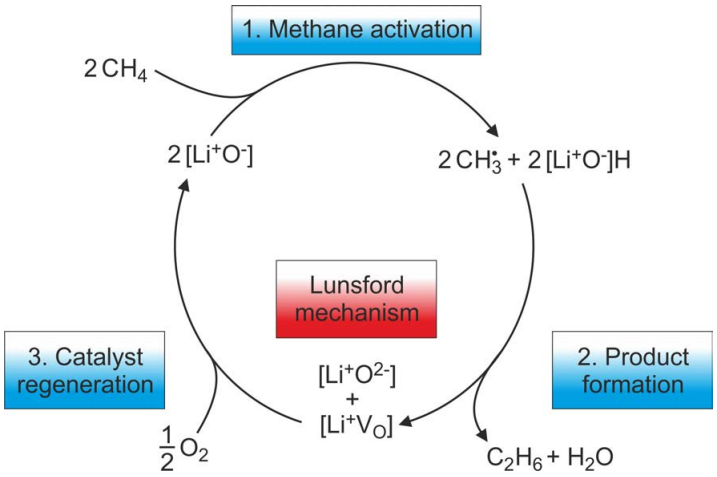

Figure 6.1: The postulated Lunsford mechanism for the oxidative coupling of methane (adapted from Ref. [446]).

As an illustrive example, with respect to active sites in oxo-clusters, serves the crucial role of a high spin density at the abstracting oxygen site. Comparing different polynuclear aluminum-oxide clusters with the only difference being the presence or absence of a M−O• radical, the former exhibit a much higher reactivity towards methane; this origins from the higher activation barrier for the C−H bond scission, as shown by DFT calculations. Thus, if these studies are of any relevance for real catalytic systems, oxygen-centered radicals should also play an important role in the chemistry at complex surfaces. In fact, a well-known example concerns the Lunsford mechanism for the OCM process on lithium-doped magnesium-oxides (Figure 6.1).[241,242] According to Lunsford´s suggestion,[241,447] the active site of metal-oxide surfaces corresponds to an oxygen-centered radical, formed *in situ* at sufficiently high temperatures. However, due to their rather low thermal stability and the difficulties to investigate the complex processes on real surfaces at elevated temperatures, the nature of the reactive sites is still under debate.[36,41,446,448,449] In a related context, more recent surface studies[360,450–453] prove that the homolytic C−H bond cleavage can be achieved by systematically generated radical M−O• moieties at ambient conditions. Briefly, as revealed by carefully conducted studies on iron-doped zeolites FeZSM-5, so called α-sites are formed at high temperatures.[452,454–457] These α-sites correspond to Fe^{II} moieties which are produced from auto-reduction of Fe^{III} to Fe^{II} concomitant with the evolution of O_2. Further, the $(Fe^{II})_\alpha$ sites can be oxidized by use of N_2O, generating the highly active radical oxygen species $(Fe^{III}\text{-}O^\bullet)_\alpha$. This active site selectively activates methane to methanol as the only observed reaction product at room temperature and mechanistic studies show that

the rate-determining step corresponds to the C−H bond cleavage. This holds true for both mechanistic scenarios occurring on the surface, deduced from the ratio of CH_4 to the number of α-oxygen sites at the surface (Figure 6.2). [452] Thus, the combined studies presented in this thesis serve as excellent example for the possible effective interplay between gas-phase and surface chemistry.

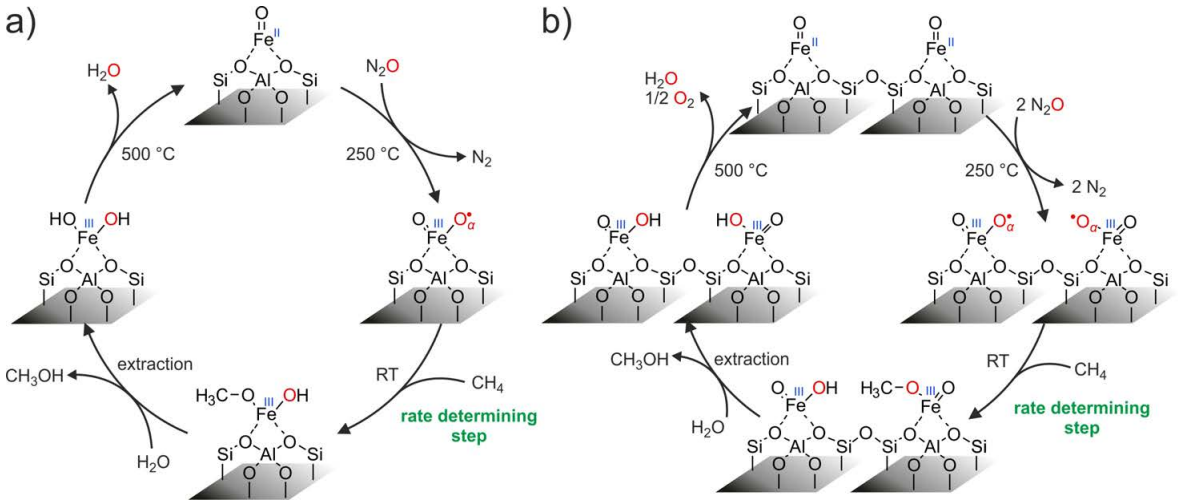

Figure 6.2: Catalytic cycles for the oxidation of CH_4 by N_2O over FeZSM-5. Mechanistic studies suggest that the reaction proceeds as a combination of both pathways, either at a single (a) or at two adjacent $(Fe^{III}\text{-}O^{\bullet})_\alpha$ sites (b). However, for both cycles, the HAT process is the rate determining step and facilitated by the high spin density at the radical $(Fe^{III}\text{-}O^{\bullet})_\alpha$ site (Cycle (a) is identical to that described by Wood *et al.* [456]).

Also the investigation of small, diatomic oxo-cations provides substantial insights into the nature of chemical processes. For the $[CuO]^+$ ion, even though formally a *closed-shell* system, the rather high spin density at the oxygen atom in the triplet-ground state enables the kinetically demanding, homolytic C−H bond activation step, giving rise to either the HAT products or the direct formation of methanol (OAT); moreover, two-state reactivity in combination with the rather small bond energy of $[Cu^+\text{−}O]$ triggers the latter conversion process. Quite remarkably, the two metal-oxides that initiate HAT as well as OAT in the thermal ion/molecule reaction with methane, *i.e.* $[FeO]^{\bullet+}$ and $[CuO]^+$, are composed of the same metals that facilitate the biological oxidation of methane to methanol by the two methane monooxygenases, *i.e.* iron in soluble and copper in particulate MMO. Thus, there is a remarkable agreement between the gas-phase chemistry of these systems with observation in biological chemistry. Besides, this study represents *„the final piece in an intriguing puzzle“*, [143] since bare $[CuO]^+$ was predicted a decade ago to be a suitable methane-to-methanol converter and was so far the only bare transition-metal oxide cation of the first row whose reactivity towards methane had not been experimentally investigated.

Moreover, the investigation on the carbon and silicon oxides with respect to their reactivity towards methane completes the chapter on the group 14 metal-oxide cations. $[SiO]^{\bullet+}$ reacts in line with the previously reported heavier analogues of germanium, tin, and lead, while $[CO]^{\bullet+}$ represents the very first cationic system which is able to react at two reactive sites, *i.e.* the oxygen- as well as the carbon-site, thus resulting in two HAT processes. Finally, the reaction of $[MO]^{+}$ (M = Mn, Mg, Ca) with valeronitrile clearly suggests the potential as well as the feasibility of *remote functionalization* of C−H bonds by bare metal oxides in the gas phase. Accordingly, this work emphasizes the conceptual idea of *remote functionalization* and may stimulate prospective research to develop new methods based on it, improving the regioselectivity of C−H bond activation processes along saturated carbon chains.

In summary, the present work aims at a better, more fundamental understanding on the nature of oxidation processes in homogeneous, heterogeneous and enzymatic catalysis. However, returning to the initial statement of Max Planck that „*insight must precede application*“, [1] the knowledge presented in this thesis provides just a small step on the long way to fulfill Plancks initial idea of research; in fact, fundamental research will presumably never be able to catch up with the fast spreading of industrial applications. Thus, only by continuous efforts in fundamental research, the underlying concepts of chemistry can be revealed, leading to a more effective utilization of natural resources.

APPENDIX

A List of Abbreviations

BDE	bond dissociation energy
br	branching ratio
CID	collision-induced dissociation
CRM	charge-residue model
$\Delta E^{\neq}$	activation energy
DFT	density-functional theory
ECD	electron-capture dissociation
ESI	electrospray ionization
FID	free induction decay
FT-ICR	fourier-transform ion cyclotron resonance
fwhm	full width at half maximum
HAT	hydrogen-atom transfer
HIA	hydride ion affinity
HOMO	highest occupied molecular orbital
I	intensity
IE	ionization energy
IEM	ion-evaporation model
IMR	ion/molecule reaction
IRMPD	infrared multiphoton dissociation
ISC	intersystem crossing
ISCID	in-source collision-induced dissociation
IVR	intramolecular vibrational relaxation
k	rate constant
KIE	kinetic isotope effect
LDI	laser desorption/ionization
LUMO	lowest unoccupied molecular orbital
MMO	methane monoxygenase
MS	mass spectrometry
OAT	oxygen-atom transfer
OCM	oxidative coupling of methane
ODH	oxidative dehydrogenation
O_t	terminal oxygen atom
p	pressure
PES	potential-energy surface

RF	radio frequency
rt	room temperature
SET	single-electron transfer
SOMO	semi-occupied molecular orbital
TOF	time-of-flight
TS	transition state
TSR	two-state reactivity
UHV	ultra-high vacuum
ZPE	zero-point energy

B Experimental Details

B.1 Chemicals

The majority of the chemicals required for the mass spectrometric investigations within the framework of the present thesis were commercially available; thus, they were purchased from Sigma-Aldrich, Fluka, Alfa Aesar, Linde, or TCI and used without further purification. Deuterated organic substrates were purchased from Sigma-Aldrich, C/D/N Isotopes, or Cambridge Isotope Laboratories. For those chemicals that were nor commercially available, their preparation is described in the following.

B.2 Preparative details

Targets for the laser-induced generation of $[V_2P_2O_{10}]^{\bullet+}$ and $[V_3PO_{10}]^{\bullet+}$

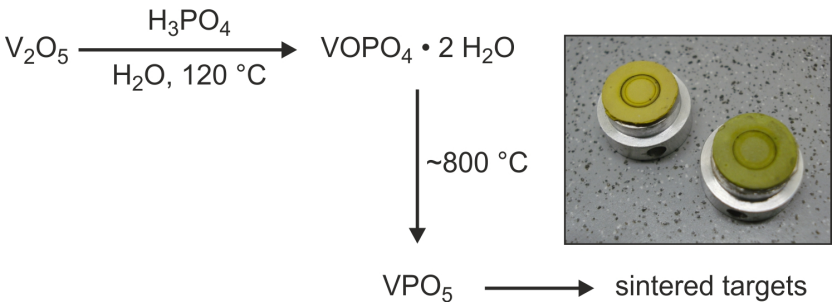

Figure B.1: Preparation and image of suitable *VPO*-targets.

The inorganic precursor $VOPO_4{\cdot}2H_2O$ was prepared by a slightly modified literature-known procedure:[458] In a reaction flask, vanadium(V) oxide V_2O_5 (24 g, 132 mmol) was suspended in distilled water (550 ml) and concentrated phosphoric acid H_3PO_4 (150 ml) and the resulting mixture was refluxed at 120 °C for 24 hours. Afterwards, the green-yellow, crystalline solid was isolated by vacuum filtration. The product was washed sparingly with water, ethanol and then acetone and dried for several days under high vacuum at room temperature. $VOPO_4{\cdot}2H_2O$ (42 g, 211 mmol, 80 %) was recovered as a yellow powder and identified by X-ray powder diffraction (Siemens D 5000 diffractometer, Cu-$K_{\alpha 1}$ radiation, Bragg-Brentano geometry). The exact water content of the

$VOPO_4 \cdot xH_2O$ phase was determined to x = 1.95 by thermogravimetric analysis (NETZSCH STA 409). Additional thermoanalytical measurements in air point to complete water loss at 150 °C and melting of the resulting powder at 800 °C. The powder, which can be described as poorly crystalline vanadyl phosphate, was pressed to pellets (diameter: 12 mm, thickness 1-1.5 mm) and sintered in air for 24 h at 700 - 750 °C in a conventional chamber furnace. The mechanical stability of the resulting pellets is sufficient for the laser laser desorption/ionization procedures described in Chapter 2.1.2.

Deuterated valeronitriles

The general procedure for the synthesis of valeronitrile is depicted in Figure B.2. It consists of three (repeating) steps, *i.e.* the reduction of the acid with $LiAlH_4$, the Grignard reaction of the halides with carbon dioxide, and the nucleophilic substitution with deprotonated acetonitrile. For mechanistic studies, the deuterated isotopomers $LiAlD_4$ 98 % D_4; CD_3COOD 99.5 % D_4 and CD_3CN 99.8 % D_3 were employed to achieve the regiospecific labeling at the respective positions. The label content was determined by means of NMR and mass spectrometry and corresponds to the isotopic purity of the reagents employed; corrections for incomplete labeling were made where appropriate.

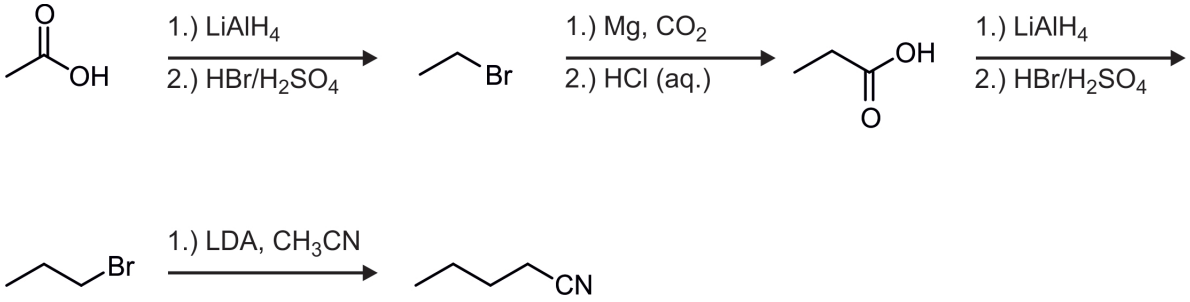

Figure B.2: Total synthesis of valeronitrile.

General procedure for the reduction of the acid with $LiAlH_4$: First, 0.5 eq. of $LiAlH_4$ (2 eq. of H^-) were suspended in diethylether (100 ml per 4 g of $LiAlH_4$) and cooled down to 0 °C. A solution of 1 eq. of the acid in diethylether (2.2 M) was added dropwise and afterwards, the mixture was stirred for 2 hours at 50 °C. After cooling down to room temperature (rt), the solvent was completely removed and the resulting, white residue was cooled down to -78 °C. Then, an excess (1 ml per 1 mmol of organic acid) of hydrobromic acid (conc.) was added carefully. After final addition of concentrated sulfuric acid (tenth part of the volume of the hydrobromic acid), the resulting bromide was removed from the mixture by distillation. The raw product was washed with K_2CO_3-solution and water and dried over $CaCl_2$. After second distillation, the product was obtained as a colorless oil with an overall yield of 48 %.[xxviii]

[xxviii] The yield can be improved by 10 %, if the acyl chloride is commercially available and used as starting material instead of the corresponding acid.

General procedure for the Grignard reaction with carbon dioxide: In a reaction flask, 1.1 eq. of magnesium were suspended in diethylether (10 ml per 1 g of Mg) under a N_2-atmosphere. Then, a small part of a solution of 1.0 eq. of the bromide in diethylether (3 M) was added and the mixture carefully heated, till the reaction started (continuous boiling of the ether), followed by dropwise addition of the residual solution. After the addition had been completed, the mixture was stirred for 15 minutes at rt and another 30 minutes at 45 °C. Then, the mixture was cooled down to -78 °C and a few chunks of solid CO_2 were added. Hence, the solution was allowed to heat up to rt to complete the reaction, and cooled down again to 0 °C. After complete hydrolysis with hydrochloric acid (2 M HCl) and threefold extraction with diethylether, the organic layers have been dried over $MgSO_4$ before the solvent was removed under reduced pressure. The clean product was obtained by *bulb-to-bulb* distillation as a colorless oil with a yield of 60 %.

General procedure for the nucleophilic substitution with deprotonated acetonitrile: The reaction flask was charged with 1.0 eq. of lithium diisopropylamide (LDA) as a suspension in *n*-hexane; two-third of the solvent were subsequently removed (via syringe) and replaced with dry tetrahydrofuran (THF). After the suspension was cooled down to -78 °C, a solution of 1 eq. of the acetonitrile in THF (5 M) was added dropwise and stirred for 10 minutes. Then, 1.1 eq. of the bromide were added dropwise before the mixture was stirred for another 60 minutes at -78 °C and rt, respectively. In the following, hydrochloric acid (1 M HCl, 2 ml per 1 mmol of acetonitrile) was added to the mixture, which was then washed with $NaHCO_3$-solution and water. The organic layer was dried over $MgSO_4$ before the solvent was removed under reduced pressure. The clean product was obtained by *bulb-to-bulb* distillation as a colorless oil with an yield of 91 %.

B.3 Details on ion generation and experimental setup

Generation of $[V_xP_{4-x}O_{10}]^{\bullet+}$ (x = 0, 2 - 4)

For $[P_4O_{10}]^{\bullet+}$ experiments were carried out with the Bonn FT-ICR mass spectrometer. Commercially available P_4O_{10} was introduced in the EI-source with a direct inlet probe at 350 °C (source temperature 180 °C).

For the mixed clusters $[V_xP_{4-x}O_{10}]^{\bullet+}$ (x = 2,3), the reactivity experiments were performed with the Kiel FT-ICR mass spectrometer. The cluster cations were produced via laser vaporization of the previously prepared, rotating VPO-target with a 5 ns laser pulse of a frequency-doubled Nd:YAG laser (Continuum Surelite II, 10 Hz, 5 mJ pulse energy), followed by supersonic expansion of the hot plasma in a triggered helium pulse.

Table B.1: List of the FT-ICR mass spectrometer employed in the framework of this thesis.

Location of the machine	Mass Spectrometer	Source-type	Magnet	Special Modifications
Kiel	Bruker/Spectrospin CMS47X	homebuilt, modified Smalley-type [132,133] cluster-ion source	4.7 T	Apex III data station
Berlin	Spectrospin CMS47X	external, homebuilt Smalley-type cluster-ion source [459,460]	7.05 T	
Bonn	Bruker APEX IV	standard (Bruker Bremen) 70 eV EI-source	7.05 T	
Rome	EXTREL FTMS 2001 double-cell MS	single batch inlet systems (Extrel) with EI in „source cell“	2.8 T	MKS ion gauge controller type 290, electronic and operative systems (IONSPEC)

For the control experiments with $[V_4O_{10}]^{\bullet+}$, the experiments were carried out using the triple quadrupole mass spectrometer with QHQ configuration and equipped with an ESI source (Section 2.2.1). Briefly, the vanadium oxide cluster were generated by ESI of a millimolar solution of $V_6O_7(OCH_3)_{12}$ in CD_3OD, which were introduced through a fused-silica capillary to the ESI source by syringe pump (ca. 4 μl min^{-1}). Nitrogen was used as nebulizing and drying gas at a source temperature of 80 °C. Maximal yield of the desired metal oxide was achieved by adjusting the cone voltage to 190 V.

Generation of $[VPO_4]^{\bullet+}$ and $[V_2O_4]^{\bullet+}$

The reactivity and CID experiments were carried out using the triple quadrupole mass spectrometer with QHQ configuration equipped with an electrospray ionization source (Section 2.2.1). $[VPO_4]^{\bullet+}$ cluster was generated by ESI of a millimolar solution of $VOCl_3$ and $PO(OEt)_3$ (both purchased from Sigma-Aldrich) in methanol, which were introduced through a fused-silica capillary to the ESI source by a syringe pump (ca. 3 μl min^{-1}); for $[V_2O_4]^{\bullet+}$ a millimolar solution of $VO(O\mathit{i}Pr)_3$ (Sigma-Aldrich) was emploied. Nitrogen was used as nebulizing and drying gas at a source temperature of 80 °C. Maximal yield of the desired oxide cation was achieved by adjusting the cone voltage to 140 V for $[VPO_4]^{\bullet+}$ and 160 V for $[V_2O_4]^{\bullet+}$, respectively.

IRPD experiments with $[VPO_4]^{\bullet+}$

The IRPD experiments are carried out using the ion trap-tandem mass spectrometer described in Chapter 2.2.3. [169,170] Gas-phase ions are produced in a commercial Z-spray source. The beam of ions passes a 4 mm skimmer and is then collimated in a RF decapole ion guide. The collimated ion beam enters a quadrupole mass filter that serves to mass-select the $[VPO_4]^{\bullet+}$ parent ions, which are subsequently focused into a cryogenically-cooled RF ring electrode ion trap. The trap is continuously filled with a helium buffer gas at an ion trap temperature of 15 K, allowing the accumulation and thermalization of the ions. Inside the ion trap, the mass-selected $[VPO_4]^{\bullet+}$ ions undergo three-body collisions with the buffer gas which promote the formation of weakly bound ion-He atom complexes. Under the present experimental conditions a distribution of helium-tagged complexes $[VPO_4]^{\bullet+}\cdot He_n$ is formed, ranging from n = 1 - 3 (Figure B.3), with n = 2 corresponding to the most abundant species; these complexes are used for the IRPD measurements. After loading the ion trap for 98 ms, all ions are extracted and focused both temporally and spatially into the center of the extraction region of an orthogonally mounted linear time-of-flight (TOF) mass spectrometer. Here, the ion packet is irradiated with an IR laser pulse, and high-voltage extraction pulses are applied for recording TOF mass spectra. Pulsed IR radiation is provided by a tabletop OPO/OPA/$AgGaSe_2$ IR laser system (LaserVision) [173] which is pumped by a pulsed, seeded Nd:YAG laser (Continuum, Powerlite P-8000). The pump laser operates at a repetition rate of 10 Hz and provides 7 ns long pulses. The IR laser system is operated in the spectral region from 800 cm^{-1} to 1500 cm^{-1}, in which IR pulses with pulse energies $\geq$ 4 mJ and a spectral bandwidth of 1.8 cm^{-1} are typically produced.

Measuring an IRPD spectrum of each complex $[VPO_4]^{\bullet+}\cdot He_n$ with n = 1 - 3 individually, is generally not straightforward. All of these complexes are present in the ion packet, which is extracted from the trap, and simultaneously interact with the IR laser pulse. When the laser is on resonance with a vibrational transition, all ions can dissociate, *e.g.* via loss of helium atoms, which may lead to „cross-talk“ between the different dissociation channels. For example, the n = 2 mass channel may contain contributions from both parent and photofragment ions, *i.e.* the n = 2 complex can dissociate into lighter species (n = 0, 1) and the former can be formed by dissociation of the heavier complex n = 3. This makes the distinction of ion signals into parent and fragment ions ambiguous. In the present experiment, this problem is circumvented by irradiating the ion packet during the acceleration phase in the TOF mass spectrometer, *i.e.* the IR laser pulse is applied 1 μs after the high-voltage extraction pulses. As a consequence, parent and photofragment ions of identical mass acquire different amounts of kinetic energy and thus lead to separate peaks in the TOF mass spectrum (see Figure S1 B.3), *i.e.* IRPD spectra can be measured background-free. This technique has been described earlier in IRPD studies on krypton-tagged suberate dianions. [170] IRPD spectra of the most abundant helium-tagged complexes n = 2 and n = 1 are measured. At typical

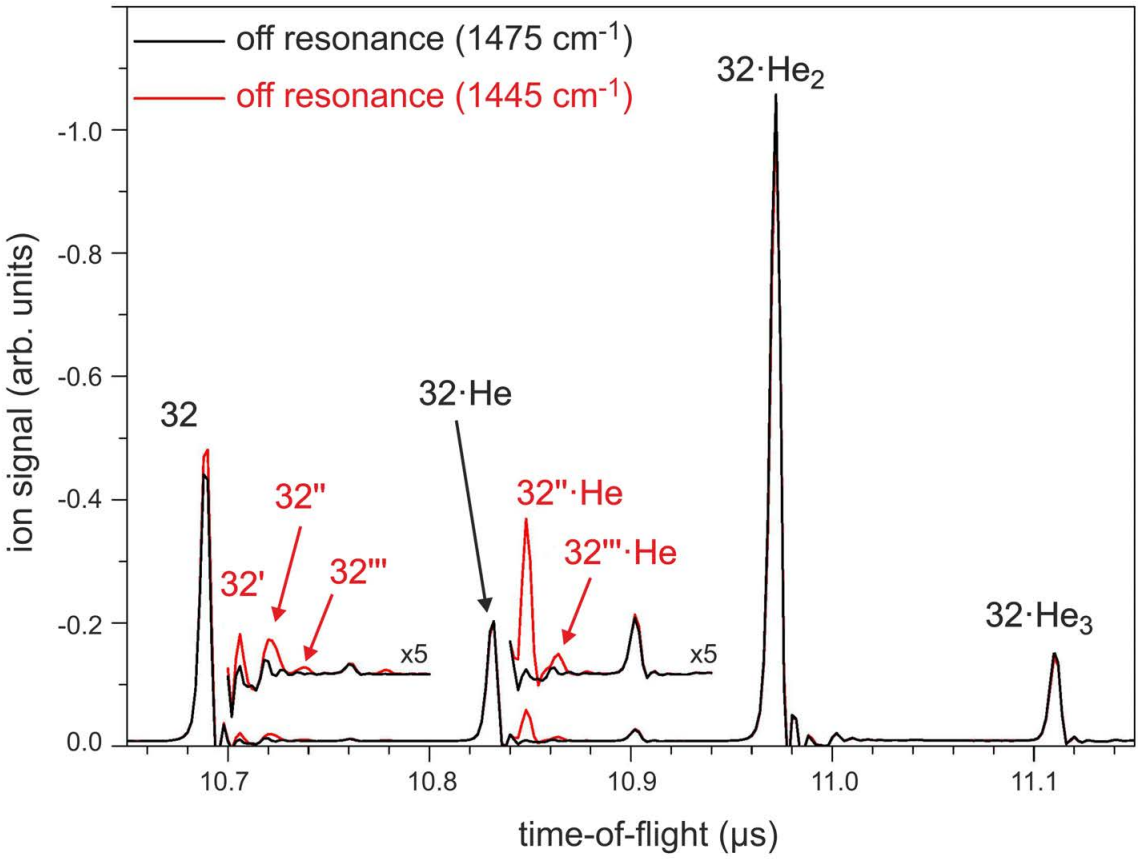

Figure B.3: TOF mass spectra of helium-tagged $[VPO_4]^{\bullet+}$(**32**) ions recorded after irradiation by an IR laser pulse. When the laser wavenumber is tuned off resonance (1475 cm^{-1}) with a vibrational transition, the spectrum (black trace) reflects the distribution of ion−He atom complexes **32**·He_n (n = 0 - 3) formed inside the ion trap. The red trace corresponds to the ion yield when the laser wavenumber is tuned on resonance with a vibrational transition around 1445 cm^{-1}. The laser pulse is triggered shortly after (1 μs) the high voltages pulses have been applied to the TOF extraction plates. As a consequence, the photofragment ions arising from dissociation of the complexes n = 1 - 3 can be discriminated and detected background-free (red labels). For example, complex n = 2 loses two helium atoms leading to the formation of the helium complex **32**''·He (10.85 μs) and the bare ion **32**'' (10.72 μs).

pulse energies $\geq$ 4 mJ, IRPD of these complexes proceeds only via loss of one or more helium atoms. TOF spectra are recorded 50 - 70 times for each wavelength step. IRPD spectra are obtained by plotting the relative photodissociation cross section σ according to $\sigma \propto ln[1 - I_F(\nu)/(I_F(\nu) + I_P(\nu))]/P(\nu)$ with the parent ion $(I_P(\nu))$ and photofragment ion $(I_F(\nu))$ intensities and the frequency-dependent laser pulse energy $P(\nu)$.

Generation of $[CuO]^+$

The experiments with $[CuO]^+$ were performed at the Kiel FT-ICR mass spectrometer. The $[CuO]^+$ cation was produced by laser vaporization of a rotating, isotopically pure ^{63}Cu-target, followed by supersonic expansion of the hot plasma in a triggered helium/N_2O pulse; depending on the pulve valve emploied, the ratio varies from 5:1 to 100:1. The isotopically pure copper sample was purchased from STB Isotope Germany GmbH (^{63}Cu 99.3 %).

Generation of $[CO]^{\bullet+}$ and $[SiO]^{\bullet+}$

The experiments with $[SiO]^{\bullet+}$ were performed at the Berlin FT-ICR mass spectrometer. The silicon cation $[Si]^{\bullet+}$ was generated by laser ablation of a rotating silicon wafer (Sigma-Aldrich) using a Nd:YAG laser operating at 1064 nm, followed by supersonic expansion of the hot plasma in a triggered helium pulse. Next, the mass-selected ion $[Si]^{\bullet+}$ is reacted with pulsing in N_2O in the ICR cell to generate $[SiO]^{\bullet+}$.

The FT-ICR experiments with $[CO]^{\bullet+}$ were carried out with the Rome FT-ICR mass spectrometer. CO was admitted into the „source cell“ and $[CO]^{\bullet+}$ ions were generated by electron impact (100 ms, 40 eV). In all experiments, the $[CO]^{\bullet+}$ ions were isolated after a cooling period of 2.9 seconds, and transferred into the „analyzer cell“ containing the neutral reactant.

C Supplementary Material

Additional Figures for Chapter 3

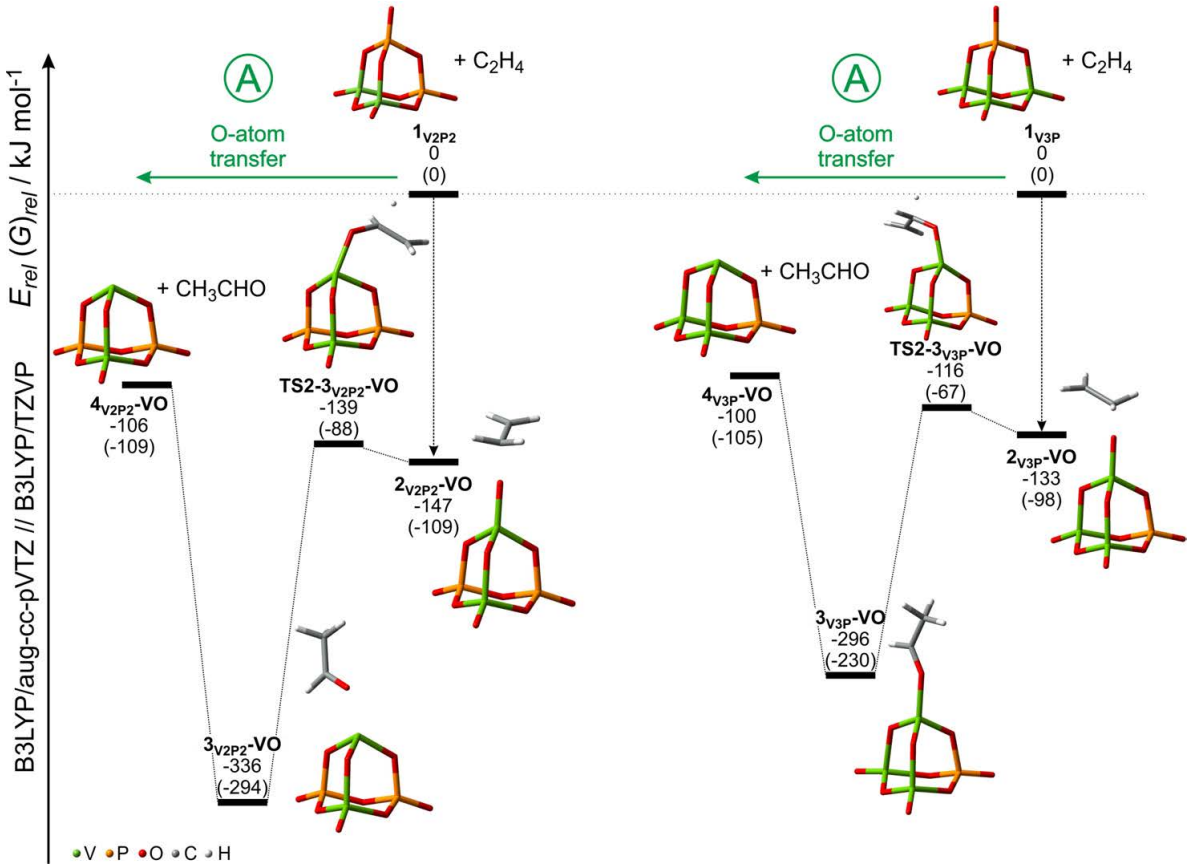

Figure C.1: Alternative OAT pathway for the reactions of $[V_2P_2O_{10}]^{\bullet+}$and $[V_3PO_{10}]^{\bullet+}$with C_2H_4, concerning the transfer of the oxygen atom from the V=O moiety, calculated at the B3LYP/aug-cc-pVTZ//B3LYP/TZVP level of theory (green V, yellow P, red O, gray C, white H). The electronic energies and relative Gibbs free energies (in parentheses) are given in kJ mol^{-1}and corrected for unscaled zero-point energy contributions.

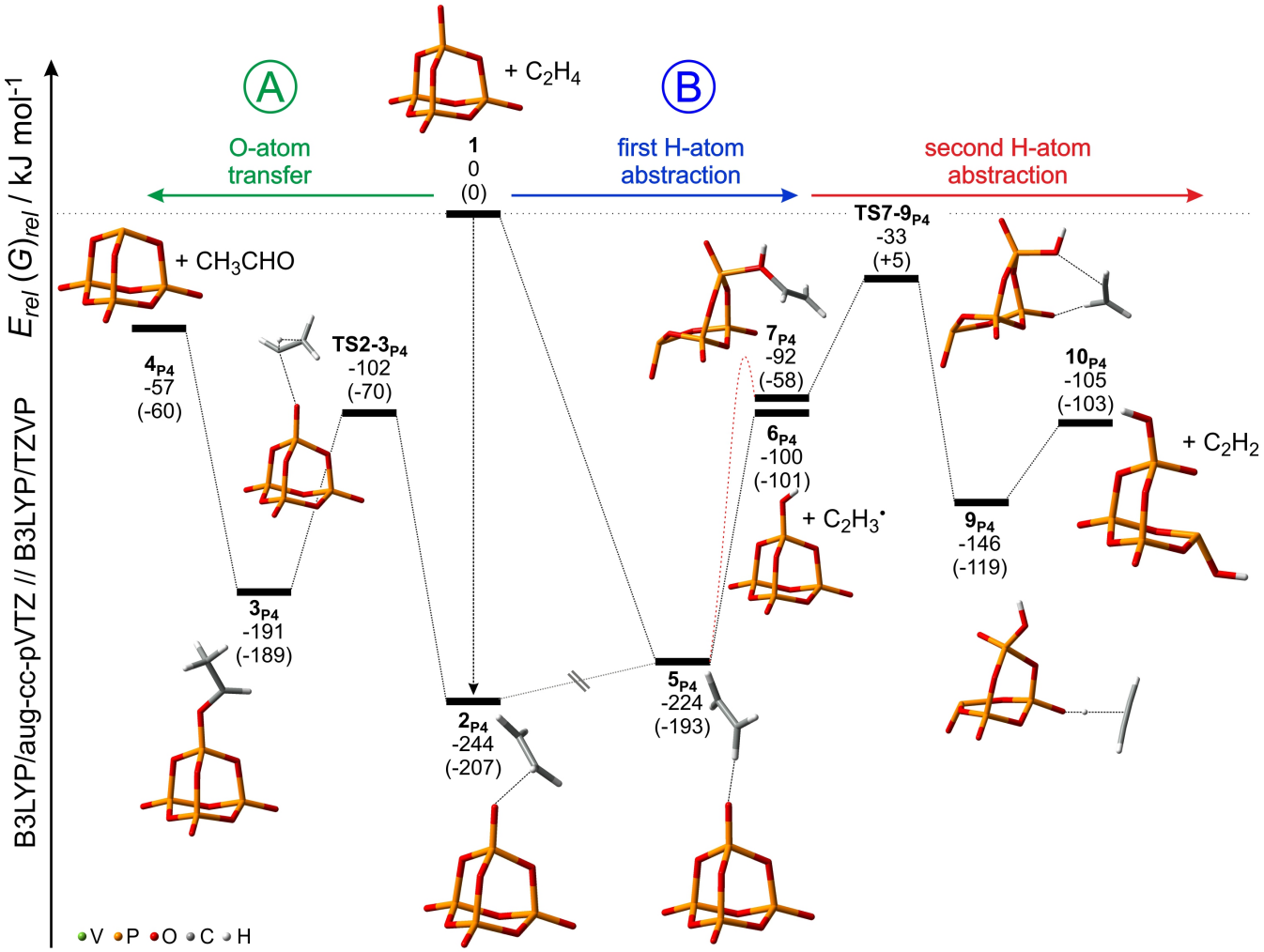

Figure C.2: PES for the reaction of $[P_4O_{10}]^{\bullet+}$ with C_2H_4, calculated at the B3LYP/aug-cc-pVTZ//B3LYP/TZVP level of theory (green V, yellow P, red O, gray C, white H). The electronic energies and relative Gibbs free energies (in parentheses) are given in kJ mol^{-1} and corrected for unscaled zero-point energy contributions.

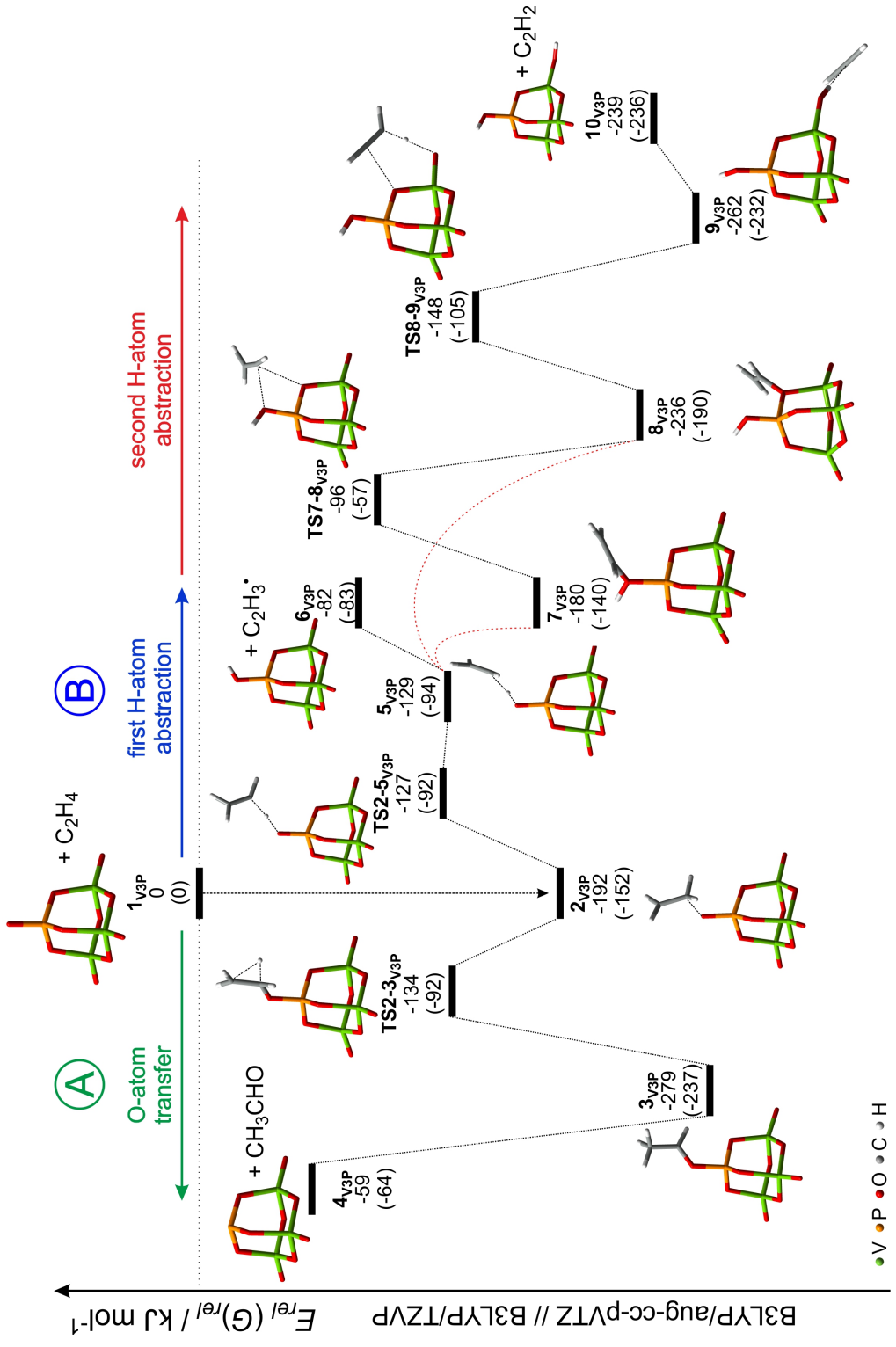

Figure C.3: PES for the reaction of $[V_3PO_{10}]^{\bullet+}$ with C_2H_4, calculated at the B3LYP/aug-cc-pVTZ//B3LYP/TZVP level of theory (green V, yellow P, red O, gray C, white H). The electronic energies and relative Gibbs free energies (in parentheses) are given in kJ mol^{-1} and corrected for unscaled zero-point energy contributions.

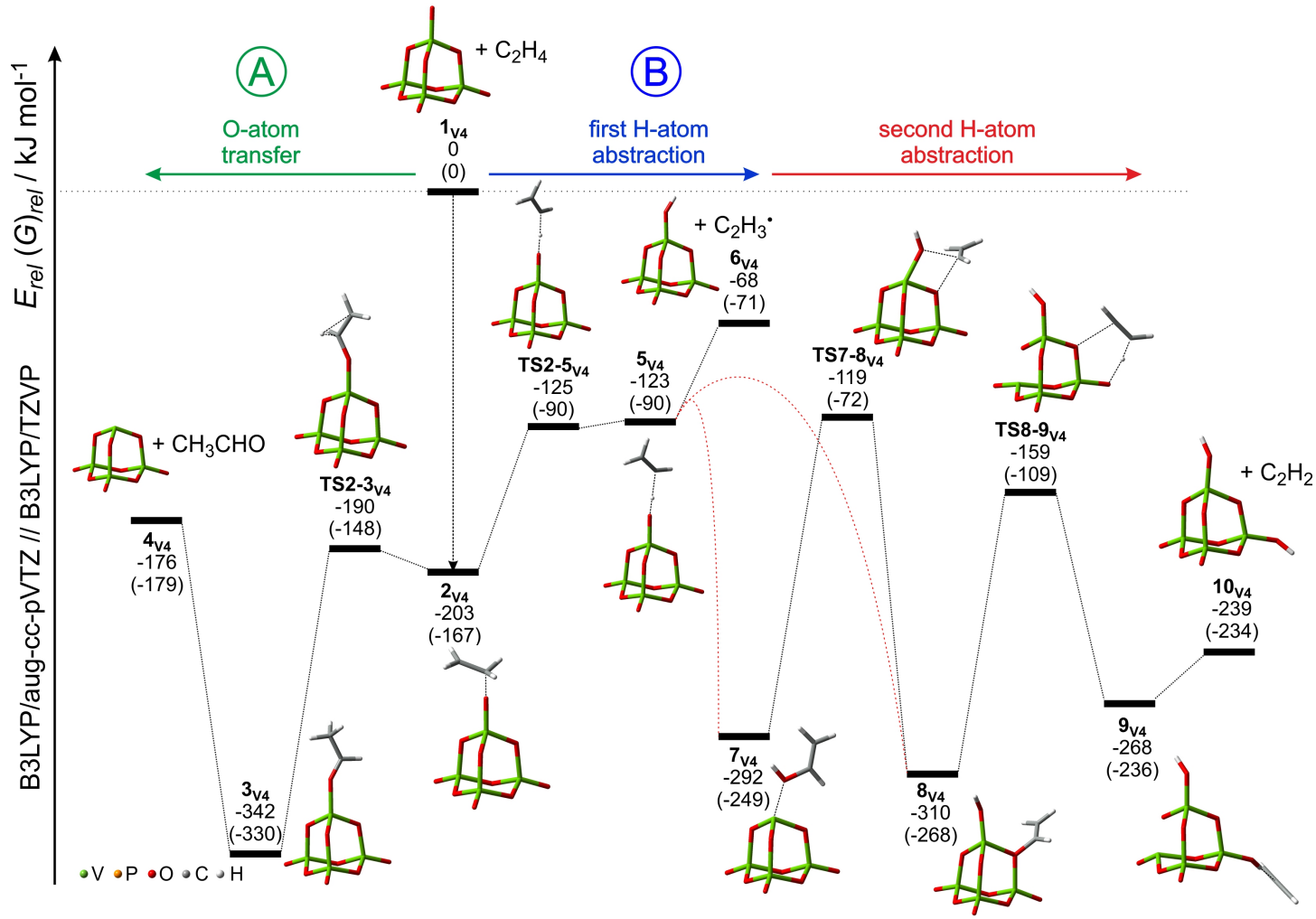

Figure C.4: PES for the reaction of $[V_4O_{10}]^{\bullet+}$ with C_2H_4, calculated at the B3LYP/aug-cc-pVTZ//B3LYP/TZVP level of theory (green V, yellow P, red O, gray C, white H). The electronic energies and relative Gibbs free energies (in parentheses) are given in kJ mol^{-1} and corrected for unscaled zero-point energy contributions.

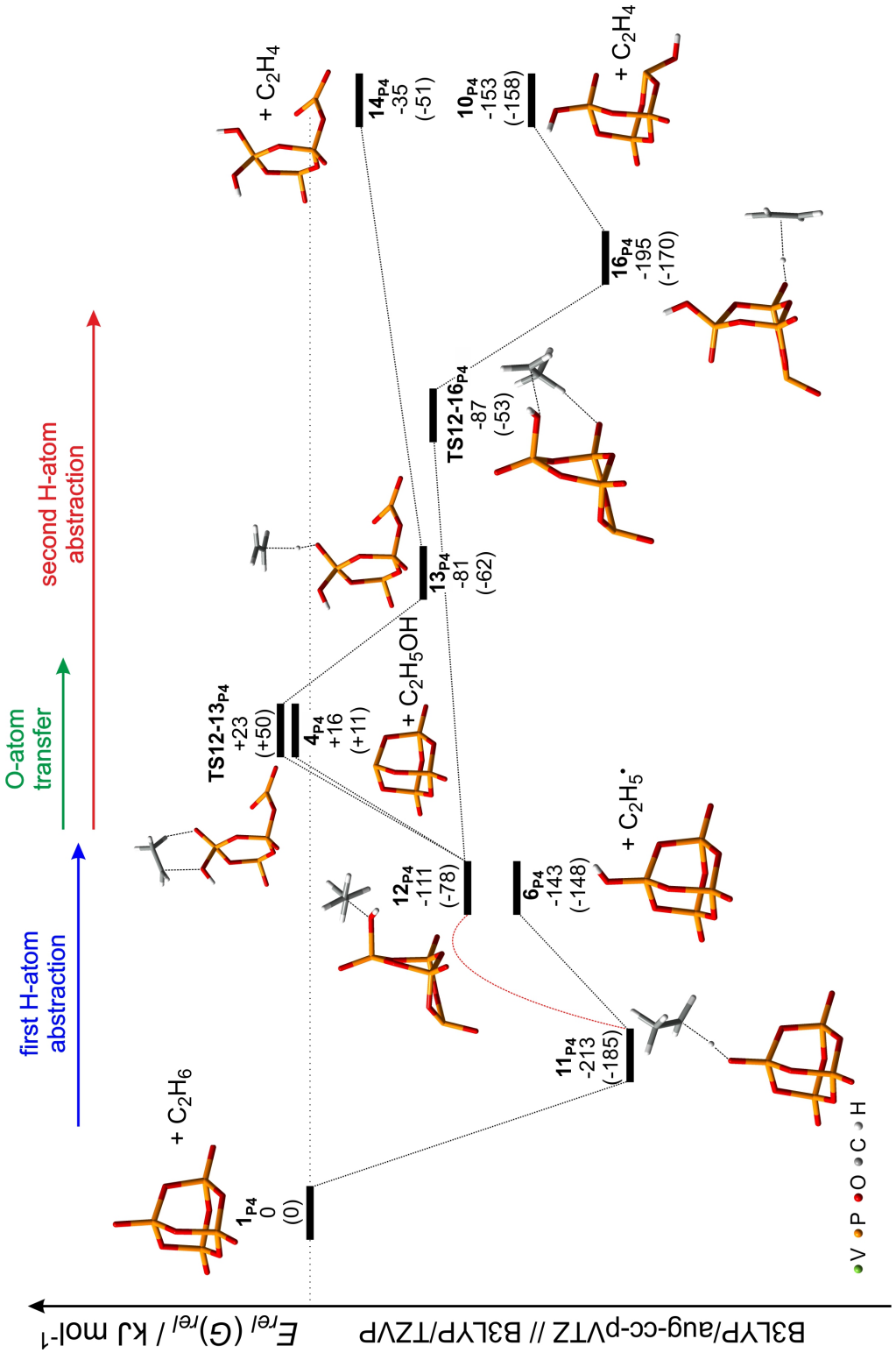

Figure C.5: PES for the reaction of $[P_4O_{10}]^{\bullet+}$ with C_2H_6, calculated at the B3LYP/aug-cc-pVTZ//B3LYP/TZVP level of theory (green V, yellow P, red O, gray C, white H). The electronic energies and relative Gibbs free energies (in parentheses) are given in kJ mol^{-1} and corrected for unscaled zero-point energy contributions.

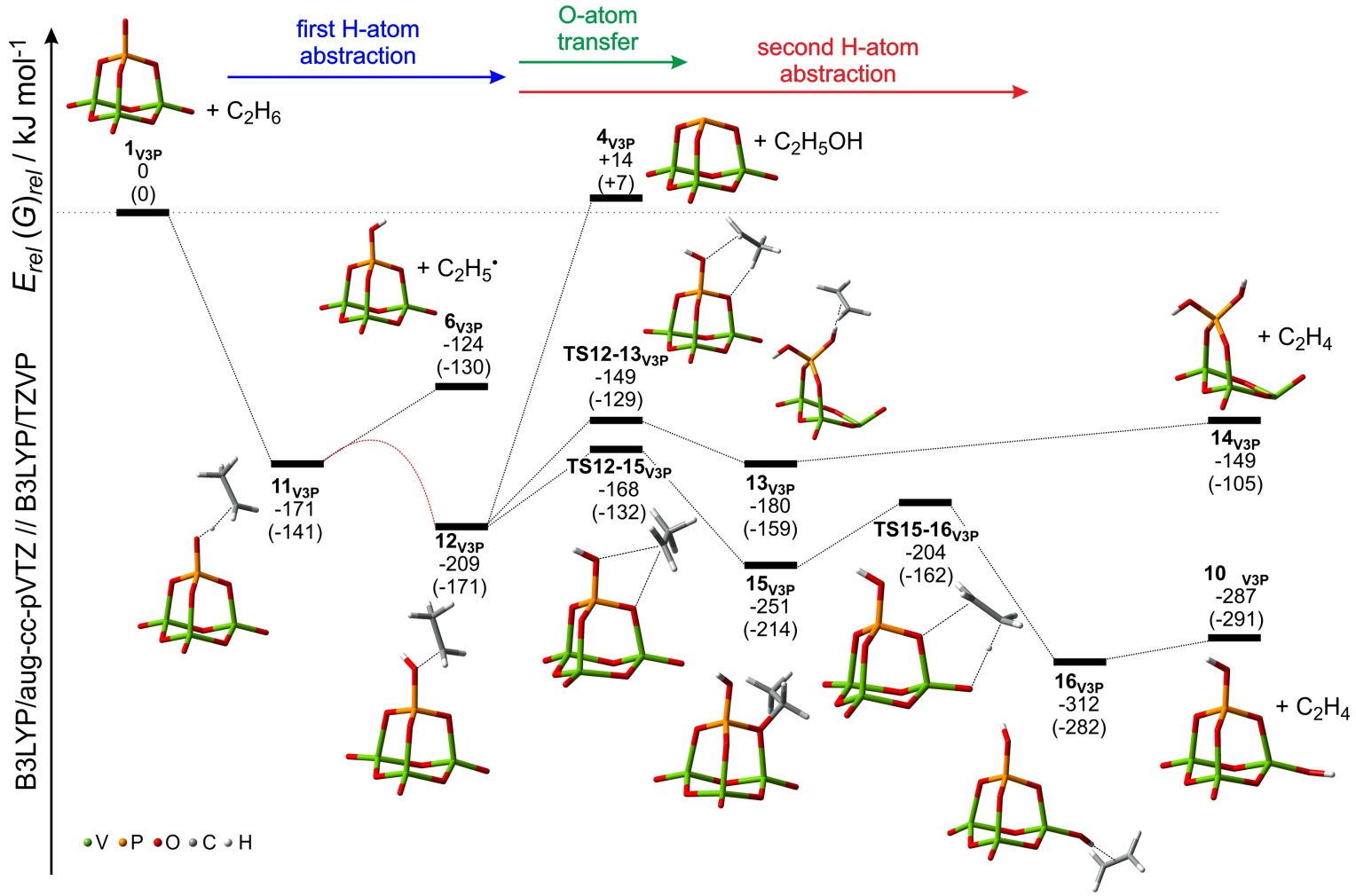

Figure C.6: PES for the reaction of $[V_3PO_{10}]^{\bullet+}$ with C_2H_6, calculated at the B3LYP/aug-cc-pVTZ//B3LYP/TZVP level of theory (green V, yellow P, red O, gray C, white H). The electronic energies and relative Gibbs free energies (in parentheses) are given in kJ mol^{-1} and corrected for unscaled zero-point energy contributions.

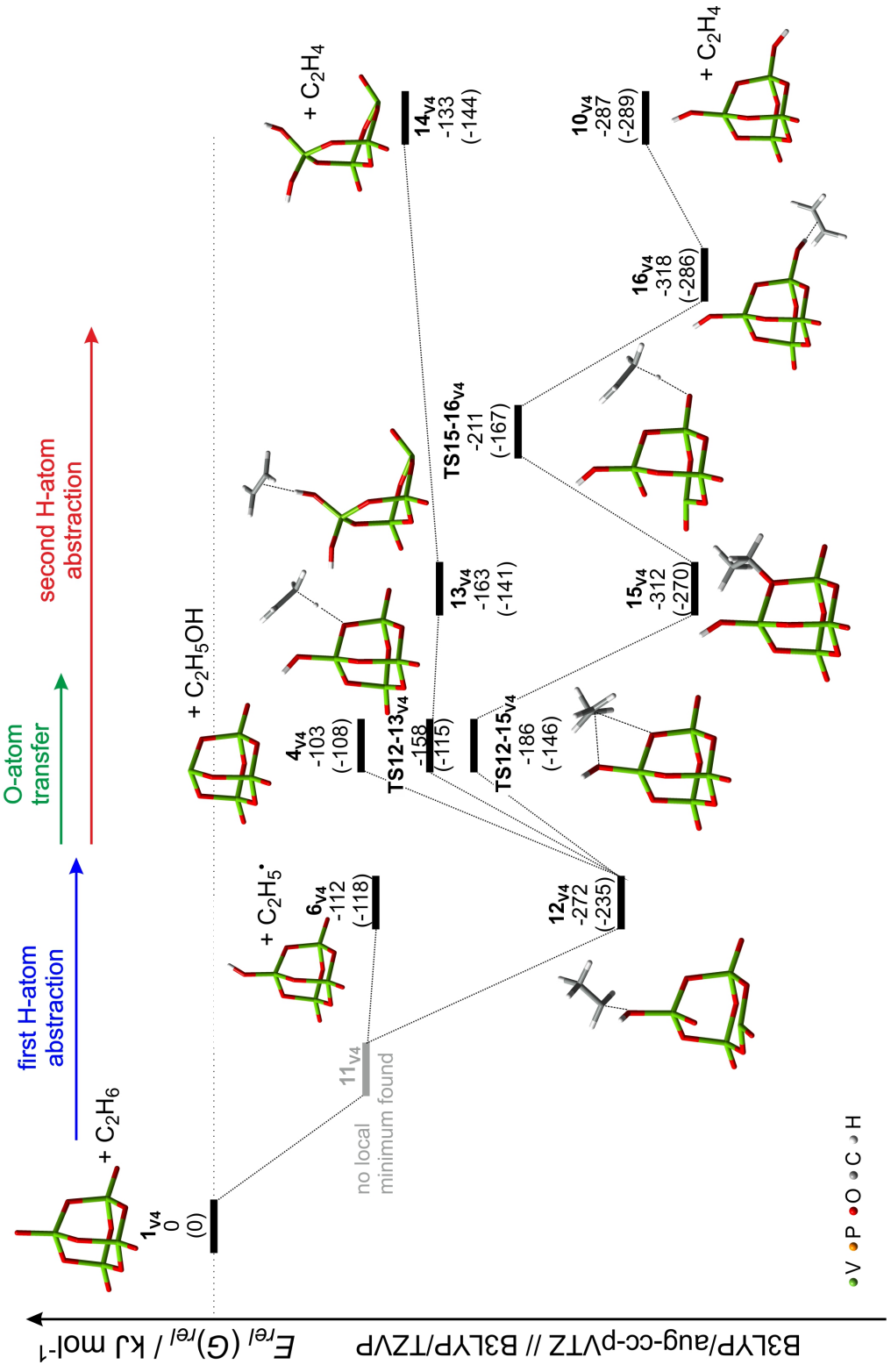

Figure C.7: PES for the reaction of $[V_4O_{10}]^{\bullet+}$ with C_2H_6, calculated at the B3LYP/aug-cc-pVTZ//B3LYP/TZVP level of theory (green V, yellow P, red O, gray C, white H). The electronic energies and relative Gibbs free energies (in parentheses) are given in kJ mol^{-1} and corrected for unscaled zero-point energy contributions.

Additional Figures for Chapter 4.2.3

Figure C.8 reports the reaction profiles obtained by correction of the $[HCO]^+$ and $[CH_4]^{\bullet+}$ intensities.

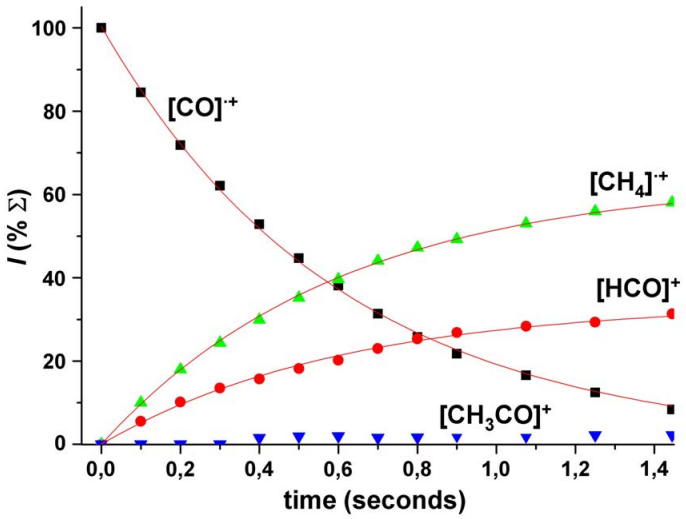

Figure C.8: Kinetic plots and best-fit lines for the reaction between $[CO]^{\bullet+}$ and CH_4 using a $CO/^{13}CO$ mixture (1:1) at the pressure of $p(CO/^{13}CO) = 2.9 \cdot 10^{-7}$ mbar; $p(CH_4) = 7.3 \cdot 10^{-8}$ mbar.

Figure C.9 shows that contributions of the side reactions matter only at higher reaction times and high pressures of CH_4.

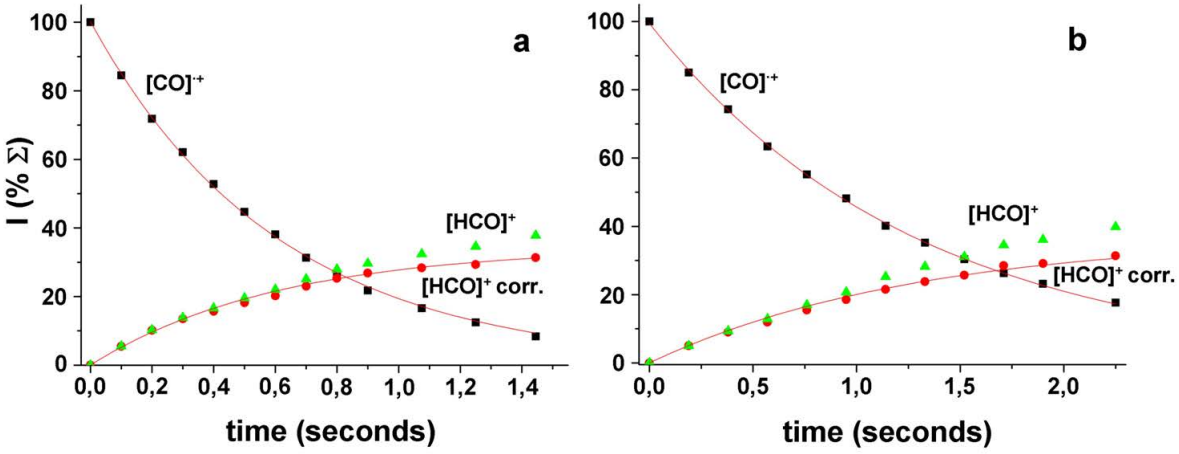

Figure C.9: Corrected $[HCO]^+$ profiles (red dots) and $[HCO]^+$ profiles with no correction applied (green triangles): $p(CO/^{13}CO)) = 2.9 \cdot 10^{-7}$ mbar with (a) $p(CH_4) = 7.3 \cdot 10^{-8}$ mbar (same experiment as Figure C.8) and (b) $p(CH_4) = 3.6 \cdot 10^{-8}$ mbar.

D References

[1] M. Planck, *Naturwissenschaften* **1919**, *48*, 124.

[2] A. P. Kieboom, J. Moulijn, P. W. N. M. van Leeuwen, R. A. van Santen in *Catalysis: An Integrated Approach.* (Eds.: R. A. van Santen, P. W. N. M. van Leeuwen, J. Moulijn, B. A. Averill), Elsevier, Amsterdam, **1999**, pp. 3.

[3] J. J. Berzelius, *Ann. Chim. Phys.* **1836**, *61*, 146.

[4] W. Ostwald, *Z. Elektrochem. Angew. Phys. Chem.* **1901**, *7*, 995.

[5] S. J. Green, *Industrial Catalysis,* E. Benn Limited, London, **1928**.

[6] M. Beller, *Eur. J. Lipid Sci. Technol.* **2008**, *110*, 789.

[7] J. N. Armor, *Catal. Today* **2011**, *163*, 3.

[8] C. F. Cullis, D. J. Hucknell in *Catalysis, Vol. 5* (Eds.: G. C. Bond, G. Webb), The Royal Society of Chemistry, **1982**, pp. 273.

[9] J. Haggin, *Chem. Eng. News.* **1993**, *71*, 27.

[10] J. A. Labinger, J. E. Bercaw, *Nature* **2002**, *417*, 507.

[11] J.-L. DuBois, *Catal. Today* **2005**, *99*, 5.

[12] G. P. McGlacken, L. M. Bateman, *Chem. Soc. Rev.* **2009**, *38*, 2447.

[13] J. R. Webb, T. Bolaño, T. B. Gunnoe, *ChemSusChem* **2011**, *4*, 37.

[14] D. H. R. Barton, *Aldrichimica Acta* **1990**, *23*, 3.

[15] B. A. Arndtsen, R. G. Bergman, T. A. Mobley, T. H. Peterson, *Acc. Chem. Res.* **1995**, *28*, 154.

[16] E. V. Anslyn, D. A. Dougherty, *Modern Physical Organic Chemistry*, University Science Books, Sausalito, CA (USA) **2006**.

[17] R. A. Periana, D. J. Taube, S. Gamble, H. Taube, T. Sato, H. Fuji, *Science* **1998**, *280*, 560.

[18] R. H. Crabtree, *Chem. Rev.* **1995**, *95*, 987.

[19] S. S. Stahl, J. A. Labinger, J. E. Bercaw, *Angew. Chem. Int. Ed.* **1998**, *37*, 2181.

[20] W. D. Jones, *Top. Organomet. Chem.* **1999**, *3*, 9.

[21] H. M. Davies, *J. Mol. Catal. A: Chem.* **2002**, *189*, 125.

[22] A. A. Fokin, P. R. Schreiner, *Chem. Rev.* **2002**, *102*, 1551.

[23] M. Lersch, M. Tilset, *Chem. Rev.* **2005**, *105*, 2471.

[24] D. Balcells, E. Clot, O. Eisenstein, *Chem. Rev.* **2010**, *110*, 749.

[25] A. Gunay, K. H. Theopold, *Chem. Rev.* **2010**, *110*, 1060.

[26] T. Newhouse, P. S. Baran, *Angew. Chem. Int. Ed.* **2011**, *50*, 3362.

[27] A. E. Shilov, G. B. Shul'pin, *Chem. Rev.* **1997**, *97*, 2879.

[28] G. Centi, F. Cavani, F. Trifiro (Ed.), *Selective Oxidation by Heterogeneous Catalysis,* Kluwer Academic/Plenum Publishers, New York, **2001**.

[29] G. J. Hutchings, *Ann. Rev. Mater. Res.* **2005**, *35*, 143.

[30] G. Ertl, H. Knözinger, F. Schüth, J. Weitkamp (Ed.), *Handbook of Heterogeneous Catalysis*, Wiley-VCH, Weinheim, **2008**.

[31] S. M. Thomas, *J. Chem. Phys.* **2008**, *128*, 182502.

[32] M. J. Climent, A. Corma, S. Iborra, *Chem. Rev.* **2010**, *111*, 1072.

[33] P. L. G. Gunter, J. W. Niemantsverdriet, F. H. Ribeiro, G. A. Somorjai, *Catal. Rev.* **2009**, *39*, 77.

[34] G. L. Bond, M. A. Keane, H. Kral, J. Lercher, *Catal. Rev. Sci. Eng.* **2000**, *42*, 323.

[35] F. Zaera, *Top. Catal.* **2005**, *34*, 129.

[36] C. R. A. Catlow, S. A. French, A. A. Sokol, J. M. Thomas, *Philos. Trans. Royal Soc. Ser. A* **2005**, *363*, 913.

[37] G. Ertl, *Angew. Chem. Int. Ed.* **2008**, *47*, 3524.

[38] J. K. Norskov, T. Bligaard, B. Hvolbaek, F. Abild-Pedersen, I. Chorkendorff, C. H. Christensen, *Chem. Soc. Rev.* **2008**, *37*, 2163.

[39] F. Zaera, *Acc. Chem. Res,* **2009**, *42*, 1152.

[40] N. Nilius, T. Risse, S. Schauermann, S. Shaikhutdinov, H.-J. Freund, *Top. Catal.* **2011**, *54*, 4.

[41] S. Arndt, G. Laugel, S. Levchenko, R. Horn, M. Baerns, M. Scheffler, R. Schlögl, R. Schomäcker, *Catal. Rev.* **2011**, *53*, 424.

[42] D. Schröder, H. Schwarz, *Angew. Chem. Int. Ed. Engl.* **1995**, *34*, 1973.

[43] D. Schröder, S. Shaik, H. Schwarz, *Struct. Bonding (Berlin)* **2000**, *97*, 91.

[44] H. Schwarz, D. Schröder, *Pure. Appl. Chem.* **2000**, *72*, 2319.

[45] D. K. Böhme, H. Schwarz, *Angew. Chem. Int. Ed.* **2005**, *44*, 2336.

[46] D. Schröder, H. Schwarz, *Top. Organomet. Chem.* **2007**, *22*, 1.

[47] K. R. Asmis, A. Fielicke, G. von Helden, G. Meijer, *Chem. Phys. Solid Surf.* **2007**, *12*, 327.

[48] G. E. Johnson, E. C. Tyo, A. W. Castleman Jr., *Proc. Natl. Acad. Sci.* **2008**, *105*, 18108.

[49] D. Schröder, H. Schwarz, *Proc. Natl. Acad. Sci.* **2008**, *105*, 18114.

[50] M. Schlangen, H. Schwarz, *J. Chem. Soc., Dalton Trans.* **2009**, 10155.

[51] G. E. Johnson, R. Mitric, A. W. C. V. Bonacic-Koutecký, *Chem. Phys. Lett.* **2009**, *475*, 1.

[52] J. Roithová, D. Schröder, *Chem. Rev.* **2010**, *110*, 1170.

[53] H. Schwarz, *Angew. Chem. Int. Ed.* **2011**, *50*, 10096.

[54] Y.-X. Zhao, X.-N. Wu, J.-B. Ma, S.-G. He, X.-L. Ding, *Phys. Chem. Chem. Phys.* **2011**, *13*, 1925.

[55] M. Schlangen, H. Schwarz, *J. Catal.* **2011**, *284*, 126.

[56] R. Kretschmer, M. Schlangen, H. Schwarz, *Chem. Eur. J.* **2012**, *18*, 40.

[57] X.-L. Ding, X.-N. Wu, Y.-X. Zhao, S.-G. He, *Acc. Chem. Res.* **2012**, *45*, 382.

[58] K. A. Zemski, D. R. Justes, A. W. Castleman Jr., *J. Phys. Chem. B* **2002**, *106*, 6136.

[59] A. Fielicke, P. Gruene, G. Meijer, D. M. Rayner, *Surf. Sci.* **2009**, *603*, 1427.

[60] W. J. van der Hart, *Int. J. Mass Spectrom. Ion Processes* **1992**, *118*, 617.

[61] E. J. Bieske, O. Dopfer, *Chem. Rev.* **2000**, *100*, 3963.

[62] M. A. Duncan, *Int. J. Mass Spectrom.* **2000**, *200*, 545.

[63] M. A. Duncan, *Int. Rev. Phys. Chem.* **2003**, *22*, 407.

[64] J. Oomens, B. G. Sartakov, G. Meijer, G. von Helden, *Int. J. Mass Spectrom.* **2006**, *254*, 1.

[65] K. R. Asmis, J. Sauer, *Mass Spectrom. Rev.* **2007**, *26*, 542.

[66] J. S. Brodbelt, J. J. Wilson, *Mass Spectrom. Rev.* **2009**, *28*, 390.

[67] K. R. Asmis, D. M. Neumark, *Acc. Chem. Res.* **2012**, *45*, 43.

[68] L. Radom, *Org. Mass Spectrom.* **1991**, *26*, 359.

[69] E. Uggerud, *Mass Spectrom. Rev.* **1999**, *18*, 285.

[70] M. Alcami, O. Mó, M. Yánez, *Mass Spectrom. Rev.* **2001**, *20*, 195.

[71] D. A. Plattner, *Top. Curr. Chem.* **2003**, *225*, 153.

[72] M. N. Eberlin, *Eur. J. Mass Spectrom.* **2007**, *13*, 19.

[73] B. Butschke, H. Schwarz, *Chem. Sci.* **2012**, *3*, 308.

[74] D. Schröder, in *Methods in Physical Chemistry* Wiley-VCH, Weinheim, **2012**, pp. 63.

[75] R. Poli, J. N. Harvey, *Chem. Soc. Rev.* **2003**, *32*, 1.

[76] S. Shaik, D. Danovich, A. Fiedler, D. Schröder, H. Schwarz, *Helv. Chim. Acta* **1995**, *78*, 1393.

[77] S. Shaik, M. Filatov, D. Schröder, H. Schwarz, *Chem. Eur. J.* **1998**, *4*, 193.

[78] D. Schröder, S. Shaik, H. Schwarz, *Acc. Chem. Res.* **2000**, *33*, 193.

[79] S. Shaik, S. P. de Visser, F. Ogliaro, H. Schwarz, D. Schröder, *Curr. Opin. Chem. Biol.* **2002**, *6*, 556.

[80] J. N. Harvey, R. Poli, K. M. Smith, *Coord. Chem. Rev.* **2003**, *238*, 347.

[81] H. Schwarz, *Int. J. Mass Spectrom.* **2004**, *237*, 75.

[82] P. E. M. Siegbahn, T. Borowski, *Acc. Chem. Res.* **2006**, *39*, 729.

[83] S. Shaik, H. Hirao, D. Kumar, *Acc. Chem. Res.* **2007**, *40*, 532.

[84] L. Bernasconi, E. J. Baerends, *Eur. J. Inorg. Chem.* **2008**, 1672.

[85] C. Geng, S. Ye, F. Neese, *Angew. Chem. Int. Ed.* **2010**, *49*, 5717.

[86] D. Schröder, A. Fiedler, M. F. Ryan, H. Schwarz, *J. Phys. Chem.* **1994**, *98*, 68.

[87] D. Schröder, A. Fiedler, J. Hrusak, H. Schwarz, *J. Am. Chem. Soc.* **1992**, *114*, 1215.

[88] D. Schröder, H. Schwarz, D. E. Clemmer, Y. Chen, P. B. Armentrout, V. I. Baranov, D. K. Böhme, *Int. J. Mass Spectrom. Ion Processes* **1996**, *161*, 175.

[89] J. C. Schöneboom, S. Cohen, H. Lin, S. Shaik, W. Thiel, *J. Am. Chem. Soc.* **2004**, *126*, 4017.

[90] C. Hazan, D. Kumar, S. P. de Visser, S. Shaik, *Eur. J. Inorg. Chem.* **2007**, 2966.

[91] H. Hirao, L. Que Jr., W. Nam, S. Shaik, *Chem. Eur. J.* **2008**, *14*, 1740.

[92] H. Wu, M. B. Hall, *C. R. Chim.* **2008**, *11*, 790.

[93] D. Kumar, G. N. Sastry, S. P. de Visser, *J. Phys. Chem. B* **2011**, *116*, 718.

[94] A. Rosa, G. Ricciardi, *Inorg. Chem.* **2012**, *51*, 9833.

[95] G. Altinay, M. Citir, R. B. Metz, *J. Phys. Chem. A* **2010**, *114*, 5104.

[96] R. Breslow, *Chem. Soc. Rev.* **1972**, *1*, 553.

[97] R. Breslow, *Acc. Chem. Res.* **1980**, *13*, 170.

[98] R. Breslow, A. Adams, T. Guv, J. Hunger, *Lect. Heterocycl. Chem.* **1987**, *9*, 43.

[99] R. Breslow, *Supramol. Chem.* **1995**, *6*, 41.

[100] H. Schwarz, *Acc. Chem. Res.* **1989**, *22*, 282.

[101] J. Loos, D. Schröder, H. Schwarz in *The Encyclopedia of Mass Spectrometry - Vol. 4 Fundamentals of and Applications to Organic and Organometallic Compounds* (Ed.: N. M. M. Nibbering), Elsevier, Amsterdam, **2005**, pp. 659.

[102] R. H. A. Plasterk, *Science* **2011**, *331*, 32.

[103] M. Dole, L. L. Mack, R. L. Hines, R. C. Mobley, L. D. Ferguson, M. B. Alice, *J. Chem Phys.* **1968**, *49*, 2240.

[104] M. Yamashita, J. B. Fenn, *J. Phys. Chem.* **1984**, *88*, 4451.

[105] C. M. Whitehouse, R. N. Dreyer, M. Yamashita, J. B. Fenn, *Anal. Chem.* **1985**, *57*, 675.

[106] J. B. Fenn, M. Mann, C. K. Meng, S. F. Wong, C. M. Whitehouse, *Science* **1989**, *246*, 64.

[107] J. B. Fenn, *Angew. Chem. Int. Ed.* **2003**, *42*, 3871.

[108] W. Henderson, B. K. Nicholson, L. J. McCaffrey, *Polyhedron* **1998**, *17*, 4291.

[109] J. C. Traeger, *Int. J. Mass Spectrom.* **2000**, *200*, 387.

[110] N. B. Cech, C. G. Enke, *Mass Spectrom. Rev.* **2001**, *20*, 362.

[111] P. Chen, *Angew. Chem. Int. Ed.* **2003**, *42*, 2832.

[112] Z. Takáts, J. M. Wiseman, B. Gologan, R. G. Cooks, *Science* **2004**, *306*, 471.

[113] A. Hirabayashi, M. Sakairi, H. Koizumi, *Anal. Chem.* **1995**, *67*, 2878.

[114] J. Zeleny, *Phys. Rev.* **1917**, *10*, 1.

[115] G. Taylor, *Proc. Royal Soc. London A* **1964**, *280*, 383.

[116] G. Schmelzeisen-Redecker, L. Buttering, F. W. Röllgen, *Int. J. Mass Spectrom. Ion Phys.* **1989**, *90*, 139.

[117] D. Schröder, *Angew. Chem. Int. Ed.* **2004**, *43*, 1329.

[118] D. C. Taflin, T. L. Ward, E. J. Davis, *Langmuir* **1989**, *5*, 376.

[119] D. Duft, T. Achtzehn, R. Muller, B. A. Huber, T. Leisner, *Nature* **2003**, *421*, 128.

[120] J. W. Strutt (Lord Rayleigh), *Phil. Mag.* **1882**, *14*, 184.

[121] J. Iribarne, B. Thomson, *J. Chem. Phys.* **1976**, *64*, 2287.

[122] B. Thomson, *J. Chem. Phys.* **1979**, *71*, 4451.

[123] J. F. de la Mora, G. J. V. Berkel, C. G. Enke, R. B. Cole, M. Martinez-Sanchez, J. B. Fenn, *J. Mass Spectrom.* **2000**, *35*, 939.

[124] B. S. Freiser, *Talanta* **1985**, *32*, 697.

[125] J. S. McIndoe, *Transition Met. Chem.* **2003**, *28*, 122.

[126] M. Karas, U. Bahr, *Trends Anal. Chem.* **1990**, *9*, 321.

[127] R. Zenobi, R. Knochenmuss, *Mass Spectrom. Rev.* **1998**, *17*, 337.

[128] F. Hillenkamp, *MALDI MS - A practical to instrumentation, methods and applications,* Wiley-VCH, Weinheim, **2007**.

[129] K. Tanaka, *Angew. Chem. Int. Ed.* **2003**, *42*, 3860.

[130] M. Karas, F. Hillenkamp, *Anal. Chem.* **1988**, *60*, 2299.

[131] F. Hillenkamp, M. Karas, R. C. Beavis, B. T. Chait, *Anal. Chem.* **1991**, *63*, 1193.

[132] T. G. Dietz, M. A. Duncan, D. E. Powers, R. E. Smalley, *J. Chem. Phys.* **1981**, *74*, 6511.

[133] S. Maruyama, L. R. Anderson, R. E. Smalley, *Rev. Sci. Instrum.* **1990**, *61*, 3686.

[134] C. Berg, T. Schindler, G. Niedner-Schatteburg, V. E. Bondybey, *J. Chem. Phys.* **1995**, *102*, 6252.

[135] C. Berg, T. Schindler, M. Kantlehner, G. Niedner-Schatteburg, V. E. Bondybey, *Chem. Phys.* **2000**, *262*, 143.

[136] K. A. Zemski, D. R. Justes, A. W. Castleman Jr., *J. Phys. Chem. A* **2001**, *105*, 10237.

[137] S. Feyel, J. Döbler, R. Höckendorf, M. K. Beyer, J. Sauer, H. Schwarz, *Angew. Chem. Int. Ed.* **2008**, *47*, 1946.

[138] G. E. Johnson, R. Mitric, E. C. Tyo, V. Bonaci-Koutecky, A. W. Castleman Jr., *J. Am. Chem. Soc.* **2008**, *130*, 13912.

[139] Y.-X. Zhao, X.-N. Wu, Z.-C. Wang, S.-G. He, X.-L. Ding, *Chem. Commun.* **2010**, *46*, 1736.

[140] X.-L. Ding, Y.-X. Zhao, X.-N. Wu, Z.-C. Wang, J.-B. Ma, S.-G. He, *Chem. Eur. J.* **2010**, *16*, 11463.

[141] N. Dietl, R. F. Hoeckendorf, M. Schlangen, M. Lerch, M. K. Beyer, H. Schwarz, *Angew. Chem. Int. Ed.* **2011**, *50*, 1430.

[142] K. Kwapien, M. Sierka, J. Doebler, J. Sauer, M. Haertelt, A. Fieleicke, G. Meijer, *Angew. Chem. Int. Ed.* **2011**, *50*, 1716.

[143] N. Dietl, C. van der Linde, M. Schlangen, M. K. Beyer, H. Schwarz, *Angew. Chem. Int. Ed.* **2011**, *50*, 4966.

[144] Z.-C. Wang, T. Weiske, R. Kretschmer, M. Schlangen, M. Kaupp, H. Schwarz, *J. Am. Chem. Soc.* **2011**, *133*, 16930.

[145] M. K. Beyer, *Mass Spectrom. Rev.* **2007**, *26*, 517.

[146] R. F. Hoeckendorf, O. P. Balaj, C. van der Linde, M. K. Beyer, *Phys. Chem. Chem. Phys.* **2010**, *12*, 3772.

[147] C. van der Linde, A. Akhgarnusch, C.-K. Siu, M. K. Beyer, *J. Phys. Chem. A* **2011**, *115*, 10174.

[148] D. Schroeder, H. Weiske, H. Schwarz, *Int. J. Mass Spectrom.* **2002**, *219*, 729.

[149] A. G. Harrison, *Rapid Commun. Mass Spectrom.* **1999**, *13*, 1663.

[150] D. Schroeder, J. Roithová, H. Schwarz, *Int. J. Mass Spectrom.* **2006**, *254*, 197.

[151] D. Schroeder, J. Roithová, E. Alikhani, K. Kwapien, J. Sauer, *Chem. Eur. J.* **2010**, *16*, 4110.

[152] N. Dietl, M. Schlangen, H. Schwarz, *Chem. Eur. J.* **2011**, *17*, 1738.

[153] R. Kretschmer, X. Zhang, M. Schlangen, H. Schwarz, *Chem. Eur. J.* **2011**, *17*, 3886.

[154] D. Schröder, M. Engeser, M. Brönstrup, C. Daniel, J. Spandl, H. Hartl, *Int. J. Mass. Spectrom.* **2003**, *228*, 743.

[155] X. Zhang, H. Schwarz, *Chem. Eur. J.* **2010**, *16*, 1163.

[156] W. Paul, H. Steinwedel, *Z. Naturforsch.* **1953**, *8A*, 448.

[157] W. Paul, M. Raether, *Z. Phys.* **1955**, *140*, 262.

[158] J. H. Gross, *Mass Spectrometry*, Springer, 1. Ed., **2004**.

[159] W. Paul, *Angew. Chem. Int. Ed. Engl.* **1990**, *29*, 739.

[160] A. G. Marshall, C. L. Hendrickson, G. S. Jackson, *Mass Spectrom. Rev.* **1998**, *17*, 1.

[161] M. Wang, A. G. Marshall, *Int. J. Mass Spectrom. Ion Processes* **1990**, *100*, 323.

[162] A. G. Marshall, C. L. Hendrickson, *Int. J. Mass Spectrom.* **2002**, *215*, 59.

[163] A. G. Marshall, *Acc. Chem. Res.* **1996**, *29*, 307.

[164] A. J. R. Heck, F. A. P. L. J. de Koning, N. M. M. Nibbering, *Rapid Commun. Mass Spectrom.* **1991**, *5*, 406.

[165] R. A. Forbes, F. H. Laucien, J. Wronka, *Int. J. Mass Spectrom. Ion Processes* **1988**, *83*, 23.

[166] J. G. Black, E. Yablonovitch, N. Bloembergen, S. Mukamel, *Phys. Rev. Lett.* **1977**, *38*, 1131.

[167] O. Dopfer, *J. Phys. Org. Chem.* **2006**, *19*, 540.

[168] M. Okamura, L. I. Yeh, Y. T. Lee, *J. Chem. Phys.* **1985**, *83*, 3705.

[169] D. J. Goebbert, G. Meijer, K. R. Asmis, *AIP Conf. Proc.* **2009**, *1104*, 22.

[170] D. J. Goebbert, T. Wende, R. B. G. Meijer, K. R. Asmis, *J. Phys. Chem. A* **2009**, *113*, 5874.

[171] M. Brüummer, C. Kaposta, G. Santambrogio, K. R. Asmis, *J. Chem. Phys.* **2003**, *119*, 12700.

[172] L. Lin, P. Claes, T. Höltzl, E. Janssens, T. Wende, R. Bergmann, G. Santambrogio, G. Meijer, K. R. Asmis, M. T. Nguyen, P. Lievens, *Phys. Chem. Chem. Phys.* **2010**, *12*, 13907.

[173] W. R. Bosenberg, D. R. Guyer, *J. Opt. Soc. Am. B* **1993**, *10*, 1716.

[174] R. Zahradník, *Acc. Chem. Res.* **1995**, *28*, 306.

[175] L. Sleno, D. A. Volmer, *J. Mass Spectrom.* **2004**, *39*, 1091.

[176] F. W. McLafferty, *Anal. Chem.* **1959**, *31*, 82.

[177] F. W. McLafferty, P. F. I. Bente, R. Kornfeld, S.-C. Tsai, I. Howe, *J. Am. Chem. Soc.* **1973**, *95*, 2120.

[178] K. Levsen, H. Schwarz, *Mass Spectrom. Rev.* **1983**, *2*, 77.

[179] S. A. McLuckey, *J. Am. Chem. Soc. Mass Spectrom.* **1992**, *3*, 599.

[180] D. P. Stevenson, D. O. Schissler, *J. Chem. Phys* **1958**, *29*, 282.

[181] G. Gioumousis, D. P. Stevenson, *J. Chem. Phys* **1958**, *29*, 294.

[182] W. N. Olmstead, J. I. Brauman, *J. Am. Chem. Soc.* **1977**, *99*, 4219.

[183] J. E. Bartmess, R. M. Georgiadis, *Vacuum* **1983**, *33*, 149.

[184] M. P. Langevin, *Ann. Chim. Phys.* **1905**, *5*, 245.

[185] T. Su, M. Bowers, *Int. J. Mass Spectrom. Ion. Phys.* **1973**, *12*, 347.

[186] T. Su, E. C. F. Su, M. T. Bowers, *J. Chem. Phys* **1978**, *69*, 2243.

[187] T. Su, W. J. Chesnavich, *J. Chem. Phys.* **1982**, *76*, 5183.

[188] T. Su, *J. Chem. Phys.* **1988**, *88*, 4102.

[189] T. Su, *J. Chem. Phys.* **1988**, *89*, 5355.

[190] D. Schröder, R. Wesendrup, R. H. Hertwig, T. K. Dargel, H. Grauel, W. Koch, B. R. Bender, H. Schwarz, *Organometallics* **2000**, *19*, 2608.

[191] A. V. Willi, *Isotopeneffekte bei chemischen Reaktionen*, Georg Thieme Verlag, Stuttgart/New York, **1983**.

[192] S. A. Blum, K. L. Tan, R. G. Bergman, *J. Org. Chem* **2003**, *68*, 4127.

[193] G. C. Lloyd-Jones, M. P. Munoz, *J. Labelled Compd. Radiopharm.* **2007**, *50*, 1072.

[194] T. Giagou, M. P. Meyer, *Chem. Eur. J.* **2010**, *16*, 10616.

[195] M. Gómez-Gallego, M. A. Sierra, *Chem. Rev.* **2011**, *111*, 4857.

[196] J. Mattson, M. Simon, *The Pioneers of NMR and Magnetic Resonance in Medicine: The Story of MRI*, Jericho & New York: Bar-Ilan University Press, **1996**, pp. 278.

[197] E. Uggerud, *Mass Spectrom. Rev.* **1992**, *11*, 389.

[198] E. Schrödinger, *Ann. Phys.* **1926**, *79*, 361.

[199] P. W. Atkins, *Molecular Quantum Mechanics*, Oxford University Press, New York, **1983**.

[200] M. Born, R. Oppenheimer, *Ann. Phys.* **1927**, *389*, 457.

[201] P. Hohenberg, W. Kohn, *Phys. Rev. B* **1964**, *136*, 864.

[202] W. Koch, M. C. Holthausen, *A Chemist's Guide to Density Functional Theory 2nd ed.*, Wiley-VCH, Weinheim, **2001**.

[203] W. Kohn, L. J. Sham, *Phys. Rev. A* **1965**, *140*, 1133.

[204] D. Rappoport, N. R. M. Crawford, F. Furche, K. Burke *Which functional should I choose?* (Ed.: E. I. Solomon, R. A. Scott, R. B. King), John-Wiley & Sons, Hoboken, **2009**.

[205] P. E. M. Siegbahn, M. R. A. Blomberg, *Annu. Rev. Phys. Chem.* **1999**, *50*, 221.

[206] M. Diedenhof, T. Wagener, G. Frenking in *Computational Organometallic Chemistry* (Ed.: T. R. Cundari), CRC Press, Boca Raton, **2001**, pp. 69.

[207] T. Ziegler, J. Autschbach, *Chem. Rev.* **2005**, *105*, 2695.

[208] J. N. Harvey, *Annu. Rep. Prog. Chem. Sect. C: Phys. Chem.* **2006**, *102*, 203.

[209] F. Neese, *J. Biol. Inorg. Chem.* **2006**, *11*, 702.

[210] A. D. Becke, *Phys. Rev. A* **1988**, *38*, 3098.

[211] C. Lee, W. Yang, R. G. Parr, *Phys. Rev. B* **1988**, *37*, 785.

[212] A. D. Becke, *J. Chem. Phys.* **1993**, *98*, 5648.

[213] J. Cizek, *J. Chem. Phys.* **1966**, *45*, 4256.

[214] R. J. Bartlett in *Modern electronic structure theory. Part. II* (Ed.: D. R. Yarkony), World Scientific, Singapore, **1995**, pp. 1047.

[215] J. A. Pople, M. Head-Gordon, K. Raghavachari, *J. Chem. Phys.* **1987**, *87*, 5968.

[216] K. Raghavachari, G. W. Trucks, J. A. Pople, M. Head-Gordon, *Chem. Phys. Lett.* **1989**, *157*, 479.

[217] T. J. Lee, P. R. Taylor, *Int. J. Quantum Chem.* **1989**, *23*, 199.

[218] J. W. Ochterski, G. A. Petersson, J. A. Montgomery Jr., *J. Chem. Phys.* **1996**, *104*, 2598.

[219] J. A. Montgomery Jr., M. J. Frisch, J. W. Ochterski, G. A. Petersson, *J. Chem. Phys.* **1999**, *110*, 2822.

[220] J. A. Montgomery Jr., M. J. Frisch, J. W. Ochterski, G. A. Petersson, *J. Chem. Phys.* **2000**, *112*, 6532.

[221] G. A. Petersson, T. G. Tensfeldt, J. A. Montgomery Jr., *J. Chem. Phys.* **1991**, *94*, 6091.

[222] J. M. L. Martin, G. De Oliveira, *J. Chem. Phys.* **1999**, *111*, 1843.

[223] S. Parthiban, J. M. L. Martin, *J. Chem. Phys.* **2001**, *114*, 6014.

[224] Gaussian 03 (Revision E.02), M. J. Frisch, G. W. Trucks, H. B. Schlegel, G. E. Scuseria, M. A. Robb, J. R. Cheeseman, V. G. Zakrzewski, J. A. Montgomery, R. E. Stratmann, J. C. Burant, S. Dapprich, J. M. Millam, A. D. Daniels, K. N. Kudin, M. C. Strain, O. Farkas, J. Tomasi, V. Barone, M. Cossi, R. Cammi, B. Mennucci, C. Pomelli, C. Adamo, S. Clifford, J. Ochterski, G. A. Petersson, P. Y. Ayala, Q. Cui, K. Morokuma, P. Salvador, J. J. Dannenberg, D. K. Malick, A. D. Rabuck, K. Raghavachari, J. B. Foresman, J. Cioslowski, J. V. Ortiz, A. G. Baboul, B. B. Stefanov, G. Liu, A. Liashenko, P. Piskorz, I. Komaromi, R. Gomperts, R. L. Martin, D. J. Fox, T. Keith, M. A. Al-Laham, C. Y. Peng, A. Nanayakkara, M. Challacombe, P. M. W. Gill, B. Johnson, W. Chen, M. W. Wong, J. L. Andres, C. Gonzalez, M. Head-Gordon, E. S. Replogle, J. A. Pople, Gaussian, Inc., Pittsburgh, PA, **2004**.

[225] Gaussian 09 (Revision A.1), M. J. Frisch, G. W. Trucks, H. B. Schlegel, G. E. Scuseria, M. A. Robb, J. R. Cheeseman, G. Scalmani, V. Barone, B. Mennucci, G. A. Petersson, H. Nakatsuji, M. Caricato, X. Li, H. P. Hratchian, A. F. Izmaylov, J. Bloino, G. Zheng, J. L. Sonnenberg, M. Hada, M. Ehara, K. Toyota, R. Fukuda, J. Hasegawa, M. Ishida, T. Nakajima, Y. Honda, O. Kitao, H. Nakai, T. Vreven, Montgomery, Jr., J. A., J. E. Peralta, F. Ogliaro, M. Bearpark, J. J. Heyd, E. Brothers, K. N. Kudin, V. N. Staroverov, R. Kobayashi, J. Normand, K. Raghavachari, A. Rendell, J. C. Burant, S. S. Iyengar, J. Tomasi, M. Cossi, N. Rega, J. M. Millam, M. Klene, J. E. Knox, J. B. Cross, V. Bakken, C. Adamo, J. Jaramillo, R. Gomperts, R. E. Stratmann, O. Yazyev, A. J. Austin, R. Cammi, C. Pomelli, J. W. Ochterski, R. L. Martin, K. Morokuma, V. G. Zakrzewski, G. A. Voth, P. Salvador, J. J. Dannenberg, S. Dapprich, A. D. Daniels, Ö. Farkas, J. B. Foresman, J. V. Ortiz, J. Cioslowski and D. J. Fox, Gaussian, Inc., Wallingford, CT, **2009**.

[226] A. Schäfer, C. Huber, R. Ahlrichs, *J. Chem. Phys.* **1994**, *100*, 5829.

[227] F. Weigend, R. Ahlrichs, *Phys. Chem. Chem. Phys.* **2005**, *7*, 3297.

[228] D. E. Woon, T. H. Dunning, *J. Chem. Phys.* **1993**, *99*, 3730.

[229] H. B. Schlegel in *Modern electronic structure theory.* (Ed.: D. R. Yarkony), World Scientific, Singapore, **1995**, pp. 459.

[230] C. Peng, H. B. Schlegel, *Isr. J. Chem.* **1993**, *17*, 49.

[231] K. Fukui, *J. Phys. Chem.* **1970**, *74*, 4161.

[232] K. Fukui, *Acc. Chem. Res.* **1981**, *14*, 363.

[233] C. Gonzalez, H. B. Schlegel, *J. Phys. Chem.* **1990**, *94*, 5523.

[234] D. G. Truhlar, M. S. Gordon, *Science* **1990**, *249*, 491.

[235] M. Schröder, *Fractals, Chaos, Power Laws: Minutes from an Infinite Paradise,* W.H. Freeman, New York, **1991**, pp. 429.

[236] H. Arakawa, M. Aresta, J. N. Armor, M. A. Barteau, E. J. Beckman, A. T. Bell, J. E. Bercaw, C. Creutz, E. Dinjus, D. A. Dixon, K. Domen, D. L. DuBois, J. Eckert, E. Fujita, D. H. Gibson, W. A. Goddard, D. W. Goodman, J. Keller, G. J. Kubas, H. H. Kung, J. E. Lyons, L. E. Manzer, T. J. Marks, K. Morokuma, K. M. Nicholas, R. Periana, L. Que Jr., J. Rostrup-Nielson, W. M. H. Sachtler, L. D. Schmidt, A. Sen, G. A. Somorjai, P. C. Stair, B. R. Stults, W. Tumas, *Chem. Rev.* **2001**, *101*, 953.

[237] C. Limberg, *Angew. Chem. Int. Ed.* **2003**, *42*, 5932.

[238] J. Sauer in *Computational Modeling of Principles and Mechanisms of Transition Metal-Based Catalytic Processes* (Eds.: K. Morokuma, J. Musaev), Wiley-VCH, Weinheim, **2008**, pp. 231.

[239] L. Que Jr., W. B. Tolman, *Nature* **2008**, *455*, 333.

[240] C. Limberg, *Angew. Chem. Int. Ed.* **2009**, *48*, 2270.

[241] J. H. Lunsford, *Angew. Chem. Int. Ed. Engl.* **1995**, *34*, 970.

[242] J. H. Lunsford, *Catal. Today* **2000**, *63*, 165.

[243] A. A. Fokin, P. R. Schreiner, *Adv. Synth. Catal.* **2003**, *345*, 1035.

[244] J. A. Labinger, *J. Mol. Catal. A* **2004**, *220*, 27.

[245] H. Liu, R. S. Liu, K. Y. Liew, R. E. Johnson, R. H. Lunsford, *J. Am. Chem. Soc.* **1984**, *106*, 4117.

[246] S. T. Ceyer, *Science* **1990**, *249*, 133.

[247] R. Zahradnik, *J. Mol. Catal.* **1993**, *82*, 265.

[248] M.-A. Stiakaki, A. C. Tsipsis, C. A. Tsipsis, C. E. Xanthopoulos, *New J. Chem.* **1994**, *18*, 203.

[249] Z. Zhang, X. E. Verykios, M. Baerns, *Catal. Rev. Sci. Eng*. **1994**, *36*, 507.

[250] X. Bao, M. Muhler, R. Schlögl, G. Ertl, *Catal. Lett.* **1995**, *32*, 185.

[251] D. Nachtigallova, M. Roeselova, R. Zahradnik, *Chem. Phys. Lett.* **1997**, *270*, 357.

[252] A. J. Nagy, G. Mestl, R. Schlögl, *J. Catal.* **1999**, *188*, 58.

[253] P. E. M. Siegbahn, R. H. Crabtree, *J. Am. Chem. Soc.* **1999**, *121*, 117.

[254] M. Lundberg, M. R. A. Blomberg, P. E. M. Siegbahn, *Inorg. Chem.* **2004**, *43*, 264.

[255] D. Balcells, C. Raymand, R. H. Crabtree, O. Eisenstein, *Chem. Commun.* **2008**, 744.

[256] D. Balcells, C. Raymand, R. H. Crabtree, O. Eisenstein, *Inorg. Chem.* **2008**, *47*, 10090.

[257] D. Balcells, C. Raymand, R. H. Crabtree, O. Eisenstein, *Chem. Commun.* **2009**, 1772.

[258] N. Dietl, M. Schlangen, H. Schwarz, *Angew. Chem. Int. Ed.* **2012**, *51*, 5544.

[259] W. Lai, C. Li, H. Chen, S. Shaik, *Angew. Chem. Int. Ed.* **2012**, *51*, 5556.

[260] I. E. Wachs, *Catal. Today* **2005**, *100*, 79.

[261] M. V. Ganduglia-Pirovano, C. P. J. Sauer, H. Abbott, A. Uhl, M. Baron, D. Stacchiola, O. Bondarchuk, S. Shaikhutdinov, H.-J. Freund, *J. Am. Chem. Soc.* **2010**, *132*, 2345.

[262] K. K. Ikura, J. L. Beauchamp, *J. Am. Chem. Soc.* **1989**, *111*, 75.

[263] M. K. Beyer, C. B. Berg, V. E. Bondybey, *Phys. Chem. Chem. Phys.* **2001**, *3*, 1840.

[264] S. Feyel, D. Schröder, X. Rozanska, J. Sauer, H. Schwarz, *Angew. Chem. Int. Ed.* **2006**, *45*, 4677.

[265] S. Feyel, J. Döbler, D. Schröder, J. Sauer, H. Schwarz, *Angew. Chem. Int. Ed.* **2006**, *45*, 4681.

[266] D. Schröder, J. Roithová, *Angew. Chem. Int. Ed.* **2006**, *45*, 5705.

[267] J. Roithová, D. Schröder, *J. Am. Chem. Soc.* **2007**, *129*, 15311.

[268] G. de Petris, A. Troiani, M. Rosi, G. Angelini, O. Ursini, *Chem. Eur. J.* **2009**, *15*, 4248.

[269] X. Zhang, H. Schwarz, *ChemCatChem* **2010**, *2*, 1391.

[270] X.-N. Wu, Y.-X. Zhao, W. Xue, Z.-C. Wang, S.-G. He, X.-L. Ding, *Phys. Chem. Chem. Phys.* **2010**, *12*, 3984.

[271] K. Chen, Z.-C. Wang, M. Schlangen, Y.-D. Wu, X. Zhang, H. Schwarz, *Chem. Eur. J.* **2011**, *17*, 9619.

[272] Z.-C. Wang, X.-N. Wu, Y.-X. Zhao, J.-B. Ma, X.-L. Ding, S.-G. He, *Chem. Phys Lett.* **2010**, *489*, 25.

[273] Z.-C. Wang, X.-N. Wu, Y.-X. Zhao, J.-B. Ma, X.-L. Ding, S.-G. He, *Chem. Eur. J.* **2011**, *17*, 3449.

[274] L. Jiang, T. Wende, P. Claes, S. Bhattacharyya, M. Sierka, G. Meijer, P. Lievens, J. Sauer, K. R. Asmis, *J. Phys. Chem. A* **2011**, *115*, 11187.

[275] Y.-X. Zhao, X.-N. Wu, J.-B. Ma, S.-G. He, X.-L. Ding, *J. Phys. Chem. C* **2010**, *114*, 12271.

[276] *Appl. Catal. A* **1997**, *157*, the entire volume is dedicated to the issue of *VPO*–catalysts.

[277] G. J. Hutchings, *J. Mater. Chem.* **2004**, *14*, 3385.

[278] V. V. Guliants, M. A. Carreon, *Catalysis* **2005**, *18*, 1.

[279] J.-M. Millet, *Top. Catal.* **2006**, *38*, 83.

[280] Y. Taufiq-Yap, G. H. C. Goh, N. Dummer, J. Bartley, *Catal. Lett.* **2009**, *130*, 327.

[281] K. Kourtakis, L. Wang, E. Thompson, P. L. Gai, *Appl. Catal. A* **2010**, *376*, 40.

[282] G. Centi, F. Trifiro, J. R. Ebner, V. M. Franchetti, *Chem. Rev.* **1988**, *88*, 55.

[283] Y. Zhanglin, M. Forissier, R. P. Sneeden, J. C. Vedrine, J. C. Volta, *J. Catal.* **1994**, *145*, 256.

[284] B. Chen, E. J. Munson, *J. Am. Chem. Soc.* **1999**, *121*, 11024.

[285] G. J. Hutchings, *Catal. Lett.* **2001**, *75*, 1.

[286] B. Chen, E. J. Munson, *J. Am. Chem. Soc.* **2002**, *124*, 1638.

[287] D. J. Thompson, M. O. Fanning, B. K. Hodnett, *J. Mol. Catal. A: Chem.* **2003**, *198*, 125.

[288] D. J. Thompson, M. O. Fanning, B. K. Hodnett, *J. Mol. Catal. A: Chem.* **2003**, *206*, 435.

[289] M. Kaczorowska, H. Schwarz, D. Schröder, *Eur. J. Inorg. Chem.* **2007**, 3335.

[290] F. Cavani, D. D. Santi, S. Luciani, A. Löfberg, E. Bordes-Richard, C. Cortelli, R. Leanza, *Appl. Catal. A* **2010**, *376*, 66.

[291] R. C. Bell, K. A. Zemski, K. P. Kerns, H. T. Deng, A. W. Castleman Jr., *J. Phys. Chem. A* **1998**, *102*, 1733.

[292] D. R. Justes, R. Mitric, N. A. Moore, V. Bonaci-Koutecky, A. W. Castleman Jr., *J. Am. Chem. Soc.* **2003**, *125*, 6289.

[293] N. A. Moore, R. Mitric, D. R. Justes, V. Bonaci-Koutecky, A. W. Castleman Jr., *J. Phys. Chem. B* **2006**, *110*, 3015.

[294] S. Feyel, D. Schröder, H. Schwarz, *J. Phys. Chem. A* **2006**, *110*, 2647.

[295] S. Feyel, D. Schröder, H. Schwarz, *J. Phys. Chem. A* **2007**, *111*, 3278.

[296] S. Feyel, D. Schröder, H. Schwarz, *Eur. J. Inorg. Chem.* **2008**, 4961.

[297] A. K. Chowdhury, M.-B. Liu, A. Gulbenkian, *Ind. Eng. Chem. Res.* **1993**, *32*, 989.

[298] A. Hashizume, N. Wasada, T. Tsuchiya, *Bull. Chem. Soc. Jpn.* **1966**, *39*, 150.

[299] J. Berkowitz, G. B. Ellison, D. Gutman, *J. Phys. Chem. B* **1994**, *98*, 2744.

[300] J.-B. Ma, X.-N. Wu, Y.-X. Zhao, X.-L. Ding, S.-G. He, *Phys. Chem. Chem. Phys.* **2010**, *12*, 12223.

[301] T. Wende, J. Döbler, L. Jiang, P. Claes, E. Janssens, P. Lievens, G. Meijer, K. R. Asmis, J. Sauer, *Int. J Mass Spectrom.* **2010**, *297*, 102.

[302] R. D. Johnson III (Ed.), NIST Computational Chemistry Comparison and Benchmark Database, NIST Standard Reference Database Number 101 Release 15b, **2011**, http://cccbdb.nist.gov/.

[303] A. Lee, R. L. Leroy, Z. Herman, R. Wolfgang, *Chem. Phys. Lett.* **1972**, *12*, 569.

[304] P. R. LeBreton, A. D. Williamson, J. L. Beauchamp, W. T. Huntress, *J. Chem. Phys.* **1975**, *62*, 1623.

[305] W. Chesnavich, M. T. Bowers, *J. Am. Chem. Soc.* **1976**, *98*, 8301.

[306] J. K. Kim, V. G. Anicich, W. T. Huntress, *J. Phys. Chem.* **1977**, *81*, 1798.

[307] X. Zhang, H. Schwarz, *Theor. Chem. Acc.* **2011**, *129*, 389.

[308] P. B. Armentrout, B. L. Kickel, *Organometallic Ion Chemistry,* Kluwer Academic Publishers, Dordrecht, **1996**.

[309] X. Rozanska, J. Sauer, *J. Phys. Chem. A* **2009**, *113*, 11586.

[310] P. C. Burgers, J. K. Terlouw, *Encyclopedia of Mass Spectrometry, Vol. 4,* Elsevier, Amsterdam, **2005**, pp. 173.

[311] *The Ultimate Quotable Einstein,* (Ed.: A. Calaprice), Princeton University Press, Princeton, New Jersey **2010**, pp. 475.

[312] M. Nößler, R. Mitric, V. Bonaci-Koutecky, G. E. Johnson, E. C. Tyo, A. W. Castleman Jr., *Angew. Chem. Int. Ed.* **2010**, *49*, 407.

[313] Z.-C. Wang, N. Dietl, R. Kretschmer, T. Weiske, M. Schlangen, H. Schwarz, *Angew. Chem. Int. Ed.* **2011**, *50*, 12351.

[314] J.-B. Ma, Z.-C. Wang, M. Schlangen, S.-G. He, H. Schwarz, *Angew. Chem. Int. Ed.* **2012**, *51*, 5991.

[315] *Vanadium Compounds: Chemistry, Biochemistry, and Therapeutic Applications*, (Eds.: A. S. Traycey, D. C. Crans), ACS Symposium Series 711, American Chemical Society, Washington DC, **1998**.

[316] K. R. Asmis, G. Meijer, M. Brummer, C. Kaposta, G. Santambrogio, L. Woste, J. Sauer, *J. Chem. Phys.* **2004**, *120*, 6461.

[317] E. Podstawka-Proniewicz, N. Piergies, D. Skoluba, P. Kafarski, Y. Kim, L. M. Proniewicz, *J. Phys. Chem. A* **2011**, *115*, 11067.

[318] D. Boczula, A. Caly, D. Dobrzynska, J. Janczak, J. Zon, *J. Mol. Struct.* **2012**, *1007*, 220.

[319] G. von Helden, A. Kirilyuk, D. van Heijnsbergen, B. Sartakov, M. A. Duncan, G. Meijer, *Chem. Phys.* **2000**, *262*, 31.

[320] D. Schröder, H. Schwarz, *Angew. Chem. Int. Ed. Engl.* **1990**, *29*, 1431.

[321] D. R. Lide (Ed.), *CRC Handbook of Chemistry and Physics - 69th Edition*, CRC Press, Boca Raton, Florida **1988**.

[322] J. L. Holmes, C. Aubry, P. M. Mayer, *Assigning Structures to Ions in Mass Spectrometry*, CRC Press, Taylor & Francis Group, Boca Raton, London, New York **2007**.

[323] W. Koch, B. Liu, P. v. R. Schleyer, *J. Am. Chem. Soc.* **1989**, *111*, 3479.

[324] W. Koch, P. v. R. Schleyer, P. Buzek, B. Liu, *Croat. Chem. Acta* **1992**, *65*, 655.

[325] B. Chiavarino, M. E. Crestoni, A. A. Fokin, S. Fornarini, *Chem. Eur. J.* **2001**, *7*, 2916.

[326] B. Chiavarino, M. E. Crestoni, S. Fornarini, J. Lemaire, L. Mac Aleese, P. Maître, *ChemPhysChem* **2004**, *5*, 1679.

[327] J. M. Mayer, *Acc. Chem. Res.* **2011**, *44*, 36.

[328] J. T. Hynes, J. P. Klinman, H.-H. Limbach, R. L. Schowen, *Hydrogen-Transfer Reactions*, Wiley-VCH Verlag GmbH & Co. KGaA, Weinheim/New York, **2006**.

[329] M. H. V. Huynh, T. J. Meyer, *Chem. Rev.* **2007**, *107*, 5004.

[330] J. J. Warren, T. A. Tronic, J. M. Mayer, *Chem. Rev.* **2010**, *110*, 6961.

[331] S. Shai, H. Chen, D. Janardanan, *Nat. Chem.* **2011**, *3*, 19.

[332] O. Tishchenko, D. G. Truhlar, A. Ceulemans, M. T. Nguyen, *J. Am. Chem. Soc.* **2008**, *130*, 7000.

[333] S. Hammes-Schiffer, A. V. Soudackov, *J. Phys. Chem. B* **2008**, *112*, 14108.

[334] A. Sirjoosingh, S. Hammes-Schiffer, *J. Phys. Chem. A* **2011**, *115*, 2367.

[335] M. G. Evans, M. Polanyi, *Trans. Faraday Soc.* **1938**, *34*, 11.

[336] J. M. Mayer, *Annu. Rev. Phys. Chem.* **2004**, *55*, 363.

[337] J. M. Mayer, *J. Phys. Chem. Lett.* **2011**, *2*, 1481.

[338] R. A. Marcus, *Angew. Chem. Int. Ed. Engl.* **1993**, *32*, 1111.

[339] S. Shaik, A. Shurki, *Angew. Chem. Int. Ed.* **1999**, *38*, 586.

[340] A. M. Khenkin, D. Kumar, S. Shaik, R. Neumann, *J. Am. Chem. Soc.* **2006**, *128*, 15451.

[341] J. N. Harvey, M. Diefenbach, D. Schröder, H. Schwarz, *Int. J. Mass Spectrom.* **1999**, *183*, 85.

[342] I. Kretzschmar, A. Fiedler, J. N. Harvey, D. Schröder, H. Schwarz, *J. Phys Chem. A* **1997**, *101*, 6252.

[343] M. F. Ryan, A. Fiedler, D. Schröder, H. Schwarz, *J. Am. Chem. Soc.* **1995**, *117*, 2033.

[344] A. Božovic, D. K. Bohme, *Phys. Chem. Chem. Phys.* **2009**, *11*, 5940.

[345] R. P. Bell, *Proc. R. Soc. Lond. A* **1938**, *154*, 414.

[346] J. M. Mayer, *Acc. Chem. Res.* **1998**, *31*, 441.

[347] K. Kwapien, M. Sierka, J. Döbler, J. Sauer, *ChemCatChem* **2010**, *2*, 819.

[348] M.-H. Baik, M. Newcomb, R. A. Friesener, S. J. Lippard, *Chem. Rev.* **2003**, *103*, 2385.

[349] R. L. Liebermann, A. C. Rosenzweig, *Nature* **2005**, *434*, 177.

[350] A. S. Hakemian, A. C. Rosenzweig, *Annu. Rev. Biochem.* **2007**, *76*, 223.

[351] R. A. Himes, K. D. Karlin, *Curr. Opin. Chem. Biol.* **2009**, *123*, 119.

[352] R. Balasubramanian, S. M. Smith, S. Rawat, L. A. Yatsunyk, T. L. Stemmler, A. C. Rosenzweig, *Nature* **2010**, *465*, 115.

[353] K. Yoshizawa, Y. Shiota, *J. Am. Chem. Soc.* **2006**, *128*, 9873.

[354] R. Balasubramanian, A. C. Rosenzweig, *Acc. Chem. Res.* **2007**, *40*, 573.

[355] S. I. Chan, S. S.-F. Yu, *Acc. Chem. Res.* **2008**, *41*, 969.

[356] R. A. Himes, K. Barnese, K. D. Karlin, *Angew. Chem. Int. Ed.* **2010**, *49*, 6714.

[357] E. I. Solomon, J. W. Ginsbach, D. E. Heppner, M. T. Kieber-Emmons, C. H. Kjaergaard, P. J. Smeets, L. Tian, J. S. Woertink, *Faraday Discuss.* **2011**, *148*, 11.

[358] Y. Shiota, K. Yoshizawa, *J. Am. Chem. Soc.* **2000**, *122*, 12317.

[359] M. H. Groothaert, P. J. Smeets, B. F. Sels, P. A. Jacobs, R. A. Schoonheydt, *J. Am. Chem. Soc.* **2005**, *127*, 1394.

[360] J. S. Woertink, P. J. Smeets, M. H. Groothaert, M. A. Vance, B. F. Sels, R. A. Schoonheydt, E. I. Solomon, *Proc. Natl. Acad. Sci.* **2009**, *106*, 18908.

[361] P. J. Smeets, R. G. Hadt, J. S. Woertink, P. Vanelderen, R. A. Schoonheydt, B. F. Sels, E. I. Solomon, *J. Am. Chem. Soc.* **2010**, *132*, 14736.

[362] D. Schröder, M. Holthausen, H. Schwarz, *J. Phys. Chem. B* **2004**, *108*, 14407.

[363] E. R. Fisher, J. L. Elkind, D. E. Clemmer, R. Georgiadis, S. K. Loh, N. Aristov, L. S. Sunderlin, P. B. Armentrout, *J. Phys. Chem.* **1990**, *93*, 2676.

[364] M. T. Rodgers, B. Walker, P. B. Armentrout, *Int. J. Mass Spectrom.* **1999**, *182*, 99.

[365] D. Hippe, S. D. Peyerimhoff, *Mol. Phys.* **1992**, *76*, 293.

[366] E. Rezabal, J. Gauss, J. M. Matxain, R. Berger, M. Diefenbach, M. C. Holthausen, *J. Chem. Phys.* **2011**, *134*, 064304.

[367] E. Rezabal, F. Ruipérez, J. M. Ugalde, *Phys. Chem. Chem. Phys.* **2013**, *15*, 1148.

[368] D. Schröder, J. Roithová, E. Alikhani, K. Kwapien, J. Sauer, *Chem. Eur. J.* **2010**, *16*, 4110.

[369] C. E. Moore, *Atomic Energy Levels*; National Bureau of Standards: Washington, DC, 1952; *Natl. Bur. Stand. Circular* **1959**, *2*, 467.

[370] A. Irigoras, O. Elizalde, I. Silanes, J. E. Fowler, J. M. Ugalde, *J. Am. Chem. Soc.* **2000**, *122*, 114.

[371] A. Fiedler, D. Schröder, S. Shaik, H. Schwarz, *J. Am. Chem. Soc.* **1994**, *116*, 10734.

[372] D. Schröder, H. Schwarz, S. Shaik, *Structure and Bonding*, Springer-Verlag, Berlin-Heidelberg, **2000**, *97*, 231.

[373] R. Sarangi, N. Aboelella, K. Fujisawa, W. B. Tolman, B. Hedman, K. O. Hodgson, E. I. Solomon, *J. Am. Chem. Soc.* **2006**, *128*, 8286.

[374] K. M. Lancaster, S. D. George, K. Yokoyama, J. B. Richards, H. B. Gray, *Nat. Chem.* **2009**, *1*, 711.

[375] P. J. Donoghue, J. Tehranchi, C. J. Cramer, R. Sarangi, E. I. Solomon, W. B. Tolman, *J. Am. Chem. Soc.* **2011**, *133*, 17602.

[376] J. N. Harvey, M. Aschi, H. Schwarz, W. Koch, *Theor. Chem. Acc.* **1998**, *99*, 95.

[377] T. Chachiyo, J. H. Rodriguez, *J. Chem. Phys.* **2005**, *123*, 094711/1.

[378] N. G. Adams, D. Smith, D. Grief, *Int. J. Mass Spectrom. Ion Phys.* **1978**, *26*, 405.

[379] W. T. Huntress, M. J. McEwan, Z. Karpas, V. G. Anicich, *Astrophys. J. Suppl. Ser.* **1980**, *44*, 481.

[380] S. Wlodek, A. Fox, D. K. Bohme, *J. Am. Chem. Soc.* **1987**, *109*, 6663.

[381] D. K. Bohme, *Int. J. Mass Spectrom. Ion Processes* **1990**, *100*, 719.

[382] R. Srinivas, D. Sülzle, W. Koch, C. H. DePuy, H. Schwarz, *J. Am. Chem. Soc.* **1991**, *113*, 5970.

[383] B. E. Turner, *The Astrophysical Journal* **1998**, *495*, 804.

[384] J. C. Gómez-Martín, J. M. C. Plane, *Phys. Chem. Chem. Phys.* **2011**, *13*, 3764.

[385] D. W. Fahey, F. C. Fehsenfeld, E. E. Ferguson, L. A. Viehland, *J. Chem. Phys.* **1981**, *75*, 669.

[386] V. G. Anicich, *J. Phys. Chem. Ref. Data* **1993**, *22*, 1469.

[387] M. B. Comisarow, V. Grassi, G. Parisod, *Chem. Phys. Lett* **1978**, *57*, 413.

[388] A. S. Goldman, K. Krogh-Jespersen, *J. Am. Chem. Soc.* **1996**, *118*, 12159.

[389] A. J. Lupinetti, S. Fau, G. Frenking, S. H. Strauss, *J. Phys. Chem. A* **1997**, *101*, 9551.

[390] J. Grunenberg, R. Streubel, G. von Frantzius, W. Marten, *J. Chem. Phys.* **2003**, *119*, 165.

[391] R. F. Fenske, R. L. DeKock, A. C. Sarapu, *Inorg. Chem.* **1971**, *10*, 38.

[392] P. C. Burgers, J. L. Holmes, A. A. Mommers, *J. Am. Chem. Soc.* **1985**, *107*, 1099.

[393] S. G. Lias, J. E. Bartmess, J. F. Liebmann, J. L. Holmes, R. D. Levin, W. G. Mallard, *Gas-Phase Ion and Neutral Thermochemistry, J. Phys. Chem. Ref. Data, Supp. I.,* AIP Press, Washington DC, **1988**.

[394] T. D. Fridgen, J. L. Holmes, *Eur. J. Mass Spectrom.* **2004**, *10*, 747.

[395] Y. Yamaguchi, C. A. Richards Jr., H. F. Schaefer III, *J. Chem. Phys.* **1994**, *101*, 8945.

[396] F. George D.X, S. Kumar, *Chem. Phys.* **2010**, *373*, 211.

[397] W. Kutzelnigg, *Angew. Chem. Int. Ed. Engl.* **1984**, *23*, 272.

[398] M. Kaupp in *Anorganische Chemie - Prinzipien von Struktur und Reaktivität, Vol. 4* (Eds.: J. E. Huheey, E. A. Keiter, R. L. Keiter, R. Steudel), De Gruyter Verlag Berlin/Boston, **2012**, pp. 1043.

[399] Y.-X. Zhao, X.-L. Ding, Y.-P. Ma, Z.-C. Wang, S.-G. He, *Theor. Chem. Acc.* **2010**, *127*, 449.

[400] J. H. Poincaré, *Science and Method: Definitions and Education,* Thomas Nelson and Sons, London, **1914**, pp. 129.

[401] S. Das, G. W. Brudvig, R. H. Crabtree, *Chem. Commun.* **2008**, 413.

[402] K. Chen, A. Eschenmoser, P. S. Braun, *Angew. Chem. Int. Ed.* **2009**, *48*, 9705.

[403] M. S. Chen, M. C. White, *Science* **2010**, *327*, 566.

[404] L. Ackermann, *Chem. Commun.* **2010**, 4866.

[405] B. Breit, P. Demel, C. Schudte, *Angew. Chem. Int. Ed.* **2004**, *42*, 3786.

[406] S. Das, C. D. Incarvito, R. H. Crabtree, G. W. Brudvig, *Science* **2006**, *312*, 1941.

[407] J.-J. Li, R. Giri, J.-Q. Yu, *Tetrahedron* **2008**, *64*, 6979.

[408] C. U. Grünanger, B. Breit, *Angew. Chem. Int. Ed.* **2010**, *49*, 967.

[409] J. Wang, B. Stefane, D. Jaber, J. A. I. Smith, C. Vickery, M. Diop, H. O. Sintim, *Angew. Chem. Int. Ed.* **2010**, *49*, 3964.

[410] D. A. Colby, A. S. Tsai, R. G. Bergman, J. A. Ellman, *Acc. Chem. Res.* **2012**, *45*, 814.

[411] D. Leow, G. Li, T.-S. Mei, J.-Q. Yu, *Nature* **2012**, *486*, 518.

[412] C. B. Lebrilla, T. Drewello, H. Schwarz, *Int. J. Mass Spectrom. Ion Processes* **1987**, *79*, 287.

[413] C. B. Lebrilla, C. Schulze, H. Schwarz, *J. Am. Chem. Soc.* **1987**, *109*, 98.

[414] C. B. Lebrilla, T. Drewello, H. Schwarz, *J. Am. Chem. Soc.* **1987**, *109*, 5639.

[415] G. Czekay, K. Eller, D. Schröder, H. Schwarz, *Angew. Chem. Int. Ed. Engl.* **1989**, *28*, 1277.

[416] K. Eller, W. Zummack, H. Schwarz, *Int. J. Mass Spectrom. Ion Processes* **1990**, *100*, 803.

[417] K. Eller, W. Zummack, H. Schwarz, L. M. Roth, B. S. Freiser, *J. Am. Chem. Soc.* **1991**, *113*, 833.

[418] M. C. Holthausen, G. Hornung, D. Schröder, S. Sen, W. Koch, H. Schwarz, *Organometallics* **1997**, *16*, 3135.

[419] S. Karras, T. Prüsse, K. Eller, H. Schwarz, *J. Am. Chem. Soc.* **1989**, *111*, 9018.

[420] T. Prüsse, A. Fiedler, H. Schwarz, *Helv. Chim. Acta* **1991**, *74*, 1127.

[421] T. Prüsse, J. Allison, H. Schwarz, *Int. J. Mass Spectrom. Ion Processes* **1991**, *107*, 553.

[422] D. Schröder, H. Schwarz, *Chimia* **1989**, *43*, 317.

[423] D. Schröder, H. Schwarz, *J. Am. Chem. Soc.* **1990**, *112*, 5947.

[424] D. Schröder, F. Jeske, H. Schwarz, *Int. J. Mass Spectrom. Ion Processes* **1991**, *107*, 559.

[425] D. Schröder, H. Schwarz, *J. Am. Chem. Soc.* **1993**, *115*, 8818.

[426] D. Schröder, H. Schwarz, *J. Organomet. Chem.* **1995**, *504*, 123.

[427] S. Karras, K. Eller, C. Schulze, H. Schwarz, *Angew. Chem. Int. Ed. Engl.* **1989**, *28*, 607.

[428] S. Karrass, D. Stöckigt, D. Schröder, H. Schwarz, *Organometallics* **1993**, *12*, 1449.

[429] C. Schulze, H. Schwarz, *J. Am. Chem. Soc.* **1988**, *110*, 67.

[430] C. Schulze, T. Weiske, H. Schwarz, *Organometallics* **1988**, *7*, 898.

[431] N. Steinrück, H. Schwarz, *Organometallics* **1989**, *8*, 759.

[432] D. K. MacMillan, M. L. Gross, C. Schulze, H. Schwarz, *Organometallics* **1992**, *11*, 2079.

[433] D. Schröder, K. Eller, H. Schwarz, *Helv. Chim. Acta* **1990**, *73*, 380.

[434] D. Schröder, R. Wesendrup, C. A. Schalley, W. Zummack, H. Schwarz, *Helv. Chim. Acta* **1996**, *79*, 123.

[435] N. Dietl, M. Engeser, H. Schwarz, *Chem. Eur. J.* **2009**, *15*, 11100.

[436] M. Engeser, M. Schlangen, D. Schröder, H. Schwarz, T. Yumura, K. Yoshizawa, *Organometallics* **2003**, *22*, 3933.

[437] C. Trage, D. Schröder, H. Schwarz, *Organometallics* **2003**, *22*, 693.

[438] A. Thibblin, P. Ahlberg, *Chem. Soc. Rev.* **1989**, *18*, 209.

[439] U. Dreyer, D. Sülzle, D. Schröder, H. Schwarz, *Helv. Chim. Acta* **1990**, *73*, 2179.

[440] K. Seemeyer, T. Prüsse, H. Schwarz, *Helv. Chim. Acta* **1993**, *76*, 1632.

[441] N. Raabe, S. Karraß, H. Schwarz, *Chem. Ber.* **1994**, *127*, 261.

[442] J. Schwarz, H. Schwarz, *Helv. Chim. Acta* **1995**, *78*, 1013.

[443] A. Thibblin, *J. Phys. Org. Chem.* **1998**, *11*, 161.

[444] R. Stirzaker *Out of the Scientist's Garden,* CSIRO Publishing, Colingwood **2010**, pp. 174.

[445] K. R. Asmis, T. Wende, M. Brümmer, O. Gause, G. Santambrogio, E. C. Stanca-Kaposta, J. Döbler, A. Niedziela, J. Sauer, *Phys. Chem. Chem. Phys.* **2012**, *14*, 9377.

[446] K.-P. Dinse, H.-J. Freund, M. Geske, R. Horn, O. Korup, K. Kwapien, S. Mavlyankariev, N. Nilius, T. Risse, J. Sauer, R. Schlögl, U. Zavyalova, *2. Meeting des Scientific Advisory Board von UniCat*, Fritz-Haber-Institut Berlin, 27.-28.05.**2010**, Poster A1 - 3.

[447] J. X. Wang, J. H. Lunsford, *J. Phys. Chem.* **1986**, *63*, 505.

[448] M. Y. Sinev, Z. T. Faltakhova, V. I. Lomonosov, Y. A. Gordienko, *J. Nat. Gas Chem.* **2009**, *18*, 273.

[449] C. Hammond, S. Conrad, I. Hermans, *ChemSusChem* **2012**, *5*, 1668.

[450] W. Liang, A. T. Bell, M. Head-Gordon, A. K. Chakraborty, *J. Phys. Chem. B* **2004**, *108*, 4362.

[451] M. F. Fellah, I. Onal, *Catal. Today* **2011**, *171*, 52.

[452] E. V. Starokon, M. V. Parfenov, L. V. Pirutko, S. I. Abornev, G. I. Panov, *J. Phys. Chem. C* **2011**, *115*, 2155.

[453] P. Vanelderen, R. G. Hadt, P. J. Smeets, E. I. Solomon, R. A. Schoonheydt, B. F. Sels, *J. Catal.* **2011**, *284*, 157.

[454] K. A. Dubkov, N. S. Ovanesyan, A. A. Shteinman, E. V. Starokon, G. I. Panov, *J. Catal.* **2002**, *207*, 341.

[455] E. J. M. Hensen, Q. Zhu, M. M. R. M. Hendrix, A. R. Overweg, P. J. Kooyman, M. V. Sychev, R. A. van Santen, *J. Catal.* **2004**, *221*, 560.

[456] B. R. Wood, J. A. Reimer, A. T. Bell, M. T. J. adn K. C. Ott, *J. Catal.* **2004**, *225*, 300.

[457] G. D. Pirngruber, P. K. Roy, R. Prins, *J. Catal.* **2007**, *249*, 67.

[458] J. W. Johnson, A. J. Jacobsen, J. F. Brody, S. M. Rich, *Inorg. Chem.* **1982**, *21*, 3820.

[459] K. Eller, H. Schwarz, *Int. J. Mass Spectrom. Ion Processes* **1989**, *93*, 243.

[460] K. Eller, W. Zummack, H. Schwarz, *J. Am. Chem. Soc.* **1990**, *112*, 621.

Publications

1. *Room-Temperature C−H Bond Activation of Methane by Bare $[P_4O_{10}]^{\bullet+}$*, N. Dietl, M. Engeser, H. Schwarz, *Angew. Chem. Int. Ed.* **2009**, *48*, 4863.

2. *Thermal Homo- and Heterolytic C−H Bond Activation of Ethane and Propane by Bare $[P_4O_{10}]^{\bullet+}$: Regioselectivities, Kinetic Isotope Effects, and Density Functional Theory Based Potential-Energy Surfaces*, N. Dietl, M. Engeser, H. Schwarz, *Chem. Eur. J.* **2009**, *15*, 11100.

3. *Competitive Hydrogen-Atom Abstraction versus Oxygen-Atom and Electron Transfers in Gas-Phase Reactions of $[X_4O_{10}]^{\bullet+}$ (X = P, V) with C_2H_4*, N. Dietl, M. Engeser, H. Schwarz, *Chem. Eur. J.* **2010**, *16*, 4452.

4. *Generation, Reactivity Towards Hydrocarbons, and Electronic Structure of Heteronuclear Vanadium Phosphorous Oxygen Cluster Ions*, N. Dietl, R. F. Höckendorf, M. Schlangen, M. Lerch, M. K. Beyer, H. Schwarz, *Angew. Chem. Int. Ed.* **2011**, *50*, 1466.

5. *Directed, Remote Gas-Phase C−H and C−C Bond Activations by Metal Oxide Cations Anchored to a Nitrile Group*, N. Dietl, M. Schlangen, H. Schwarz, *Chem. Eur. J.* **2011**, *17*, 1783.

6. *Diatomic $[CuO]^+$ and Its Role in the Spin-Selective Hydrogen- and Oxygen-Atom Transfers in the Thermal Activation of Methane*, N. Dietl, C. van der Linde, M. Schlangen, M. K. Beyer, H. Schwarz, *Angew. Chem. Int. Ed.* **2011**, *50*, 5068.

7. *Catalytic Redox Reactions in the CO/N_2O System Mediated by the Bimetallic Oxide-Cluster Couple $AlVO_3{}^+/AlVO_4^{+}{}^+$*, Z.-C. Wang, N. Dietl, R. Kretschmer, T. Weiske, M. Schlangen, H. Schwarz, *Angew. Chem. Int. Ed.* **2011**, *50*, 12351.

8. *Direct Conversion of Methane into Formaldehyde Mediated by $[Al_2O_3]^{\bullet+}$ at Room Temperature*, Z.-C. Wang, N. Dietl, R. Kretschmer, J.-B. Ma, T. Weiske, M. Schlangen, H. Schwarz, *Angew. Chem. Int. Ed.* **2012**, *51*, 3703.

9. *Thermal Hydrogen-Atom Transfer from Methane: The Role of Radicals and Spin States in Oxo-Cluster Chemistry* , N. Dietl, M. Schlangen, H. Schwarz, *Angew. Chem. Int. Ed.* **2012**, *51*, 5544.

10. *Gas-Phase Reactions of Cationic Vanadium-Phosphorous Oxide Clusters with C_2H_x (x = 4,6): A DFT-based Analysis of Reactivity Patterns*, N. Dietl, X. Zhang, C. van der Linde, M. K. Beyer, M. Schlangen, H. Schwarz, *Chem. Eur. J.* **2013**, *19*, 3017.

11. *Structure and Chemistry of the Heteronuclear Oxo-Cluster $[VPO_4]^{\bullet+}$: A Model System for the Gas-phase Oxidation of Small Hydrocarbons*, N. Dietl, T. Wende, K. Chen, M. Schlangen, X. Zhang, K. R. Asmis, H. Schwarz, *J. Am. Chem. Soc.* **2013**, *135*, 3711.

12. *Mechanistic Aspects of Gas-phase Hydrogen-Atom Transfer from Methane to $[CO]^{\bullet+}$ and $[SiO]^{\bullet+}$: Why do They Differ?*, N. Dietl, A. Troiani, M. Schlangen, O. Ursini, G. Angelini, Y. Apeloig, G. de Petris, H. Schwarz, *Chem. Eur. J.* **2013**, *DOI: 10.1002/chem.201204157*.

Curriculum Vitae

Name	Nicolas Paul Richard Dietl
Born	November 6, 1984 in West Berlin
Nationality	german
Marital Status	living in partnership

10/2009 - 03/2013	PhD thesis „*Gaseous Oxo-Clusters as Model Systems for C−H-Bond Activation and Oxidation Processes – Towards a Better Understanding of Catalytic Mechanisms*“ under the supervision of Prof. Helmut Schwarz at the Technische Universität Berlin.
03/2009 - 09/2009	Diploma Thesis: „*C−H bond activation by open-shell oxide cations*“ under the supervision of Prof. Dr. Drs. h. c. Helmut Schwarz, Technische Universität Berlin.
10/2004 - 03/2009	Studies in chemistry at the Technische Universität Berlin and the ETH Zürich (Switzerland).
2004	Abitur and Baccalauréat général en *SERIE SCIENTIFIQUE* (equivalent to A levels/high school diploma - in German and French) from the Rückert-Gymnasium, Berlin, Germany.
08/1997 - 06/2004	High-school studies at the Rückert-Gymnasium, Berlin, Germany.